ADVERTIMENT. L'accés als continguts d'aquesta tesi queda condicionat a l'acceptació de les condicions d'ús establertes per la següent llicència Creative Commons: http://cat.creativecommons.org/?page_id=184

ADVERTENCIA. El acceso a los contenidos de esta tesis queda condicionado a la aceptación de las condiciones de uso establecidas por la siguiente licencia Creative Commons: http://es.creativecommons.org/blog/licencias/

WARNING. The access to the contents of this doctoral thesis it is limited to the acceptance of the use conditions set by the following Creative Commons license: https://creativecommons.org/licenses/?lang=en

Thermal characterization of Si-based nanostructures

PhD Thesis submitted by

Pablo Ferrando Villalba

To apply for the degree of Doctor in Materials Science

Supervised by

Prof. Javier Rodríguez Viejo

Dr. Aitor Lopeandía Fernández

Nanomaterials and Microsystems Group

Physics Department

Science Faculty

September 2016

El Prof. Javier Rodríguez Viejo, catedràtic d'universitat numerari del Departament de Física de la Facultat de Ciències de la Universitat Autònoma de Barcelona i el Dr. Aitor Lopeandía Fernández, professor agregat interí del Departament de Física de la Facultat de Ciències de la Universitat Autònoma de Barcelona,

CERTIFIQUEN que en Pablo Ferrando Villalba, Graduat en Física per la Universitat Autònoma de Barcelona, i en possessió del Màster oficial en Nanotecnologia i Ciència de Materials, ha realitzat sota la direcció d'ambdós el treball que porta com a títol *Thermal characterization of Si-based nanostructures* el qual recull en aquesta memòria per tal d'optar al Títol de Doctor en Ciència de Materials per la Universitat Autònoma de Barcelona.

Prof. Javier Rodríguez Viejo	Dr. Aitor Lopeandía Fernández
Bellaterra, Setembre 2016	Bellaterra, Setembre 2016

Caminante, son tus huellas
el camino y nada más;
caminante, no hay camino,
se hace camino al andar.

Antonio Machado

Agradecimientos

A lo largo de los últimos cuatro años he tenido el placer de recorrer esta larga travesía que supone el doctorado acompañado de gente maravillosa sin la cual puede que no hubiera terminado la tesis. Por eso, quiero agradecer:

A Javier Rodríguez la oportunidad que me dio de entrar en su laboratorio cuando yo cursaba cuarto de física, momento en el que me decanté por las maravillas de la nanotecnología. Sin esa oportunidad, hoy no estaría aquí. Gracias por eso y por tu amabilidad y proximidad de trato durante todo este tiempo. A Aitor Lopeandía por enseñarme con paciencia y esmero todo relativo al laboratorio entre risas y bromas y por resolverme siempre las dudas que me han surgido. A Manel Molina per permetre'm ser una lapa durant el meu primer estiu al grup, pels infinits bons moments al despatx i al bar, que ajuden a aixecar la moral, i per les barbacoes a casa teva! A Cristian Rodríguez, por tus ideas controvertidas que, aunque fastidie, le hacen a uno pensar, y por ser una fuente de locura que me permitió conservar la cordura, especialmente hacia el final de la tesis. A Joan Ràfols, pels consells sensats, les birres casolanes i els Catans de cap de setmana. A Marta González, per ajudar-me a veure el món d'una altra perspectiva, per ser *heviata* a la intimitat i sobretot per qualificar com a bones les meves paelles! A Antonio Pablo Pérez, por tus frases inigualables, tu labia y sobretodo tu simpatía. A Gemma Garcia per ajudar-me sempre que ho he necessitat i per ser l'exploradora pionera dels restaurants xinesos a Barcelona. A Gustavo Dalkiranis por ayudarme con las últimas medidas, por la comida brasileña compartida y por la alegría que transmites cuando no estás preocupado por nimiedades ;-). A Iván Álvarez i Ana Vila, per les bones estones compartides.

Quiero agradecer especialmente esta tesis a Núria Martínez por tu apoyo incondicional, celebrando los éxitos y apoyando en los fracasos (sin ti desde luego no la habría acabado) y por obligarme a viajar tanto ☺. A mis padres, Salvador y Vicen, que plantasteis la semilla de la curiosidad en mi cuando era un niño, y la habéis regado con paciencia y esmero hasta hoy. A vosotros y al resto de mi familia, Andrés, Manuel, tíos, primos y familia política por apoyarme siempre en mi decisión de estudiar un doctorado. A Isabel González, Pilar Domingo y Mercedes Marsal por inocularme el espíritu crítico desde pequeño. A vosotras y a todos los profesores que me han enseñado algo alguna vez.

A Maria Cabello, pels dinars de dijous on hem compartit desventures i pels teus consells. A Emili Gutiérrez, per ser el meu insustituible *zorro espacial*. A Alba Boix per fer-me creure amb les teves bajanades (JCG) que podia arribar a estudiar un doctorat. A Sebastià Agramunt, per demostrar-me que hi ha vida fora del doctorat. A Jose Maria, por surfear las ondas gravitacionales y ser mi Cicerone de Pisa. A Jorge, Parra, Turpin y demás compañeros físicos, por ser malas influencias.

A la gente de la JOC: Axel, Alberto, Muñacas, Natàlia, l'Eric Be, Rosa, Mr. Pareja, Jose, Pilar, Elisenda y demás, por darlo todo en cada concierto y en cada fiesta. A la gente que he tenido el placer de conocer en Crisol de cuerda por haberme ayudado a tomarme un respiro en medio de una larga temporada sin descanso.

A Llibertat Abad, por ser la jefa de los Runs y tirar para adelante todos mis dispositivos y sesiones de microscopía. A Jordi Llobet, per ser l'amo del FIB i implicar-te tant en totes les sessions. A Isabel Alonso i Miquel Garriga per la fabricació de les mostres Graded. A Alejandro Goñi por las medidas de Raman y por los momentos compartidos. A Xavier Alvarez, per desenvolupar teories tan imaginatives i per ser el prototip de físic teòric. Thanks to Luca Boarino and Natascia di Leo and Luca d'Ortenzi for the great evenings we have shared (Sempre Forza Toro!). Thanks to you and Emanuele Enrico for the great work producing and manipulating the porous nanowires.

A Belén Ballesteros, Marcos Rosado, Francisco Belarre, Irati Golvano y Emma Rossinyol, por las sesiones de microscopía que tanto han desvelado. A Manel Garcia i la resta de tècnics del departament per tota l'ajuda que m'heu donat sempre. A todos los técnicos del CNM y el ICMAB que alguna vez han participado de la fabricación de mis dispositivos. En especial a Marta Gerbolès, per implicar-te tant amb els wet etchings. A Mari Ángeles i a Raquel per tenir sempre les portes de Sala Blanca obertes i per ajudar-me en tot el que he necessitat.

A Anna Fontcuberta, per permetre'm participar de la recerca del teu grup, i per ser sempre tan amable i propera. Thanks to Heidi Potts, Gözde Tütüncüoglu, Luca Francaviglia, Jelena Vukajlovic, Luca del Carro, Hubert Flieger, Dmitry Mikulic, Esther Alarcón, Anna Dalmau and Martin Friedl for being a great company during the time I spent in Lausanne.

Gracias a Marisol Martín por acogerme en tu grupo de investigación, por tu cercanía y por todos tus consejos certeros. A Olga Caballero, por ser tan maja y ayudarme tanto en mi investigación, ¡te lo curraste *mazo*! Y porque siempre que entrabas por la puerta me

arrancabas una sonrisa (generalmente friki). A Miguel Muñoz, por ser siempre tan atento conmigo y por darme consejos siempre que lo necesité. A Raquel Álvaro y a Maria Ujue González por las sesiones y conocimientos de FIB. A Begoña Abad, Marta Rull, Liliana Vera, Jaime Andrés Pérez, András Görög, Eduardo Santos, Eduardo Lugo, Manuel Vázquez y toda la gente de la comuna de becarios, por hacerme pasar tantos buenos ratos durante los dos meses que compartimos.

A todos los que no estáis en esta lista pero que de alguna manera u otra habéis hecho de mí una mejor persona.

¡Gracias! Esta tesis es más vuestra que mía.

Table of contents

1. MOTIVATION 1

1.1 The energy problem 1

1.2 Thermoelectricity as energy scavenger technology 4

1.3 Thesis summary 5

2. HEAT TRANSPORT THEORY 7

2.1 Introduction to Thermoelectricity 7

2.2 Classical thermal transport theory 10
2.2.1 Heat equation 11

2.3 Phonons 13

2.4 Boltzmann transport equation 16
2.4.1 Phononic transport 17
2.4.2 Thermal conductivity in nanomaterials 21
2.4.3 Electronic transport 22
2.4.4 Electric current 23
2.4.5 Heat carried by electrons 24

2.5 Improving the figure of merit 25
2.5.1 Methods in bulk materials 26
2.5.1.1 Alloying 26
2.5.1.2 Doping 26
2.5.1.3 Complex unit cell 26
2.5.1.4 Lattice anharmonicity 27
2.5.1.5 Phase transitions 27
2.5.1.6 Resonant levels 27
2.5.2 Methods at the nanoscale 28
2.5.2.1 Nanomaterials and nanostructured materials 28
2.5.2.2 Confinement effects 29
2.5.2.3 Rough nanomaterials 29
2.5.2.4 Surface decoration and passivation 30
2.5.2.5 Phononic band engineering 30
2.5.2.6 Surface states 31

3. EXPERIMENTAL METHODS 33

3.1 Introduction 33

3.2 Common systems and methods 33
3.2.1 Cryostats 33
3.2.1.1 LN2 Cryostat 33
3.2.1.2 He Cryostat 35

3.2.2 Calibration of the sensors 37
3.2.2.1 $R(T)$ calibration in the LN2 cryostat 37
3.2.2.2 $R(T)$ calibration in the He cryostat 39

3.3 Suspended structures 41
3.3.1 Motivation and description 41
3.3.2 Microfabrication 42
3.3.3 Heat flow analysis 46
3.3.4 Electrical measurements 48
3.3.5 Measurement cycle 50
3.3.5.1 Resistance Calibration 50
3.3.5.2 Thermal conductivity measurement 51
3.3.6 Data reduction 51
3.3.7 Analysis of uncertainties and errors in the measurements of G_{SMP} 53
3.3.8 Corrections measuring large conductive samples. 57
3.3.8.1 Application to a real measurement on low-dimensional Si 61

3.4 3ω method 63
3.4.1 Description 63
3.4.2 Generation of $V_{3\omega}$ 64
3.4.3 Thermal analysis of the 3ω method 66
3.4.4 Sensor fabrication 70
3.4.4.1 Dielectric layer deposition 70
3.4.4.2 Sensor deposition 71
3.4.5 Electronics 71
3.4.6 Measurement cycle 72
3.4.7 Data reduction 72
3.4.8 Experimental results 72

3.5 3ω Völklein method 73
3.5.1 Motivation and description 73
3.5.2 Thermal model of the 3ω-Völklein method 74
3.5.3 Sensor optimization 78
3.5.4 Deposition of a thin-film 79
3.5.5 Microfabrication of the thermal sensor 82
3.5.6 Electronics 83
3.5.7 Experimental results 84

3.6 Conclusions 87

4. SI THIN FILMS AND NANOSTRUCTURES 89

4.1 Introduction 89

4.2 Thermal conductivity measurement 91

4.3 FIB nanopatterning 94
4.3.1 Si nanostrips 96
4.3.2 Dose optimization 97
4.3.3 Asymmetric micro/nanostructures 102

4.4 Summary 106

5. THERMAL CONDUCTIVITY OF POROUS SI NANOWIRES 109

5.1 Introduction 109

5.2 Experimental Methods 111
5.2.1 Nanowire fabrication 111
5.2.2 Manipulation 112
5.2.3 Structural characterization 113
5.2.4 Thermal measurements 116

5.3 Results 117

5.4 Conclusions 122

6. SIGE GRADED SUPERLATTICES 125

6.1 Introduction 125

6.2 Experimental Section 127
6.2.1 SL growth 127
6.2.2 Microstructural characterization 129
6.2.3 Thermal characterization 130

6.3 Results and discussion 130
6.3.1 Thermal transport across SLs 135
6.3.2 Lattice dynamics 138

6.4 Conclusions 140

7. REAL TIME THERMAL CONDUCTIVITY MEASUREMENT DURING GROWTH OF ULTRATHIN LAYERS 141

7.1 Introduction 141

7.2 Experimental Setup 142

7.3 Results 143
7.3.1 Organic thin-film layers 143
7.3.2 Metallic thin-film layers 150

7.4 Conclusions 152

8. CONCLUSIONS 155

9. BIBLIOGRAPHY 157

10. GLOSSARY 171

11. PUBLICATIONS 175

1. Motivation

1.1 The energy problem

During the last 3 centuries, the worldwide energetic production has been based on coal and oil burning. Throughout the 1st Industrial Revolution (late 1700s to early 1800s), coal was used as the main energy source for heating up steam engines and foundries. Later, during the 2nd industrial revolution (late 1800s to early 1900s), oil started to substitute coal in some processes as the steam engine was supplanted by the internal combustion engine, which was fed with fuels derived from oil. Nowadays, although there is a rapid increase of renewable sources in the developed countries, the worldwide share of primary energy production of coal, oil and natural gas sums up to 81.7% [1] (Figure 1.1).

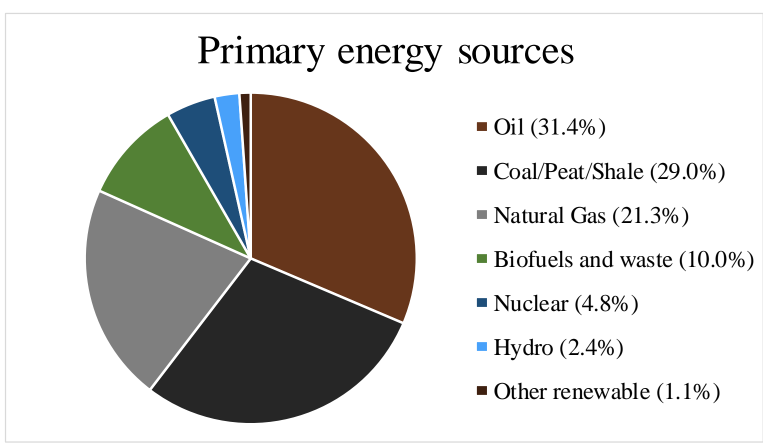

Figure 1.1 Primary energy sources in 2014[1]

There are several problems associated with this: First of all, the combustion of such fuels generates mainly CO_2, among other noxious gases like nitrogen oxides. CO_2 is transparent for visible light coming from the sun, but it reflects infrared radiation emitted by the Earth that would otherwise escape back to space. This causes the greenhouse effect that is producing a global warming (Figure 1.2) and ultimately generating a climate change, being one of the major concerns faced by humanity. As agreed by Policymakers, the rise of the world's average temperature should not exceed 1.5ºC – 2ºC, and thus, the carbon

emissions must be sharply reduced in the following decades[2]. Depending on the average temperature rise, the world will face more extreme temperatures, stronger storms, draughts and rise in the sea level[3]. All these phenomena will deeply impact the human economy and development, and will threaten the entire biosphere.

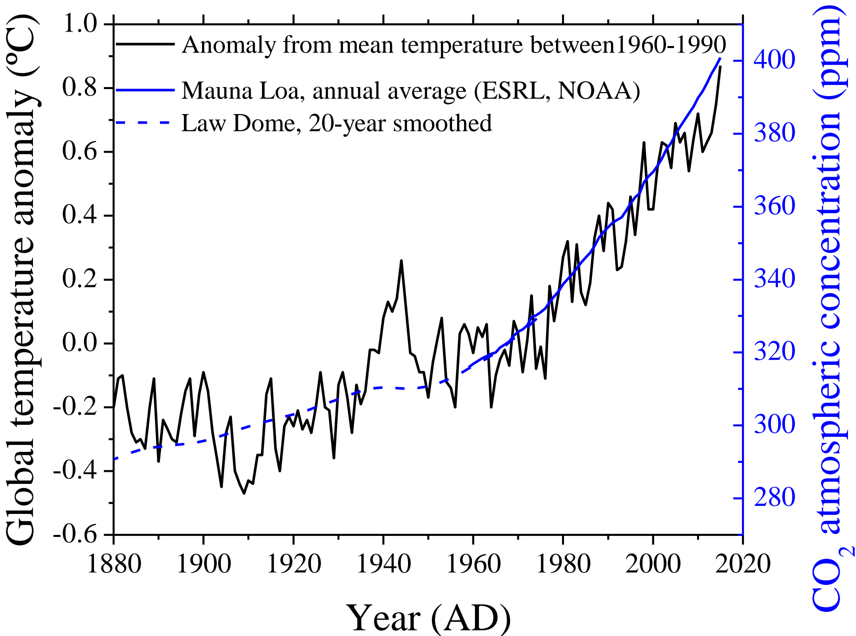

Figure 1.2 Global temperature anomaly[4,5] and CO_2 atmospheric concentration[6–8] from 1880 to 2016

Another drawback of fossil fuels is that they are non-renewable (they are not naturally replenished in a human timescale), so the reserves will come to an end if the actual consumption pace is maintained. The production rate of such energy sources is characterized by a peak function, first described by Hubbert. First, the production of the resource grows exponentially as new fuel reservoirs are found, but when all the existing reservoirs are being exploited, the extraction becomes more difficult and it starts decreasing until all the existing fuel has been extracted. Although this model has some limitations that difficult the prediction of the peak position[9], it can shed light on how much fuel is left in the world. For oil, the peak in production is estimated to appear in the upcoming years.

In order to avoid the aforementioned issues, the worldwide use of fossil fuels must be reduced. There are mainly four possible ways of doing so:

1) Reduce the global energy demand

This is very difficult to achieve in the short to mid-term, since the energy demand is closely related with the GDP per capita: while there are some differences between countries, a higher GDP implies a higher energy demand. This demand has been steadily increasing at a rate of 2.4%/year during the last 165 years, and thus it is very unlikely that this trend will change soon[10]. Only in developed countries, where the GDP per capita and the population growth tends to stabilize, the increased energy productivity (GDP per energy consumption) allows the reduction of energy demand driven by the increase in the consumption efficiency.

2) Increase the efficiency of energy generation, conversion and transport

Regarding the efficiency of energy production, transport and usage, there is a lot of room for improvement. The efficiency in the generation of electricity using a thermodynamic cycle (like Stirling or Rankine) is always ideally limited by the Carnot's cycle efficiency, which only depends on the temperature of the heat source and the heat sink of the engine:

$$\eta_C = 1 - \frac{T_C}{T_H} \tag{1.1}$$

Nowadays, the energy efficiency of coal-, oil-, and nuclear-powered plants is about 32%, whereas for natural gas-powered plants this value is 23.6%[11]. There are many ways of improving this efficiency, for example the implementation of new burning methods like Pulverized Coal Combustion (PCC) combined with supercritical and ultra-supercritical steam can boost the efficiency up to 40% or even 50% in coal-powered plants [12].

The efficiency improvement in the transport of electricity can be achieved by improving the grid management. The delocalization of the power generators as well as the implementation of a smart grid[13,14] can contribute to this end, reducing the distance that the power has to travel through the grid. Also, research on materials with less electrical resistance for the cable core (ultimately the Holy Grail of room-temperature superconductors) could greatly reduce the energy waste during power transport.

Similarly, great efforts are made for improving the efficiency in transports. The fuel consumption per unit distance has been consistently decreasing for the last 11 years in automobiles[15]. Lately, this has been achieved with the introduction of hybrid technology and the optimization of both diesel and gasoline engines triggered by fuel price volatility

and emission policies. In the case of electric cars, they need less energy to work, since they do not need a thermodynamic cycle to produce the electricity. However, the electricity used in these cars must be produced by a power plant, and depending on the share of plants using fossil fuels, they can emit very different values of CO_2. This leads to the next point:

3) Change the primary energy sources for carbon-free and renewable ones.

The share of renewable power plants is also a critical factor for reducing the dependence on fossil fuels. These power plants rely on resources that are quasi-infinite for a human scale. For example: solar, wind or geothermal. The development of solar and wind power during the last 2 decades has outpaced the production of coal and oil power-plants in some countries. More concretely, the photovoltaic solar production has exponentially increased while the cost per peak Watt ($/Wp) of solar panels has sunk also exponentially.

Although renewable sources are ultimately necessary for fulfilling the energy demand in the long term, they cannot just replace fossil fuels. The reason is that while the production of regular power plants can be controlled matching instantly the power demand, solar and wind plants rely on fluctuating sources. Thus, extra effort must be put in developing energy storing technologies like batteries or heat storage.

4) Close the carbon cycle

Carbon dioxide capture and Storage (CCS) is a technology with the potential of cutting up to 90% of the carbon emissions in fossil fuel fired plants[12]. Although this method is very promising for reducing the carbon emissions in the mid-term, it does not solve the problem of the availability of fossil fuels. However, this method can push forward the transition to zero-carbon energy generation during the proliferation of renewable source power plants.

1.2 Thermoelectricity as energy scavenger technology

Thermoelectricity is another way of scavenging energy not only from nature but also from the exhaust heat of human activities. To do so, a thermoelectric material must be placed between two bodies at different temperatures, which will produce a voltage in open circuit proportional to the Seebeck coefficient of the material. If a pn junction (thermocouple) is placed in the hot or cold side, the Seebeck coefficients of both materials sum up and

produce a higher voltage. A thermoelectric generator (TEG) can be formed by connecting many thermocouples electrically in series and thermally in parallel.

The potential of this technology is very high as it could increase the efficiency of already existing power plants and automobiles, even it could become alone a new power generation technology from naturally occurring temperature gradients in nature (geothermal or sun-generated, for example). However, nowadays this inversion would not produce a proper economical return due to the low efficiency and high price of such devices. Even if prices may reduce in the future thanks to the optimization of device fabrication and materials, their use would still be confined to scavenger applications. As in the case of piezoelectric generators, TEGs can actually be used to power up small devices that should otherwise be plugged. This permits, for example, using wearable medical sensors, charging a mobile phone or powering sensors in inaccessible places.

1.3 Thesis summary

This thesis is committed to give a better insight into the processes that affect thermal transport in potential materials for thermoelectric generation, which is key for achieving a high efficiency. Moreover, the study of thermal properties of nanomaterials is necessary for improving heat management in solid-state devices, where a high thermal conductivity is needed to avoid high temperatures that would produce long-term irreversible damage. This research would also allow the conception of new logical devices that work with heat flow instead of electrons.

In the first part of the thesis, the necessary tools for measuring the thermal conductivity of nanomaterials are developed. Two cryostats are set up along with the temperature control systems that allow measuring at stable temperatures. Later, three sensors are developed for measuring the thermal conductivity of different materials. First, suspended structures intended for measuring the in-plane thermal conductivity of suspended membranes and nanowires are fabricated, and the errors and uncertainties produced in such measurements are characterized. Second, the 3ω method is introduced, allowing the measurement of the out-of-plane thermal conductivity in thin films. The emergence of the 3ω voltage is demonstrated, and the relation between this voltage and the thermal conductivity of the substrate and the thin-film is found. Finally, a sensor for measuring with the 3ω-Völklein method is developed, which allows characterizing the in-plane thermal conductivity of thin-films during the layer growth.

With these tools, several Si-based materials are studied. First, the thermal conductivity of suspended Si membranes is measured, finding the expected reduction in thermal conductivity due to phonon surface scattering. Moreover, the nanopatterning of these Si membranes with focused ion beam (FIB) is optimized through a systematic study of its amorphization, paving the way to produce nanostructures with reduced thermal conductivity. Second, the thermal conductivity of porous Si nanowires is studied for wires with different porosity, length and diameters, showing an unexpected dependence on its diameter that suggests that the wire core is generally less porous than the shell. Next, the thermal conductivity of a novel SiGe graded superlattice is measured, showing a considerable reduction in its thermal conductivity, even below the thin-film alloy limit. Finally, the thermal conductance of a suspended SiN_x membrane is measured with a high precision while depositing on it organic (TPD) and metallic (Indium) materials. The results show an initial conductance reduction that cannot be explained with the Fourier law. This reduction is found to be related to an increased diffusive boundary scattering, which could be easily extrapolated to other thermoelectric nanomaterials, reducing their thermal conductivity.

2. Heat transport theory

2.1 Introduction to Thermoelectricity

Thermoelectricity is the ability of some materials to produce a voltage in response of a temperature gradient and to generate a heat flux when a current is fed through them. These phenomena were independently discovered by Thomas Johann Seebeck in 1822 and Jean Athanase Peltier in 1834, respectively.

Thomas Seebeck found that when imposing a temperature gradient on a circuit made of two close-looped dissimilar metals, the magnetic needle from a compass that was placed between the junctions was deflected[16,17], which induced him to assume the existence of a thermomagnetic effect. Hans Christian Oersted, having recently found that electrical currents generated magnetic fields and reacted to them, realized that the underlying mechanism for which the needles aligned was the generation of a current inside them, and coined the term *Thermoelectricity*[18].

The Seebeck effect (Figure 2.1a) can be quantitatively described by the following equation:

$$V = (S_1 - S_2)\Delta T \tag{2.1}$$

Where V is the voltage generated in open circuit, S_1 and S_2 are the Sebeck coefficients of materials 1 and 2, and ΔT is the temperature difference between the junction and the measurement point.

Some years later, Jean Charles Athanase Peltier discovered that when feeding a current through a circuit made of several materials, the junctions heated or cooled depending on the polarity of the applied voltage. This result was named the Peltier effect (Figure 2.1b), which is described by the formula:

$$Q = (\Pi_1 - \Pi_2)I \tag{2.2}$$

Where I is the current fed to the circuit, Π_1 and Π_2 are the Peltier coefficients of materials 1 and 2 and Q is the heat flux generated.

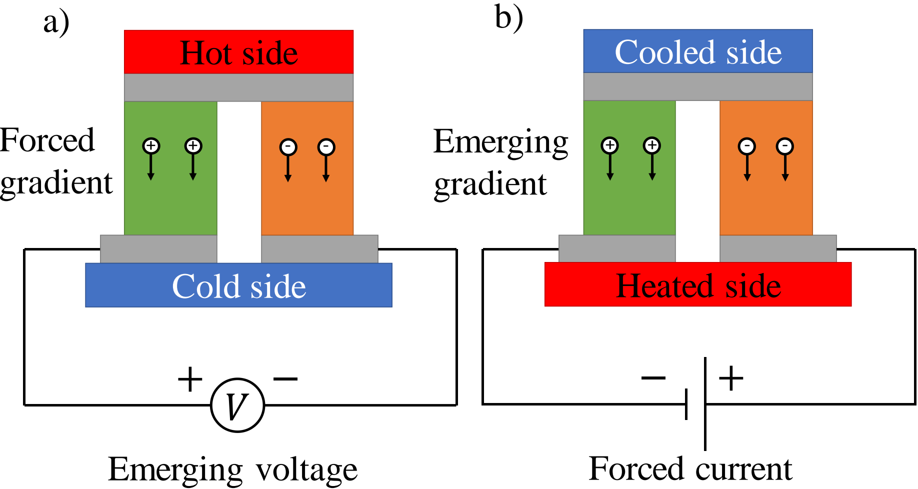

Figure 2.1 Visual description of the Seebeck effect (a) and the Peltier effect (b). In the first case, a temperature gradient produces a voltage along the thermocouple, while in the second case a current flowing through the thermocouple generates a heat flux.

A thermoelectric generator is a heat engine that transforms a heat flow into work. The efficiency of this process (and any other heat engine) is limited by the Carnot cycle efficiency. This cycle is composed of four processes, two isothermal and two isentropic, that do not generate entropy overall, meaning that the cycle is reversible and thus ideal. For this reason, the Carnot cycle has the maximum efficiency possible for the conversion of heat into work, which is related only to the heat source and the heat sink temperatures (T_H and T_C) through the expression:

$$\eta_C = 1 - \frac{T_C}{T_H} \tag{2.3}$$

The efficiency of a real heat engine (that generates entropy) is always lower than the Carnot cycle efficiency, and is generally written as the product between η_C and a factor that is smaller than one. In the case of a thermoelectric generator, the efficiency can be expressed as[19]:

$$\eta_{TE} = \eta_C \frac{\sqrt{1+\overline{ZT}}-1}{\sqrt{1+\overline{ZT}}+\frac{T_C}{T_H}} \quad (2.4)$$

Here, $\overline{ZT}$ is the combined thermoelectric figure of merit of the materials forming the generator at the mean temperature $\bar{T} = (T_H + T_C)/2$. The figure of merit of an individual material is defined as

$$ZT = \frac{\sigma S^2}{k} T = \frac{\sigma S^2}{k_l + k_e} T \quad (2.5)$$

where σ is the electrical conductivity, S is the Seebeck coefficient and $k = k_e + k_l$ is the thermal conductivity, the sum of the electronic, k_e, and the lattice, k_l, components. As appears from equation (2.5), increasing σ and S and reducing k leads to a higher figure of merit and thus, to a better conversion efficiency. Alternatively, for some applications (like generating a voltage from a quasi-infinite heat reservoir) it is not necessary to have the best efficiency but the best performance, which is achieved by maximizing the power factor σS^2, regardless of k.

Improving the figure of merit of a material is challenging, since the main parameters involved in equation (2.5) are linked and cannot be independently modified. This explains the absence of suitable thermoelectric materials in nature. The Wiedemann-Franz law states that the ratio between the electronic component of the thermal conductivity and the electrical conductivity at a given temperature is the same for any metal or degenerated semiconductor:

$$\frac{k_e}{\sigma T} = L \quad (2.6)$$

Where L is the Lorentz number and is approximately constant. The relationship holds in such materials because the electrons carry both the current and the vast majority of the heat (as compared to the lattice). This law impedes the improvement of the thermoelectric figure of merit by either reducing the thermal conductivity or increasing the electrical one, since in both cases the ratio σ/k_e will stay constant. For this reason, the poor thermoelectric properties of metals cannot be easily improved.

Another coupling in the variables of the ZT relation is the reciprocity relation between the Seebeck coefficient and the electrical conductivity: generally, doping a semiconductor

(either p or n) increases its electrical conductivity, but it also reduces its Seebeck coefficient given that the Seebeck voltage emerging from a temperature difference is reduced through the increased conductivity of the material itself. The relationship between S and the doping concentration is called the Pisarenko relation.

During the 20th century, the figure of merit of the most efficient thermoelectric materials improved almost exclusively with the development in the 70's of alloyed materials, especially Bi_2Te_3-based, that reached values of ZT near 1. However, after this improvement, ZT values remained around 1 for almost 30 years. In 1993 Hicks and Dresselhaus published a seminal paper[20] predicting an increase of the thermoelectric performance in artificially nanostructured materials. This work induced a boost of new research and activities in the field of thermoelectricity that persists today. In parallel, the increased ability to synthesize nanostructured materials via top-down or bottom-up approaches has resulted in new materials with promising characteristics reaching ZT values over 2 [21,22].

In the next sections, the classical thermal transport theory is introduced in order to derive the heat equation, which will be used in Chapter 3 to describe the sensors used in the thesis. Then, phononic and electronic transport mechanisms will be briefly discussed and the thermoelectric effect will be derived from the Boltzmann Transport Equation. Finally, with the knowledge acquired through the chapter, several methods for improving the thermoelectric figure of merit will be discussed.

2.2 Classical thermal transport theory

Classical Irreversible Thermodynamics (CIT) is a theoretical framework that has been widely used for modeling the thermal behavior of many systems since the 19th century and relies in the fact that one can define a local equilibrium at any point of a system slightly out of equilibrium. However, it was later found to be incapable of explaining some phenomena like ballistic transport and the evolution of systems with ultrafast heating rates or very large heating gradients. Thermodynamics have since evolved for solving the issues of CIT and to explain new discoveries like the second sound. In this framework, Extended Irreversible Thermodynamics was developed, among others, to explain a wide variety of physical phenomena[23]. In this thesis we will mainly use CIT to describe the thermal behavior of the sensors used given that they are not submitted to high heating rates.

2.2.1 Heat equation

In order to find the heat equation, we start with the general balance equation

$$\frac{\partial}{\partial t}(\rho b) = -\nabla \boldsymbol{J}^b + \sigma^b \tag{2.7}$$

Where ρ is the density of the medium, b is in general any quantity, $\boldsymbol{J}^b$ is the flux of b per unit area and σ^b is the rate of production of b per unit volume. The balance equation states the continuity of b which means that the variation of b inside a volume equals the generated amount of b inside that volume minus the outgoing flux through the boundary of the volume. If this equation is applied to the internal energy of a system, namely u, and ρ is assumed to be constant in time, this yields:

$$\rho \frac{\partial u}{\partial t} + \nabla \boldsymbol{q} = q \tag{2.8}$$

Where $\boldsymbol{q}$ is the heat flux per unit area and q is the internally generated heat rate per unit volume. The internal energy can be written in terms of the temperature and the heat capacity, c:

$$\left(\frac{\partial u}{\partial T}\right)_{p=cte} = c \rightarrow \partial u = c \partial T \tag{2.9}$$

Also, in the frame of Classical Irreversible Thermodynamics (CIT) where local equilibrium is assumed, the heat flux obeys the Fourier law (if the effect on the heat flux produced by other driving forces is ignored):

$$\boldsymbol{q} = -k \nabla T \tag{2.10}$$

Substituting (2.10) and (2.9) in (2.8), one gets:

$$\rho \frac{\partial (cT)}{\partial t} - \nabla \cdot (k \nabla T) = q \tag{2.11}$$

Assuming that c and k are constant and escalar, the equation reads as:

$$\rho c \frac{\partial T}{\partial t} - k\nabla^2 T = q \tag{2.12}$$

This is a parabolic differential equation commonly named as Heat Equation. It describes the diffusion of heat inside a material with a temperature gradient and/or an internal heat source, and by applying the correct initial and boundary conditions it can be used to find the temperature distribution in any system. Applying it to a thermal sensor is ultimately necessary for relating the thermal conductivity of the material under test to the measured temperatures. In Chapter 3 this equation is applied to the sensors used in the thesis (Suspended structures, 3ω sensor and 3ω-Völklein sensor).

Now we will find the behavior of a solid connected to a heat bath at temperature T_0 by a given thermal conductance (Figure 2.2) using the heat equation, which will shed light on the stabilization time of an arbitrary system. We start by integrating (2.12) through the volume of the solid:

$$\int_V \rho c \frac{\partial T}{\partial t} dV - \int_V k\nabla^2 T dV = \int_V q dV \tag{2.13}$$

Applying Gauss' Theorem in the second term of the left-hand side (Assuming the solid has a surface area A):

$$\int_V k\nabla \cdot (\nabla T) dV = \int_A k\nabla T dS \tag{2.14}$$

One gets:

$$C \frac{\partial T}{\partial t} + kA\nabla T = Q \tag{2.15}$$

Where $C = \rho c V$ and $Q = qV$. The plus sign in the second term of (2.15) appears from the selection of the gradient direction towards the system. If the gradient is linearized as $\nabla T = (T - T_0)/L = \Delta T/L$, we get:

$$C \frac{\partial T}{\partial t} + G\Delta T = Q \tag{2.16}$$

Where $G = kA/L$ is the thermal conductance from the solid to the bath at temperature T_0.

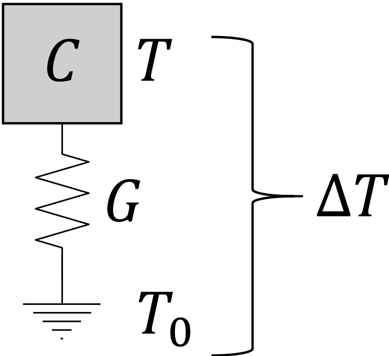

Figure 2.2: 0-Dimensional system consisting of a thermal mass C at temperature T connected to a heat bath at T_0 through a thermal conductance G.

This equation states clearly the conservation of energy: if a total heat Q is generated inside the solid, it is spent in the dynamical heating $C\frac{\partial T}{\partial t}$ and in heat conduction through the surface, $G\Delta T$. Assuming zero heat generation, $Q = 0$, one can rearrange the terms:

$$\frac{dT}{\Delta T} = -\frac{dt}{C/G} \equiv -\frac{dt}{\tau} \tag{2.17}$$

Where $\tau \equiv C/G$ is the thermal relaxation time of the system. The integral at both sides of the equation yields:

$$\ln\frac{\Delta T}{\Delta T_0} = -\frac{\Delta t}{\tau} \rightarrow \Delta T = \Delta T_0 e^{-\frac{\Delta t}{\tau}} \tag{2.18}$$

Where ΔT_0 is the initial temperature difference and Δt is the amount of time elapsed after the system was in its initial state. As can be seen, τ is the characteristic time of the exponential decay of ΔT. This important parameter should be characterized in any thermal sensor, since in order to have a stable measurement the system must be thermally in steady state, which happens only at a times $t \gg \tau$ after creating a perturbation (for example, generating heat by Joule effect). Although this analysis has been performed in a 0D system, it can be extrapolated to a 3D system in most cases.

2.3 Phonons

The equations derived in the previous section analyze the heat flow from the perspective of a continuous medium, ignoring the microscopic nature of temperature and heat. In order to truly understand thermal transport (especially in nanomaterials), the microscopic

picture is inevitably needed, as the atomic interactions with the boundaries, interfaces or imperfections of the lattice play an important role.

In a crystalline solid, the movement of atoms is oscillatory around the atomic position in the lattice, and the oscillations of each atom are propagated through the lattice as mechanical waves. These waves can be classified in normal modes called phonons, the superposition of which can give rise to any arbitrary lattice vibration.

The phonon dispersion relation $\omega(\boldsymbol{k})$ –that is, the energy (frequency) of the phonon for a given momentum (wavenumber), can be calculated starting with the Hamiltonian of the crystal lattice assuming the harmonicity of the potential[24]. For an infinite 1D chain composed of only 1 kind of particle with mass m, particle distance a and elastic constant g between particles, the dispersion relation is:

$$\omega(k) = \sqrt{\frac{2g(1 - \cos k_x a)}{m}} = 2\sqrt{\frac{g}{m}}\left|\sin\frac{k_x a}{2}\right| \tag{2.19}$$

As can be seen in Figure 2.3, the dispersion relation is linear near the origin and the phonon group velocity $v_g = d\omega/dk_x$ and phase velocity $v_p = \omega/k_x$ is equal. For higher wavenumbers, the curve bends until the group velocity is 0 at $k_x = \pi/a$, the limit of the 1st Brillouin Zone (BZ).

When atoms of different masses are intercalated in the chain, the unit cell is then composed of a pair of particles, instead of just one, which produces the appearance of another phononic branch –the optical one, opposing to the previous acoustic branch. In this case, the dispersion relations are:

$$\omega_{\pm}^2(k_x) = g\left(\frac{1}{m_1} + \frac{1}{m_2}\right) \pm g\sqrt{\left(\frac{1}{m_1} + \frac{1}{m_2}\right)^2 - \frac{4\sin^2 k_x a/2}{m_1 m_2}} \tag{2.20}$$

The optical modes $\omega_+(k_x)$ arise from the movement of particles against their nearest neighbor, as long as this neighbor occupies a different position in the unit cell. Their group velocity is generally smaller than the one of acoustic branches (Figure 2.3), and therefore in most bulk materials optical phonons do not contribute significantly to heat propagation.*

* However, it has been recently found that optical modes can contribute up to 20% in nanomaterials since their reduced MFP is not affected by the boundary scattering as much as the MFP of acoustic phonons[207]

In a 3-dimensional crystal, there are 3 times the branches of a 1D crystal, since each branch splits in two transverse and one longitudinal branch, representing the propagation of transversal waves (polarized in 2 orthogonal axes) and longitudinal waves, respectively. In general, the number of branches equals $d \cdot N$, where d is the dimensionality of the crystal and N is the number of atoms per unit cell. From these, the number of acoustic branches is d, while the number of optical branches is $d(N-1)$.

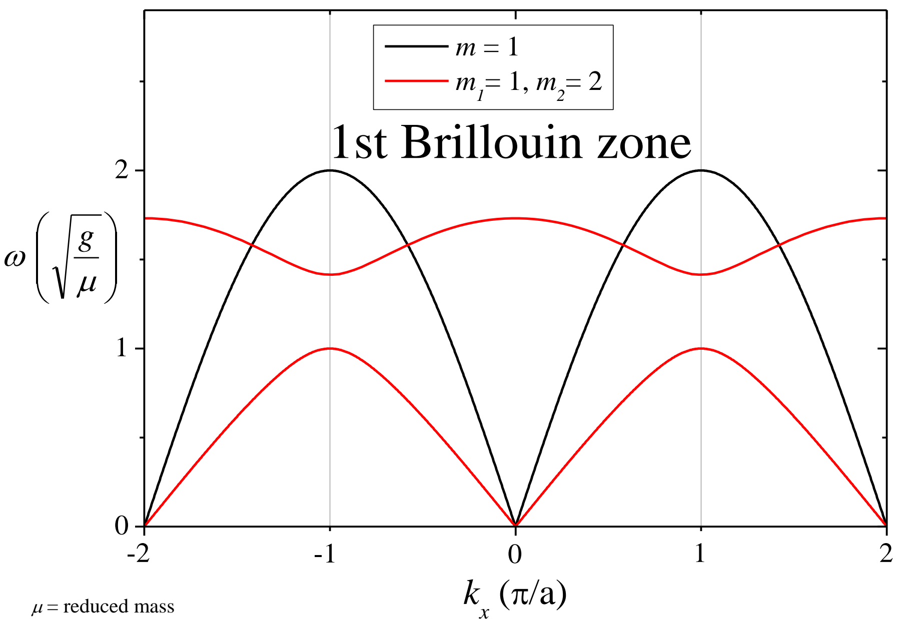

Figure 2.3: Dispersion relations of a single-particle 1D chain (black) and a two-particle 1D chain (red)

An important consequence of phononic branches is that a phonon with a momentum $k_x > \pi/a$ (this is, outside the 1st Brillouin zone, or 1st BZ) has the same energy as a phonon with a momentum $k_x' = k_x - 2\pi/a$ (Figure 2.3). The origin of this effect lays on the discontinuity of the crystal, since a vibration in an atomic chain cannot be represented by a vibration mode with a wavelength shorter than twice the atomic separation, as shown in Figure 2.4. As will be discussed later, this effect gives rise to the Umklapp scattering.

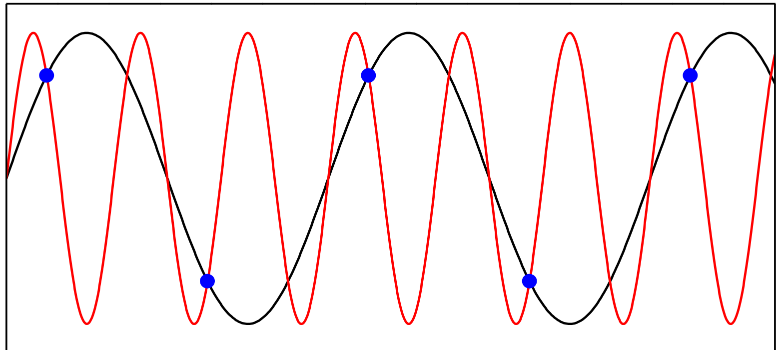

Figure 2.4: Atomic vibration represented by phonons with different frequencies. In this case, the red wave does not carry more information than the black wave since it has a wavelength shorter than twice the atomic distance.

2.4 Boltzmann transport equation

The Boltzmann Transport Equation (BTE) describes the evolution of a thermodynamic system out of equilibrium from a kinetic perspective. In this section, the BTE will be applied to phonons and electrons in order to calculate the electrical and thermal conductivities as well as the thermoelectric properties of a crystalline solid[24,25]. It is a powerful tool since it allows to understand the importance of microscopic properties in transport phenomena, and permits evaluating the transport properties of nanomaterials. Although more complex mathematical tools have been developed (like molecular dynamics or density functional theory), the kinetic theory is usually sufficient to describe the thermal properties of nanomaterials.

The general form of the BTE is the following:

$$\frac{\partial f}{\partial t} = \left(\frac{\partial f}{\partial t}\right)_{col} - \frac{d\boldsymbol{r}}{dt} \cdot \nabla f - \frac{d\boldsymbol{p}}{dt} \cdot \nabla_p f \tag{2.21}$$

Where f is the distribution function of the particles (i.e. Maxwell-Boltzmann, Fermi-Dirac or Bose-Einstein distribution depending on the nature of the particles), $\boldsymbol{r}$ is the position vector of a given point of the space and $\boldsymbol{p}$ is its momentum. The BTE states that the time variation of a given function f inside a small volume of the phase space $\boldsymbol{drdp}$ is a sum of the variation due to collisions plus the amount of f flowing into or out from the small volume. More concretely, the term $\frac{dr}{dt} \cdot \nabla f$ refers to the motion of the distribution

function and $\frac{d\boldsymbol{p}}{dt} \cdot \nabla_p f$ to the application of an external force that changes the momentum of the distribution function.

2.4.1 Phononic transport

When applying the BTE to phonons, the Bose-Einstein distribution function with the energy term equal to $\hbar\omega$ should be used.

$$f_0(\omega) = \frac{1}{e^{\frac{\hbar\omega}{k_B T}} - 1} \tag{2.22}$$

The sub index 0 denotes that the system is in equilibrium. The application of the BTE to this distribution function implies the drop of the term $\frac{d\boldsymbol{p}}{dt} \cdot \nabla_p f$, since no force can be applied to phonons. On the other hand, the term $\frac{d\boldsymbol{r}}{dt} \cdot \nabla f$ can be rewritten as:

$$\frac{d\boldsymbol{r}}{dt} \cdot \nabla f(\omega) = \frac{\partial f(\omega)}{\partial T} \boldsymbol{v}_g(\omega) \cdot \nabla T \tag{2.23}$$

Where $\boldsymbol{v}_g$ is the group velocity. Introducing (2.23) and (2.22) in (2.21) and considering the system to be in steady state (this is, $\frac{\partial f(\omega)}{\partial t} = 0$) yields:

$$\frac{\partial f(\omega)}{\partial T} \boldsymbol{v}_g(\omega) \cdot \nabla T = \left(\frac{\partial f(\omega)}{\partial t}\right)_{col} \tag{2.24}$$

Now, if the distribution function is near equilibrium, this is $f - f_0 \ll f_0$, the collision term can be approximated by the next formula:

$$\left(\frac{\partial f}{\partial t}\right)_{col} = -\frac{f(\omega) - f_0(\omega)}{\tau(\omega)} \tag{2.25}$$

This is the relaxation time approximation, which states that due to scattering processes, the out-of-equilibrium distribution tends exponentially to the equilibrium one with a characteristic time τ. The relaxation time is a result of all the scattering processes that the phonon experiences, and according to the Matthiessen's rule, it can be calculated by adding all the inverse relaxation times produced by independent processes

$$\frac{1}{\tau(\omega)} = \sum_i \frac{1}{\tau_i(\omega)} \tag{2.26}$$

Generally, the relaxation time is frequency dependent as phonons with different frequencies have different scattering rates for the same process. With this approximation, the BTE results in:

$$\frac{\partial f(\omega)}{\partial T} \boldsymbol{v}_g(\omega) \cdot \nabla T = -\frac{f(\omega) - f_0(\omega)}{\tau(\omega)} \tag{2.27}$$

Finally, near equilibrium we can also approximate $\frac{\partial f}{\partial T} \cong \frac{\partial f_0}{\partial T}$:

$$f(\omega) - f_0(\omega) = -\frac{\partial f_0(\omega)}{\partial T} \tau(\omega) \boldsymbol{v}_g(\omega) \cdot \nabla T \tag{2.28}$$

This final form of the BTE relates the difference between the out-of-equilibrium and the equilibrium distributions with the product of the temperature derivative of the equilibrium distribution, the relaxation time, the group velocity and the temperature gradient.

Now, the heat flux generated by a temperature gradient in the x direction can be calculated as the product of phonon states out of equilibrium per unit volume, the speed at which phonons propagate and the energy carried by each phonon mode:

$$dq_x = v_{g,x}\big(f(\omega) - f_0(\omega)\big)D(E)dE = \hbar v_{g,x}\big(f(\omega) - f_0(\omega)\big)D(\omega)d\omega \tag{2.29}$$

Where $D(\omega)$ or $D(E)$ is the phonon density of states. Substituting the equation (2.28) into (2.29) and integrating, one gets

$$\begin{aligned} q_x &= -\int_0^{\omega_{max}} \hbar \frac{\partial f_0(\omega)}{\partial T} \tau v_{g,x}^2(\omega) \frac{\mathrm{d}T}{dx} D(\omega) d\omega \\ &= -\frac{1}{3}\int_0^{\omega_{max}} \hbar \frac{\partial f_0(\omega)}{\partial T} \tau v_g^2(\omega) \frac{\mathrm{d}T}{dx} D(\omega) d\omega \end{aligned} \tag{2.30}$$

Where $v_{g,x}^2 = \frac{v_g^2}{3}$, as we are also considering the random movement of phonons in the y and z directions. Also, the limiting frequency of the integral is usually defined as $\omega_{max} = k_B T_D/\hbar$, where T_D is the Debye temperature.

With the expression of the heat flux, the thermal conductivity can be calculated. According to the Fourier law,

$$k_l = -\frac{\boldsymbol{q}}{\nabla T} = -\frac{q_x}{dT/dx} = \frac{1}{3}\int_0^{\omega_{max}} \hbar \frac{\partial f_0(\omega)}{\partial T} \tau(\omega) v_g^2(\omega) D(\omega) d\omega \quad (2.31)$$

This expression can be rewritten as

$$k_l = \frac{1}{3}\int_0^{\omega_{max}} v_g^2(\omega)\tau(\omega)C(\omega)d\omega \quad (2.32)$$

By introducing the spectral heat capacity

$$C(\omega) = \frac{\partial f_0(\omega)}{\partial T} D(\omega)\hbar\omega \quad (2.33)$$

Finally, summing up all the phononic branches leads to:

$$k_l = \frac{1}{3}\sum_{\lambda}\int_0^{\omega_{max}} v_g^2(\omega)\tau(\omega)C(\omega)d\omega \quad (2.34)$$

This general expression allows us to calculate the thermal conductivity of a crystalline material knowing its phononic band structure and the frequency dependent scattering rate of phonons. It can also be written as

$$k_l = \frac{1}{3}\sum_{\lambda}\int_0^{\omega_{max}} v_g(\omega)l(\omega)C(\omega)d\omega \quad (2.35)$$

Where $l(\omega) = v_g(\omega)\tau(\omega)$ is the mean free path (MFP) of phonons (this is, the average distance traveled by a phonon between scatterings) and can be also added up using the Matthessien's rule.

$$\frac{1}{l(\omega)} = \sum_i \frac{1}{l_i(\omega)} \quad (2.36)$$

In order to calculate the thermal conductivity, the main phonon scattering sources must be known. The most important scattering mechanisms in bulk materials are the following[26]:

Umklapp scattering: this is a phonon-phonon scattering where the resulting phonon falls outside the 1st BZ. As this resulting phonon has an equivalent momentum inside the 1st BZ, the momentum is not conserved. This scattering happens mostly at high temperatures, since is only produced with the collision of two phonons with high momentum. Usually, the MFP of this scattering mechanism is modeled as $l_U^{-1} \propto T^3 e^{-A/T}$.

Impurity scattering: This accounts for the scattering events between a phonon and an impurity in the crystal e.g. a doping atom or an interstitial atom. Usually it is modeled as the Rayleigh scattering of light, i.e. with a ω^4 dependence: $l_I^{-1} \propto \omega^4$.

Strain scattering: This scattering mechanism originates with the interaction between phonons and strain fields inside the crystal due to the anharmonicity of the vibrations (a harmonic vibration is insensitive to the strain fields). The strain fields may be created by crystalline defects or macroscopic material bending. In this case, $l_S^{-1} \propto \omega$.

Boundary scattering: Depending on the average phonon MFP of the material, the boundary scattering can become an important scattering source in bulk crystalline materials, especially at low temperatures. This scattering mechanism is produced when a phonon reaches the boundary of a material and is reflected, either in a specular or diffusive way. In polycrystalline materials, it also applies when phonons reach a grain boundary. The MFP of the boundary scattering is $l_B^{-1} \propto \frac{1}{L}\frac{1-s}{1+s}$, where L is the size of the material/grain and s is the specularity parameter (the probability that a given phonon scatters specularly).

Normal scattering: This phonon scattering mechanism consists on elastic collisions between phonons with the resulting phonon laying inside the 1st BZ. This scattering term cannot be included with the other inelastic scattering sources since it does not produce a relaxation of the distribution function into f_0. Other strategies, like the one used in the Callaway model[27] (where he defined another relaxation process that led to a displaced distribution function) may be followed in order to take this scattering mechanism into account.

Another method of taking into account normal scattering was proposed by Guyer and Krumhansl[28]. They propose a collective transport regime in which all the phonons interact normally with each other much more frequently than any other resistive scattering mechanism. A linear combination between this collective regime and the usual kinetic

regime with a weighting factor that depends on the ratio between normal and resistive relaxation times results in thermal conductivity values in good agreement with experimental data[29].

2.4.2 Thermal conductivity in nanomaterials

Thermal conductivity has been classically considered an intrinsic property of any material, meaning that it does not depend on the material size or shape (in contrast to extrinsic magnitudes like the internal energy or the entropy). However, with the study of the thermal properties of nanomaterials it was experimentally found that their thermal conductivity was much lower than the one of their bulk counterparts[30]. This reduction can be explained by equation (2.35), as in nanomaterials the total mean free path shrinks due to the enhanced boundary scattering, effectively reducing the thermal conductivity when L approaches the bulk mean free path.

The boundary scattering also arises in the heat flow perpendicular to thin films. In this case, when the film thickness is much smaller than the bulk MFP, phonons only scatter against the interface between the thin film and the surrounding materials, generating the so called ballistic transport (Figure 2.5). In the ballistic limit, the Fourier law is no longer valid since this kind of transport generates discontinuous temperature profiles in the interfaces, while the temperature inside the thin film may be constant throughout its thickness. This can be macroscopically modeled with a thermal boundary resistance at the interface of dissimilar materials.

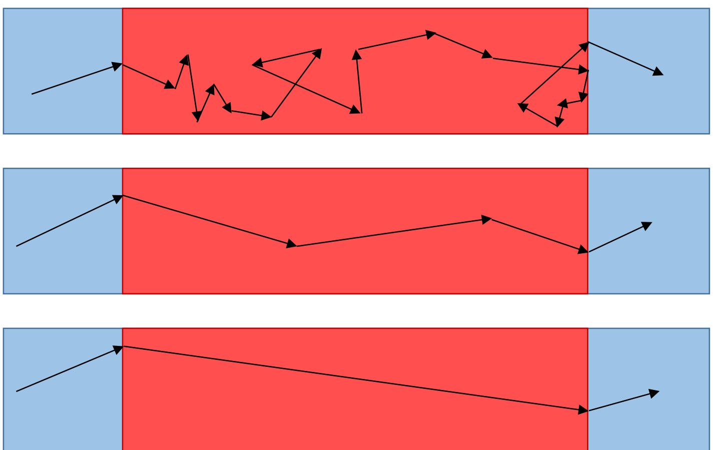

Figure 2.5: From top to bottom, schemes of diffusive transport, quasi-ballistic transport and ballistic transport inside a nanomaterial.

2.4.3 Electronic transport

The BTE can also be used to find the origin of the thermoelectric effect by calculating the heat and the charge transported by electrons in the presence of an arbitrary temperature gradient and electric field. In the case of electrons, equation (2.21) in steady state and with $\frac{dp_x}{dt} = (-e)E_x$ reads

$$f - f_0 = -\tau\left(v_x \frac{\partial f_0}{\partial x} - \frac{eE_x}{m}\frac{\partial f_0}{\partial v_x}\right) \tag{2.37}$$

Here m is the electron effective mass and f_0 is the statistical distribution for electrons, which is the Fermi-Dirac distribution:

$$f_0 = \frac{1}{e^{\frac{\varepsilon-\zeta}{k_B T}} + 1} \tag{2.38}$$

Where ε and ζ are the electron energy and the chemical potential measured from the conduction band edge:

$$\varepsilon = E - E_c = \frac{\hbar^2 \boldsymbol{k}^2}{2m} = \frac{1}{2} m\boldsymbol{v}^2 \tag{2.39}$$

$$\zeta = \mu - E_c \tag{2.40}$$

The spatial derivative of the Fermi-Dirac distribution in equation (2.37) can be calculated in the presence of a thermal gradient in the x direction. Since the chemical potential is temperature dependent, we cannot neglect its spatial derivative:

$$\frac{\partial f_0}{\partial x} = -\frac{\partial f_0}{\partial \varepsilon}\left(\frac{d\zeta}{dx} + \frac{\varepsilon - \zeta}{T}\frac{dT}{dx}\right) \tag{2.41}$$

The derivative of the distribution with respect to the velocity is easily evaluated:

$$\frac{\partial f_0}{\partial v_x} = \frac{\partial f_0}{\partial \varepsilon} m v_x \tag{2.42}$$

Substituting (2.41) and (2.42) into (2.37) one gets

$$f - f_0 = \tau v_x \left(\frac{d\zeta}{dx} + \frac{\varepsilon - \zeta}{T} \frac{dT}{dx} + eE_x \right) \frac{\partial f_0}{\partial \varepsilon} \qquad (2.43)$$

2.4.4 Electric current

With equation (2.43) one can calculate the electric current density (similarly to the heat current of phonons) as the product of the particle charge, the particle velocity and the particle density:

$$J_x = \int_0^\infty (-e) v_x D(\varepsilon)(f - f_0) d\varepsilon \qquad (2.44)$$

Introducing (2.43) into (2.44) yields:

$$J_x = L_{11} E'_x + L_{12} \left(-\frac{dT}{dx} \right) \qquad (2.45)$$

With

$$L_{11} = -\frac{e^2}{3} \int_0^\infty v^2 \tau D(\varepsilon) \frac{\partial f_0}{\partial \varepsilon} d\varepsilon \qquad (2.46)$$

$$L_{12} = \frac{e}{3T} \int_0^\infty v^2 \tau D(\varepsilon) \frac{\partial f_0}{\partial \varepsilon} (\varepsilon - \zeta) d\varepsilon \qquad (2.47)$$

$$E'_x = \frac{1}{e} \frac{d\zeta}{dx} + E_x \qquad (2.48)$$

Here, the effective electric field E'_x takes into account the gradient in the chemical potential, which can produce by itself an electron flow. Equation (2.45) can be used to calculate both the electrical conductivity and the Seebeck coefficient. In the absence of a temperature gradient, equation (2.45) becomes:

$$J_x = L_{11} E_x \equiv \sigma E_x \qquad (2.49)$$

Where σ is the electrical conductivity, as it is the ratio between the current density and the electric field applied. As can be seen it is defined positive, since the negative slope of the Fermi-Dirac distribution cancels out the minus sign in front of equation (2.46). Also,

given the peak nature of the derivative of (2.38), the electrons that contribute most to the conduction are the ones located around the chemical potential ζ.

On the other hand, if we impose the current density to be 0, equation (2.45) reads:

$$E'_x = \frac{L_{12}}{L_{11}}\frac{dT}{dx} \equiv S\frac{dT}{dx} \tag{2.50}$$

Here, the Seebeck coefficient S is defined as L_{12} divided by L_{11}. It must be noted that the S is negative in the case of an increasing $D(\varepsilon)$, meaning that the electric field opposes the temperature gradient. This is an expected result in the electron gas model, since at higher temperatures its density is lower than at low temperatures, thus creating a particle (and charge) accumulation at the cold side. In the case of p-doped Si, where carriers can be thought to be positive holes instead of electrons, the accumulation of positive charges in the cold side produces an electric field parallel to the temperature gradient.

2.4.5 Heat carried by electrons

Now we will calculate the amount of heat transported by electrons. In contrast to the phonon heat flux, in the case of electrons we must take into account the energy flux and the particle flux since we are treating an open system with a chemical potential:

$$dq_x = dU - \zeta dN = (\varepsilon - \zeta)dN = v_x D(\varepsilon)(f - f_0)(\varepsilon - \zeta)d\varepsilon \tag{2.51}$$

Integrating both sides of the equation one gets

$$q_x = \int_0^\infty v_x D(\varepsilon)(f - f_0)(\varepsilon - \zeta)d\varepsilon = L_{21}E'_x + L_{22}\left(-\frac{dT}{dx}\right) \tag{2.52}$$

Where

$$L_{21} = \frac{e}{3}\int_0^\infty v^2\tau D(\varepsilon)\frac{\partial f_0}{\partial \varepsilon}(\varepsilon - \zeta)d\varepsilon = TL_{12} \tag{2.53}$$

$$L_{22} = -\frac{1}{3T}\int_0^\infty v^2\tau D(\varepsilon)\frac{\partial f_0}{\partial \varepsilon}(\varepsilon - \zeta)^2 d\varepsilon \tag{2.54}$$

From this set of equations, one can easily find the Peltier coefficient, defined as the heat flux generated when a current is flowing, and the thermal conductivity of the material. For doing this, we should first substitute the electric field from equation (2.45) into equation (2.52), yielding:

$$q_x = \frac{L_{21}}{L_{11}} J_x + \left(L_{22} - \frac{L_{21}L_{12}}{L_{11}}\right)\left(-\frac{dT}{dx}\right) \tag{2.55}$$

If we impose the temperature gradient to be 0, it turns out that

$$q_x = \frac{L_{21}}{L_{11}} J_x \equiv \Pi J_x \tag{2.56}$$

Where Π is the Peltier coefficient. Alternatively, imposing a null current density yields

$$q_x = \left(L_{22} - \frac{L_{21}L_{12}}{L_{11}}\right)\left(-\frac{dT}{dx}\right) \equiv k_e\left(-\frac{dT}{dx}\right) \tag{2.57}$$

Where k_e is the electronic thermal conductivity. Here, the effect of the Peltier heat flow created by the Seebeck voltage arising with the gradient has been taken into account. Without thermoelectric effects, the electronic thermal conductivity reads $k_e = L_{22}$.

From the parameters derived in this section, the ratio between the electronic component of the thermal conductivity and the electrical conductivity can be approximated to:

$$\frac{k_e}{\sigma T} = \frac{\pi^2 k_B^2}{3e} \equiv L \tag{2.58}$$

This is, in fact, the Wiedemann-Franz Law, and shows that the Lorentz number is constant.

2.5 Improving the figure of merit

Up to date, many strategies have been followed to increase the figure of merit of a given material. With the information provided in this chapter, some of these strategies are discussed here.

2.5.1 Methods in bulk materials

2.5.1.1 Alloying

The simplest yet effective way of improving the thermoelectric performance of a semiconducting material composed of only one element is alloying it with other elements. This increases the phonon impurity scattering, which scatters high frequency phonons and reduces k_l, leaving the electrical transport practically unaffected[31].

2.5.1.2 Doping

The doping level in a semiconductor has a huge influence in its thermoelectric performance, since it affects S, σ, k_l and k_e. First, increasing the doping concentration increases the carrier concentration (either electrons or holes), which directly enhances σ and also k_e through the Wiedemann-Franz law. Also, as stated by the Pisarenko relation, the increase in the carrier concentration reduces S due to the improved electrical connection between the hot and cold parts of the material, which reduces the emerging voltage (it can be seen in (2.50) with the relationship between S and σ). Finally, k_l is reduced due to the increased scattering produced by the randomly positioned atomic impurities. Generally speaking, the optimal doping density is found around 10^{19} cm^{-3} [31].

2.5.1.3 Complex unit cell

Various materials with complex unit cells have been studied for their enhanced thermoelectric performance. Here, Clathrates and Skutterudites are discussed.

A Clathrate is a general denomination for such crystals where a matrix structure cages another atom or molecule. In thermoelectricity, the most efficient Clathrates are produced by a type IV atomic framework (Si, Ge or Sn). The host atoms, usually heavy species like Ba, Ga, Eu or Sr, are poorly bonded to the surrounding atoms, producing a rattling effect that reduces the thermal conductivity. Nevertheless, the electrical conductivity is enhanced due to the increased carrier concentration provided by the dangling bonds of the filling atoms. Values of ZT around 1.5 have been found in Clathrates of type I[32,33].

Skutterudites are crystalline materials with the general formula $(Co,Ni,Fe)(P,Sb,As)_3$ that have a large unit cell with 2 voids inside it. These voids can be filled with other atomic substances that both provide free electrons to the material and reduce the thermal conductivity through an increased impurity scattering as well as the rattling effect also found in Clathrates[34]. In this way, filled Skutterudites show good thermoelectric figures of merit, above unity[35].

2.5.1.4 Lattice anharmonicity

The anharmonicity of a crystalline structure represents the deviation of the atomic vibrations from a harmonic oscillation. An increased lattice anharmonicity produces more frequent phonon-phonon collisions, both Normal and Umklapp, which reduce vastly the thermal transport. It can be represented by the Grüneisen paramenter, which is a measure of how much the phonon mode frequencies change if the unit cell volume is altered. Generally, high Grüneisen numbers are associated with high anharmonicities. Materials with high Grüneisen parameters can be produced by generating lone pair electrons inside the structure, which yields cation-cation repulsion generating soft phonon modes[36]. As an example, the effect of the anharmonicity is very pronounced in SnSe, a crystalline material with lone pairs around Sn^{2+} ions which shows a maximum value of $ZT = 2.6$. In this case, the high Grüneisen parameters (the maximum being 7.2 in the a axis) are correlated with the anomalously low values of the thermal conductivity that contribute to such a high figure of merit.

2.5.1.5 Phase transitions

In a phase transition, the material properties can significantly change due to a rearrangement of the crystalline structure, improving the figure of merit[37]. As demonstrated by Liu et al.[38], the 2nd order phase transition in Cu_2Se produces a huge increment in the thermopower, while the thermal conductivity is vastly reduced and the electrical one slightly increases. This produces a peak in the figure of merit 7 times higher than the value at room temperature. The authors argue that this enhancement is produced by a critical electron and phonon scattering arising from the coexistence of phases. Doping the material with iodine allows shifting the transition temperature and thus the temperature range at which ZT is boosted.

2.5.1.6 Resonant levels

The Seebeck coefficient has a direct dependence on the Fermi level (ζ) position respect to the density of states. Looking at L_{12} (expression (2.47)), the term $\frac{\partial f_0}{\partial \varepsilon} v^2(\varepsilon - \zeta) = \frac{\partial f_0}{\partial \varepsilon} \frac{2\varepsilon}{m}(\varepsilon - \zeta)$ is antisymmetric around ζ if $\zeta \gg k_B T$, and considering $\tau D(\varepsilon)$ to be nearly constant around ζ, the integral of such a function would yield zero. In order to achieve a non-antisymmetric function, the density of states $D(\varepsilon)$ should have a sharp variation around ζ. In a 3-dimensional material[39], $D(\varepsilon) \propto \sqrt{\varepsilon}$, which has a sharp slope near $\varepsilon = 0$. In this case, the chemical potential ζ should be slightly above 0 in order to produce a big

value for L_{12}. This would also produce a very small electrical conductivity, i.e. L_{11}, yielding a high S. This is observed for example in slightly doped Si, which presents a huge Seebeck coefficient $S_{Si} \cong 800\ \mu V/K$. If the DoS presents other peaked shapes this also allows to create a huge S by a precise doping of the material[40]. Another method to improve S consists on doping the material with resonant impurities, which generate new electronic states that can produce sharp variations on the density of states in energies near the Fermi Level (Figure 2.6). This was demonstrated in Tl doped PbTe, achieving a maximum figure of merit of 1.5 [41].

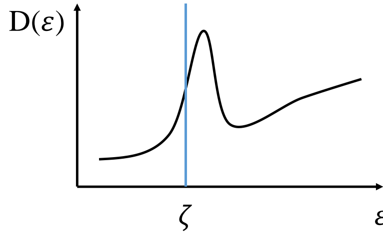

Figure 2.6: The coincidence of the Fermi level with a high slope in the density of states produces an enhanced Seebeck coefficient. This can be achieved, for example, via resonant impurities or nanoscaling.

2.5.2 Methods at the nanoscale

2.5.2.1 Nanomaterials and nanostructured materials

The main drive of the ZT improvement in the last 20 years has been the reduction of the thermal conductivity in nanosized materials compared with their bulk counterparts due to the added boundary scattering contribution that reduces the heat flow produced by high-MFP phonons[42,43]. In addition, this scattering term does not affect significantly the electronic transport in the mesoscale (material size around 100 nm) since electrons generally present lower MFP values, so the electrical conductivity is preserved. The same effect is produced in nanostructured materials like superlattices, where the added thermal boundary resistances reduce the heat flow, while the good crystalline quality preserves the electronic conduction[44–46].

Another approach to boost the figure of merit is to combine several scattering mechanisms at different length scales in order to reduce the propagation of all-range-frequency phonons. Several combinations so far used are point-defect + boundary scattering[47,48], point-defect + nanosized-inclusion scattering[49] and the three mechanisms at once[21]. To perform the last strategy, the authors first produced atomic disorder by doping PbTe with Na. Second, they included nanometer-sized endotaxial precipitates of SrTe to scatter mid-frequency phonons. Finally, grain boundaries in the mesoscale were produced by spark

plasma sintering to scatter low-frequency phonons. With this method, a promising $ZT = 2.2$ was achieved.

In another study, Zhao et al.[22] reduced significantly the thermal conductivity of bulk PbTe by including MgTe inclusions with sizes of 2 nm into a matrix of polycrystalline PbTe with 2 μm grains. In this case, the ambipolar contribution to the thermal conductivity (this is, the one produced by thermally excited electrons and holes) got reduced through an increased bandgap produced by the MgTe inclusions. All together produced a high value of the figure of merit, $ZT = 2$.

2.5.2.2 Confinement effects

In materials smaller than roughly 30 nm another effect may come into play. At this scale, the size of the material is comparable to the phonon wavelength in some materials like Si, and thus vibrational modes are constrained by the dimensionality of the material[50].This produces several changes in the material properties. To start with, an elastic softening is produced by the coupling of acoustic and flexural modes. This reduces the frequencies of the acoustic branches, which in the end diminishes the group velocity of such phonons. This effect alone can produce a thermal conductivity below the amorphous limit of the bulk material[51].

In even smaller materials, the electron confinement gives rise to peaked or sharply varying electronic density of states, corresponding to the quantized states in the confined directions[52]. More concretely, the density of states of a 2-Dimensional electron gas (2DEG) is of the form $D(\varepsilon) \propto \theta(\varepsilon)$, where $\theta(\varepsilon)$ is the Heaviside step function, whereas in a 1DEG, $D(\varepsilon) \propto 1/\sqrt{\varepsilon}$ at each quantized energy level. As has been previously stated, these sharp changes can produce an enhanced thermopower if they are coincident with the Fermi level (Figure 2.6).

2.5.2.3 Rough nanomaterials

The surface quality is an important parameter in nanomaterials that can affect many of its properties since they present a very high surface-to-volume ratio. It has been shown that an increased roughness reduces the thermal conductivity compared with smooth nanomaterials[30,53,54]. The effect of surface roughness has been thoroughly studied in the literature[53,55–58]. In general, the boundary scattering is characterized with a specularity parameter that takes into account the amount of phonons that scatter specularly with the boundaries (Figure 2.7). The boundary roughness generates a multifrequency diffusive

scattering that reduces the specularity parameter. The spectral distribution of the roughness plays an important role, and a high intensity of the roughness at different wavelengths is key to reduce the thermal transport, as demonstrated by Lim et al.[53].

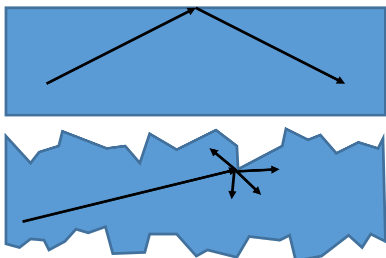

Figure 2.7: Boundary scattering is enhanced in rough boundaries due to an increased diffuse scattering.

2.5.2.4 Surface decoration and passivation

As was stated in the previous method, the alteration of the surface produces enhanced phonon scattering. This alteration can be produced by other means different than changing the surface topography. For example, the deposition of discrete particles (surface decoration) can also reduce the thermal conductivity, as was found in Ge-decorated Si nanowires[59]. In this case, according to molecular dynamics simulations[60], the reduction was likely produced by the strong interaction between the decorating particles and the nanomaterial, inducing a reduction in the vibrational DoS of the Si atoms and the localization of low frequency phonons. According to similar simulations presented in the same paper, the surface passivation of the nanowire with continuous films can also reduce the thermal conductivity values of a nanowire as a consequence of phonon interference in the core-shell interface. However, it was experimentally shown that for very thin Ge-Si core-shell nanowires there was no k reduction, but a difference in the trend of the curve $k(T)$ compared with the Ge nanowires[61]. The effect of the surface passivation can be generalized to all materials, especially those with high phonon MFP where boundary scattering is the main source of phonon scattering.

2.5.2.5 Phononic band engineering

Manipulating a material in the same length scale than the wavelength of a phonon allows altering the vibrational mode and thus the wave propagation and the mechanical response of the material to external stimuli. This can be done in the macroscopic scale (sound waves), microscopic scale (hypersound) and down to the nanometer scale (thermal vibrations)[62]. Exploiting this concept, several structures can be produced that, for example, backscatter sound waves only in one direction or isolate a region of space from

external mechanical waves. An interesting example for thermoelectric applications is the Phononic Crystal (PnC) [63], consisting of a crystalline material with periodic inclusions of other materials or gaps, like for example a 2-dimensional Si nanomesh[64,65]. These inclusions, apart from producing an increased phonon scattering, alter the vibrational modes of atoms, effectively flattening the phonon branches and reducing the group velocity v_g, which has a direct impact in the thermal conductivity (as stated in equation (2.35)).

2.5.2.6 Surface states

The electronic states of a material near its surface can vary sharply due to the proximity of the vacuum potential barrier producing the so-called surface states. These states appear in the energy bandgap of a semiconductor and can produce free electrons near the surface, increasing the electrical conductivity of the material. As was demonstrated by Kim et al.[66] surface states can be produced in Bi, which due to the reduced effective electron mass (~$0.001m_e$), become important in wires with diameters as large as 30 nm. They found an increase in σ as well as reduction in the thermopower from the expected values, both probably due to the surface states. However, the combined power factor $S^2\sigma$ found was as high as 0.005 $W \cdot m^{-1} \cdot K^{-2}$. This method may be extended to other metallic materials with low electron effective mass.

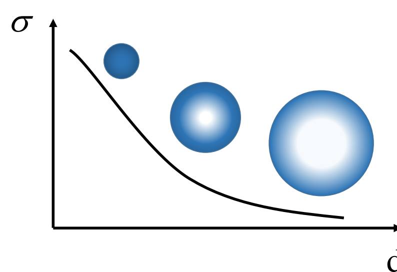

Figure 2.8: The presence of surface states in thin nanowires enhances the electrical conductivity. The darker regions of the wires depict zones where the electron density of the surface states is high. In the thinnest wires, the surface states are prevalent in the whole wire.

3. Experimental Methods

3.1 Introduction

There is a variety of new techniques developed in the past 20 years or so aimed at measuring heat transport in thin films or nanowires[67]. In this chapter, we will describe the techniques and setups built during this thesis. 3 techniques have been developed for measuring the thermal conductance of nanowires and thin films both in the in-plane and the out-of-plane directions: Suspended structures, the 3ω method and the 3ω Völklein method. They are electrical-based methods where metallic elements are used both as heaters and temperature sensors to stablish non-equilibrium thermal scenarios required for transport measurements.

First, the common systems and methods used in all the measurements are discussed, and then each one of these 3 techniques for measuring thermal conductivity as well as the sensors developed are deeply analyzed.

3.2 Common systems and methods

3.2.1 Cryostats

All the measurements performed with the sensors described in this chapter have been carried out in high vacuum and at a controlled temperature. For this purpose, two cryostats have been used: a liquid nitrogen (LN2) immersion cryostat and a closed-cycle He gas cryostat.

3.2.1.1 LN2 Cryostat

This is a home-made cryostat consisting of a tubular vessel made of 5 mm thick steel (Figure 3.1a). The electrical connections are inserted into the chamber using a feedthrough with a 15 pin D-Sub connector. Inside the chamber, the wiring consists of varnished copper wires with a diameter of 0.75 mm.

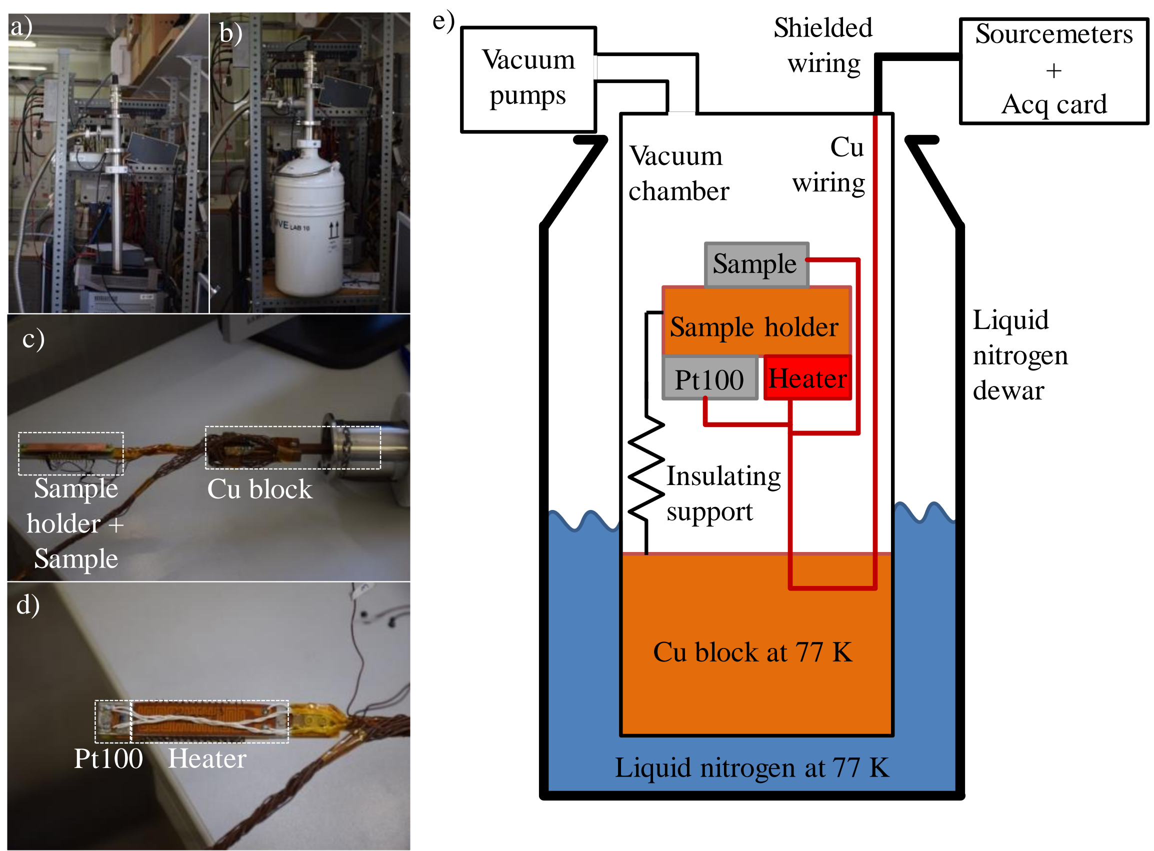

Figure 3.1: Liquid nitrogen cryostat. a) Cryostat. b) Cryostat inside the LN2 Dewar. c) Elements inside the cryostat (Sample holder and Cu block). d) Backside of the sample holder (with visible Pt100 and heater). e) Sketch of the whole cryostat.

The vacuum is achieved with a scroll pump (that produces primary vacuum from room pressure) and a turbomolecular pump (that produces high vacuum starting from the primary one). This system can achieve a pressure of 10^{-5} mbar at room temperature after just 1h of turbomolecular pumping. Below this pressure, the convection and conduction through air is completely suppressed, which is a necessary condition for all measurements performed here.

In order to cool down the cryostat, it must be immersed into liquid nitrogen, or LN2 (Figure 3.1b). Normally this is done by slowly introducing the chamber into a LN2 Dewar (avoiding LN2 fast evaporation and boiling) and letting it thermalize during 1-2 hours. Inside the cryostat, there is a copper block that cools down by contact with the steel walls. The large thermal mass of this copper block helps damping temperature oscillations and therefore allows using it as a temperature reference bath to which the sample holder and all the wiring are connected (Figure 3.1c). Connecting the wires to this block prevents the heat carried by them from the feedthrough to heat up the sample and stabilizes the

temperature gradients along them, therefore minimizing fluctuations of the thermoelectric potential that may appear during operation.

The sample holder, which is made by a 3 mm thick Al plate with an area of 100x12 mm^2, is connected to the copper block with a steel stick. Since steel is quite thermally insulating ($k_{steel} \cong 14 \frac{W}{m \cdot K}$), the thermal constant of the sample holder ($\tau = \frac{C}{G}$) is high, damping any fluctuation inside it.

The sample holder temperature is controlled using a custom-made PID system developed in Labview. The temperature is determined by measuring the resistance of a cryogenic Pt100 sensor with a Keithley 2700, and the heat is produced by feeding a controlled current into a kapton-based heater using a Keithley 2400 (Figure 3.1d). The use of high precision sourcemeters (6,5 digits) permits reaching reduced temperature peak-to-peak noises (below 1 mK) in the whole range of operation temperatures from 150 to 400 K.

The sample is mounted to the sample holder using a commercial ceramic socket (Kyocera KD-S84015-A). The sample is glued to the socket with silver paste, and the socket is fixed to the sample holder with metallic clamps and with N-Apiezon grease in between. This procedure greatly enhances the thermal contact between the sample and the sample holder, which permits a better control of the sample temperature. Finally, a radiation shield is mounted on the sample in order to prevent heat exchange with the cryostat walls, which can be at a temperature several hundreds of Kelvin below the sample temperature. The shield is made of copper foil, and is clamped to the sample holder also with N-Apiezon.

3.2.1.2 He Cryostat

This cryostat is a commercial model fabricated by Advanced Research Systems (ARS) (Figure 3.2a,e). It is a closed cycle cryostat, which has the benefit of reusing indefinitely the He inside it. The functioning principle is the following: The He is compressed up to 260 psi in the external compressor, which heats up the He. Then, it is cooled down to room temperature using a water stream. The helium is then conduced to the cryostat through an insulated pipe. Once there, it is decompressed, absorbing heat from the cold finger (where the sample is placed, Figure 3.2c,d). Finally, the He is re-conduced to the compressor through another insulated pipe, closing the cycle. This system allows cooling the cryostat down to 4K, temperature at which He condenses.

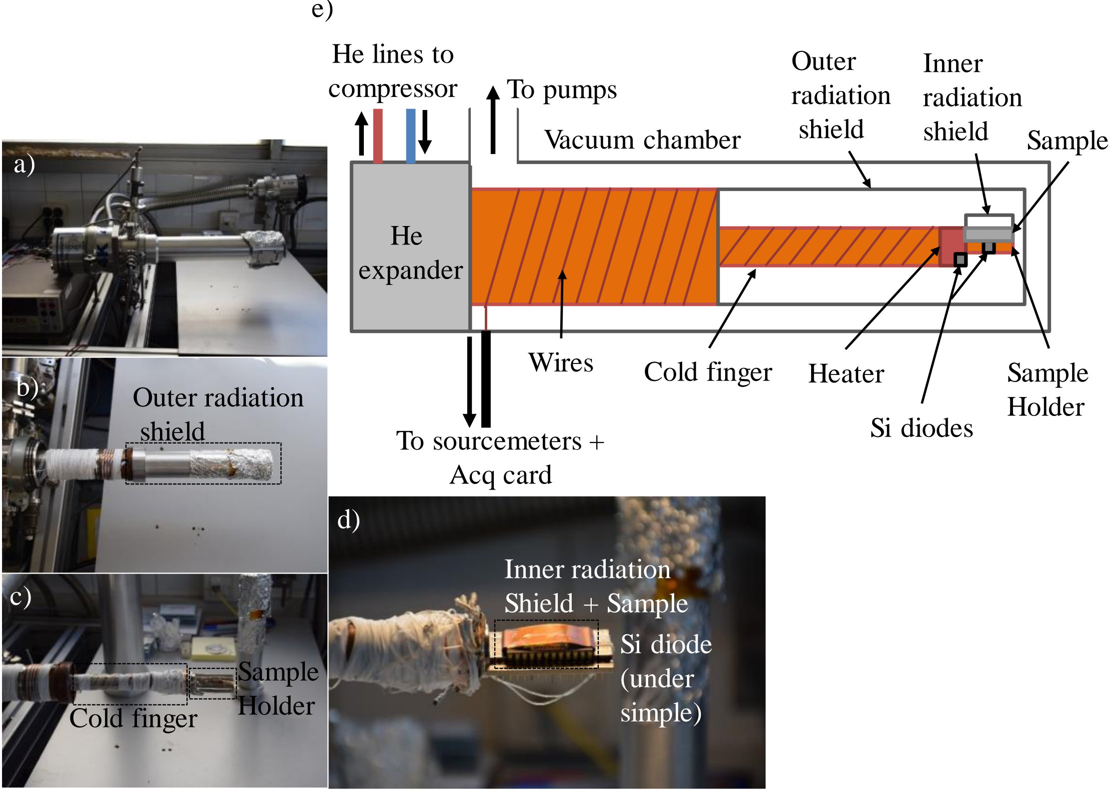

Figure 3.2: Closed cycle He cryostat. a) Cryostat. b) Inside the cryostat, the outer radiation shield is attached to the first stage. c) Inside the outer shield, the sample holder is attached to the cold finger. d) Detail of the sample holder with the inner radiation shield. e) Sketch of the whole cryostat.

The temperature is controlled by a commercial PID system that introduces heat by means of a Kapton heater and reads the temperature from a Si diode beneath the heater. There is a second Si diode beneath the sample used to measure its temperature, which may differ as much as 1 K from the other diode. The temperature fluctuations are around 0.05 K and are mainly produced by the He expander. The use of Si diodes instead of Pt100 sensors owes to the enhanced sensitivity of diodes at low temperatures compared to Pt100 sensors, which are no longer temperature-sensitive at low temperatures since their resistance is dominated by electron-boundary scattering (which is temperature independent).

The sample is mounted using the same procedure as in the LN2 cryostat on the tip of the cold finger, clamping it on the Si diode. An inner Cu radiation shield at the holder temperature is introduced in order to bring the temperature of the sample closer to the diode temperature (Figure 3.2d). In this cryostat, an outer radiation shield at 10-15 K is placed around the cold finger so it can reduce its thermal contact with the environment, which is at approx. 290 K.

3.2.2 Calibration of the sensors

When a sensor is slightly heated during operation, its resistance increases due to the positive dependence of the resistivity with the temperature of metals. This increase can be approximated, for low temperature variations with

$$R = R_0 + \frac{dR}{dT}\Delta T \quad (3.1)$$

Where R_0 and R are the sensor base resistance and heated resistance, respectively, dR/dT is the temperature dependence of the resistance and ΔT is the temperature rise of the sensor. In order to transform the measured resistance to a temperature rise, the term dR/dT must be calibrated by measuring at several base temperatures the resistance, avoiding the self-heating of the sensor.

The procedure used to calibrate the sensors resistance as a function of the temperature is the following: First, the temperature is stabilized using the PID system (normally, the stabilization time is set to 30 minutes). Then, the resistance of the sensor is measured using an AC current small enough to avoid the self-heating of the sensor. The possible high uncertainty arising from the use of such a low current is compensated by performing the measurement several times. This procedure is repeated at several temperatures that span throughout the range at which the final experiment is performed.

After this, the data points are fitted with a function the derivative of which is used as the $\frac{dR}{dT}$ at any temperature.

3.2.2.1 $R(T)$ calibration in the LN2 cryostat

For the measurements performed inside the LN2 cryostat, the fitting function used is a parabola:

$$R = A + BT + CT^2 \quad (3.2)$$

Where A, B and C are the parameters of the fit. In this way, the $\frac{dR}{dT}$ applied at each temperature is computed as

$$\frac{dR}{dT} = B + 2CT \tag{3.3}$$

An example of this can be seen in Figure 3.3.

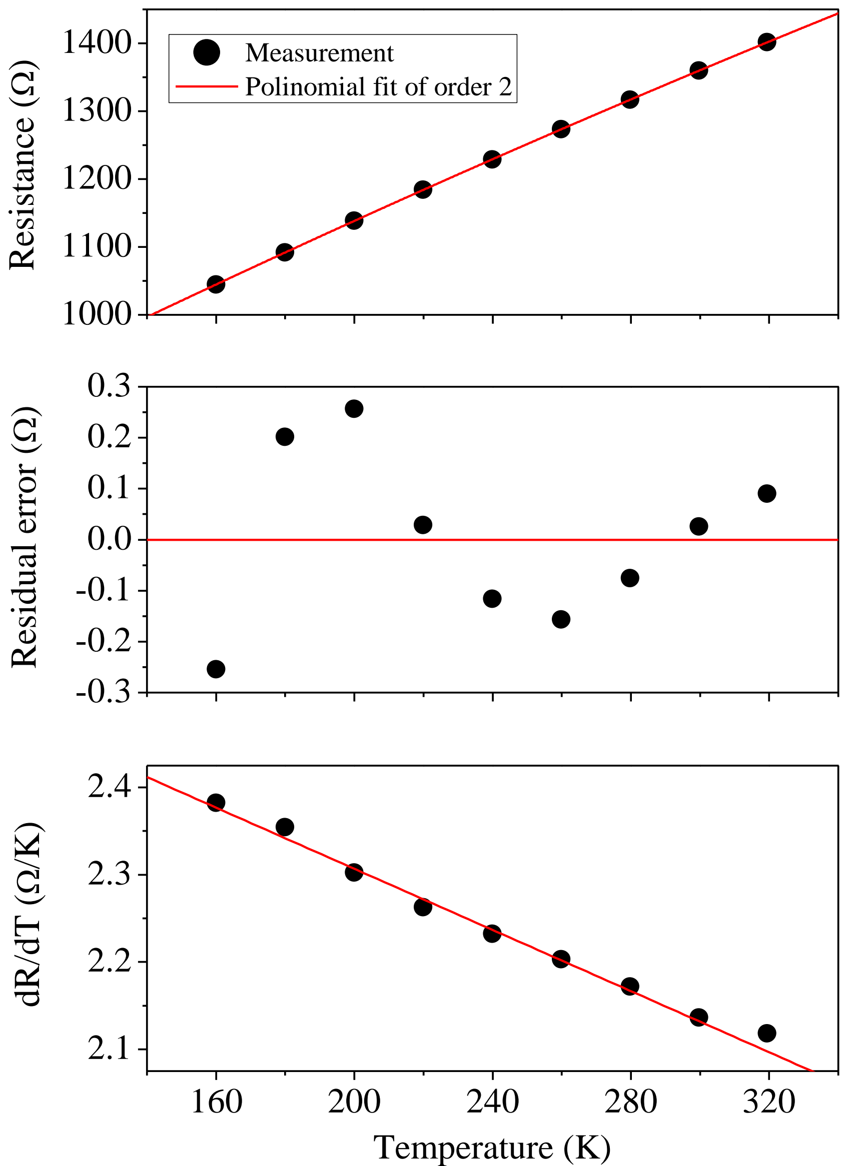

Figure 3.3: Measured $R(T)$ and fitted curve using polynomial of order 2. a) Resistance, b) residual error of the fit and c) numerical derivative of the data and the fitted curve.

3.2.2.2 $R(T)$ calibration in the He cryostat

In the case of the measurements performed in the He cryostat, the function used is more complex in order to account for the curve flattening at low temperatures (below 80K). The fitting function is:

$$R = \sqrt[8]{A + BT^2 + CT^3 + DT^4 + ET^5} \tag{3.4}$$

Where A, B, C, D and E are the parameters of the fit. The derivative is:

$$\frac{dR}{dT} = \frac{2BT + 3CT^2 + 4DT^3 + 5ET^4}{8(A + BT^2 + CT^3 + DT^4 + ET^5)^{7/8}} \tag{3.5}$$

This function is not derived from any theory of electronic conduction in metals, but it was empirically found to fit very well and with few parameters the complex $R(T)$ curve. The comparison with the usually used 4th degree polynomial makes this clear (Figure 3.4). Note that the linear contribution inside the root is avoided to force the function to be flat at $T = 0\ K$.

The numerical derivative at 20 K is far from the fitted curve because of the lack of a neighbor data point that is necessary for the evaluation of the numerical derivative (equation (3.6)).

$$\left(\frac{dy}{dx}\right)_i = \frac{1}{2}\left(\frac{y_{i+1} - y_i}{x_{i+1} - x_i} + \frac{y_i - y_{i-1}}{x_i - x_{i-1}}\right) \tag{3.6}$$

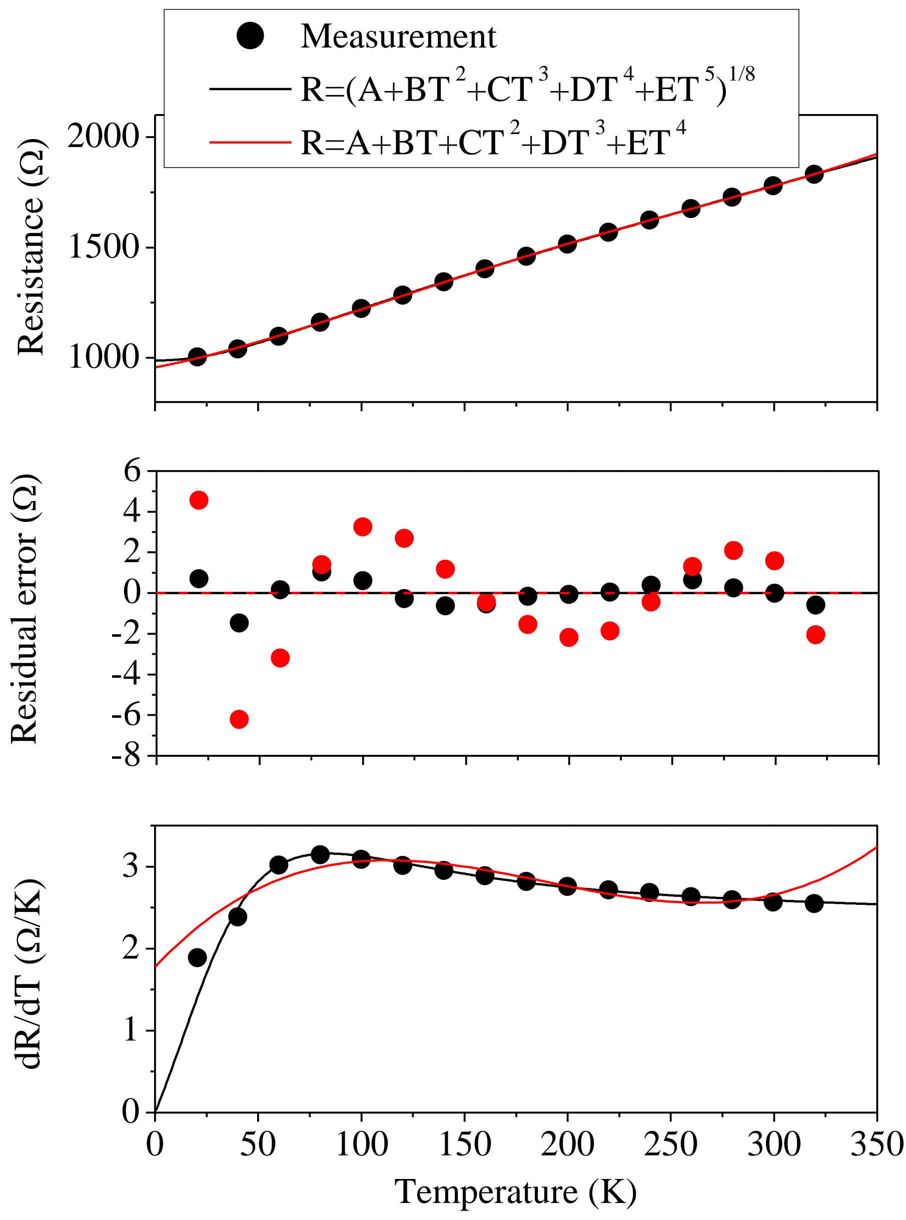

Figure 3.4: Comparison between fitting the R(T) curve with a polynomial of order 4 or the nonlinear equation presented above. a) Resistance, b) residual error of the fit and c) numerical derivative of the data and the fitted curves.

3.3 Suspended structures

3.3.1 Motivation and description

Generally, for measuring transport properties in any material, the sensing structure must be more insulating than the sample under test, which prevents the leakage of heat or current (this applies both for electrical and thermal measurements). However, whereas the electrical conductivity of materials spans over 20 orders of magnitude, the thermal conductivity of any solid lies within a 4 orders of magnitude range (0.1 $W \cdot m^{-1} \cdot K^{-1}$ to 1000 $W \cdot m^{-1} \cdot K^{-1}$). This implies that the measurement of the thermal conductivity cannot be performed in the same conditions than the electrical conductivity one.

For example, the electrical conductivity of a semiconducting nanowire can be measured by just placing the nanowire on a bulk quartz chip (10^{15}-10^{20} times more insulating than the semiconductor) and connecting it to a couple of electrodes that impose a voltage. In this way, the current will only flow through the nanowire. The measurement of this current will lead directly to the value of the resistance and ultimately to the electrical conductivity, if the dimensions of the wire are known. However, using the same setup in a thermal conductivity measurement (changing the electrodes for temperature baths) would produce a heat leakage through the substrate much larger than the heat actually flowing through the nanowire.

Although it is still possible to measure the thermal conductivity of nanomaterials in this way by applying some corrections[68], the high uncertainty of the technique only allows measuring quite conductive samples (thermal conductance higher than 25 nW/K), where the heat flow through the material is comparable to the heat flow through the substrate. For this reason, in order to measure very low conductive materials, the thermal insulation of the sensor must be achieved via a geometrical design that suppresses the thermal conduction through the structural materials. Following these guidelines, Shi et al. reported the first suspended structure consisting of two platforms that hang from the substrate through long insulating beams[69], between which the sample is placed. The platforms are equipped with two heater/sensors that allow producing a temperature difference by Joule effect heat generation and measuring the temperature at both platforms from the resistance measurement. This system allows measuring the sample thermal conductance with a resolution of 1 nW/K.

Suspended structures are typically used to measure the thermal conductivity of nanowires produced by a bottom-up method (like vapor-liquid-solid, or VLS) which are placed on the structure either by micromanipulation or by drop casting from a solution containing the NWs in suspension. To improve the thermal contact between the wire and the heater/sensors, an amorphous carbon film is subsequently deposited at the contact region. However, this procedure inevitably introduces a contact thermal resistance, which is difficult to measure and introduces uncertainty in the experimental data. Recently, a suspended structure was reported in which through a four-probe measurement of the temperature, the contact resistance was cancelled out[70].

Here we show the feasibility of fabricating a suspended structure with Si membranes as thin as 17.5 nm connecting the suspended platforms. The proposed device minimizes the adverse contribution of the contact thermal resistance found in previous structures since the Si layer spreads beneath both platforms enlarging the thermal contact areas and minimizing its influence. This structure also allows nanopatterning the Si membrane using Focused Ion Beam (FIB), as will be discussed in Section 4.3, allowing the measurement of phononic crystals or asymmetric nanostructures.

3.3.2 Microfabrication

The Si-based microchips are fabricated using standard microfabrication techniques on silicon wafers. Up to 480 devices per each 4-inch wafer are processed at a time. The common fabrication sequence for all devices is as follows (scheme of the steps in Figure 3.5):

i) The fabrication starts with a (001) 4-inch silicon-on-insulator (SOI) wafer from Soitec, with 340 nm of Si device layer, 400 nm buried silicon dioxide (SiO_2) and 525 μm of bulk Si.

ii) The Si device layer is thinned with a series of thermal oxidations at 1000 ºC and subsequent dips in buffered HF (hydrofluoric acid) solutions. During the oxidation, every nm of SiO_2 grows at expenses of 0.45 nm of Si, and a careful oxidation growth ensures a good control of the final Si layer thickness. In the middle of the thinning sequence, the thickness of the device layer is verified with a non-contact spectroscopic reflectometer (Nanospec), at 49 different points around the wafer to check the homogeneity.

iii) The Si is selectively etched combining standard photolithography with Reactive Ion Etching (RIE) using SF_6 gas. In this way, the membrane to be measured is defined.

iv) Both sides of the wafer are coated with a 450 nm thick layer of amorphous, low residual stress, silicon nitride (SiN_x) grown by low-pressure chemical vapor deposition (LPCVD) at 800 ºC. Prior to the deposition, an oxygen plasma treatment is performed on the wafer to remove organic contamination.

v) The beams and platforms are defined in the silicon nitride layer by combining standard photolithography with RIE. In this case, C_4HF_8 and methane gas remove the non-protected SiN_x. The use of a chemical etchant with selectivity between SiN_x and Si is essential to prevent the over-etching of the Si layer exposed between the sensing platforms. In the rest of the wafer, the RIE stops on the buried SiO_2 layer, where small over-etches are not critical. The 450 nm thick SiN_x provides enough mechanical stability to suspend each sensing platform (21x23 μm^2) with four very long beams (410 µm long and only 4.9 µm wide). Moreover, this geometry also ensures a large thermal insulation of the sensing platforms.

vi) Stepper photolithography is combined with an electron-beam evaporation of metals to define the sensing circuit, which is composed by: 1) the metallic heater/sensor meander in the platforms (with 800 nm wide lines), 2) the macroscopic contact pads in the external Si frame and 3) the electrical connection lines (2 µm wide) along the beams. The metallic circuit is formed by a 4nm Cr layer (used as an adhesion layer chemically resistant to subsequent HF etchings) and a 40 nm Pt layer (used as the temperature sensor due to its good sensitivity to temperature variations). On the meander layout, the central lines have been designed with reduced width compared to the connecting beam lines to increase the resistance ratio between the central meander and the connecting lines. This geometry ensures a factor close to 1.

vii) Using plasma-enhanced chemical vapor deposition (PE-CVD), a 300 nm protective layer of SiO_2 (Low Temperature Oxide or LTO) is deposited on the whole wafer.

viii) A 400 nm thick Al layer is selectively deposited in the backside of the wafer. First, the pattern is transferred to the wafer using double-side alignment photolithography and then the Al is deposited by e-beam evaporation. Finally, the Al is lifted-off.

ix) Using the Al deposited in the previous step as a mask, the backside SiN_x layer is etched with RIE.

x) The exposed bulk Si is etched away using deep-RIE based on a mixture of SF_6 and C_4F_8 gases. The etching is typically stopped when the buried oxide (BOX) layer is reached, although premature stops increase the survival ratio. At this step, the suspended structures are still clad between the BOX and LTO capping layer.

xi) The wafer is diced in chips of 7.5 mm by 7.5 mm (the clad structure provides enough mechanical protection to do so). Each chip includes 4 different devices with slightly different layouts, varying the width of the Si membrane (1-20 μm) and the distance between the sensing platforms (1-10 μm).

xii) After dicing the wafer, the chips are processed individually, removing the remaining Si with a 5% tetramethylammonium hydroxide (TMAH) wet etching. The oxides in the clad structure are then chemically etched by placing with a micropipette four 8 μl drops of 2.5 % HF on the chip. Once the etchant has extended along all the chip, it is left for 15'-25'. After this time, the chip is rinsed in hot water (~90 ºC) and in isopropyl alcohol (IPA) at room temperature. In order to dry the chip without breaking the Si strip, it is placed on a hot plate at a temperature below the boiling temperature of IPA (82.6 ºC) until it is completely vaporized. This method reduces the risk of breaking the Si platform during drying owing to the low surface tension of IPA (23 mN/m) compared with water (72.8 mN/m). If there is any organic contamination on the structure, a last step can be performed, consisting on immersing the chip in a Piranha solution ($1H_2O_2:6H_2SO_4:10H_2O$) at 100 ºC during approximately 20'. Nevertheless, this will slightly etch the Pt sensor, increasing its resistance as much as x1.5. To verify that the SiO_2 has been completely removed, the silicon strip is examined with an optical microscope. If the surface of the strip is homogeneous and does not present any diffraction pattern, SiO_2 is considered to be completely etched.

A field emission scanning electron microscope (FESEM) image of a suspended structure with a 17.5 nm layer connecting the platforms is shown in Figure 3.6a. The crystallinity of the silicon layer has been verified through an electron diffraction pattern during TEM observation with a JEM 2011. Figure 3.6b shows the TEM micrograph of the suspended structure. Diffraction patterns collected in different regions of the ultrathin Si layer with a spot diameter of 150 nm show identical periodic arrangements, characteristics of the single crystalline nature of the layer (Figure 3.6c).

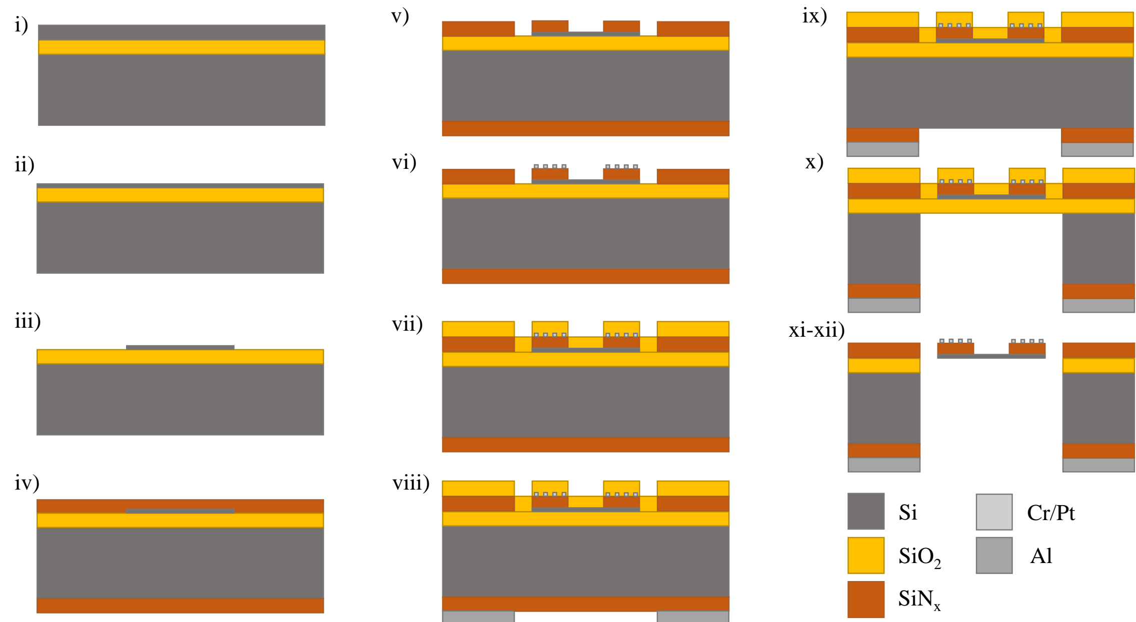

Figure 3.5 a) Schematics of the microfabrication process in cross-sectional view. i) Starting wafer ii) Thinning of the top Si layer. iii) Patterning of Si device layer. iv) SiN_x deposition by LPCVD. v) Patterning of the SiN_x layer. vi) Patterning of the metallic layer defining by lift-off process the electric circuit. vii) Deposition of a protective LTO layer by PECVD. viii) Deposition and patterning of an Al layer on the backside. ix) RIE of the backside SiN_x layer. x) Deep RIE of the substrate Si from the backside. xi-xii) Final Si and SiO_2 wet etchings.

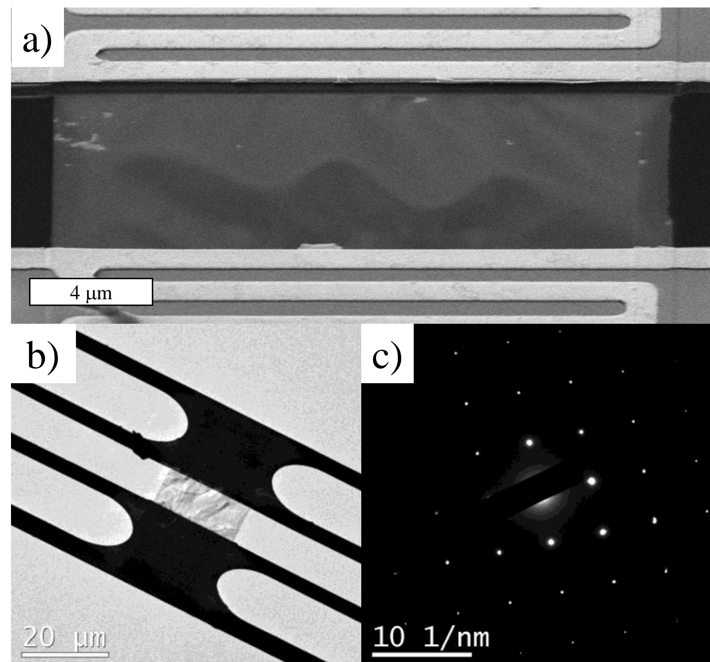

Figure 3.6 Micrographs of a suspended structure with a Si membrane 17.5 nm thick. a) Field-emission SEM image (Tilt = 52°) Notice the strain in form of waves produced in the Si membrane by the SiN_x induced tension. b) TEM micrograph showing the electronic reflections produced by the purely crystalline Si membrane. c) TEM diffraction pattern obtained by focusing an electron beam with 150 nm spot diameter in the central part of the layer, showing a monocrystalline pattern.

3.3.3 Heat flow analysis

In normal operation, an electrical current is injected in the metallic meander of one of the suspended platforms, hereafter denoted as heater, releasing heat by Joule effect in the center of the platform (Q_H) and in the two electrical lines used to feed the meander ($2Q_{HL}$). This rises the sensor temperature and produces several heat flows that can be seen in Figure 3.7. By measuring the temperature rise of the heating and sensing platforms respect to the thermal bath, respectively ΔT_H and ΔT_S, and applying an accurate analysis of the heat flow when the device is operating in the steady-state regime, the thermal conductance of the sample can be derived.

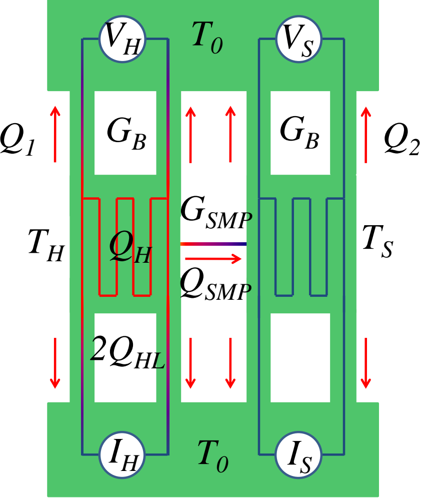

Figure 3.7 Scheme of the heat flow in the sensor.

Applying the heat flow continuity equation to the heated platform in steady state conditions yields that the amount of heat released, $Q_H + 2Q_{HL}$, should be compensated by the heat lost through the beams, heated and non-heated, towards the Si frame and through the sample to the sensing platform (Q_{SMP}).

$$Q_H + 2Q_{HL} = Q_1 + Q_{SMP} \tag{3.7}$$

A one dimensional analysis of heat diffusion along the beams permits to estimate the amount of heat released to the Si frame (Q_1) in each case. In the two non-heated beams, a linear temperature profile is expected and the heat lost per beam can be taken as $G_B \Delta T_H / 2$, where G_B is the thermal conductance for the four beams. In the two beams with heating lines, it is possible to solve the 1D differential equation for heat diffusion (equation (2.12)), imposing temperatures (T_H and T_o) as boundary conditions and

approximating the density of heat released per unit length to be constant along the beams. Under this assumption the heat lost in the pair of heated beams is $G_B \Delta T_H / 2 + Q_{HL}$. The heat flow continuity equation results in the following simplified expression:

$$Q_H + Q_{HL} = G_B \Delta T_H + Q_{SMP} \tag{3.8}$$

In an analogous manner, the continuity equation for the sensing platform should include the amount of heat arriving from the heater through the Si layer and the heat lost through the four non-heated lines:

$$Q_{SMP} = Q_2 = G_B \Delta T_S \tag{3.9}$$

Along this analysis, the temperature distribution maps in the platforms are considered to be uniform. Nevertheless, when measuring samples with high thermal conductance comparable to the internal thermal conductance of the platforms, temperature non-uniformities may result in an incorrect evaluation of the thermal conductance[71]. The use of finite elements modelling to determine the 2D temperature map in the layer becomes mandatory in these situations. Details on these small corrections will be discussed in section 3.3.8.

Combining equations (3.8) and (3.9), the thermal conductance associated to each beam can be calculated as:

$$G_B = \frac{(Q_H + Q_{HL})}{(\Delta T_H + \Delta T_S)} \tag{3.10}$$

The effective thermal conductance between the suspended platforms can be inferred applying the Fourier law to the temperature difference between them:

$$G_{SMP} = \frac{Q_{SMP}}{\Delta T_H - \Delta T_S} \tag{3.11}$$

where Q_{SMP} can be calculated from (3.9) and (3.10), yielding:

$$G_{SMP} = \frac{\Delta T_S \cdot (Q_H + Q_{HL})}{{\Delta T_H}^2 - {\Delta T_S}^2} \tag{3.12}$$

The effective thermal conductance includes the intrinsic conductance component of the sample and a component associated to the thermal contact between the platforms and layer. In the design presented here, the thermal contact between the suspended platforms and the Si strip has been maximized by spreading the Si layer beneath the whole platform areas and thus increasing the thermal contact area. Considering sample dimensions (cross section S_{SMP} and thickness t_{SMP}), the thermal conductivity can be derived as:

$$k_{SMP} = \frac{t_{SMP}}{S_{SMP}} \left[\frac{\Delta T_S \cdot (Q_H + Q_{HL})}{{\Delta T_H}^2 - {\Delta T_S}^2} \right] \tag{3.13}$$

Also, assuming the linear relationships $\alpha \equiv \Delta T_S / \Delta T_H$ and $\beta \equiv \Delta T_H / (Q_H + Q_{HL})$, equation (3.13) can be rewritten as

$$k_{SMP} = \frac{L_{SMP}}{S_{SMP}} \frac{\alpha}{\beta(1 - \alpha^2)} \tag{3.14}$$

This equation is especially useful, since the parameters α and β can be determined from the linear fits near the origin (where there are not nonlinear effects) of the curves $\Delta T_S(\Delta T_H)$ and $\Delta T_H(Q_H + Q_{HL})$, effectively cancelling out any offset.

3.3.4 Electrical measurements

Figure 3.8 shows the schematic diagram of the electronic circuit used for the thermal conductance measurements. An Agilent 33500B dual true-form wave generator is used both to heat one platform by Joule effect (by feeding V_1) and to polarize the resistor of the sensor (by feeding V_2). In the circuit, a couple of identical load charge resistors ($R_{LH,LS}$~100 kΩ) are connected in series with the heater and sensor, respectively, to accommodate the voltage output capabilities of the generator with the reduced current requirements.

In this circuit, the voltage drops in the heater and sensor meanders (V_H and V_S) are measured in a 4-probe configuration in order to access the temperature of each platform. Also, through the measurement of the voltage drop in the load resistances, V_{IH} and V_{IS}, the current flowing in each branch can be calculated directly by the Ohm's law. Finally, the voltage drop along the complete heater, including the central meander and the

connection lines in the beam (V_{HT}) is measured for calculating Q_L. The symmetry of the branches enables the inversion of the roles of the suspended structures (heater↔sensor).

Especially when the platforms are bridged by samples with reduced thermal conductance (several nW/K), ΔT_S signals are very small and thus ΔV_S is also very small. This fact combined with the need to polarize with very small currents results in poor signal to noise ratios (SNR) using four probe configuration. As shown by Wingert et al.[72], the use of a Wheatstone bridge with another non-suspended structure increases the experimental sensitivity of the measurement of ΔT_S by amplifying the differential signal and rejecting common noises or fluctuations of the base temperature. This bridge is implemented in our setup by connecting the sensor circuit branch with another branch composed of another Pt element of the same chip connected in series with a variable resistance (used to initially balance the bridge). This branch can be selectively connected to both heater and sensor by just activating a switch, which preserves the symmetry of the system.

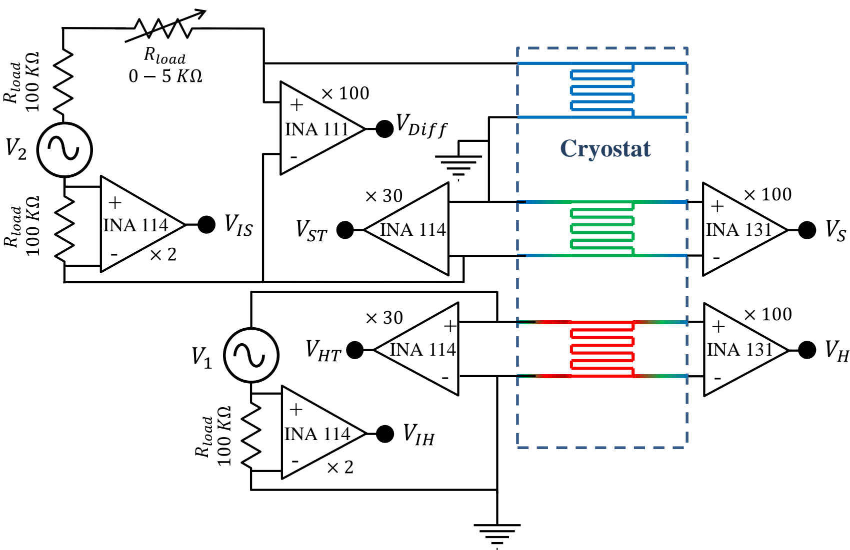

Figure 3.8 Electrical diagram of the custom-made setup for thermal conductivity measurements in suspended structures.

All voltage signals are acquired with a PC equipped with a NI-FPGA-7855R, a 16-bit resolution multichannel data acquisition card with variable gain. The signals are acquired in data packages of about 10^4 samples at rates of 100000 samples/s per channel. The number of periods in each package is forced to be integer by eliminating some data points, so that the Fourier analysis does not produce signal leakage to the surrounding frequencies. Applying the Fast Fourier Transform (FFT) the amplitude of the first harmonic component is evaluated for each voltage signal. A set of instrumentation amplifiers accommodates the signals before acquisition, adapting the amplitudes to the

maximum input range of the ADC in order to maximize the SNR. Voltages V_{IH} and V_{IS} are typically quite large (1-3V) and they are amplified with a gain x3 using an INA114. For voltages dropping in the meander of the suspended structures, V_H and V_S, a fix amplification gain x100 is achieved with an INA131 and for V_{HT} and V_{ST} the gain is set to x30. Finally, the differential signal in the Wheatstone bridge V_{Diff} is amplified x1000 with an INA111. These amplifiers have been selected considering: i) a low input bias current ($I < 2$ nA), to guard the suspended device from current shunting from the multiplexor, ii) a high common mode rejection ratio since all signals are differential, iii) a bandwidth higher than 30KHz in the respective gains and iv) low voltage spectral noises $\left(10 - 12\ \mathrm{nV}/\sqrt{\mathrm{Hz}}\right)$.

3.3.5 Measurement cycle

For each temperature, the measurement cycle comprises the resistance calibration and the thermal conductance measurement.

3.3.5.1 Resistance Calibration

After the temperature of the sample holder has been stabilized, the resistance of the heater (R_H) and sensor (R_S) is measured. This is done by polarizing both metallic elements with small AC currents (900 nA at 179 Hz) to prevent the self-heating of the platform, as explained in section 3.2.2. In this case, the resistance of the platforms can be directly calculated considering Ohms law

$$R_{H,S} = \frac{V_{H,S}}{I_{H,S}} \tag{3.15}$$

Where

$$I_{H,S} = \frac{V_{IH,IS}}{R_{LH,LS}} \tag{3.16}$$

yielding typical values of around 1.5 KΩ at room temperature. A calculation of the resistivity for the 40 nm Pt film, considering the meander geometry, gives values 3 times larger than the ones commonly found for bulk Pt, which can be ascribed to structural defects formed during the deposition. The TCR values obtained are also quite low (TCR~0.0016 K^{-1}) compared with similar layers of Pt deposited using Ti as adhesion layer[73], indicating the negative impact of inter-metallic phase formations at the interface

between Cr and Pt for such a thin metallic strip and also the small dimensions of the crystalline domains.

3.3.5.2 Thermal conductivity measurement

Once the resistance has been measured with low current, the current in the heater is scanned from 900 nA through 40 µA in DC mode while the sensor current is kept at 900 nA (in order to avoid self -eating) in AC mode using a frequency of 179 Hz. The voltage at each point of the scan is measured, taking a total time of 30 s/scan. The scan is repeated 50-100 times in order to average any thermal fluctuation of the system. Also, exciting the heater with DC and sensing the resistance with AC minimizes the electronic cross-talking between the sensor and the heater, yielding lower noise.

After these scans, the temperature is changed and stabilized, and the measuring cycle is repeated.

3.3.6 Data reduction

The heat released by Joule effect in the heating platform can be computed from the $V(I)$ measurements, using the current calculated with equation (3.16):

$$Q_H = V_H I_H \tag{3.17}$$

In the same way, to determine the heat released in each feeding line Q_{HL}, the measurement of the voltage drop in the complete heater is also required:

$$Q_{HL} = (V_{HT} - V_H) I_H / 2 \tag{3.18}$$

While the heater excitation ΔT_H is kept below 20 K, a linear behavior is expected for the temperature evolution as function of the input power:

$$\Delta T_H = \frac{Q_H + Q_{HL}}{G_{eff}} = \frac{\left(R_{HT,0} - R_{H,0}\right) I_H^2}{G_{eff}} \tag{3.19}$$

Where $R_{H,0}$ and $R_{HT,0}$ are the heater resistance and the total circuit resistance when I_H is zero, and G_{eff} is the effective resistance from the heater to the substrate. From equation (3.19) and applying (3.1) to R_H yields

$$R_H = R_{H,0} + \frac{dR_H}{dT}\frac{\left(R_{HT,0} - R_{H,0}\right)I_H^2}{G_{eff}} \tag{3.20}$$

Then, the voltage drop in the heater V_H depends cubically on the current

$$V_H = I_H R_H = I_H R_{Ho} + \frac{dR_H}{dT}\frac{\left(R_{HT,0} - R_{H,0}\right)}{G_{eff}} I_H^3 \tag{3.21}$$

From this expression the differential resistance $R_H = dV_H/dI$ is obtained, and ΔT_H is calculated:

$$R_H = \frac{dV_H}{dI_H} = R_{H0} + 3\frac{dR_H}{dT}\frac{\left(R_{HT,0} - R_{H,0}\right){I_H}^2}{G_{eff}} = R_{H0} + 3\frac{dR_H}{dT}\Delta T_H \tag{3.22}$$

Isolating the temperature yields:

$$\Delta T_H = \frac{\frac{dV_H}{dI} - R_{H0}}{3\, dR_H/dT} \tag{3.23}$$

Thus, when calculating the resistance of the heater using the derivative of the voltage, a factor 3 appears owing to the implicit dependence of the heater voltage to the cube of the current.

Opposed to the heater, the sensor is excited with a constant amplitude AC current, and the resistance R_S can be directly calculated with the Ohms law from the voltage and current measured. In this case, to find ΔT_S equation (3.1) is directly applied to the resistance difference:

$$\Delta T_S = \frac{R_S - R_{S0}}{dR_H/dT} \tag{3.24}$$

Where $R_{S,0}$ is the sensor resistance with $I_H = 0$.

By measuring the temperature rise for different heating powers, the parameters α and β can be calculated as explained in Section 3.3.3. However, the curves $\Delta T_H(Q_H + Q_{HL})$ and $\Delta T_S(\Delta T_H)$ are not linear at high heating powers due to the change in conductance of the beams and the radiation heat losses (Figure 3.9). For this reason, these curves are fitted with polynomials in order to get the slope in the origin: the curve $\Delta T_H(Q_H + Q_{HL})$ is

adjusted with a polynomial of order 3, whereas the curve $\Delta T_S(\Delta T_H)$ is adjusted with a polynomial of order 2 (since a fit with a higher order polynomial would yield a high uncertainty in the linear term). The 1st and the last data points are always discarded (not fitted) because the derivative dV_H/dI incorporates an error in them, since they do not have adjacent data points. Finally, the fitting of the polynomial functions is performed using a statistical weight: $w_i = \frac{1}{y_i}$, which means that the data points with smallest y values are more weigthed. This is done to take more into account the data points in the linear region of the curves (near the origin).

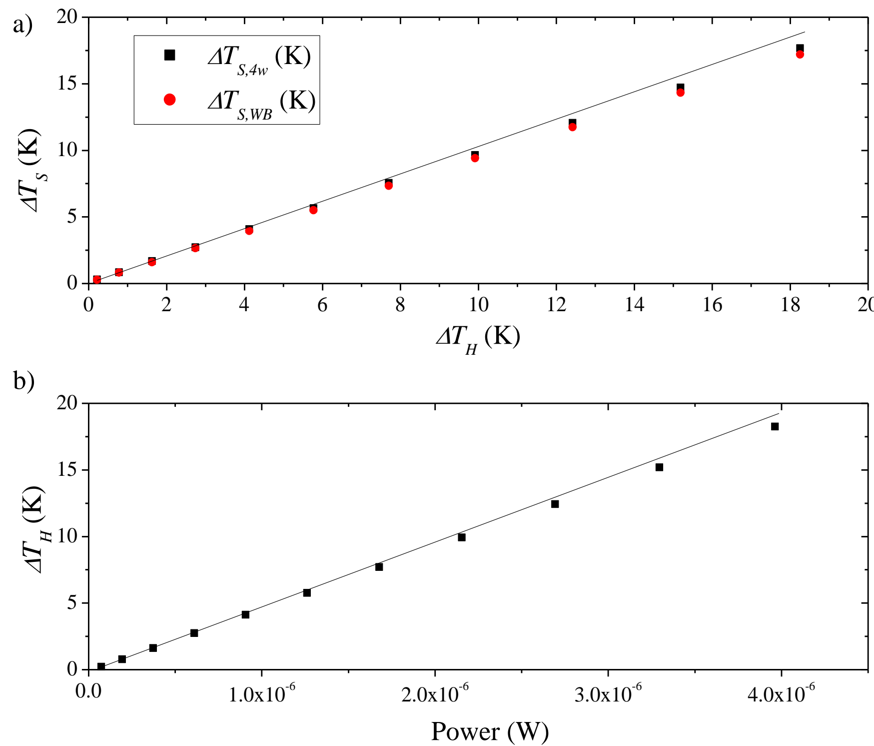

Figure 3.9 Thermal conductance measurement of a Si membrane. From these points, a polynomial curve is fitted to get the slope at the origin. a) $\Delta T_S(\Delta T_H)$ b) $\Delta T_H(Q_H + Q_{HL})$. A line is introduced to better appreciate the deviation from the linear behavior.

3.3.7 Analysis of uncertainties and errors in the measurements of G_{SMP}

As it has been described in equation (3.12), the determination of the thermal conductance of the sample, G_{SMP}, depends on the measurement of the heat dissipated in the heating lines, Q_{HL}, the heat dissipated in the heating meander, Q_H, and mainly on the temperature rise on the sensor, ΔT_S, and the temperature rise on the heater, ΔT_H. The measurement of the power term is usually achieved with a high precision and the final uncertainty in G_{SMP} turns out to be dominated by the temperature terms, intrinsically noisier. Considering that

detail, the uncertainty in the measured G_{SMP} can be found by applying the standard uncertainty propagation from the measured temperatures, resulting in

$$\delta G_{SMP} = \sqrt{\left(\frac{\partial G_{SMP}}{\partial \Delta T_S}\delta \Delta T_S\right)^2 + \left(\frac{\partial G_{SMP}}{\partial \Delta T_H}\delta \Delta T_H\right)^2} \tag{3.25}$$

where

$$\frac{\partial G_{SMP}}{\partial \Delta T_S} = \frac{(Q_{HL} + Q_H)\left(\Delta T_H{}^2 + \Delta T_S{}^2\right)}{\left(\Delta T_H{}^2 - \Delta T_S{}^2\right)^2} \tag{3.26}$$

$$\frac{\partial G_{SMP}}{\partial \Delta T_H} = \frac{-2(Q_{HL} + Q_H)\Delta T_H \Delta T_S}{\left(\Delta T_H{}^2 - \Delta T_S{}^2\right)^2} \tag{3.27}$$

The total uncertainty δG_{SMP} can be thus written as:

$$\delta G_{SMP} = \frac{(Q_{HL} + Q_H)}{\left(\Delta T_H{}^2 - \Delta T_S{}^2\right)^2}\sqrt{\left(\Delta T_H{}^2 + \Delta T_S{}^2\right)^2 \delta \Delta T_S{}^2 + (2\Delta T_H \Delta T_S)^2 \delta \Delta T_H{}^2} \tag{3.28}$$

This expression can be rewritten by substituting the measured temperatures with the nominal conductance of the sample and the beams. Those can be calculated using the 1D heat equation on the suspended structure, a similar analysis to the one performed in section 3.3.3. The temperature rise in the heater can be written as:

$$\Delta T_H = \frac{(Q_{HL} + Q_H)}{G_{eff}} = (Q_{HL} + Q_H)\frac{(G_B + G_S)}{(G_B)^2 + 2G_B G_S} \tag{3.29}$$

Here, G_{eff} is the effective thermal conductance from the heater to the substrate (taking into account all the conducting channels). On the other hand, in order to calculate ΔT_S one has to apply the conservation of the heat flowing through the sensor (incoming heat equals outgoing heat), and then apply Fourier's law:

$$G_{SMP}(\Delta T_H - \Delta T_S) = G_B \Delta T_S \tag{3.30}$$

Now, substituting ΔT_H from (3.29) in (3.40) and simplifying, one obtains

$$\Delta T_S = \frac{(Q_{HL} + Q_H)G_{SMP}}{(G_B)^2 + 2G_B G_{SMP}} \tag{3.31}$$

Finally, substituting into (3.28) expressions (3.29) and (3.31), the uncertainty becomes (simplifying):

$$\delta G_{SMP} = \frac{1}{(Q_{HL} + Q_H)} \sqrt{\left(G_B{}^2 + 2G_{SMP}{}^2 + 2G_B G_{SMP}\right)^2 \delta\Delta T_S{}^2 + 4\left(G_{SMP}{}^2 + G_B G_{SMP}\right)^2 \delta\Delta T_H{}^2} \tag{3.32}$$

The absolute uncertainty δG_{SMP} and the relative uncertainty $\delta G_{SMP}/G_{SMP}$ are plotted as function of G_{SMP} in Figure 3.10 using an input power of 600 nW and imposing G_B=75 nW/K, a reasonable value in our real suspended structures[74]. δG_{SMP} has a value of 18 pW/K for sample conductance below 1.5 nW/K and follows a steady increase above this value. On the other hand, $\delta G_{SMP}/G_{SMP}$ shows a minimum plateau that spans over several orders of magnitude in G_{SMP} (from 1 to 100 nW/K). For high G_{SMP} values, the heating and sensing platforms are very well linked compared to their link to the frame, and thus, their temperature is very similar. Therefore, the term $\Delta T_H^2 - \Delta T_S^2$ is predominant in equation (3.12) as well as in the relative uncertainties of δG_{SMP} respect to ΔT_H and ΔT_S (Eq. (3.26) and (3.27)), which increases δG_{SMP} as the temperature of both platforms equalize. On the other hand, at low values of G_{SMP}, the sensing platform is almost thermally disconnected from the heating platform, and thus no heat flows between them. For this reason, the term ΔT_S goes to 0 as G_{SMP} does, and $\delta\Delta T_S$ becomes the predominant source of uncertainty. In this case, the absolute error tends to a constant value, and thus the relative error $\delta G_{SMP}/G_{SMP}$ tends to infinite. Figure 3.10b indicates that this particular structure is ideally suited to measure samples with conductance between 0.5-800 nW/K. Outside this region the uncertainty rapidly increases.

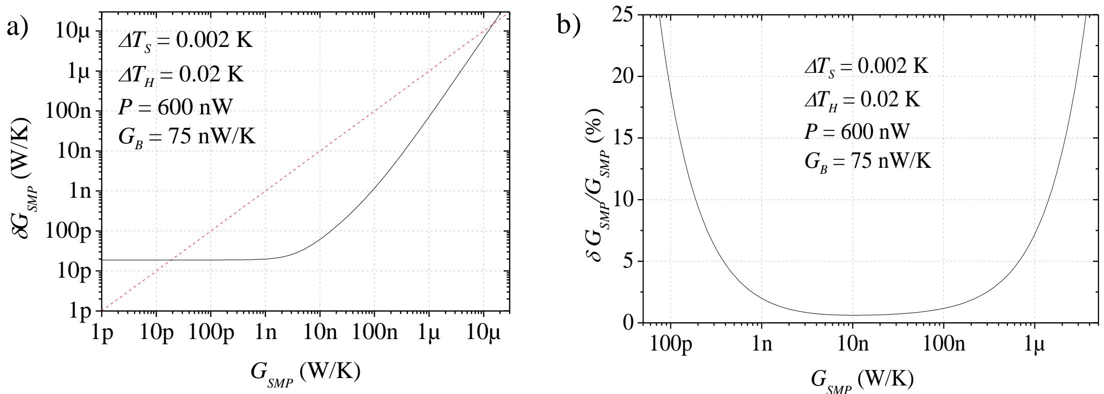

Figure 3.10 a) Absolute and b) relative uncertainty in the measurement of the thermal conductance δG_{SMP} as a function of G_{SMP}. The red dashed line in b) indicates 100% uncertainty. The parameters have been chosen using plausible values.

In order to adapt the optimal measurement range of the suspended structure to the estimated conductance of the sample under test, it is necessary to consider several aspects:

i) Reduce the uncertainty of the measurement. This can be achieved in two ways: First, increasing the power released in the structure will improve the sensitivity in the whole range of conductance, as can be directly seen from equation (3.32). Of course, this solution is limited since a high power output in the heater would lead to high ΔT_H, and radiation losses may become an issue. Second, improving the temperature sensitivity would also improve the measurement sensitivity in the whole range of conductance. Specifically, at high G_{SMP}, $\delta G_{SMP}/G_{SMP} \propto \sqrt{\delta \Delta T_s{}^2 + \delta \Delta T_h{}^2}$ while at low G_{SMP}, $\delta G_{SMP}/G_{SMP} \propto \delta \Delta T_s$, as can be seen by calculating the limits of equation (3.32). One option to reduce $\delta \Delta T_s$ is to introduce a Wheatstone bridge, as already demonstrated by Wingert et al.[72]. This way, $\delta \Delta T_s$ can be reduced below 1 mK.

ii) Adapt the structure to the desired conductance (Figure 3.11). To measure high (low) conductive samples with small uncertainty, the beams must be more (less) conductive, and the power released in the heated platform has to be higher (lower) in order to keep ΔT_h at the same level. A multibeam (many beams linking the platforms with the frame) structure where the number of thermal links with the frame can be adjusted at will appears to be the best option for a whole range of materials and conductance ranges. Another possible strategy is to adapt the thermal conductance of the beam by depositing extra material in the backside of the structure (platforms and beams), permitting to measure highly conductive samples.

Figure 3.11 shows how combining both strategies, increasing power input and thermal conductance of the beams, the plateau of minimal uncertainty can be moved to measure correctly samples with higher thermal conductance. After increasing by a factor of ten both the beam conductance and the power released, the low-uncertainty plateau moves an order of magnitude to higher values of G_{SMP}.

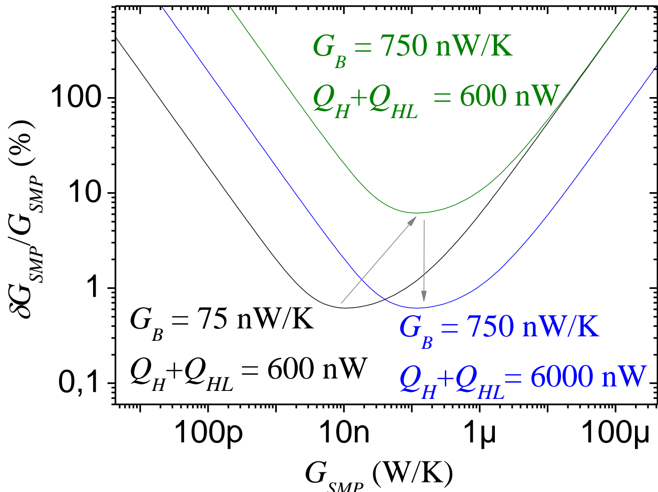

Figure 3.11 Change in the uncertainty plateau produced by the modulation of G_B and $Q_H + Q_{HL}$.

3.3.8 Corrections measuring large conductive samples.

Although the 1D heat diffusion equation is a correct approximation, it does not perfectly describe a suspended structure, since it implicitly assumes that the platforms are 0D. This model thus labels the whole platform with a unique temperature, while temperature gradients are known to appear within the platform area. This temperature non-uniformity can be neglected when the conductance of the sample is small compared with the internal conductance of the platforms, since under this assumption the temperature difference between the heater and the sensor is much higher than the temperature inhomogeneity inside the platform. However, when measuring samples with large conductance, like carbon nanotubes or silicon strips [75], the temperature difference between platforms shrinks down while inhomogeneity in the temperature map of the platforms is maintained. In such cases, temperature gradients can produce inaccuracies in the measurement of the thermal conductance and should be estimated.

A previous study has already reported the importance of temperature inhomogeneity to obtain a correct value of the thermal conductance in a structure where the sample is supported on a SiO_2 bridge between two platforms with micro-thermometers [71]. The

errors appearing in the evaluation of the thermal conductance when combining suspended structures with highly conductive samples require to solve the 3D heat equation for each case. Nevertheless, this equation has a difficult analytical solution (if any) for this complex structure, so the best way to solve it is numerically with Finite Element Modeling (FEM).

The microfabricated structure has been modeled with COMSOL Multiphysics® (Figure 3.12). The mesh consists of approximately 30000 triangular prisms, formed by sweeping triangles throughout the thickness of the structure. The aim of the simulation is to perform a virtual experiment where one of the platforms is heated up. From this experiment, the conductance of the sample is calculated with equation (3.12) and compared to the known imposed value to estimate the difference between both solutions.

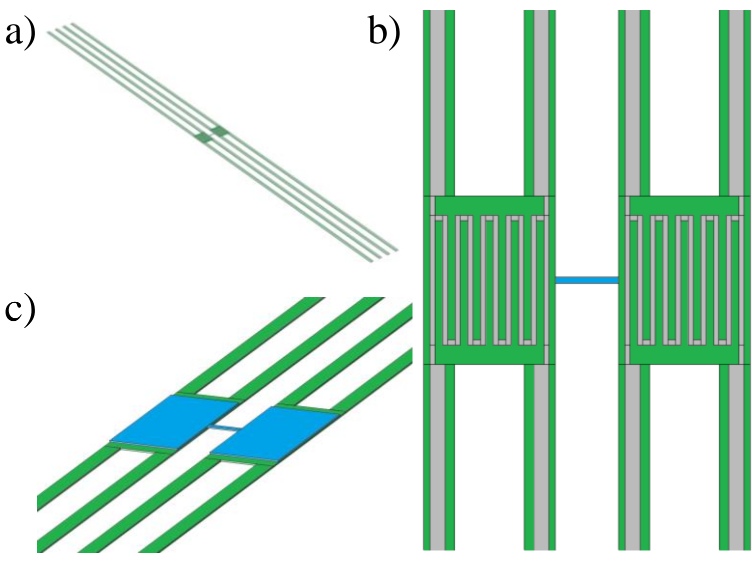

Figure 3.12 Different views of the modeled suspended structure. SiN_x is depicted green, Pt/Cr strips are grey, and the Si sample is blue. a) Complete view of the suspended structure. The bridges are 400 μm long and 5 μm wide. b) Detail of the platforms (which are 20.8x26 μm^2). The meander is 0.8 μm wide, while the incoming and outgoing lines are 2.5 μm wide. c) Rear view of the device. The Si membrane is attached to the sensing and heating platforms through a 20.8x22 μm interface.

We have implemented the 3D model for two different suspended structures: one, including just the structural SiN_x and the metallic Pt lines and, a second one, incorporating the c-Si plates underneath the SiN_x platforms (Figure 3.12c), that homogenize the temperature distribution inside the platform.

The simulations have been performed using the material properties of Table 3.1. The thermal conductivity of SiN_x was previously measured using the 3ω-method on a 450 nm thin film [76]. The electrical conductivity σ and the temperature coefficient of resistance

TCR of the Pt/Cr strip were experimentally measured in a suspended structure loaded into a cryostat measuring the resistance as a function of temperature using a very low current to prevent self-heating. On the other hand, from this measurement the thermal conductivity of Pt was extrapolated using the Wiedemann-Franz law. In the case of Si, since several thicknesses of the plate have been tested, the thermal conductivity was extrapolated from literature data[42,74,77–80]. Finally, the electrical conductivity of Si and SiN_x has been set to 10^{-10} S/m to prevent electrical leakage.

Material	Electrical conductivity (S/m)	Thermal conductivity ($W\cdot m^{-1}\cdot K^{-1}$)	TCR (1/K)
Pt/Cr	$3.74\cdot 10^{6}$ (@ RT)	26.7 (from WF Law)	$5.6\cdot 10^{-4}$ (@ RT)
SiNx	10^{-10}	2.5	0
Si	10^{-10}	9-100	0

Table 3.1 Physical parameters employed in the finite element model.

The first simulation has been performed placing as a sample a generic nanostrip 10 μm long x 400 nm wide x 100 nm thick attached on top of the SiN_x platforms by a non-resistive contact. The simulations have been performed for different values of the thermal conductance of the sample, G_{SMP}. The virtual experiment has been computed twice for each sample, one considering the structures with silicon thermal diffusive layer beneath the SiN_x platform and the other without. Figure 3.13 show the temperature maps in the platforms during the experiment for both cases. The strong temperature variation between both situations is evidenced in Figure 3.13b where the temperature profile along a line crossing the structure through the sample is plotted. These results highlight the importance of the heat conduction inside the platforms supporting the heaters: The platforms without Si have a limited self-conduction (thermal link between different points in the platforms) compared to the thermal conduction along the nanowire. Thus, the steady state temperature maps show non-homogeneous temperature profiles inside the platforms, with temperature variations of the order of the temperature difference inside the nanowire. When Si is introduced as a diffusion plate, the temperature profile in the platform is flattened and as it will be shown below, the error in the calculated conductance is smaller.

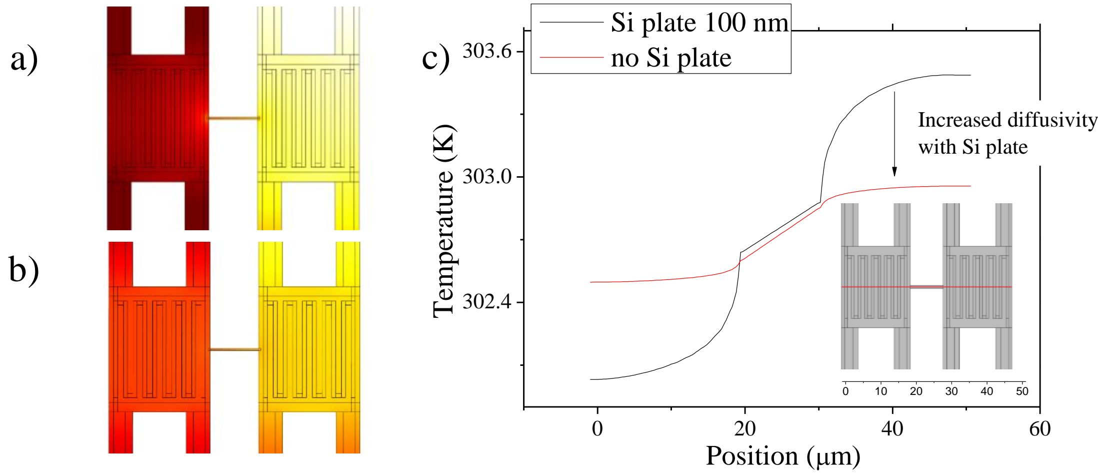

Figure 3.13 Temperature map of the suspended structures during experiments a) without and b) with a 100 nm Si plate underneath the SiN_x sample. c) Temperature profiles of the suspended structure without (black) and with (red) the Si plate. The red line in the inset determines the lateral cut use to plot the temperature profiles.

The thermal conductance $G_{SMP,1D}$ is extracted using equation (3.12) with the temperatures and powers obtained in the virtual experiment, and it is compared to the imposed thermal conductance of the simulated sample. The relative error of the thermal conductance is calculated as

$$\frac{\Delta G_{SMP}}{G_{SMP}} = \frac{G_{SMP} - G_{SMP,1D}}{G_{SMP}} \tag{3.33}$$

As can be seen in Figure 3.14a and b, the relative error assumed while using the 1D heat equation increases with G_{SMP}. Generally, the error ΔG_{SMP} obtained in the structure including the Si diffusive layer is much smaller than the value calculated in the structure without Si.

The model allows introducing a thermal boundary resistance (TBR) between the sample and the platforms. As it is shown in Figure 3.14b, when the thermal contact is poor, it dominates the temperature gradient and thus the presence of a thermal plate does not greatly reduce ΔG_{SMP}. This problem has already been analyzed in the literature[69], where the authors suggested that one can subtract the contact resistance by measuring several wires with different lengths. Recently, a modification of this technique employs an external electron beam for heating locally the nanowire, allowing a direct evaluation of G_{SMP} by estimating the influence of the thermal contact [81].

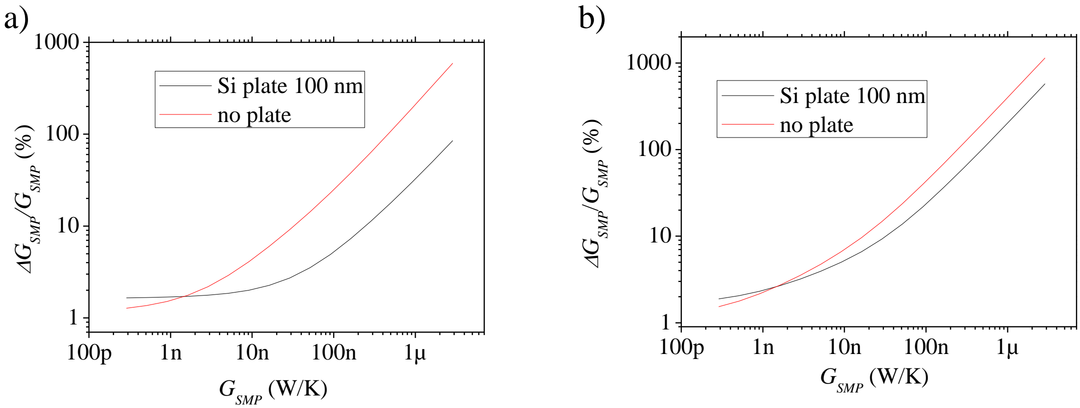

Figure 3.14 Relative error of G_{SMP} as a function of the real conductance of the sample without (a) and with (b) the presence of a TBR (10^6 K/W) between the sample and the structure.

A case of special importance here is the measurement of Si strips attached monolithically to the diffusion Si plate (Figure 3.15a). In this case, the thickness of the sample and the thermal plate are identical, and the error reaches asymptotically a maximum value because the heat diffusion of the plate scales with the one of the sample. For example, in a strip 1 µm wide and 10 µm long, the error is always below 25% (Figure 3.15b). In this case, the thermal conductance of the Si strip is evaluated for samples with different thicknesses from 10 to 200 nm taking into account the variation of thermal conductivity with thickness [42,74,77–80].

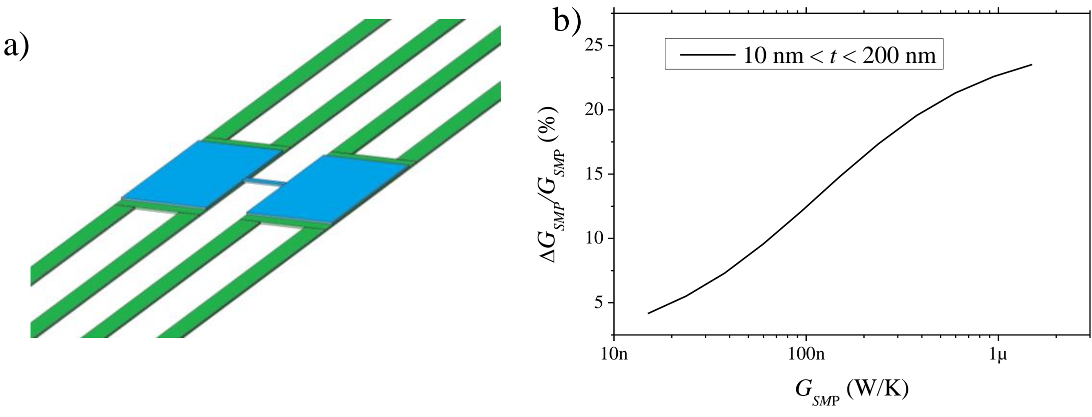

Figure 3.15 a) Rear view of the device with Si membrane. b) Relative error in G_{SMP} as a function of the sample conductance for a Si strip 1µm x 10µm x t where t is the modulated thickness.

3.3.8.1 Application to a real measurement on low-dimensional Si

According to the results of the simulation, the thermal conductivity determined by applying the 1D model in two samples of the same material with different geometries, and therefore different thermal conductances, can differ due to the presence of temperature gradients inside the platforms. In order to test the model outlined above, two

single-crystalline Si thin-films with the same thickness but different geometries have been measured. Sample A is 9.5 µm x 22 µm x 67 nm (length x width x thickness), whereas sample B is 4 µm x 0.6 µm x 67 nm. The thermal conductivity should be essentially the same for both samples. As shown in Figure 3.16, the different results for samples A and B derived with the 1D heat equation highlight the importance of the overall conductance of the sample in the determination of the thermal conductivity, since the disagreement in k goes beyond the uncertainty of the measurement. In order to find $G_{SMP,3D}$ the thermal conductivity of the modeled sample has been swept through different values, from which the one that produced the same $G_{SMP,1D}$ than the real experiment has been picked. This correction permits to stablish the right value of the thermal conductance considering the real temperature distribution of the platforms. The uncertainty has been calculated with the error propagation of the 1D model, and the relative uncertainty has been transferred to the thermal conductivity of the 3D model.

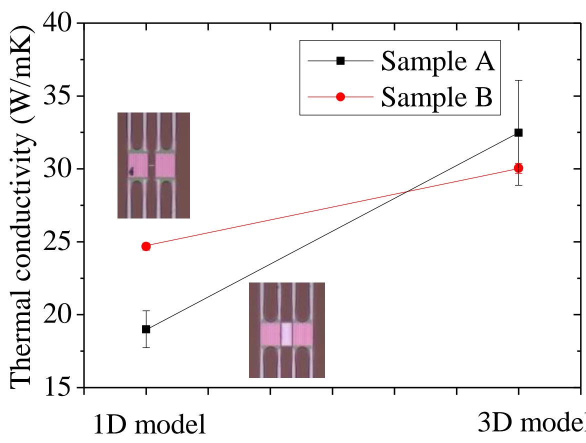

Figure 3.16. Thermal conductivity of samples A and B calculated applying the 1D model and the 3D model.

The formula for the conductance uncertainty (equation (3.12)) has also been checked with experiments performed on different samples with a wide range of thermal conductances. Here, we have compared the standard deviation of G_{SMP} (experimental uncertainty) with the uncertainty propagated from the standard deviation of the measured temperatures. The samples are Si strips of different geometries except for the least conductive measurement, which is performed on structures with no sample in the middle (the thermal conductance measured corresponds to the residual heat flowing from platform to platform through the substrate). As can be seen in Figure 3.17a, the data fits very well with the predicted error, which validates the applied model and the assumption that the error introduced by the

power is negligible. The level of uncertainty is estimated carrying out a large number of experiments and evaluating the dispersion as shown in Figure 3.17b. Consecutive experiments should be uncorrelated in the sense that the time between measurements should be longer than the time constant of the microdevice or the measuring instrument. Additionally, time lag should be small compared to the thermal drift of the bridge and instrumentation drifts. Figure 3.17b shows the stability of the measurements over time (consecutive number of the experiment), since a change in the measured G_{SMP} would increase the measured uncertainty above the one predicted.

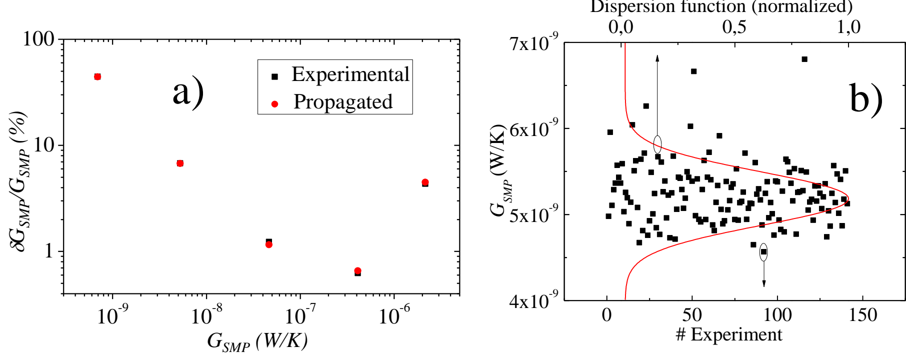

Figure 3.17 a) Relative uncertainty of the thermal conductance of various samples compared to the uncertainty calculated from the error propagation formula. b) Dispersion of the measurements of one of the samples measured.

3.4 3ω method

3.4.1 Description

This method, first described by Cahill in 1990[82], was intended for measuring the thermal conductivity of bulk insulating materials. It relies on the third harmonic component of the voltage signal that emerges in a metallic strip deposited on the sample under test when is heated with an AC current by Joule effect. This $V_{3\omega}$ component of the voltage is directly related to the thermal evolution of the substrate, and thus the thermal conductivity can be calculated from its value. The advantage of this method is that only one sensor is needed to measure the thermal conductivity of a bulk material by monitoring the frequency dependence of the temperature amplitude. This method was later modified to measure the thermal conductivity of thin films in the out-of-plane direction[83]. In this measuring mode, the thermal conductivity of the thin film is found by subtracting the total thermal resistance of a reference chip (without sample) from that of the sample chip and then applying a simple 1D model to find the heat flow inside the thin film.

Owing to the need of having only one heater instead of two, the reduced thermal losses via radiation and the great sensitivity of $V_{3\omega}$ to the thermal conductivity, the 3ω method is one of the most used methods for determining the thermal conductivity of bulk materials and thin films in the out of plane direction, competing with optical methods like Time domain ThermoReflectance (TDTR).

3.4.2 Generation of $V_{3\omega}$

In this section the emergence of the 3ω voltage will be mathematically demonstrated for any electrical line with self-heating. Later, the thermal conduction in the system will be analyzed starting with the heat equation, and the relationship between the temperature oscillations and the thermal conductivity of the substrate/thin film will be found.

In general, the self-heating of any electrical sensor can be described with the next equations. First, the sensor is fed with an AC-modulated current

$$I = I_0 \sin(\omega t) \tag{3.34}$$

Where I_0 is the amplitude of the current wave and $\omega = 2\pi f$ is the angular frequency. The sensor dissipates power in form of heat due to the Joule effect:

$$Q = I^2 R = I_0^2 R[\sin(\omega t)]^2 = \frac{I_0^2 R}{2}[1 - \cos(2\omega t)] = Q_0[1 - \cos(2\omega t)] \tag{3.35}$$

This power has two components: the constant component Q_0 produces a transient exponential self-heating that tends to a constant temperature value, and a sinusoidal component $Q_0 \cos(2\omega t)$ that produces an oscillatory temperature evolution. After a long time ($t \gg \tau$ where τ is the thermal characteristic time of the system defined in equation (2.17)) the DC component stabilizes into the value:

$$\Delta T_{DC} \equiv \frac{Q_0}{G} \tag{3.36}$$

However, the AC component of the temperature depends on the apparent thermal conductance $G_{2\omega}$, which will generally depend on ω and on the geometry of the sensor.

$$\Delta T_{2\omega} \equiv \frac{Q_0}{G_{2\omega}} \quad (3.37)$$

For instance, in the case of the 3ω method developed by Cahill[82], $\frac{1}{G_{2\omega}} \propto -\ln(2\omega)$, while in the 3ω-Völklein method[84], $\frac{1}{G_{2\omega}} \propto \frac{1}{G\sqrt{1+A\omega^2}}$. In all the cases, this apparent thermal conductance is smaller than the real one, since in this permanently transient state (oscillation) part of the heat is spent in dynamically heating the sensor. Also, the apparent thermal conductance can be a complex number, meaning that the temperature oscillations are out of phase from the heating wave. All in all, the apparent conductance is different for the DC and the 2ω components of the power. The combined temperature is then:

$$\lim_{t\to\infty} \Delta T = \Delta T_{DC} - |\Delta T_{2\omega}|\cos(2\omega t + \phi) = \frac{Q_0}{G} - \frac{Q_0}{|G_{2\omega}|}\cos(2\omega t + \phi) \quad (3.38)$$

Where

$$\Delta T_{2\omega} = \Delta T_{2\omega,x} + i\Delta T_{2\omega,y} \quad (3.39)$$

$$\tan\phi = \frac{\Delta T_{2\omega,y}}{\Delta T_{2\omega,x}} \quad (3.40)$$

The resistance of the sensor oscillates owing to its temperature dependence:

$$R = R_0 + \frac{dR}{dT}\Delta T = R_0 + \frac{dR}{dT}[\Delta T_{DC} - \Delta T_{2\omega}\cos(2\omega t + \phi)] \quad (3.41)$$

Finally, the voltage measured between the probes results, according to Ohm's law, from multiplying equations (3.34) and (3.41):

$$V = I_0 R_0 \sin(\omega t) + I_0 \frac{dR}{dT}[\Delta T_{DC}\sin(\omega t) - \Delta T_{2\omega}\cos(2\omega t + \phi)\sin(\omega t)] \quad (3.42)$$

Which can be rewritten as:

$$V = I_0\left\{R_0 + \frac{dR}{dT}\Delta T_{DC}\right\}\sin(\omega t) + I_0\frac{dR}{dT}\frac{\Delta T_{2\omega}}{2}\sin(\omega t + \phi)$$
$$- I_0\frac{dR}{dT}\frac{\Delta T_{2\omega}}{2}\sin(3\omega t + \phi) \qquad (3.43)$$

The third term oscillates at a frequency 3ω, permitting to extract the value of $\Delta T_{2\omega}$ (and thus, of the thermal conductance) by measuring selectively $V_{3\omega}$:

$$\Delta T_{2\omega} = \frac{2V_{3\omega}}{I_0\frac{dR}{dT}} \qquad (3.44)$$

$$\Delta T_{2\omega,x} = \Delta T_{2\omega}\cos\phi \qquad (3.45)$$

$$\Delta T_{2\omega,y} = \Delta T_{2\omega}\sin\phi \qquad (3.46)$$

3.4.3 Thermal analysis of the 3ω method

The sensor used for the measurements is a thin film strip of length L and width $2w$. Since $L \gg w$, the strip can be considered to be an infinitely long and narrow line, and thus the thermal propagation can be considered –in a first approximation- to be cylindrical through the substrate (Figure 3.18a), which implies that the temperature distribution only depends on the radius. This approximation holds for depths much smaller than the length of the sensor but much higher than its width: $L \gg r \gg w$. Otherwise, the thermal transport is distorted into an ellipsoidal propagation.

The propagation of a cylindrical wave generated in the origin of the axis can be analyzed with the heat equation (equation (2.12)) which in cylindrical coordinates is:

$$\frac{1}{D}\frac{\partial T(r,t)}{\partial t} - \left(\frac{1}{r}\frac{\partial}{\partial r}r\frac{\partial T(r,t)}{\partial r} + \frac{1}{r^2}\frac{\partial^2 T(r,t)}{\partial \theta^2} + \frac{\partial^2 T(r,t)}{\partial z^2}\right) = \frac{q(t)}{k} \qquad (3.47)$$

Where $D = k/(\rho c_p)$ is the thermal diffusivity of the substrate, k is the thermal conductivity and

$$q(t) = Q_0 e^{2i\omega t}\delta^2(r)/L \qquad (3.48)$$

is the heat released per unit volume, which is only dissipated in the center of the cylinder (we only focus on the AC component of the power).

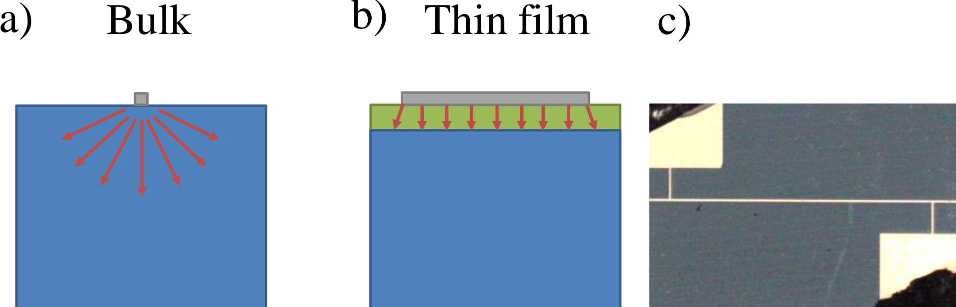

Figure 3.18 Thermal conduction from the heater through a solid. The heat flux can be considered to be cylindrical in a bulk if $w \ll L$. b) Inside a thin film, the heat conduction is quasi-1D as long as $w \gg t_{tf}$. C) Typical sensor used in the measurements ($L = 1$ mm and $w = 2.5$ µm).

Since the temperature does not depend on θ or z, (3.47) reduces to:

$$\frac{1}{D}\frac{\partial T(r,t)}{\partial t} - \left(\frac{1}{r}\frac{\partial T(r,t)}{\partial r} + \frac{\partial^2 T(r,t)}{\partial r^2}\right) = \frac{q(t)}{k} \tag{3.49}$$

The power released by the strip has an angular frequency 2ω, so the expected temperature function must have a time component $e^{2i\omega t}$:

$$T(r,t) = T(r)e^{2i\omega t} \tag{3.50}$$

Thus, equation (3.49) reads:

$$\frac{1}{r}\frac{\partial T(r)}{\partial r} + \frac{\partial^2 T(r)}{\partial r^2} = \frac{2i\omega}{D}T(r) - \frac{q}{k} \tag{3.51}$$

Here, all the time exponentials have been canceled out of the equation. The solution of such equation applied to a semi-infinite volume where the heat generation line lays on its surface depends on the modified Bessel function K_0:

$$\Delta T(r) = \frac{Q_0}{\pi L k}K_0\left(\frac{r}{d}\right) = \frac{Q_0}{\pi L k}\int_0^\infty \frac{\cos\left(\frac{rt'}{d}\right)}{\sqrt{t'^2+1}}dt' \tag{3.52}$$

Where $\Delta T(r)$ is the temperature rise with respect to the infinity

$$\Delta T(r) = T(r) - T(\infty) \quad (3.53)$$

And d is the penetration depth, which is the characteristic wavelength of the temperature evanescent wave:

$$d = \sqrt{\frac{D}{2i\omega}} \quad (3.54)$$

Of course, in this approach, the heating line is at infinite temperature as it is infinitely narrow. The next step is to find the temperature distribution created by a heating strip of width $2w$, which is in fact the convolution of many infinitely narrow heating lines along the width of the sensor. This can be done by applying the convolution theorem, which states that the transform of the convolution of two functions equals the product of the transform of each function. Here we will use the Fourier cosine transform[85] defined from 0 to ∞ as all the functions to which it is applied are even. First, the spatial heat generation function is a normalized rectangle function, since the strip generates a constant heat through its width:

$$f_2(x) = \frac{\mathrm{rect}(\frac{x}{2w})}{2w} \quad (3.55)$$

The Fourier cosine transform of (3.55) is the Sinc function:

$$f_2(k_x) = \int_0^\infty f_2(x)\cos(k_x x)\,dx = \frac{\sin(k_x w)}{k_x w} = \mathrm{sinc}(k_x w) \quad (3.56)$$

Next, the transform of equation (3.52) along the x direction can be found by first substituting $r^2 = x^2 + y^2$ and setting $y = 0$ (since we are interested in the surface temperature):

$$f_1(x) \equiv \Delta T(x) = \frac{Q_0}{\pi L k}\int_0^\infty \frac{\cos\left(\frac{|x|t'}{d}\right)}{\sqrt{t'^2 + 1}}\,dt' \quad (3.57)$$

Its transform is:

$$f_1(k_x) = \frac{Q_0}{2Lk}\int_0^{\infty}\left[\int_0^{\infty}\frac{\cos\left(\frac{|x|t'}{d}\right)}{\sqrt{t'^2+1}}dt'\right]\cos(k_x x)\,dx = \frac{Q_0}{2Lk\sqrt{k_x^2+\left(\frac{1}{d}\right)^2}} \quad (3.58)$$

The product of both transformed functions is:

$$f_1(k_x)\cdot f_2(k_x) = \frac{Q_0}{2Lk}\frac{\mathrm{sinc}(k_x w)}{\sqrt{k_x^2+\left(\frac{1}{d}\right)^2}} \quad (3.59)$$

Its inverse transform yields the real temperature distribution created by the strip:

$$\Delta T_{strip}(x) = \frac{Q_0}{\pi Lk}\int_0^{\infty}\frac{\mathrm{sinc}(k_x w)\cos(k_x x)}{\sqrt{k_x^2+\left(\frac{1}{d}\right)^2}}dk_x \quad (3.60)$$

The average of equation (3.60) results in the mean temperature measured by the strip, which can be calculated without solving the integral as:

$$\Delta T_{strip} = \frac{1}{w}\int_0^{w}\Delta T_{strip}(x)dx \quad (3.61)$$

Resulting in:

$$\Delta T_{strip} = \frac{Q_0}{\pi Lk}\int_0^{\infty}\mathrm{sinc}^2(k_x w)\frac{1}{\sqrt{k_x^2+\left(\frac{1}{d}\right)^2}}dk_x \quad (3.62)$$

The result of this equation can be found numerically[86,87], resulting in:

$$\Delta T_{strip} = \frac{Q_0}{\pi Lk}\left[\ln\frac{d}{w}+\eta\right] = \frac{Q_0}{\pi Lk}\left[\frac{1}{2}\ln\left(\frac{D}{w^2}\right)-\frac{1}{2}\ln(2\omega)+\eta+\frac{i\pi}{4}\right] \quad (3.63)$$

Where $\eta = 0.923$ in the limit that $d \gg w$. This equation shows the decrease in the temperature amplitude when the frequency increases. Also, there is a constant out-of-phase component of the temperature due to the presence of an imaginary term.

With the slope of the curve $\Delta T_{strip}(\ln(2\omega))$, namely $S_{\Delta T}$, the thermal conductivity of the bulk material can be calculated:

$$k = -\frac{Q_0}{2\pi L S_{\Delta T}} \quad (3.64)$$

When a thin film is added between the strip and the bulk, the heat propagation can be considered to be one-dimensional through it in the region where it is covered by the strip, as long as the half-width of the strip is much bigger than its thickness, $w \gg t_{tf}$ (Figure 3.18b). In this case, the contribution of the thin film to the temperature of the strip can be approximated by

$$\Delta T_{tf} = \frac{Q_0}{k_{tf}} \frac{t_{tf}}{2wL} \tag{3.65}$$

Then, adding the bulk and the thin film contributions to the temperature (equations (3.63) and (3.65)) we get:

$$\Delta T_{strip} = \frac{Q_0}{\pi L k} \left[\frac{1}{2} \ln\left(\frac{D}{w^2}\right) - \frac{1}{2} \ln(2\omega) + \eta + \frac{i\pi}{4} \right] + \frac{Q_0}{k_{tf}} \frac{t_{tf}}{2wL} \tag{3.66}$$

In order to measure the thermal conductivity of a thin film, the most used strategy is to measure the temperature rise in a chip with the thin film and in one without the thin film, using in both cases identical sensors at the same frequencies. This allows to extract directly the thermal resistance of the thin film, as will be discussed in section 3.4.7.

3.4.4 Sensor fabrication

The sensors used for measuring the thermal conductivity of thin films with the differential 3ω method have been fabricated following two steps:

3.4.4.1 Dielectric layer deposition

For measuring non-insulating samples, a dielectric thin-film must be deposited between the sample and the sensor to prevent electrical leakage through the substrate, which can greatly perturb $V_{3\omega}$. This is a challenge when covering nanostructured samples, which cannot withstand (due to the interatomic diffusion) a high-temperature (~800 ºC) deposition that would ensure the film conformity. Also, the thickness of this insulator must be the same in the sample and in the reference so that the Differential 3ω method can be safely applied.

Taking into account all these constraints, the material selected as dielectric layer is amorphous Al_2O_3 deposited by Atomic Layer Deposition (ALD) at 200 ºC. The deposition method ensures a perfect coverage of the sample, while the thickness of the

layer can only vary from point to point of a 4-inch wafer 10% of the total thickness at most.

3.4.4.2 Sensor deposition

The next step in the fabrication is the sensor deposition. In this step, photolithography is avoided in order to maintain the integrity of the dielectric layer. Instead, the deposition is performed with shadow masks. Generally, this method produces sensors with variable thickness, which is overcome by slightly modifying the data reduction procedure (see Section 3.4.7). The sensor is made of a 10 nm Cr adhesion layer plus a 100 nm Au layer. After the deposition, the sensor is annealed at 100ºC during several hours in order to thermally stabilize it.

3.4.5 Electronics

The electronic setup is shown in Figure 3.19. An AC current with amplitude I_0~30 mA is generated with a Keithley 6221, feeding in series the sample and a variable resistance or potentiometer. The voltage drops in both elements (V_{smp} for the sample and V_{ref} for the variable resistance) are extracted with INAs 111 amplified x1, since the signals are already about 2-3 V. The differential voltage V_{diff} is measured by subtracting V_{ref} from V_{smp} with another INA 111, this time with a gain x100. Since there is no temperature dependence on the variable resistance, the 3ω component of V_{Diff} is only produced by the sample heating.

The signals V_{smp} and V_{diff} are acquired with a NI-FPGA-7833R. The amplitude of the 1st harmonic of both signals is calculated, as well as the 3ω component of V_{diff} ($V_{diff,3\omega}$) and its phase respect $V_{smp,1\omega}$, which is used to calculate the in-phase and the out-of-phase components of $V_{diff,3\omega}$.

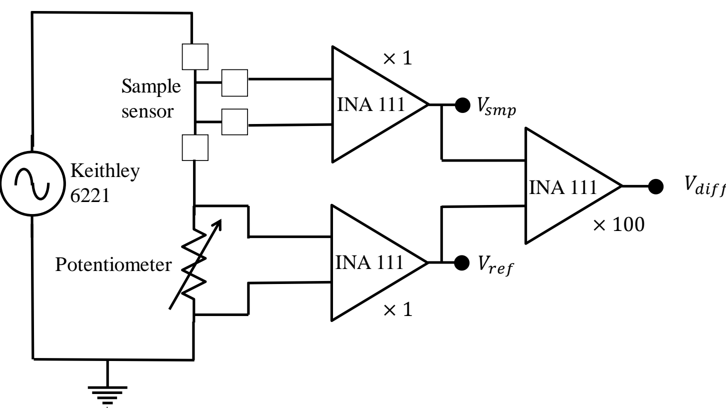

Figure 3.19: Scheme of the electronics and the cancellation circuit of the voltage signals.

3.4.6 Measurement cycle

In order to measure the thermal conductivity of thin films, the following procedure is used. First of all, the temperature is stabilized. Then, the resistance is calibrated by feeding the circuit with an AC current of 1 mA at about 75 Hz. After this, the current is set to 20-50 mA (depending on the sensor resistance and the sample thermal conductivity), and it is left until the base temperature is once again stable (about 10 minutes). Then, the frequency is swept from 75 Hz to 4000 Hz while both signal voltages are acquired. The total integration time is about 0.5 s for each frequency.

This cycle is performed for both the sample and the reference (which is identical to the sample except for the absence of the thin film under test).

3.4.7 Data reduction

The sensors used may have slightly different widths (for example, 4 μm and 5 μm) due to the fabrication method. In this case, the direct subtraction of temperature amplitudes cannot be performed, since the bulk contribution to the thermal conductance differs from the sample to the reference. Thus, a more sophisticated data reduction has to be applied.

First of all, the reference is measured, and with the slope of the measured ΔT_{ref} versus the frequency, the thermal conductivity of the bulk is calculated with equation (3.64). Knowing this value along with the thermal diffusivity of the sample and the width of the sensor, the contribution of the bulk to the temperature rise ($\Delta T_{ref,bulk}$) is calculated by applying equation (3.63). Then, by subtracting this value from the measured reference we get the temperature drop in the alumina layer ($\Delta T_{ref,Al_2O_3} = \Delta T_{ref} - \Delta T_{ref,bulk}$), from which its thermal conductivity is calculated applying equation (3.65).

With the knowledge of the alumina thermal conductivity, the contribution of the alumina plus the substrate to the sample temperature rise is calculated with equation (3.66), but now the width used for the calculations is the one of the sample sensor. In this way the simulated signal can be directly subtracted from the sample signal as if it was the measurement of the reference. Finally, the $\Delta T_{2\omega}$ difference between the simulated reference and the sample leads to the thermal conductivity of the thin film under test.

3.4.8 Experimental results

The thermal conductivity of a SiN_x thin film has been measured to test the system. In order to extract the thermal conductivity, 2 sensors have been deposited each on a chip

with a SiN_x layer 180 nm thick and 450 nm thick, respectively. Both sensors are 50 μm wide and 2 mm long. In this case the deposition of an Al_2O_3 layer is unnecessary since the SiN_x layer is already preventing electrical leakage through the substrate. The result is shown in Figure 3.27 along with the data measured with the 3ω Völklein method, showing a value of 2.31 $W \cdot m^{-1} \cdot K^{-1}$ at room temperature, in agreement with other values from the literature.

3.5 3ω Völklein method

3.5.1 Motivation and description

Several prior studies have used thermal probes to analyze ex-situ the growth of thin films [87,88]. They have found that the thermal conductivity of the grown material is conditioned by the thermal conductance reduction of the sample support due to interfacial scattering of phonons in in-plane measurements[88] and to thermal boundary resistance in out-of-plane measurements[87]. For this reason, the thermal conductivity of the thin layer cannot be calculated from the differential measurement of the thermal conductance between a sample (film + membrane) and a reference (only membrane), but must be calculated from a set of thermal conductance measurements performed by varying the film thickness. Up to date, most of these measurements have been performed ex-situ evaluating the temperature dependence of k for each selected thickness. To our knowledge, real-time studies during the early stages of film growth, including the impact of microstructure on phonon scattering, have not been previously reported. It is worth noting that Völklein & Starz[89] already demonstrated in 1997 that a thin-film based sensor operating in DC mode could be used for measuring in-situ the in-plane thermal conductance of thin films. Unfortunately, measurements of the thermal conductance on films thinner than 1 μm were limited to metallic materials. However, Sikora et al. improved later the measuring system by combining the Völklein method with the AC 3ω-method, reaching an exceptional thermal conductance sensitivity, $\frac{\Delta G}{G} \cong 10^{-3}$ [84,90].

Here we develop a modification of the 3ω-Völklein technique that allows for in-situ measurements of the thermal conductance with sub-ML sensitivity during thin film growth. The method can be applied to (ultra)thin layers of both highly insulating and conductive (electrically and thermally) materials. The use of acquisition rates about 1 Hz allows studying in real time the percolation threshold to film continuity and other surface

phenomena in a broad deposition rate interval spanning from 0.01 nm/s up to 10's of nm/s.

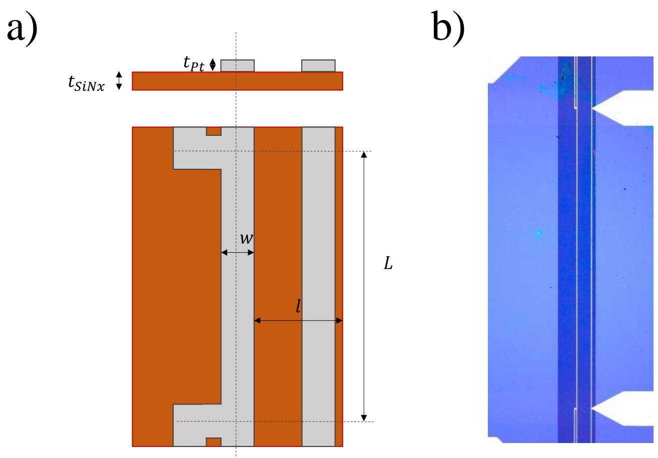

Figure 3.20: a) Scheme of the sensor (side and top views), consisting on a suspended membrane with a Pt strip on it. b) micrograph of the sensor.

The sensor developed here is composed by a long and thin suspended SiN_x membrane equipped with 2 platinum parallel lines 5 μm wide, connected in a 4-wire configuration (Figure 3.20). The thermal conductance of the whole membrane is determined with the centered Pt line (normal operation), while both lines, centered and external, are needed to measure exclusively the thermal conductance of the membrane volume portion beneath both sensors lines. In normal operation, the thermal conductance measured in DC is calculated by using the 1D Fourier law and assuming that the external line is much more conductive than the SiN_x beneath (i.e. $k_{Pt} \gg k_{SiN_x}$), which yields equation (3.67).

$$G = k_{SiN_x} t_{SiN_x} \left(\frac{L}{l} + \frac{L}{l - w} \right) \tag{3.67}$$

Where t_{SiN_x} and k_{SiN_x} are the thickness and the thermal conductivity of the silicon nitride, L is the length of the Pt strip between the voltage probes, w is the width of the Pt strip and l is the distance between the Pt strip and the substrate. However, for the AC characterization, a more complex analysis is needed, as will be shown in the next section.

3.5.2 Thermal model of the 3ω-Völklein method

The temperature oscillations on the membrane can be investigated by applying the heat equation to the system. We can use the 1D heat equation, since the heat flow between the voltage probes is perpendicular to the frame. Also, considering a single strip sensor, it is symmetric, so the membrane can just be studied in one half (from the center of the sensor to the border).

Thus, we start with equation (2.12), the Heat equation. We know that the power has AC and DC components (equation (3.35)). Since they produce completely independent temperature variations, we focus only in the sinusoidal power. For convenience, we write it in the exponential form:

$$Q = Q_0 e^{2i\omega t} \tag{3.68}$$

An oscillating power will produce throughout the membrane an oscillating temperature with the same frequency. Thus,

$$T(x,t) = T(x) e^{2i\omega t} \tag{3.69}$$

Now we can substitute equation (3.69) into (2.12), finding

$$\frac{\partial^2 T(x)}{\partial x^2} = \frac{2i\omega}{D} T(x) \tag{3.70}$$

Here, the exponential term is the same at both sides of the equation, so it is canceled out. A general solution for this expression is:

$$T(x) = A e^{\sqrt{\frac{2i\omega}{D}}x} + B e^{-\sqrt{\frac{2i\omega}{D}}x} \tag{3.71}$$

Now we can use the boundary conditions to find A and B. First of all, the temperature at the border ($x = 0$) of the membrane is forced to be 0. Thus,

$$T(x = 0) = A + B = 0 \rightarrow B = -A \tag{3.72}$$

Substituting this into (3.71) and further into (3.69), we find

$$T(x) = 2A \sinh\left((i+1)\sqrt{\frac{\omega}{D}}x\right) \tag{3.73}$$

$$T(x,t) = 2A \sinh\left((i+1)\sqrt{\frac{\omega}{D}}x\right) e^{2i\omega t} \tag{3.74}$$

Now, the boundary condition in the border of the Pt strip is that the heat generated by it (which is considered to be a perfect thermal conductor) contributes to the heat conduction and to the dynamic heating of the membrane. This can be written as:

$$Q_0 = k_{SiN_x} S \left(\frac{\partial T(x,t)}{\partial x}\right)_{x=l} + C' \left(\frac{\partial T(x,t)}{\partial t}\right)_{x=l} \tag{3.75}$$

Where k_{SiN_x} is the thermal conductivity of the membrane, S is the section of the membrane ($S = t_{SiN_x} L$) and C' is the combined heat capacity of the sensor and the membrane beneath the sensor: $C' = c_{SiN_x}\rho_{SiN_x}t_{SiN_x}L\frac{w}{2} + c_{Pt}\rho_{Pt}t_{Pt}L\frac{w}{2}$, where $c_{SiN_x,Pt}$ and $\rho_{SiN_x,Pt}$ are the heat capacity and the density of SiN_x and Pt, respectively. Inserting (3.74) into (3.75) yields:

$$A = \frac{Q_0}{2\left[k_{SiN_x} S(i+1)\sqrt{\frac{\omega}{D}} \cosh\left((i+1)\sqrt{\frac{\omega}{D}}l\right) + 2i\omega C' \sinh\left((i+1)\sqrt{\frac{\omega}{D}}l\right)\right]} \tag{3.76}$$

And thus:

$$T(x,t) = \frac{Q_0 \sinh\left((i+1)\sqrt{\frac{\omega}{D}}x\right) e^{2i\omega t}}{\left[k_{SiN_x} S(i+1)\sqrt{\frac{\omega}{D}} \cosh\left((i+1)\sqrt{\frac{\omega}{D}}l\right) + 2i\omega C' \sinh\left((i+1)\sqrt{\frac{\omega}{D}}l\right)\right]} \tag{3.77}$$

The modulus of this temperature oscillation (found as $\Delta T_{2\omega} \equiv |T| = \sqrt{T\bar{T}}$) at the position $x = l$ (in the Pt sensor) is:

$$\Delta T_{2\omega} = \frac{Q_0 \sqrt{\cosh\left(2l\sqrt{\frac{\omega}{D}}\right) - \cos\left(2l\sqrt{\frac{\omega}{D}}\right)}}{\sqrt{\frac{2\omega}{D}\left[(G'^2 l^2 - 2C'^2 D\omega)\cos\left(2l\sqrt{\frac{\omega}{D}}\right) + (G'^2 l^2 + 2C'^2 D\omega)\cosh\left(2l\sqrt{\frac{\omega}{D}}\right) + 2C'G'l\sqrt{D\omega}\left(\sinh\left(2l\sqrt{\frac{\omega}{D}}\right) - \sin\left(2l\sqrt{\frac{\omega}{D}}\right)\right)\right]}} \tag{3.78}$$

Where $G' = \frac{k_{SiNx} S}{l}$. Since our sensor has a 2nd Pt strip that slightly reduces the thermal conductance, we should substitute G' for G. This can be done if the heat capacity of the second Pt line is assumed to be negligible. In order to reduce the complexity of this equation, the trigonometric functions are expanded in series of ω:

$$\cos\left(2l\sqrt{\frac{\omega}{D}}\right) \approx 1 - \frac{2l^2}{D}\omega + \frac{2l^4}{3D^2}\omega^2 + O(\omega^4) \tag{3.79}$$

$$\cosh\left(2l\sqrt{\frac{\omega}{D}}\right) \approx 1 + \frac{2l^2}{D}\omega + \frac{2l^4}{3D^2}\omega^2 + O(\omega^4) \tag{3.80}$$

$$\sin\left(2l\sqrt{\frac{\omega}{D}}\right) \approx 2l\sqrt{\frac{\omega}{D}} - \frac{4l^3}{3}\left(\sqrt{\frac{\omega}{D}}\right)^3 + O(\omega^{5/2}) \tag{3.81}$$

$$\sinh\left(2l\sqrt{\frac{\omega}{D}}\right) \approx 2l\sqrt{\frac{\omega}{D}} + \frac{4l^3}{3}\left(\sqrt{\frac{\omega}{D}}\right)^3 + O(\omega^{5/2}) \tag{3.82}$$

This yields the expression:

$$\Delta T_{2\omega} = \frac{Q_0}{G\sqrt{1 + (2\omega)^2\left(\tau^2 + \frac{1}{3}\frac{l^2}{D}\tau + \frac{1}{6}\frac{l^4}{D^2}\right)}} \tag{3.83}$$

Where $\tau = C'/G$. In Figure 3.21 both the original and the approximated functions are compared. The behavior of the oscillation amplitude is driven by relationship between l and the penetration depth $d = \sqrt{\frac{D}{\omega}}$, which is the parameter that describes the spatial damping of the thermal wave produced by the heater. In the case $d \gg l$ (or $\omega \ll \frac{D}{l^2}$), all the heat generated by the sensor is spent in the thermal conduction through the membrane ($G\Delta T$) instead of the dynamic heating of the membrane ($C'\frac{dT}{dt}$). In this case, the oscillation amplitude of the temperature is maximum and the apparent thermal conductance $G_{2\omega}$ resembles G (equation (3.84)), which makes easy to find the thermal conductivity of the membrane since G is only related by known geometrical factors to k_{SiN_x} (equation (3.67)).

$$G_{2\omega} = \frac{Q_0}{\Delta T_{2\omega}} = G\sqrt{1 + (2\omega)^2\left(\tau^2 + \frac{1}{3}\frac{l^2}{D}\tau + \frac{1}{6}\frac{l^4}{D^2}\right)} \tag{3.84}$$

However, as the frequency increases, the temperature oscillations decrease due to the dynamic heating of the membrane and the apparent thermal conductance starts deviating from G.

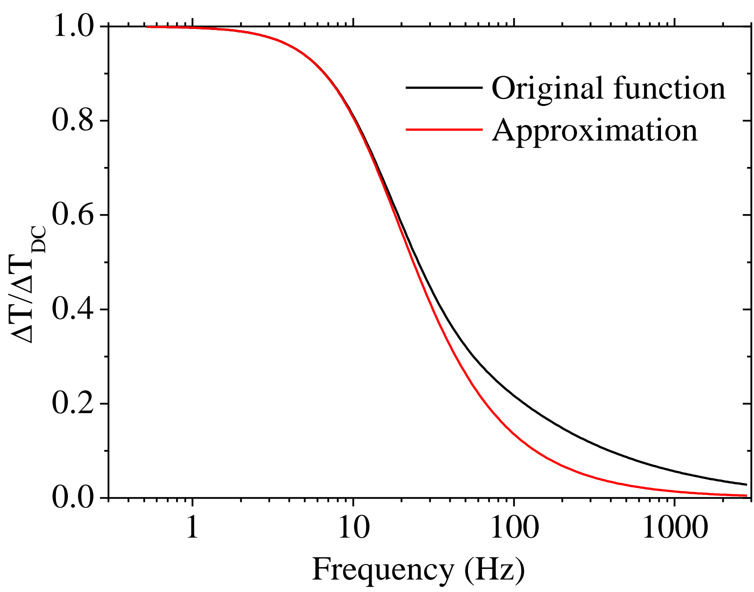

Figure 3.21: Frequency dependence of $\Delta T_{2\omega}$ according to equations (3.78) and (3.83).

3.5.3 Sensor optimization

We have modeled several sensor geometries using Finite Element Model (FEM) in COMSOL software in order to ensure temperature homogeneity between the voltage probes of the central strip, for enhanced thermal conductivity measurement accuracy (Figure 3.22). This simulation reproduces a steady state by feeding the Pt strip with a DC current. The optimum sensor (taking into account the resolution limits of the available photolithographic system and the structural stability of the SiN_x membrane) consists in a long and narrow SiN_x membrane (3mm x 250 μm x 180 nm) that supports the two Pt sensing strips (3mm x 5 μm x 100 nm) with voltage probes separated 2 mm. A key point in this design is the close proximity of the voltage probes and the central Pt strip, to avoid heat leakage and any temperature drop along the strip. The longitudinal temperature simulated profile (Figure 3.22a) shows a large and flat central plateau where the inhomogeneity is less than 3% of the total temperature rise. We notice two tiny temperature depressions at ±1000 μm, coinciding with the voltage probe locations. The transversal profile exhibits a constant slope only perturbed by minimal flat segments corresponding with the position of the Pt strips. The parameters used in the simulation are listed in Table 3.2.

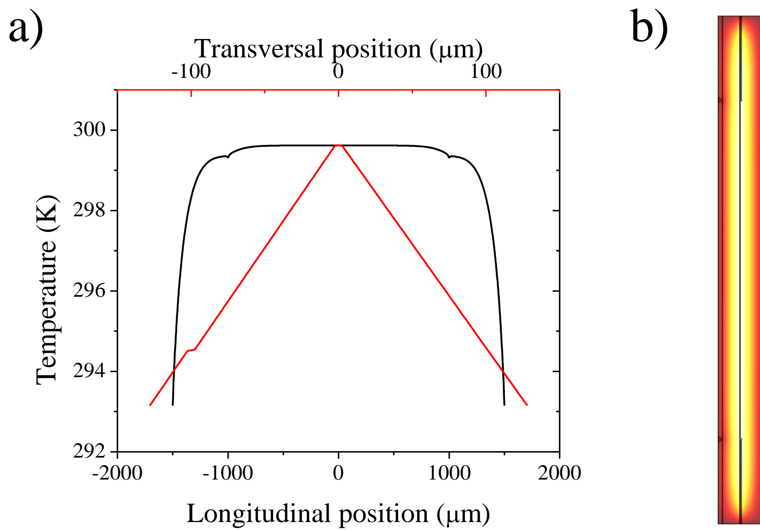

Figure 3.22: a) Longitudinal and transversal temperature distribution of the sensor in a DC study. b) Surface temperature distribution of the sensor (brighter is hotter) in a DC study.

In this modeled optimal sensor, the thermal conductance is calculated as $G = Q_0/\Delta T_{DC}$ using the average temperature between the probes (ΔT_{DC}) and the power dissipated in the same region of the Pt strip (Q_0), resulting in $1.553 \cdot 10^{-5}$ W/K. From this value one can extract the thermal conductivity of the SiN_x membrane by applying equation (3.67), finding a value of 2.652 $W \cdot m^{-1} \cdot K^{-1}$, which is in good agreement with the imposed thermal conductivity of the modeled SiN_x, 2.65 $W \cdot m^{-1} \cdot K^{-1}$ owing to the optimization process.

Parameter	Pt	SiNx
k ($W \cdot m^{-1} \cdot K^{-1}$)	33	2.65
c ($J \cdot Kg^{-1} \cdot K^{-1}$)	133	700
ρ (Kg/m^3)	21450	3180

Table 3.2: Parameters used in the COMSOL model.

3.5.4 Deposition of a thin-film

When a thin-film sample grows on the SiN_x membrane, the parameters in equations (3.78) and (3.83) may vary as k, c and ρ will no longer correspond to the bare SiN_x membrane but to a new combined sample. In this case, an effective value for these magnitudes can be calculated by pondering the different values as a function of the film thickness:

$$k_{eff} = \frac{k_{SiN_x} t_{SiN_x} + k_{smp} t_{smp}}{t_{SiN_x} + t_{smp}} \tag{3.85}$$

$$c_{eff} = \frac{c_{SiN_x} t_{SiN_x} + c_{smp} t_{smp}}{t_{SiN_x} + t_{smp}} \quad (3.86)$$

$$\rho_{eff} = \frac{\rho_{SiN_x} t_{SiN_x} + \rho_{smp} t_{smp}}{t_{SiN_x} + t_{smp}} \quad (3.87)$$

$$D_{eff} = \frac{k_{eff}}{\rho_{eff} c_{eff}} \quad (3.88)$$

In the same way, the extrinsic values G and C' (and consequently τ) will change:

$$G(t_{smp}) = (k_{SiN_x} t_{SiN_x} + k_{smp} t_{smp}) \left(\frac{L}{l} + \frac{L}{l-w}\right) \quad (3.89)$$

$$C'(t_{smp}) = wL(\rho_{SiN_x} c_{SiN_x} t_{SiN_x} + \rho_{Pt} c_{Pt} t_{Pt} + \rho_{smp} c_{smp} t_{smp}) \quad (3.90)$$

$$\tau' = \frac{C'(t_{smp})}{G(t_{smp})} \quad (3.91)$$

The derivative of equation (3.89) can be used to calculate the thermal conductivity of the sample film measuring in real-time the thermal conductance during growth ($G_{2\omega}(t_{smp})$), as shown in equation (3.92). Nevertheless, this equation is only valid if the current angular frequency is very low ($\omega \ll \frac{3D}{8l^2}$) and $G_{2\omega} \approx G$.

$$\frac{dG}{dt_{smp}} = k_{smp} \left(\frac{L}{l} + \frac{L}{l-w}\right) \rightarrow k_{smp} = \frac{\frac{dG}{dt_{smp}}}{\left(\frac{L}{l} + \frac{L}{l-w}\right)} \quad (3.92)$$

If a higher current angular frequency is used, k_{smp} can be extracted by fitting the measured $G_{2\omega}(t_{smp})$ with equation (3.93) using the thickness-dependent parameters (equations (3.85)-(3.91)):

$$G_{2\omega} = G(t_{smp}) \sqrt{1 + (2\omega)^2 \left(\tau^2 + \frac{1}{3}\frac{l^2}{D}\tau + \frac{1}{6}\frac{l^4}{D^2}\right)} \quad (3.93)$$

In Figure 3.23a the calculated $G_{2\omega}(t_{smp})$ is plotted for current frequencies of 0 Hz (DC), 1 Hz and 3 Hz (the parameters used are listed in the image caption). If the conductance is monitored with a current at 1 Hz, the apparent thermal conductance $G_{2\omega}$ is very similar to G throughout the deposition. However, at 3 Hz, there is an evident difference in the slope of the curves: Although the absolute value of the apparent thermal conductance only varies from 97% to 93% of G (Figure 3.23b), the slope of $G_{2\omega}(t_{smp})$ is up to 40% higher than the one of $G(t_{smp})$ (Figure 3.23a). Generally, measuring with higher frequencies increases the dependence of $G_{2\omega}$ with properties of the sample that may be not well known (like c or ρ), making it more difficult to find k_{smp}.

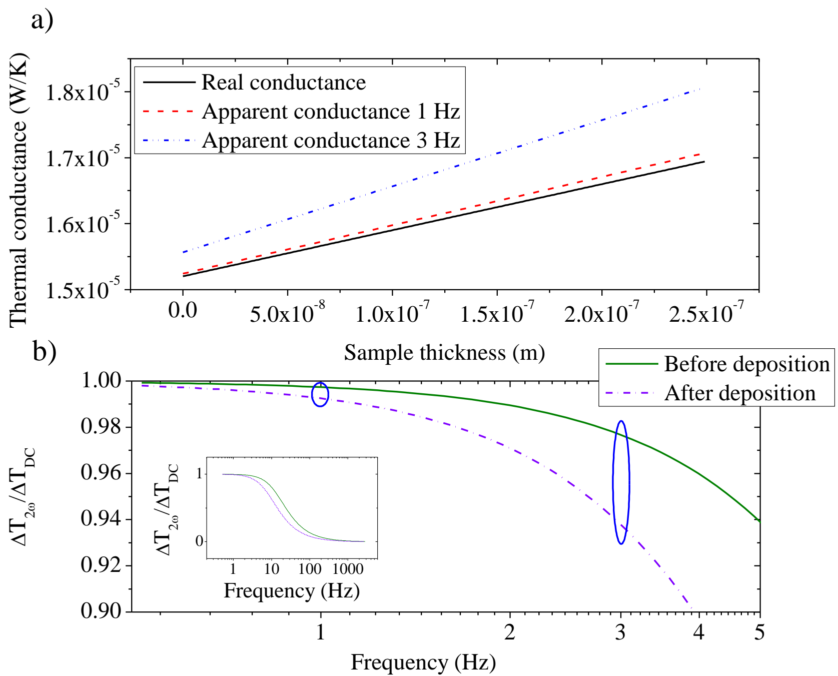

Figure 3.23: a) Calculated real thermal conductance (black) and apparent thermal conductance modeled at 1 Hz (red) and 3 Hz (blue) during the deposition of a layer. b) Calculated frequency dependence of the temperature oscillations in the sensor before and after depositing a 250 nm film (the inset is a zoom out). The material properties used in both plots are the following: $k_{SiN_x} = 2.65$ W·m^{-1}·K^{-1}, $c_{SiN_x} = 0.7$ J/(K·Kg), $\rho_{SiN_x} = 3.18$g/cm^3, $k_{Pt} = 33$ W·m^{-1}·K^{-1}, $c_{Pt} = 0.133$ J/(K·Kg), $\rho_{Pt} = 21.45$g/cm^3, $k_{smp} = 0.21$ W·m^{-1}·K^{-1}, $c_{SiN_x} = 1.05$ J/(K·Kg) and $\rho_{SiN_x} = 1.08$ g/cm^3. The structural parameters are $t_{SiN_x} = 180\ nm$, $t_{Pt} = 110\ nm$, $l = 123$ µm, $w = 5$ µm and $L = 2000$ µm.

3.5.5 Microfabrication of the thermal sensor

The sensor is fabricated following the next steps (schematized in Figure 3.24) in a clean room facility:

i) The starting point is a 4-inch and 525 μm thick Si wafer slightly p-doped (20 Ω·cm).

ii) The first step of the microfabrication is the double-side oxidation of Si, generating a 50 nm thick SiO_2 layer. The growth in the first place of the SiO_2 layer is performed in order to avoid electrical leakage due to the shunting of the SiN_x layer above 400ºC.

iii) A low stress 180 nm SiN_x film is deposited also at both sides of the wafer using LPCVD at 800ºC.

iv) The next step consists in the photolithography of the Pt strips. First, the wafer is spin-coated with positive photoresist, which is insolated and revealed. After this, a metallic thin film is deposited: First, a 10 nm thick Ti layer that will act as an adhesion layer and then a 100 nm thick Pt layer that forms the actual sensor. The photoresist is then lifted off, leaving the circuits defined.

v) At this point, the wafer is annealed at 600ºC during 2h in order to stabilize the Pt metallization, reducing the resistivity and increase the TCR ($\alpha = \frac{1}{R}\frac{dR}{dT}$).

vi) The wafer is double-side aligned in order to open windows from the backside under the sensors. The SiN_x and SiO_2 layers are selectively etched using RIE with gases C_4HF_8 and CH_4 for SiN_x and CHF_3 for SiO_2.

vii) The back-side of the wafer is anisotropically etched with KOH 35% at 80ºC. The etching is performed until only around 5-10 μm of Si are left.

viii) The wafer is cut in chips 6 mm x 6 mm. Then, the remaining Si under the sensor area is individually etched with KOH.

ix) The final step consists on removing the SiO_2 of the membrane. This is done by dropping 8 μl of 2.5% HF in the backside of the membrane during 10'.

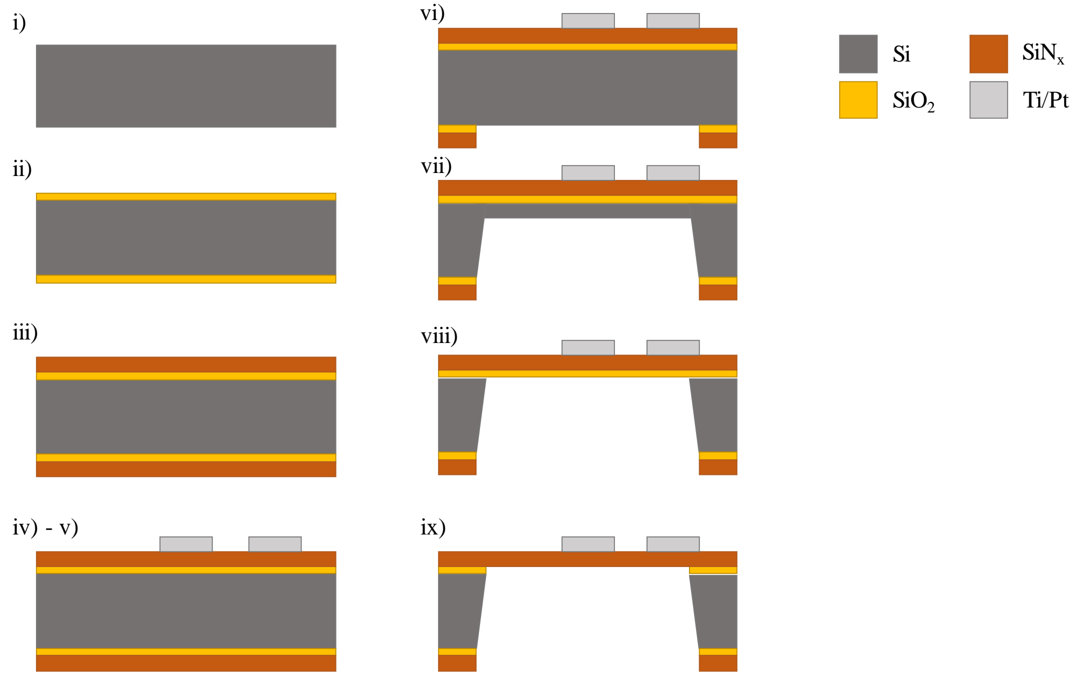

Figure 3.24: Fabrication steps of the sensor.

3.5.6 Electronics

The electronics used in the measurement of the different voltage signals is schematically shown in Figure 3.25. The experiment is performed by feeding two sensors (sample and reference) with a current wave of a given amplitude and frequency, generating a voltage drop in each sensor. The voltage signals from both sensors, as well as the differential voltage between them, are subtracted using the low-noise amplifiers INA 114 with gains 3.3 and 75, respectively. The reference sensor is a twin (equal to the sample one) non-suspended sensor. Since the thermal link from the Pt line to the substrate in this twin sensor is very high due to the presence of the bulk silicon, the self-heating is completely suppressed and the voltage measured has no 3ω component. Thus, the 3ω component of the differential voltage is only produced in the sample sensor, and owing to the cancellation of the 1ω voltage, it can be amplified with a gain of 75. The main benefit of using a twin sensor (instead of a variable resistance) as a reference for the differential measurement is that, if the temperature of the sample holder is varied, the resistance of both sensors will change hand-in-hand, making it unnecessary to build a control system for the cancellation of the 1ω voltage.

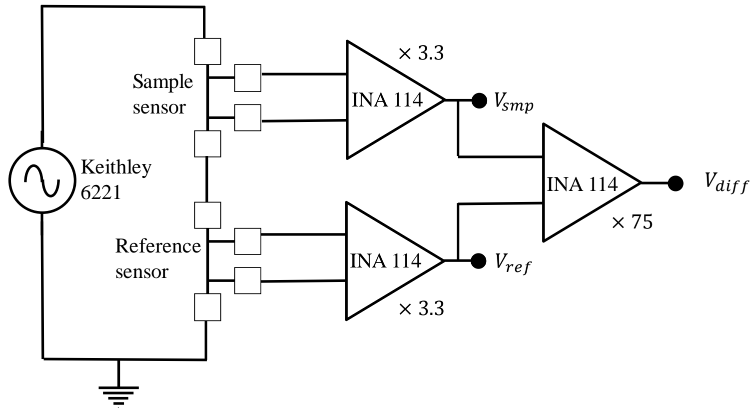

Figure 3.25: Scheme of the electronics and the cancellation circuit of the voltage signals.

The voltage signals are acquired by a multiplexed FPGA 7855R acquisition card with time windows equal to 3 current periods (The total amount of measured datapoints per window is around 15000). After this, a Discrete Fourier Transform (DFT) is performed with Labview software, and the amplitude and phase of the signals is calculated at angular frequencies ω and 3ω.

From the measured voltage signals, the resistance R_{smp} and the temperature oscillations $\Delta T_{2\omega}$ can be calculated as:

$$R_{smp} = \frac{V_{1\omega}}{I_0 \cdot 3.3} \tag{3.94}$$

$$\Delta T_{2\omega} = \frac{2V_{3\omega}}{I_0 \frac{dR_{smp}}{dT} \cdot 75 \cdot 3.3} \tag{3.95}$$

Where $V_{1\omega}$ and $V_{3\omega}$ are the 1ω and 3ω voltage components measured in the sample sensor, and $\frac{dR_{smp}}{dT}$ is the slope of the sample resistance as a function of the temperature.

3.5.7 Experimental results

Initially, the self-heating of the Pt sensor has been revealed by measuring both the 3ω voltage and the variation of the 1ω voltage with $\omega = 2\pi\ rad/s$ (Figure 3.26a). Since the frequency is very low, both signals produce the same self-heating, but as can be seen, the self-heating calculated with the 3ω voltage is less noisy. Also, the slope of $\Delta T_{2\omega}$ has a value very close to 2, demonstrating that the self-heating depends on the square of the current.

$\Delta T_{2\omega}$ has also been measured for a wide frequency range (1 Hz to 2000 Hz) and has been compared with the values found with COMSOL* in a time-dependent study, as can be seen in Figure 3.26b.The high coincidence between both datasets suggests that the behavior of the sensor is purely driven by heat transport physics. This is an important difference from the device presented by Sikora et al.[84], where the use of a NbN strip sensor allowed measurements at very low temperatures, but produced non-negligible electrical effects due to the high electrical impedance of that material.

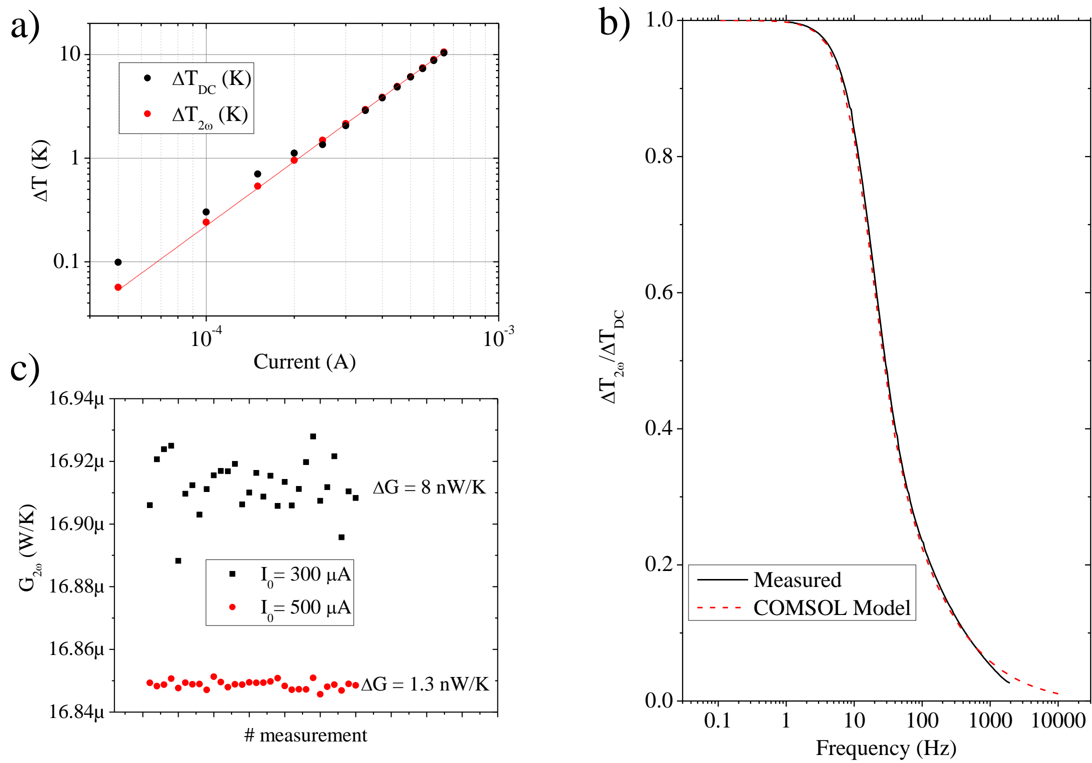

Figure 3.26: a) Self-heating of the sensor measured with the 3ω voltage and the variation of the 1ω voltage. b) Temperature oscillations as a function of the frequency. The measured values are compared with the simulated ones using the COMSOL model. c) Measurement of the uncertainty of the thermal conductance.

As shown in Figure 3.26c, the uncertainty of the conductance measurement has been determined at two different current intensities, 300 μA and 500 μA, which generated temperature amplitudes of about 2 K and 6 K, respectively and produced a standard deviation of data equal to 8 nW/K and 1.3 nW/K. This accuracy in the thermal conductance provides an extremely high resolution (low uncertainty) in the product of the

* The time-dependent study has been performed by releasing in the Pt line a 2ω modulated power that oscillates around the DC power used in the steady state study. The initial condition in this study is the temperature distribution found in the DC study. In all the different frequencies used, 5 periods of the temperature wave have been simulated with a time stepping of one hundredth of period. The oscillation amplitude has been found by fitting a sine function to the last simulated period at each frequency. The parameters used are listed in Table 3.2.

thermal conductivity and the thickness, $\delta(k \cdot t) = 0.065 \frac{\text{W}}{\text{m}\cdot\text{K}} \cdot \text{nm}$. Although there is a decrease in the data dispersion for 500 μA, there is also a noticeable reduction in the average value of the thermal conductance, from 16.91 μW/K to 16.85 μW/K that may be justified by the reduction of the sensor dR/dT due to the 4 K temperature difference between both cases.

As a first measurement, the thermal conductivity of the SiN_x membrane was evaluated for temperatures between 80 K and 230 K, as can be seen in Figure 3.27. The results match with the values found in the out-of-plane direction using the 3ω method on a similar SiN_x membrane (red circles in Figure 3.27). These values were obtained through a differential measurement of two samples with thicknesses of 180 nm and 450 nm, which means that the thermal boundary resistances between the sensor, the film and the substrate are cancelled. Thus, the coincidence of both the in-plane and the out-of-plane values confirm that there are not substantial phonon size effects or anisotropy in our layers. Both datasets have a temperature dependence quite similar to the data of Sikora et al[84,90]. The discrepancy in the absolute value may account for density or stoichiometry variations due to the different growth characteristics of the films. Finally, the different temperature trend from the data of Sultan et al.[91] could be related to a different internal order of their nitride membrane, suggesting a nanocrystalline structure.

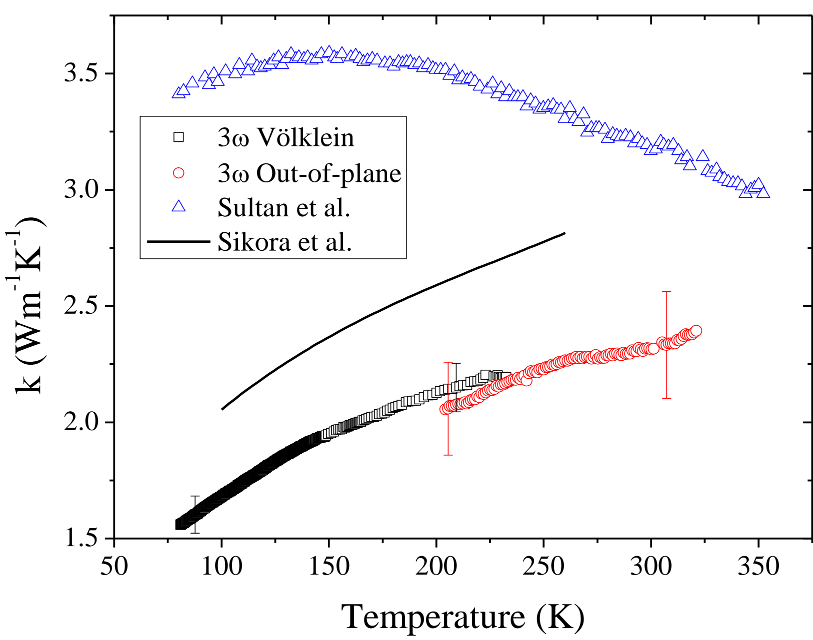

Figure 3.27: Thermal conductivity measurement of SiN_x using both the 3ω method and the 3ω Völklein method. Current frequency 1Hz. Data from Sultan et al.[91] and Sikora et al.[90] included for comparison

The main source of uncertainty in the in-plane measurement is the SiN_x membrane thickness, which was measured after its deposition throughout the wafer with a contactless optical profilometer, yielding a standard deviation of 1% of the total value of 180 nm. However, the wet etchings at the final steps of the microfabrication process could slightly reduce this thickness and inevitably increases the uncertainty up to 5%.

The thermal conductance measurement during a film growth is described and discussed in Chapter 7.

3.6 Conclusions

In this chapter we have presented the three alternative methods developed along this PhD to measure the thermal conductivity of nanomaterials. They are briefly outlined in Table 3.3.

	Scheme	Measurable samples	Direction of measurement	Approximated applicability range	Maximum Resolution
Suspended structures		nanowires, membranes	main axis, in-plane	0.5-1000 nW/K	0.02 nW/K
3ω method		thin-films, bulk	out-of-plane	1-100 K/W	0.03 K/W
3ω Völklein method		thin deposited films	in-plane	10 nW/K – 300 μW/K	1.3 nW/K or 0.065 $\frac{W}{m \cdot K} \cdot nm$

Table 3.3 General information about the measurement methods presented. The red arrows in the schemes indicate the direction of the measured heat flow of each measurement method. The temperature range of applicability is determined by the cryostat.

First, we have presented the suspended structures, a very insulated sensor designed for measuring the thermal conductivity of 1D and 2D nanomaterials in the in-plane direction. The thermal conductance range of the sensor is between 0.5 nW/K and 800 nW/K, yielding a relative uncertainty in the measured conductance below 5%. Although the 1D analysis of the structure offers a versatile way of extracting the thermal conductance from the measured temperatures on both platforms and the power released, it fails at calculating

the thermal conductance of very conductive films. For this reason, a 3D Finite Element Model has been developed that allows to correct the values calculated using the 1D model.

The 3ω method is intended for measuring the thermal conductivity of both bulk samples and thin films in the out-of-plane direction. It consists on a single heating element deposited on the sample to be measured which via an AC current at angular frequency ω is self-heated at a frequency 2ω and generates a 3ω voltage. This method allows measuring thin-films at least 20 nm thick with a thermal conductivity smaller than that of the bulk on which they are deposited. In the case of thin-film characterization, a differential measurement must be performed in order to subtract the contribution of the substrate to the thermal resistance.

Finally, we have presented a versatile method for measuring real-time thermal conductivity of in-situ deposited films, the 3ω-Völklein method. It consists on a long and narrow membrane onto which any material can be deposited, which allows to measure with a very low uncertainty the product of the thermal conductivity and the thickness of the layer, $\delta(\kappa \cdot t) = 0.065 \frac{\mathrm{W}}{\mathrm{m \cdot K}} \cdot \mathrm{nm}$. The sensor developed has been optimized using COMSOL, achieving a great accuracy in the measurement of the thermal conductivity, $\Delta k/k = 0.3\%$. Also, an equation has been derived to measure the evolution of the apparent thermal conductance during the deposition of a layer on the sensor. Finally, the thermal conductivity of a SiN_x membrane has been measured, showing a good agreement with previous measurements using the 3ω method, and thus validating the measurement method.

4. Si thin films and nanostructures

4.1 Introduction

Thermal transport in semiconductor nanostructures has been in the focus of intensive research due to practical implications in present and future technological applications[92]. Potential uses for these nanostructures include thermal management as energy scavengers[93–95], field effect transistors[96–99] or interconnects[100]. Current microelectronic devices are quickly moving into the low-nanometer regime, and the design to remove excess heat is becoming a critical parameter. As a consequence, there is an urgent need to experimentally validate the corresponding thermal behavior of the materials at the nanoscale, where unusual phonon transport phenomena, caused by boundary scattering and/or size effects, become important. Generally, when the characteristic size of a nanomaterial becomes similar or smaller than the phonon MFP, boundary scattering becomes important and the thermal conductivity shrinks drastically. This effect has been already observed in the in-plane thermal conduction of thin membranes[42,79,101–103].

The first experimental result of thermal conductivity in Si thin films was accomplished by Asheghi et al.[42] for thin films down to 400 nm. The result showed for the first time the experimental validation for the reduction in the thin film thermal conductivity due to boundary scattering, especially at low temperatures. The authors compared the experimental data with a model based in the BTE where all the boundary scattering was assumed to be diffuse, which produced a general underestimation of the modeled conductivity. Later on, Ju et al.[79] measured the thermal conductivity in the 110 direction of several films with a thickness down to 74 nm, showing a 50% reduction with respect to the bulk conductivity at room temperature. The size dependence was quite weak and thicker membranes showed only slightly higher conductivities. They also found that assuming longitudinal acoustic phonons to be the only heat carrying modes, they could reproduce reasonably well the thermal conductivity reduction. In 2004, Liu et al.[101] measured for the first time a thin film with a sub-30 nm thickness, showing a thermal conductivity of 20 $W \cdot m^{-1} \cdot K^{-1}$ for a 22 nm thin film (7.5-fold reduction from bulk Si). A similar model to the one proposed by Asheghi and coworkers in reference [42] fitted well

the thermal conductivity trend with the thickness. More recently, Chávez-Ángel et al.[103] measured the thermal conductivity of a 9 nm thin film (among others) with a result of 9 $W \cdot m^{-1} \cdot K^{-1}$. The measurement was performed with an optical contactless method based on the Raman spectrum shift with temperature, which did not need any sensor fabrication and thus prevented damaging such a thin membrane. They fitted their values with the Fuchs-Sondheimer model, which predicts quite well the thickness dependence of the thermal conductivity.

As can be seen, in recent years, the focus has been put in the thinnest membranes and nanowires. While in the mesoscale, the reduced material size generates an enhanced boundary scattering, in Si nanomaterials in the confinement regime (with characteristic sizes under 30 nm) phonons are constrained by the dimensionality of the material, since the nanomaterial size is smaller than the phonon wavelength[50]. This phenomenon affects several fundamental properties of the material itself and reduces even more the thermal conduction, which is a positive feature for thermoelectric applications. First of all, the phonon group velocity is reduced due to a flattening of the dispersion relations. Not only this, but in suspended membranes one of the transverse phononic branches (the one in the out-of-plane direction) transforms into a flexural vibrational mode due to the confinement, which changes the dispersion relation from a linear dependence to a quadratic dependence of $\omega(\boldsymbol{k})$[104]. The change in the phonon properties is produced in fact by an elastic softening of the nanomaterial. In Si nanotubes with a 5 nm thick shell, the thermal conductivity and the Young modulus followed the same trend, indicating the close relation between both and yielding an astonishing low value for the conductivity of 1.1 $W \cdot m^{-1} \cdot K^{-1}$ [51].

The thermal conductivity of nanomaterials in the confinement regime seems to be also very sensitive to small roughness and to the presence of a capping layer, which drastically increases the phonon scattering[104]. For example, Ge-Si core-shell nanowires 15-20 nm in diameter show a flatter k vs T curve compared with regular Ge nanowires of the same size[61].

Although suspended structures have been successfully used to measure the thermal and electrical conductance of various types of nanowires[30,105,106] and in general 1D nanostructures[51,61,75], the data are scarce for in-plane thermal conductivity of ultra-thin films. Few works can be found in the literature[42,77,79,101–103,107,108], where in most cases

special thermal probes using free-standing layers are used to measure monocrystalline, polycrystalline and amorphous thin films of Si. Nevertheless, in some cases researchers opted to protect the layers with a mechanical supporting layer, typically either a dielectric[108] or even with the metallic actuator itself[101], which introduces a parallel thermal path limiting the resolution in thermal conductance and potentially perturbing the heat conduction through interfacial scattering[60]. A previous development based on suspended structures has been used[109] to measure in-plane thermal conductivity and the thermoelectric properties of InAs nanofilms, reducing some of the uncertainties introduced by previous measurements on membrane structures[80]. Using a similar approach, 20 nm thick doped Si layers patterned with phononic structures where recently measured[64]. Our approach starts with SOI wafers to leave a smooth monocrystalline Si membrane that bridges the suspended heaters/sensors. The fabrication of this structure was detailed in Section 3.3.2.

In the first part of this chapter, we show thermal conductivity measurements of two Si membranes with thicknesses 17.5 nm and 67 nm. To calculate the real value of the thermal conductivity we correct the temperature profiles using COMSOL Multiphysics.

4.2 Thermal conductivity measurement

Thermal conductivity measurements are performed with the suspended structures using the methodology explained in Section 3.3.5. The measured values are subsequently corrected to take into account the inhomogeneity in the platform temperature (Figure 3.13). The different membrane thicknesses (17.5 nm and 67 nm) have been achieved by microfabricating several SOI wafers with different device layers.

The values at 300 K of the 67 nm and 17.5 nm thick single-crystalline Si layer are represented in Figure 4.1, along with other representative measurements found in the literature. The values of three different 17.5 nm membranes and four 67 nm membranes are plotted there. The in-plane dimensions of the layer (22 μm x 9.5 μm), defined initially in the lithographic process, have been accurately verified with field-emission SEM. The thickness of the layer is taken as the measured value obtained during the microfabrication process, 17.5±5 nm. Our measurements of the thermal conductivity on single-crystalline sub-20 nm Si layers are in good agreement with the extrapolation from previous data[42,77,79,102,110] and they fall around the Baowen-Li model (with the specularity parameter set to p=0.78), which is a model based on the Boltzmann Transport Equation[110].

However, it must be noted that the high variability in the thickness (especially that of the 17.5 nm membrane) produces very different values for the different membranes measured.

The model starts to deviate from the experimental values at very small thicknesses, suggesting that the specularity may be different in the thickest and thinnest membranes. This added to the fact that this model does not take into account the phononic band flattening and thus should overestimate the thermal conductivity of the thinnest membranes, indicates that the specularity is much higher than 0.78 in such membranes, probably close to 1.

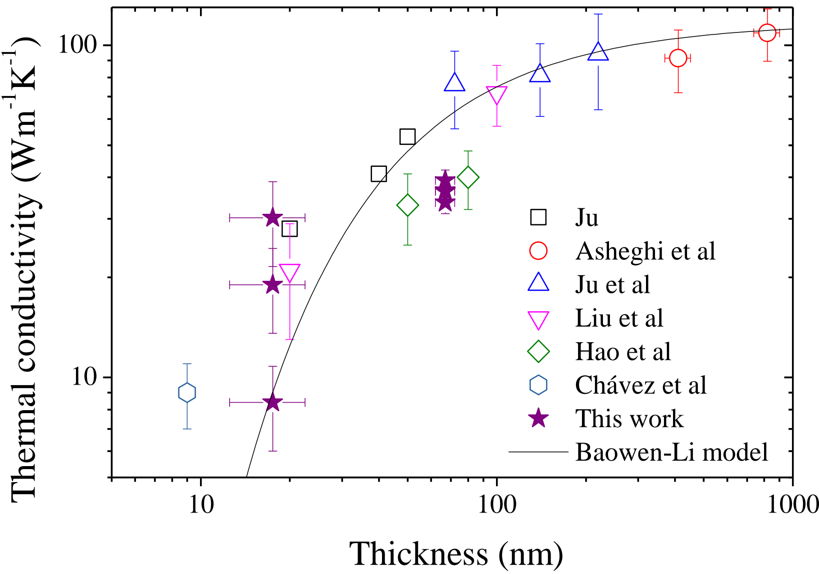

Figure 4.1: Room temperature experimental data of thermal conductivities measured on Si thin films as a function of thickness. Data from Ju[77], Asheghi et al.[111], Ju et al.[79], Liu et al.[101], Hao et al.[102] and Chávez et al.[103] included for comparison.

The thermal conductivity dependence with temperature (shown in Figure 4.2a) present a rather flat curve at high temperatures compared to bulk Si, especially in the 17.5 nm membrane, confirming the importance of boundary scattering on phonons. In bulk silicon, the main scattering mechanism at high temperatures is Umklapp scattering, responsible for the $1/T$ thermal conductivity trend. However, in our samples the boundary scattering is still important at room temperature and effectively flattens the thermal conductivity curve and shifts the thermal conductivity peak to higher temperatures.

It must also be noted that both layers show different exponents of the thermal conductivity at low temperatures: $k \propto T^{2.6}$ in the 67 nm membrane and $k \propto T^{1.7}$ in the 17.5 nm one (Figure 4.2b). Similar results can be found in the literature, with exponents ranging from

1 to 3[30,106,112,113]. At low temperatures, the dominant phonon scattering source is boundary scattering, which has been for a long time considered to be frequency and temperature independent. This consideration would suggest that at low temperatures (where all phonons have low frequencies and thus the group velocity can be considered constant too) the thermal conductivity should follow the temperature trend of the heat capacity. This magnitude, according to a modified Debye model that takes into account the dispersion relation, grows as $T^{D/\delta}$ at low temperatures (where $D = 3$ is the dimensionality of a bulk material and $\delta = 1$ is the exponent of the dispersion relation in the acoustic modes)[114], so we would expect that k also followed this trend. The observation of a reduced exponent in our thin films contradicts this prediction suggesting that there is at least one false premise in this reasoning.

This conundrum was recently solved by showing that the boundary scattering is actually frequency dependent. This is caused by the frequency dependence of the specularity parameter, which is smaller for higher frequency phonons[54,106,115]. Including this frequency dependence into a BTE based model reproduces the reduced exponent found in very thin films[116].

Apart from this, there are other effects that can potentially change the thermal conductivity exponent in nanomaterials. First, the phononic branches are influenced by the reduced dimensionality of materials in the confinement regime. In addition, the thickness reduction in a membrane transforms one of the transverse acoustic modes into a flexural out-of-plane vibration which presents a quadratic dispersion relation at low frequencies ($\omega \propto \boldsymbol{k}^2$)[104]. This has 2 separate effects: On the one hand, the flexural mode rises the overall parameter δ, which reduces the temperature exponent of the heat capacity, and thus, of the thermal conductivity too. On the other hand, the group velocity of such a quadratic branch tends to zero as the temperature gets smaller since only low-energy states are populated. For this reason, the existence of a quadratic mode implies that the mean group velocity has a positive temperature dependence that adds up to the heat capacity temperature dependence. Given that the experimental evidence show a reduced (and not increased) temperature exponent of the thermal conductivity, we conclude that this last effect is not dominant.

Finally, in very thin membranes, the dimensionality is reduced with a minimum value of $D = 2$ in a freestanding monolayer[117], directly reducing the temperature exponent of the

thermal conductivity. However, our layers are far from being 2-dimensional and this effect only starts getting important in films below 5 nm at temperatures below 10 K [50].

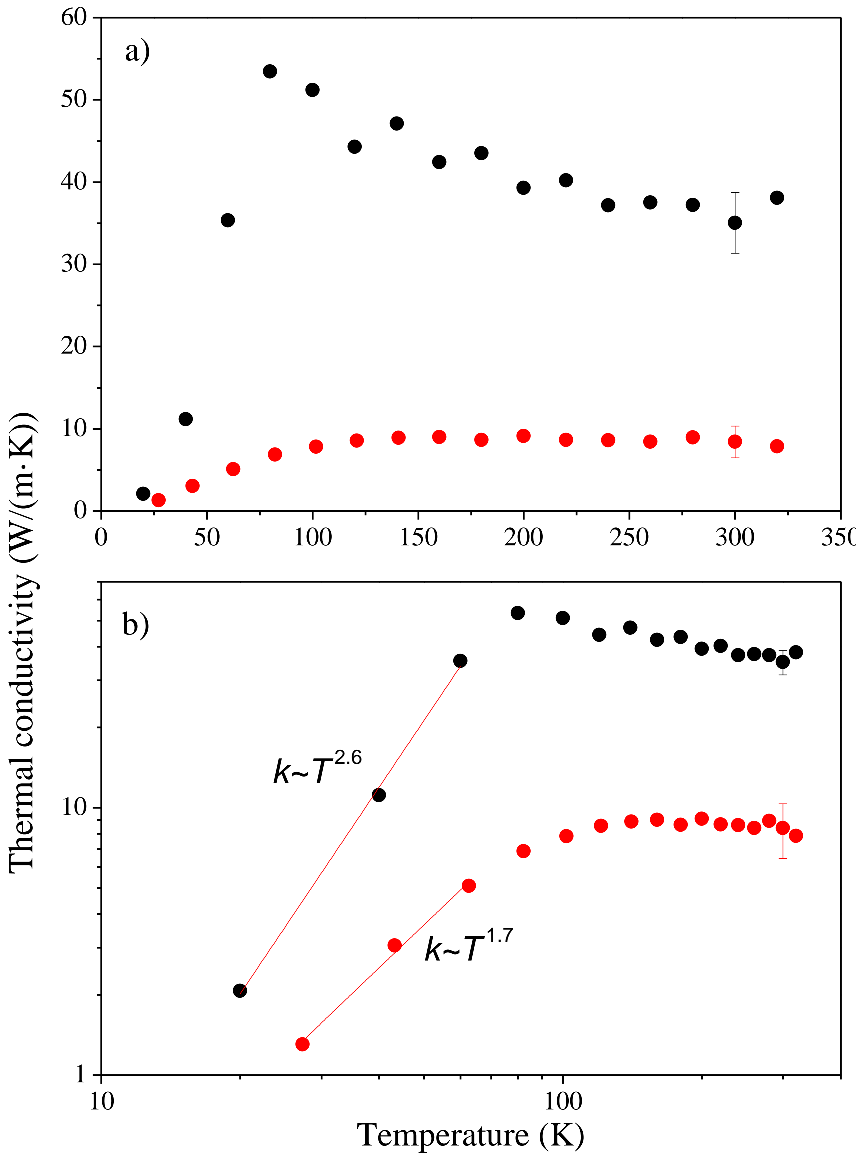

Figure 4.2: Temperature dependence of the thermal conductivity of membranes 67 nm and 17.5 nm thick. a) Linear Scale, b) log-log scale.

4.3 FIB nanopatterning

The design of the structure also opens the possibility to post-process the layer defining a variety of nanostructures (wires, arrays, strips, phononic crystals (PnCs),...) with the use of focused ion beam (FIB) etching without the use of masking strategies[118]. This nanolithographic technique consists on sending highly energetic electromagnetically focused ions against a material. When these ions arrive to the material they trigger a

variety of processes: First of all, they vaporize the surface atoms, effectively etching the material. Second, the ions also penetrate the material and scatter with many atoms, moving them from their crystalline position in a cascade effect which amorphizes the material to be etched around 50 nm in depth[119]. There are further second order effects, like re-deposition of sputtered material, that will not be discussed here[120].

The profile of the FIB is a critical parameter that must be taken into account when etching surfaces. Apart from the sharp Gaussian profile with a width of around tenths of nanometers, the FIB usually presents a couple of less intense exponential tails that spread for hundreds of nanometers[121]. Thus, while the use of FIB for producing trenches only produces a vertical amorphous layer 50 nm thick, etching a membrane produces a much wider amorphous region induced by the surface implantation of the ions in the exponential tails, which are intense enough to partially amorphize the membrane 1 μm far from the etched area (Figure 4.3). For this reason, the use of FIB on crystalline membranes must be accompanied with some procedures that prevent membrane damage. Recently, a PnC was fabricated using Cr as a protective layer to avoid the FIB-induced damage[122].

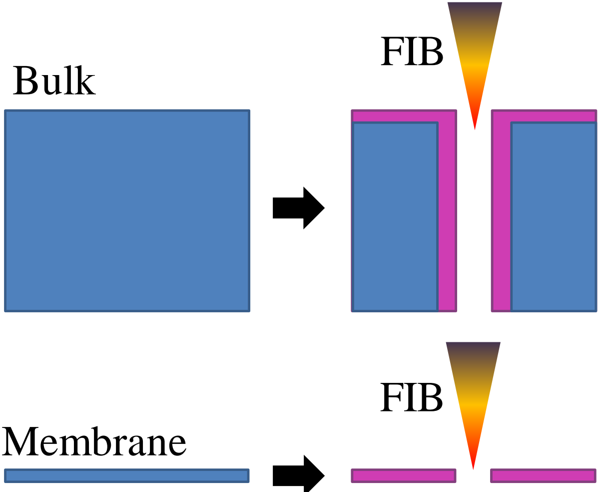

Figure 4.3: FIB etching on a bulk material compared to the suspended membrane. In the first case, only the surface and the walls get amorphous. In the second case, the whole membrane gets amorphous since ions can penetrate it completely.

The lateral amorphization of our membranes is analyzed through several etchings combined with the measurement of the thermal conductivity and Raman spectroscopy that assess the presence of optical phonons associated with crystalline Si. After some laser-induced annealings of the membranes, the Si recrystallizes into poly-Si, which is observed by electron diffraction. In order to avoid the undesired membrane amorphization, we have developed a new nanopatterning approach consisting in

implanting ions and selectively amorphizing the membrane instead of etching it. In this case, the necessary Ga dose is reduced and the non-irradiated regions of the membrane are unaffected. This approach can be especially suitable to produce nanostructures or even phononic crystals (PnCs) due to the possibility of generating periodic arrays of amorphous inclusions in a crystalline matrix.

4.3.1 Si nanostrips

In a first step, we employ FIB with nm spatial resolution (CrossBeam 1560XB Carl Zeiss) to nanostructure the 17.5 nm thick Si layer into strips (Figure 4.4) by using a current of 100 pA at 30 kV. Imaging with Ga ions was avoided to minimize ion damaging of the layer. Figure 4.4a to Figure 4.4d show a series of SEM pictures of the nanostructuration process. As has been discussed, the use of high fluxes of Ga atoms during the cutting process promotes ion incorporation with extensive lattice damage of the edges of the structure[119]. Typically, the induced lattice disorder spreads only few tens of nanometers from the etched border, but the nanostrips (500 nm wide, 17.5 nm thick and 10 μm long) turned out to be completely disordered. The amorphous structure was confirmed by micro-Raman spectroscopy performed in backscattering geometry with a high-resolution LabRam HR800 spectrometer and by TEM. Also, the thermal conductivity of the nanostrips was measured to be only 1.7 $W \cdot m^{-1} \cdot K^{-1}$, which approaches the minimum k predicted and measured for amorphous Si (1 $W \cdot m^{-1} \cdot K^{-1}$ [123]), further supporting the idea of strong lattice disorder of the suspended nanostrips after FIB processing. This amorphization is produced by the lateral spread of the Ga flux due to the exponential tails of the beam. These exponential distributions have an intensity at the center of the beam 1000 times smaller than the main Gaussian distribution, but their dependence on $e^{-r/\beta}$ (with $\beta \cong 160\ nm$) prevent them from decaying as fast as the Gaussian peak ($e^{-(r/\alpha)^2}$ with $\alpha \cong 10\ nm$) and thus become important at larger distances from the center of the beam[121]. This high lateral spread of the beam produces Ga implantation as far from the center as 1 μm with a penetration of around 50 nm, which when applied to this ultra-thin membrane induces amorphization throughout its thickness.

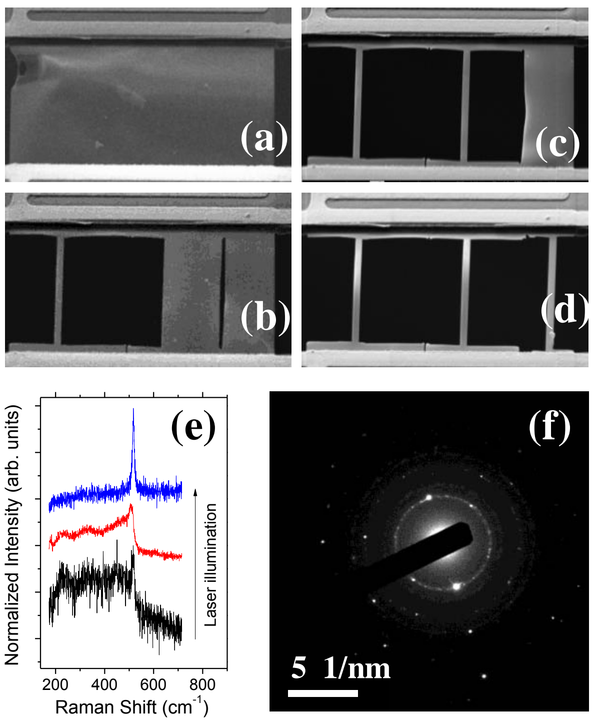

Figure 4.4 a)-d) Sequence of field-emission SEM images during the nanostructuration of the Si layer into 3 strips of 0.5x10 mm. e) Raman spectra during laser annealing of one strip showing recrystallization of the Si. f) TEM diffraction pattern obtained in the re-crystallized strip, showing polycrystalline order.

After nanofabricating the strips, we used the 514.5 nm line of the Ar-laser of the Raman setup to promote recrystallization. The power of the laser, with a spot size of about 1 μm, was increased and scanned along the sample with a xy stage to anneal the Si layer above the threshold for recrystallization. The effect of intense laser illumination is evident from the evolution of the Raman feature associated with the LO-Si phonon mode, as shown in Figure 4.4e. Electron diffraction pattern of the strips, shown in Figure 4.4f, confirms the nano-crystalline nature of the samples at this point. Also, the thermal conductivity of the Si nanostrips increases to a value of 9.5 $W \cdot m^{-1} \cdot K^{-1}$. The reduction with respect to the single-crystalline Si layer originates from the presence of grain boundaries that enhance phonon scattering.

4.3.2 Dose optimization

In a second step, we have optimized the dose to produce nanostructures with amorphous regions by implanting Ga ions and amorphizing the c-Si (This work has been performed in the group of M. Martín-González at the Microelectronics Institute of Madrid, IMM-CNM-CSIC). In order to determine the most suitable dose to create disordered regions in the membrane, we performed several implantations on 67 nm thick membranes using a

wide range of doses: from 5 μC/cm^2 to 10000 μC/cm^2. We did so by implanting 2x2 μm^2 squares in a single membrane (Figure 4.5).

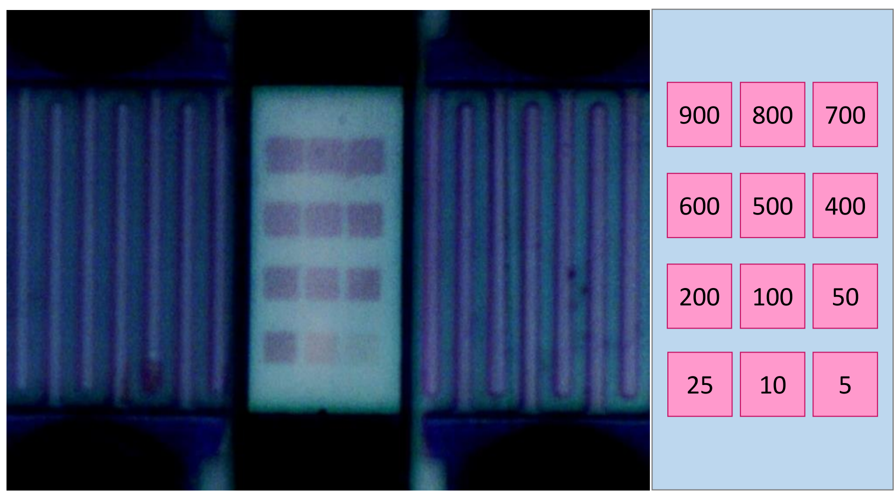

Figure 4.5: micrograph of the suspended structure with the implanted squares and a sketch with the doses used (in μC/cm^2).

The crystallinity was extracted from the measurement of the Raman spectra of each implanted square (Figure 4.6a). The data were acquired by averaging 10 spectra 10 s long each, and damping the incident laser with a D2 filter in order to reduce the membrane temperature. The spectra measured were then fitted with two Lorentzian distributions each, representing the amorphous peak (broad and centered at around 480 cm^{-1}) and the crystalline one (sharp and centered at around 520 cm^{-1}). Then, the crystallinity was calculated with the intensity of both peaks by applying the Lever rule[124], for which the intensities of the purely crystalline and purely amorphous peaks were also used.

Figure 4.6b shows that the crystallinity of the layer rapidly decreases at low dose implantations: for doses higher or equal than 50 μC/cm^2, the crystalline fraction gets below the background noise of the measurement. For this reason, 50 μC/cm^2 is the dose selected for all the further nanolithography, which corresponds to a mean Ga doping of 9.4%. However, the atomic distribution throughout the thickness of the membrane is not flat, but has a maximum at 28 nm, as is shown by the SRIM (Stopping and Range of Ions in Matter) simulation in Figure 4.7a.

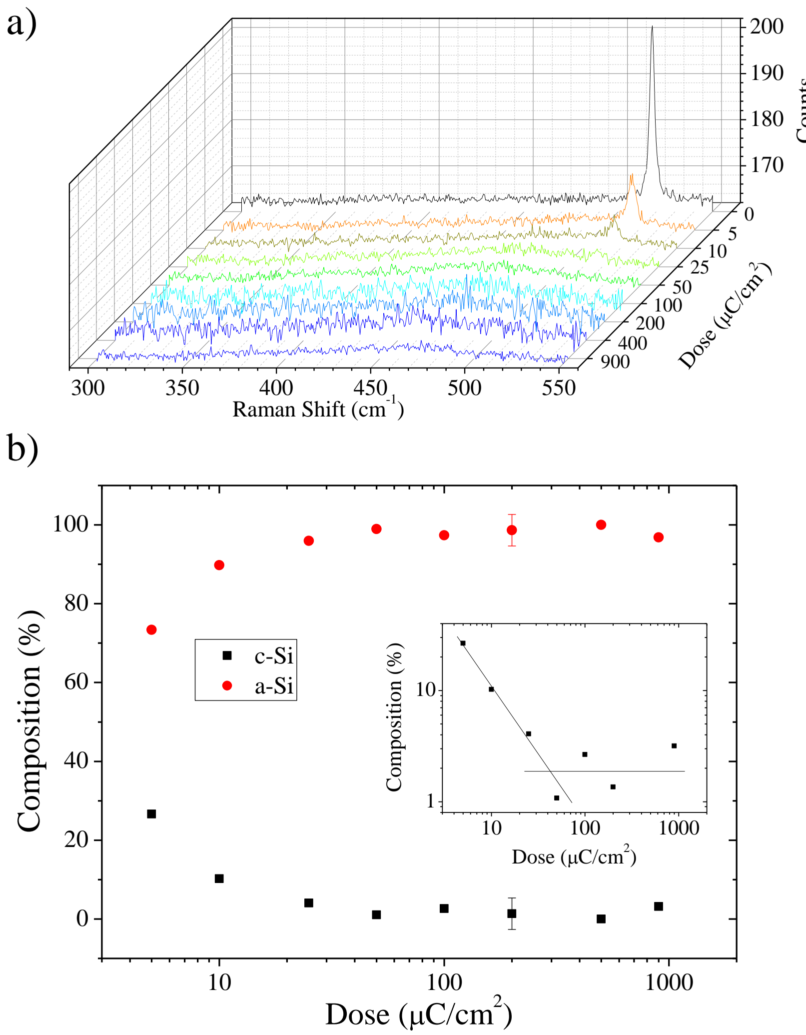

Figure 4.6: a) Raman spectra of the different squares with varying implanted doses. b) Crystalline and amorphous percentage corresponding to each implanted dose. The error bars are only shown in the data at 200 μC/cm^2, but they are equivalent in all the other data points.

Also, the simulation shows that only few atoms can completely penetrate the whole membrane, and that the damage in the backside of the membrane is very low, suggesting that there should be a semi-crystalline Si layer there (Figure 4.7b). Nevertheless, the Raman measurements show complete suppression of optical phonons in the irradiated area. This could be explained by the strong influence of the vacancy defects formed by the cascade of few Ga^+ ions on both the optical and acoustic phonons. In this way, a small defect density would make the membrane to look completely amorphous through its Raman spectrum and thermal conduction due to the strong strain fields created. This effect was found in Si nanowires with diameters around 170 nm, which after Ga irradiation with 60 μC/cm^2 showed a thermal conductivity reduction between 70% and 92%[125].

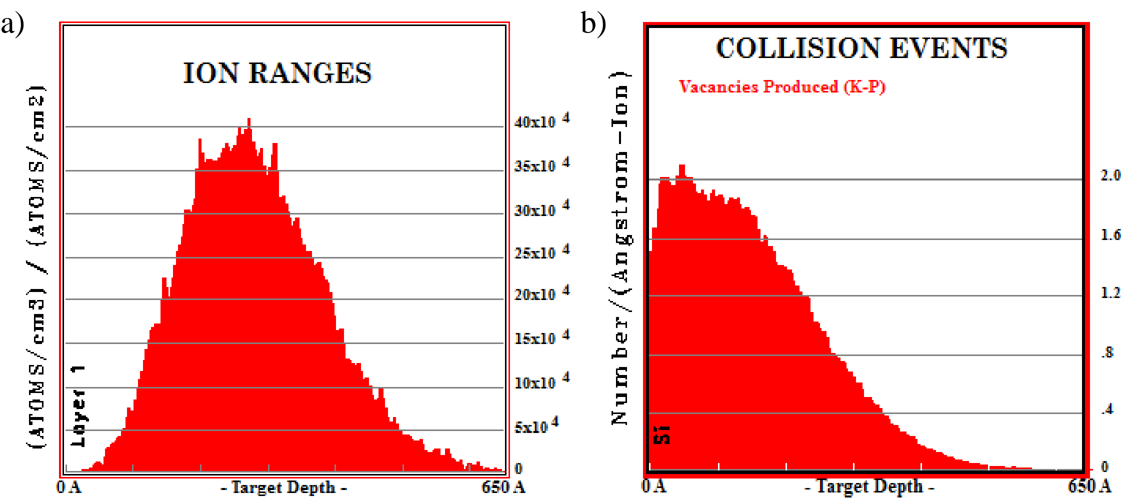

Figure 4.7: Results of a SRIM simulation where a total number of 10000 Ga ions were implanted in a Si target with an energy of 30 keV. a) Depth profile of ion implantation. b) Damage produced to the Si layer by the ions.

In order to quantitatively analyze the spatial resolution of the patterned squares, several Raman spectra have been measured throughout a line that crosses the 900 μC/cm^2 and the 50 μC/cm^2 squares. The observed crystallinity steps (Figure 4.9) have broad borders that are produced by the convolution of the laser spot and the crystallinity profile itself. For this reason, in order to quantify the broadening of the crystalline step, we perform a convolution of two functions representing the laser intensity (Gaussian) and the crystalline step (error function), and fit the resulting function to the measured crystallinity. In this way, the amorphization resolution can be approximated to be the standard deviation of the modeled step.

The spatial resolution of the Raman spectrometer is defined by the radius of the laser spot (σ_1), which is can be calculated as

$$\sigma_1 \cong \frac{0.42\lambda}{2NA} \tag{4.1}$$

being λ the wavelength of the laser and NA the Numerical aperture of the microscope lens. In this formula, the profile is assumed to be Gaussian:

$$I = \frac{1}{\sqrt{2\pi}\sigma_1} e^{\frac{x^2}{2\sigma_1^2}} \tag{4.2}$$

which is a good approximation to the real Airy pattern. The radius results in $\sigma_1 = 124\ nm$ for $\lambda = 532nm$ (this time, a Nd:YAG laser is used) and $NA = 0.9$.

The crystalline step is modeled with the function:

$$y = \frac{1}{2}\left[\operatorname{erf}\left(\frac{x - x_0}{\sqrt{2\pi}\sigma_2}\right) - \operatorname{erf}\left(\frac{x + x_0}{\sqrt{2\pi}\sigma_2}\right) + 2\right] \tag{4.3}$$

With

$$\operatorname{erf}\left(\frac{x \pm x_0}{\sqrt{2\pi}\sigma_2}\right) = \frac{2}{\sqrt{\pi}}\int_0^{\frac{x \pm x_0}{\sqrt{2\pi}\sigma_2}} e^{-t^2}dt \tag{4.4}$$

A sample of both functions together with their convolution are shown in Figure 4.8, where the increased broadening produced by the convolution of the laser spot and the crystallinity profile can be observed.

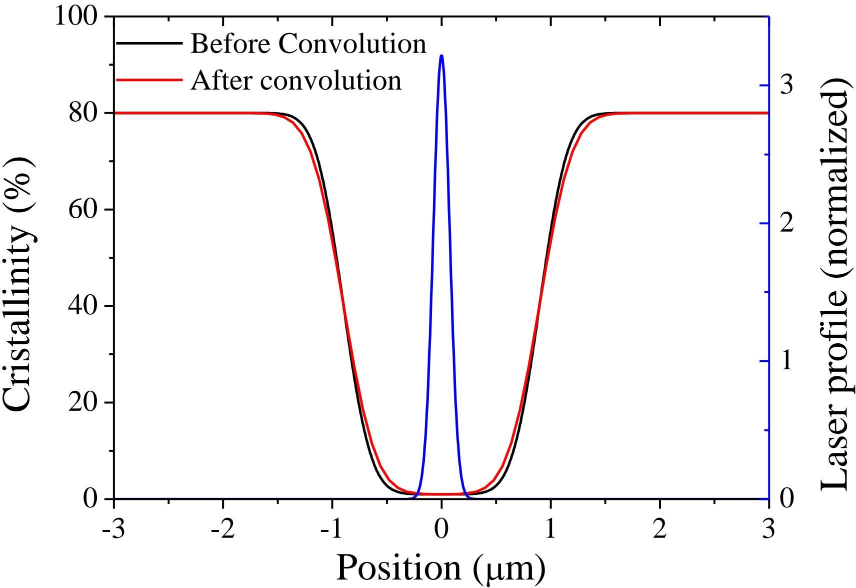

Figure 4.8: Example of a curve before and after the convolution with the laser profile.

The fitted convolutions in the 50 μC/cm^2 and 900 μC/cm^2 crystalline profiles (Figure 4.9) show that the border thickness of the amorphous region is larger in the 900 μC/cm^2 square (σ_2 = 350 nm) than in the 50 μC/cm^2 one (σ_2 = 200 nm). The crystallinity outside the squares does not recover to 100%, but instead it only arrives to 55% around the 900 μC/cm^2 square and to 80% around the 50 μC/cm^2 one. The latter is a good value but still not perfect, and reveals the extension of the Ga contamination induced by FIB.

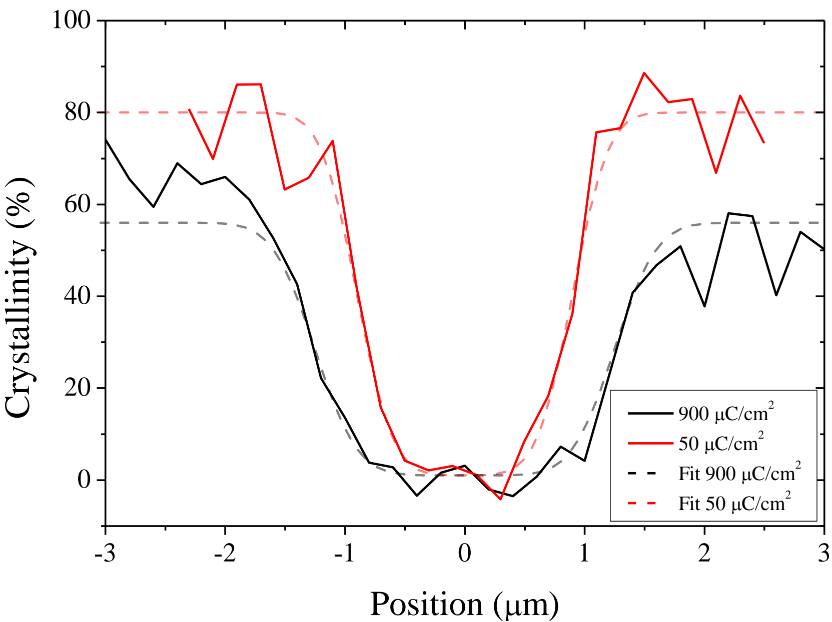

Figure 4.9: Measured crystallinity and fitted profiles.

One alternative to just doping the membranes is to etch the implanted regions. This might be done by dipping the membrane into a solution that contains HF, since there is evidence that HF etches faster a-Si than poly-Si (or c-Si)[126]. We unsuccessfully tried this etching process several times, since in all cases the membrane did not get etched at all. The reason for this procedure to fail may be related with the high amount of Ga in the amorphous regions, which might reduce the etching rate of HF.

4.3.3 Asymmetric micro/nanostructures

With the optimal dose found here, we fabricated several asymmetric structures in the membranes in order to find if there was an asymmetry in the heat flux when heating alternatively both ends of the structure. From these, two representative structures are shown in Figure 4.10.

The first structure is a curved c-Si strip, shown in Figure 4.10a (there, the a-Si is not illustrated as it is expected to contribute poorly to the thermal conduction). The purpose of fabricating this structure was to produce c-Si conductive paths with different widths in both sides of the membrane. If a high temperature gradient is applied to the membrane, the intrinsic MFP of c-Si is sensibly higher in the cold side than in the hot one due to the reduced umklapp scattering. When applying the cold temperature to the narrow c-Si side, the boundary scattering contribution would be high there, but low in the wide side, creating a heat flow bottleneck in the former. However, reversing the temperature

gradient would equalize the boundary scattering contribution in both sides and the conduction would be slightly higher[127].

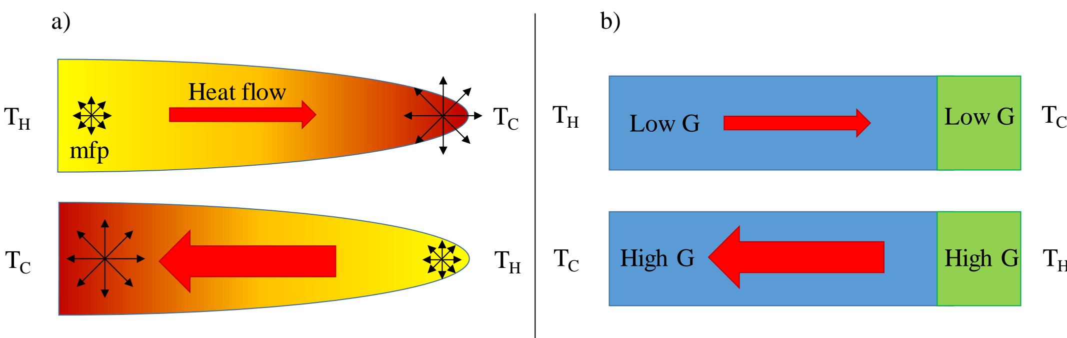

Figure 4.10: Sketch of both asymmetric structures prepared and the mechanism for which they should present heat flow asymmetries. a) curved c-Si strip. b) c-Si/a-Si stack.

The structure in Figure 4.10b has a central channel with c-Si/a-Si stack. The c-Si segment has a decreasing thermal conductivity with temperature, while the amorphous one has an increasing thermal conductivity (Figure 4.11a). In this case, heating the crystalline part while keeping the amorphous part cold would yield a low thermal conductance for both materials. However, reversing the temperature gradient would create the opposite situation, this is, a high thermal conductance for both materials. This method for producing thermal rectification was first analyzed by Dames[128] in bulk materials. In our case, both the crystalline and the amorphous regions have been designed with different lengths (10x different) due to their very different values of thermal conductivity. In this way they should produce a similar thermal resistance.

Since this rectification method can be described by the Fourier law of heat conduction, it can be easily simulated with FEM. We have produced a 1D model with two segments having the thermal conductivities extracted from Figure 4.11a, being the insulating segment 10 times shorter than the most conductive one. With the mean temperature fixed at 150 K, we have applied several temperature gradients and probed the heat flux to find the rectification shown in Figure 4.11b.

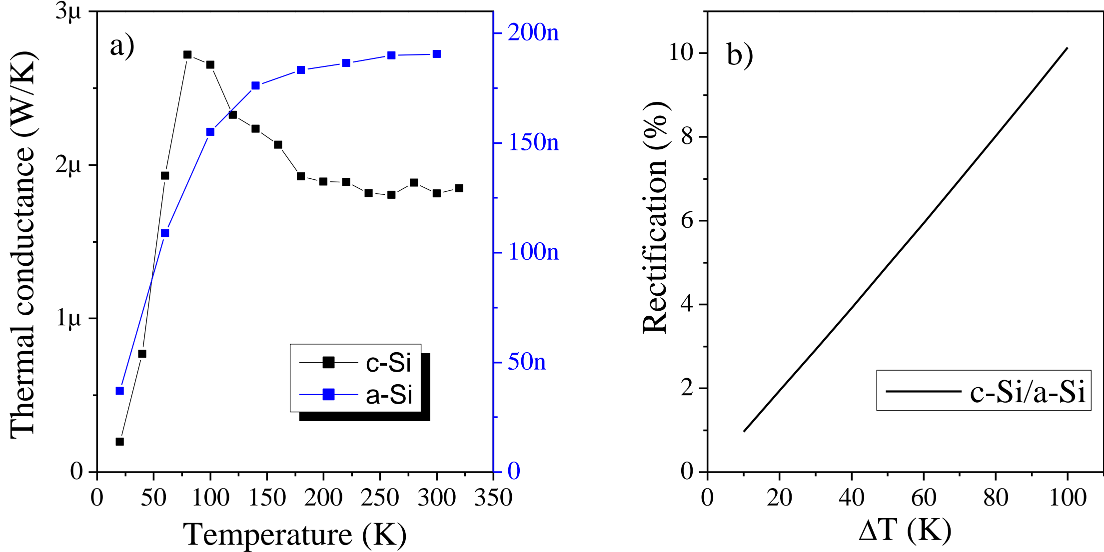

Figure 4.11 a) Thermal conductance of c-Si membrane 67 nm thick and the same membrane after FIB-induced amorphization. At 100 K the c-Si has a decreasing thermal conductance, while a-Si is still increasing, generating a different trend that could be exploited for thermal rectification. b) Simulated thermal rectification on a two-segment 1D model with thermal conductivities extracted from a).

After producing these structures, their crystallinity was assessed by Raman spectroscopy, confirming the perfect crystallinity of the non-implanted regions and the amorphous character of the implanted ones. The crystallinity can also be appreciated optically, as brighter areas of the membranes in Figure 4.12 correspond to c-Si, while the darker ones correspond to a-Si.

Since only nonlinear effects can produce asymmetry in the heat flow, it can only be observed by applying a high temperature difference along the material. With the membranes already shown this is not possible since the amorphous region is quite wide and does not allow to produce a high temperature difference with the maximum power we can produce. For this reason, we replicated these structures in Si strips 10 μm long x 0.7 μm wide x 67 nm thick and measured them.

In order to find a heat flow asymmetry, we performed the heating cycle specified in Section 3.3.5.2 first with one heater and then with the opposite one. In the case of an asymmetric heat flow, we should find different curves of $\Delta T_S(\Delta T_H)$ in both measurements, especially at high temperature differences[129]. We also changed one step in the data reduction: instead of calculating the resistance of the heater with the derivative of the curve $V(I)$, we subtracted the offset of this curve and then found the resistance as V/I. In this case, the factor 3 must be taken out from equation (3.23). Finally, the

temperature at which the asymmetry was measured was different for both samples. The curved strip was measured at the minimum temperature possible for our system, 20 K, since we expect that the MFP of c-Si phonons change abruptly with temperature at low temperatures. In the case of the c-Si/a-Si stack, we measured it at 100 K since we found that the thermal conductivity of c-Si and a-Si have the most different trend at that temperature (Figure 4.11a), which should maximize the rectification effect.

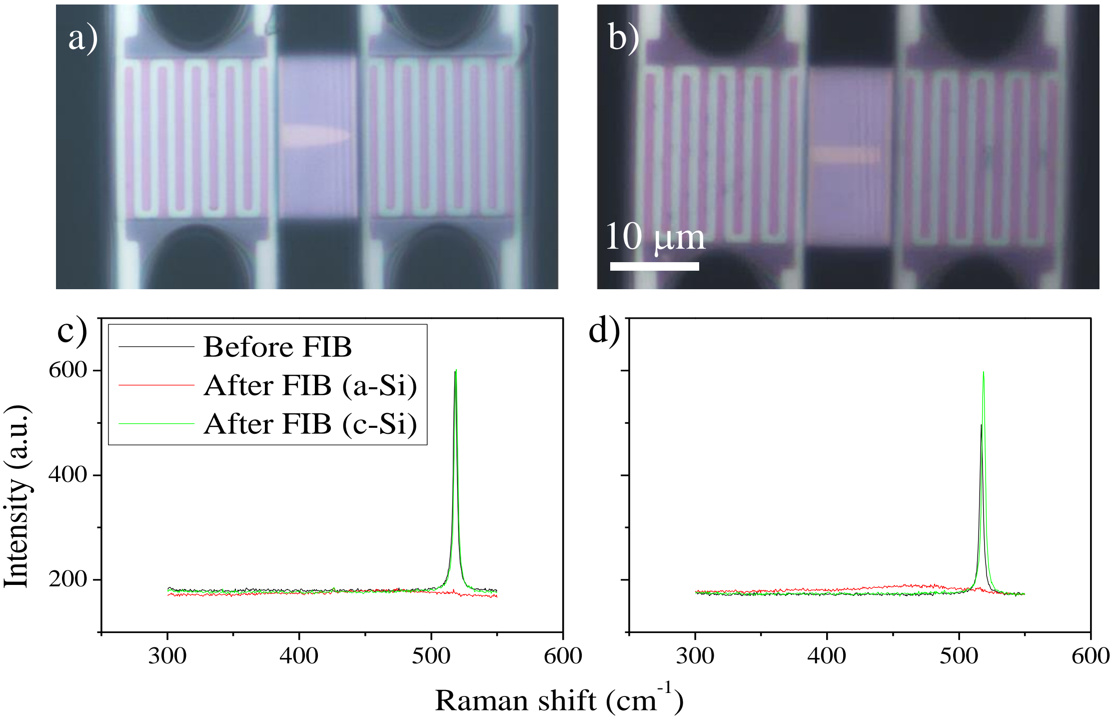

Figure 4.12 structures produced by Ga implantation with FIB. a) asymmetric channel. b) c-Si long rectangle followed by a-Si short rectangle. c) Raman spectra of membrane in a). d) Raman spectra of membrane in b).

The results of the measurement are shown in Figure 4.13. Surprisingly, none of the measured structures display asymmetry in the heat flow, but they show the same response irrespective of the side the heat is applied on. A simple analysis indicates that for the highest ΔT_H, the difference in ΔT_S is only 2% and 1% for the curved strip and the c-Si/a-Si stack, respectively, which is similar to the uncertainty of the measurement (around 1%). In the case of the curved strip, which shows the highest value, there are other possible sources of error: since we are heating from 20 K to around 75 K the hot SiN_x platform, the thermal conductance of the SiN_x beams supporting that platform increase a lot, producing the bending in the $\Delta T_S(\Delta T_H)$ curve. A slight difference in the thermal behavior of the SiN_x beams of each platform may produce an artifact that is observed as a difference in thermal conductance. In the case of the c-Si/a-Si stack, the rectification found (1%) is smaller than the one predicted with FEM (around 2.2% for $\Delta T = 23$ K),

suggesting that the real system is somehow different to the modelled one (different segment sizes or thermal conductivities, for example). To summarize, we do not observe any noticeable rectification.

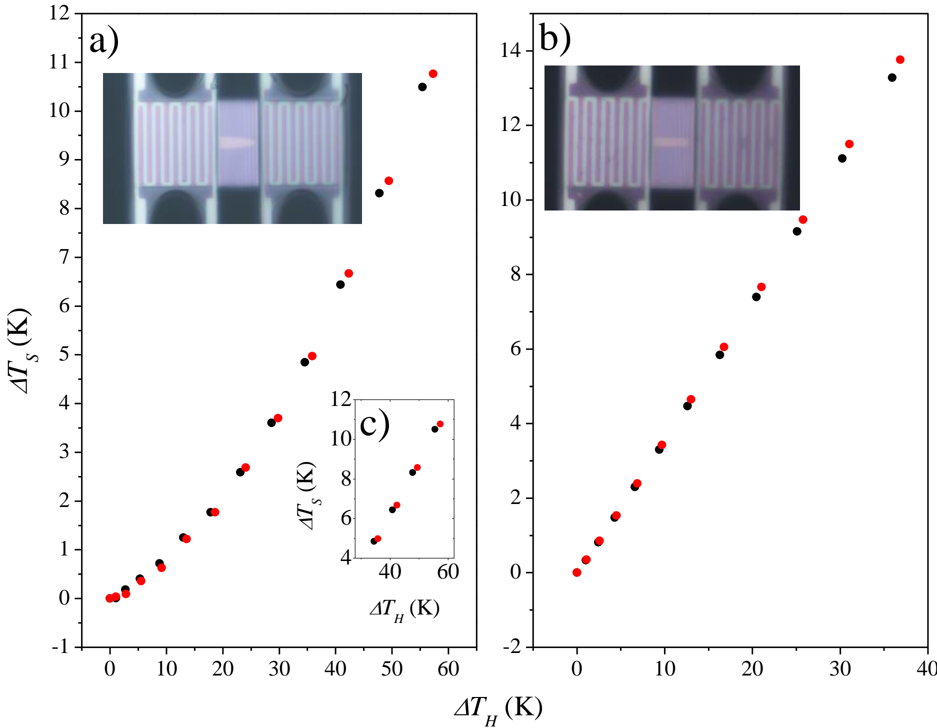

Figure 4.13 Measurements in the forward and reverse directions of the heat flow in the asymmetric nanostructures. a) Curved c-Si strip. b) c-Si/a-Si stack. c) inset of highest $\Delta T_S(\Delta T_H)$ of the curved strip.

The lack of heat flow asymmetry in the case of the curved strip suggests that the phonon MFP is already very low due to the reduced thickness of the layer, which scatters all the phonons efficiently at all temperatures. A future strategy for finding thermal rectification in that system may be increasing the thickness to values larger than the width of the strip in the narrow end, so that the lateral phonon scattering is sensibly enhanced. In the case of the c-Si/a-Si stack, a higher thickness would also help, since the bulkier the Si, the steeper the decrease of its thermal conductivity with temperature.

4.4 Summary

In this chapter we present the thermal conductivity measurement of Si membranes and the nanofabrication optimization of these membranes using ion beam lithography. First, the thermal conductivity measurement of ultra-thin membranes is reported, showing very low values compared to bulk Si. This harsh reduction is attributed to both an intense phonon boundary scattering and, in the case of the 17.5 nm membrane, phonon

confinement. The temperature dependence of samples 17.5 nm and 67 nm thick shows a flat curve at high temperature indicating a strong phonon suppression by boundary scattering, which is compatible with literature data and theoretical models, while the reduction in the temperature exponent of the thermal conductivity at low temperatures suggests the frequency-dependence of the specularity factor.

Then, the effects of the FIB nanofabrication on Si membranes is analyzed. We have first checked the amorphization produced by the ion irradiation in crystalline membranes by measuring electron diffraction patterns and the thermal conductivity, and then, after laser illumination, we have recrystallized the Si into a polycrystalline phase.

In order to produce micro and nanostructures in thin membranes, the lateral amorphization induced by FIB must be reduced. For this reason, we have substituted the etching of the membrane with the selective amorphization, which needs a much lower dose and permits to leave unaffected the non-irradiated regions. Very low doses are needed for improving the spatial resolution of the method, getting an optimal value for the spot size of 200 nm at a dose of 50 $\mu C/cm^2$. With this dose, two asymmetric structures have been produced, which did not show any heat flux asymmetry.

5. Thermal conductivity of porous Si nanowires

5.1 Introduction

The reduction in the dimensionality of solid materials to the mesoscale has been demonstrated to sharply reduce the thermal conductivity through the addition of a boundary scattering extra term, which reduces the phonon relaxation time. These size effects have been already characterized in a many semiconductors (Si[30,51,74,80], SiGe[105,130,131], Bi[66], BiTe[43], InAs[109]…) which have been nanoscaled as nanowires, thin films, nanotubes and further exotic shapes like inverse-opals[132].

Generally, the thermal conductivity shows a direct relation with the characteristic size of the nanomaterial, but it also depends greatly on the surface roughness. Recent studies showed that Si NWs 50 nm in diameter defined by wet-etching techniques (Electroless Etching) present rough surfaces and lattice thermal conductivities 100 times lower than bulk Si, approaching the amorphous limit[133,134], while smooth wires with the same diameter only show a 6 fold reduction[30]. There are some models in the literature that account for the surface roughness and they all take into account the boundary specularity[55–57], which generally shrinks with high surface roughness as the phonon-boundary scattering produces diffuse outgoing waves. Recently, phonon backscattering has been computed using Monte Carlo simulations[135] on nanowires with sawtooth roughness, demonstrating the thermal conductivity reduction with respect to smooth nanowires[134]. Next, Lim et al.[53] measured the spectral distribution of the surface roughness of several VLS etched nanowires and correlated it with thermal conductivity measurements, finding a close relationship between them. Also, the role of surface shadowing has been taken into account when calculating the thermal conductivity of rough nanowires[58].

However, in general these works have not provided a successful explanation for the ultralow values measured in the 50 nm rough Si wires by Hochbaum et al. For this reason, other phonon scattering sources have been proposed. The wires produced by Electroless Etching (EE) are highly doped[134], which may produce an enhanced impurity scattering.

Also, this fabrication method can produce small vacancies inside the nanowire (thus producing a porous nanowire) that can reduce even more the phonon transport. This last statement was verified by slightly bombarding a nanowire of diameter 170 nm with focused Ga^+ ions. While most of the ions stopped in the first 25 nm, the seldom ions that went through this depth created a cascade of vacancy defects in the lattice, which vastly reduced its thermal conductivity due to the induced lattice strain[125].

This suggests that producing nanoporous materials constitutes a step further into reducing thermal conductivity via phonon-surface scattering. Such materials present inner irregular holes with sizes and separation of few nanometers that vastly increase the surface-to-volume ratio and enhance the phonon scattering. Specifically, hydrodynamic-like approaches have shown the very low thermal conductivity of these porous structures and found an important relationship between k and the pore diameter[136,137]. The experimentally found thermal conductivities as low as 0.04 $W{\cdot}m^{-1}{\cdot}K^{-1}$ at room temperature[138], render porous materials very attractive for thermoelectric applications. This value is the one of the effective medium considering the material to be homogeneous. The relationship between both the effective and the intrinsic thermal conductivity can be found by applying a geometric correction like the Maxwell-Eucken relation[139,140], which yields an ultralow value of 0.58 $W{\cdot}m^{-1}{\cdot}K^{-1}$ for the structural Si, only comparable with the Si nanotubes measured by Wingert et al.[51].

There are several ways of fabricating porous Si. Generally, porous Si is produced by electrochemical etching with an aqueous solution of HF[138], although an ethanoic solution removes H_2 bubbles more efficiently. The resulting chemical reaction of this method is the fluorination of Si atoms, which summed up with the instability of the surface charges induces a pore nucleation into Si and the penetration of the solution into the pores. In order to produce nanoporous nanowires, another strategy is used: Metal-assisted Chemical Etching (MaCE)[141,142]. In this method, the substrate is covered with a patterned metallic thin film that acts as a catalyst for the etching to occur. The metal, typically gold or silver, catalyzes the oxidation reaction of the Si underneath by H_2O_2, while HF etches SiO_2 away. In this way, the metallic layer digs into the Si, leaving the material under the metallic film holes at first unaffected. Then, as the etching goes on and depending on the wafer doping and the etchant concentration, porosity is produced inside the wires.

A recent study of porous Si nanowires showed an enhanced thermoelectric figure of merit, achieved through a reduced thermal conductivity and increased Seebeck coefficient[142]. In this case, the larger the pore size, the higher the thermoelectric figure of merit, mainly due to the increase in the surface-to-volume ratio of the wire.

In the rest of this chapter we present the fabrication of the porous Si nanowires via MaCE and the measurement of their thermal conductivity. This method allowed us to produce pores smaller than 10 nm with average porosities around 50%, leaving ultrathin Si walls between pores. In this way, the disordered nanostructure is expected to reduce the thermal conductivity values of Si down to extremely low values.

5.2 Experimental Methods

5.2.1 Nanowire fabrication

The porous Si nanowires were produced at the Istituto Nazionale di Ricerca Metrologica (INRIM), in Torino, by means of MaCE (Metal-assisted Chemical etching). The main fabrication steps are explained below and depicted in Figure 5.1.

i) The process starts with the colloidal lithography, consisting on dispersing on the wafer small polystyrene nanospheres synthesized by emulsion polymerization.

ii) After the first step, the nanospheres are in contact with each other, so they must be reduced in order to produce separated holes in the gold thin-film deposition. This is achieved with an O_2 RIE that selectively etches the organic spheres, effectively reducing their radius.

iii) A 20 nm thick Au layer is deposited by means of e-beam evaporation.

iv) The nanospheres are removed by sonicating the wafer in DI water. The result is a holey Au mask that will be used as a template for the wires to be formed.

v) The nanowires are defined by immersing the wafer into wet etching solutions composed of HF, H_2O_2 and H_2O with proportions of 30:1:30 and 3:1:1. The etchants concentration and the initial doping level of the wafer define the final porosity of the nanowire.

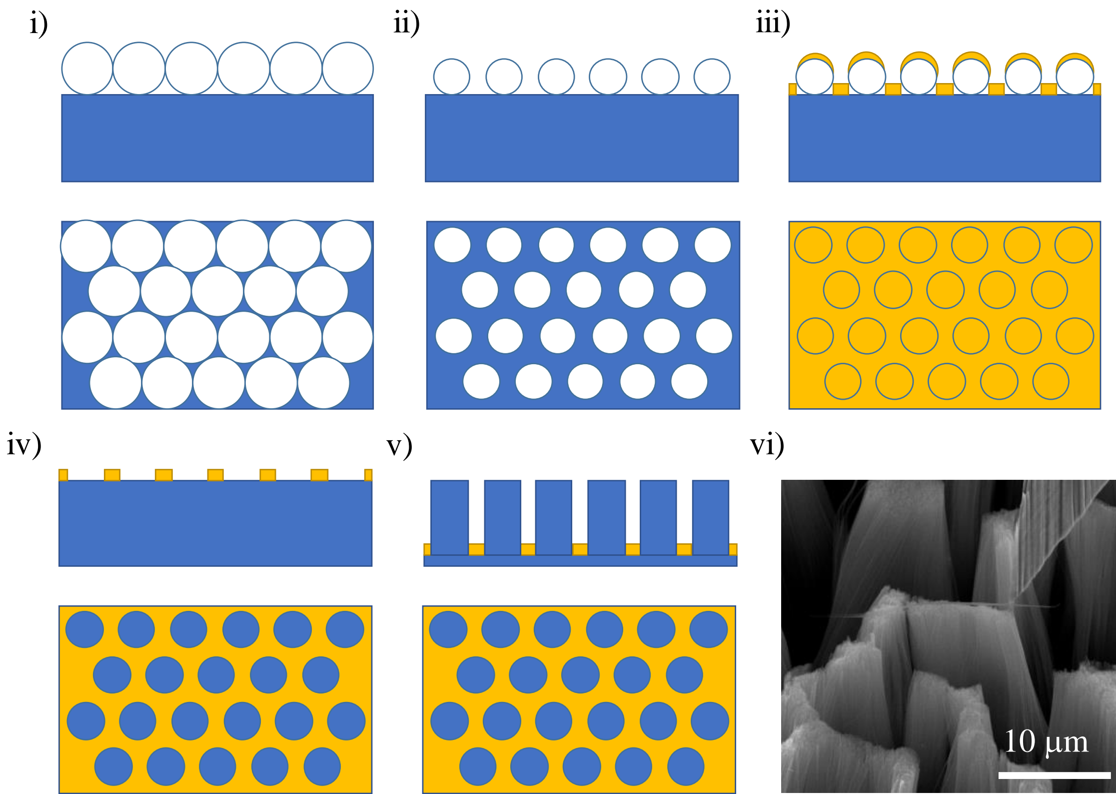

Figure 5.1 i) to v) Side and top views of each fabrication step. vi) SEM image of 1AB6 nanowires (see Table 5.1 for the batch reference) showing very long bundled wires as well as the nanomanipulator tip with a wire attached.

Using this approach very long nanowires (~30 microns) have been produced, as can be seen in Figure 5.1 vi). As briefly stated above, the doping concentration of the wafer also affects the porosity as more heavily doped wafers yield wires with higher porosity. In this work, B-doped p^+-Si wafers with a resistivity of 0.008-0.012 Ohm·cm have been used. This information is summarized in Table 5.1.

Batch	Wafer resistivity (Ohm·cm)	relative etchant concentration ($HF:H_2O_2:H_2O$)	etching time (min)
1AB2	0.008-0.012	3:1:1	1
1AB6	0.008-0.012	30:1:30	75

Table 5.1: Batches produced with the wafer resistivity, etchant concentration and etching time.

5.2.2 Manipulation

The wafers with the nanowires on top are introduced into a SEM/FIB equipment together with the suspended structures where the wires are to be attached. Using a nanomanipulator with a sharp needle (radius~200 nm), one wire is bonded through ion-induced deposited Pt. Once this is achieved, the wire is cut several microns below using the FIB. The detached wire is then placed on the sensing platform, where is bonded using Pt again, and is detached from the needle by cutting it again with Ga^+ FIB.

As has been stated in Section 4.3, Ga^+ ions can introduce disorder in the region near the cutting area. The use of an ion beam to deposit Pt will probably amorphize the region under the contact and produce some defects near them. However, since the porous wires exhibit a very low thermal conductance, we expect a small influence of the enhanced thermal resistance on the derived thermal conductivity data. This issue will be further discussed in the results section.

The surface of the wires after placing them on the suspended structure is expected to be oxidized. After the wet etching with HF the Si surface is H-terminated, which passivates the surface against oxidation for a few seconds-to-minutes[143]. However, the combined influence of oxygen from the atmosphere and the electron irradiation inside the SEM produce the elimination of the H layer and the unavoidable growth of a thin layer of native oxide. The surface passivation of a nanostructure with high surface-to-volume ratio is a very important feature that can alter significantly the value of the thermal conductivity. In particular, a recent molecular dynamics study has shown that the SiO_2 passivation of rough ultrathin Si membranes can reduce the thermal conductivity by up to 80% [104]. For this reason, the very same wires with or without the oxide layer may produce very different results. Testing the influence of surface modifications on the porous nanowires is an interesting avenue of research for future investigations.

5.2.3 Structural characterization

Several Si nanowires obtained from the very same batches used for this work have been characterized by means of Scanning and Transmission Electron Microscopy, including 3D tomography to obtain a high resolution map of the embedded porosity of the wires.

First, SEM images (Figure 5.2) were taken just after placing the wires on the suspended structures in order to measure the length and diameter of each wire, which allows the proper calculation of the thermal conductivity. The micrographs were obtained with the secondary electrons in a Field-Emission SEM at 20/30 KV and 100 pA.

The length was measured between the deposited Pt spots, but since these are sometimes poorly defined due to Pt diffusion, the value may have an added uncertainty. The diameter was measured on 2 or 3 different spots of the nanowire in order to have into account the possible variability along its length. The wire diameter ranges between 96-151 nm, while the length between 0.96-8 μm. The exact values for each wire are shown in Table 5.2.

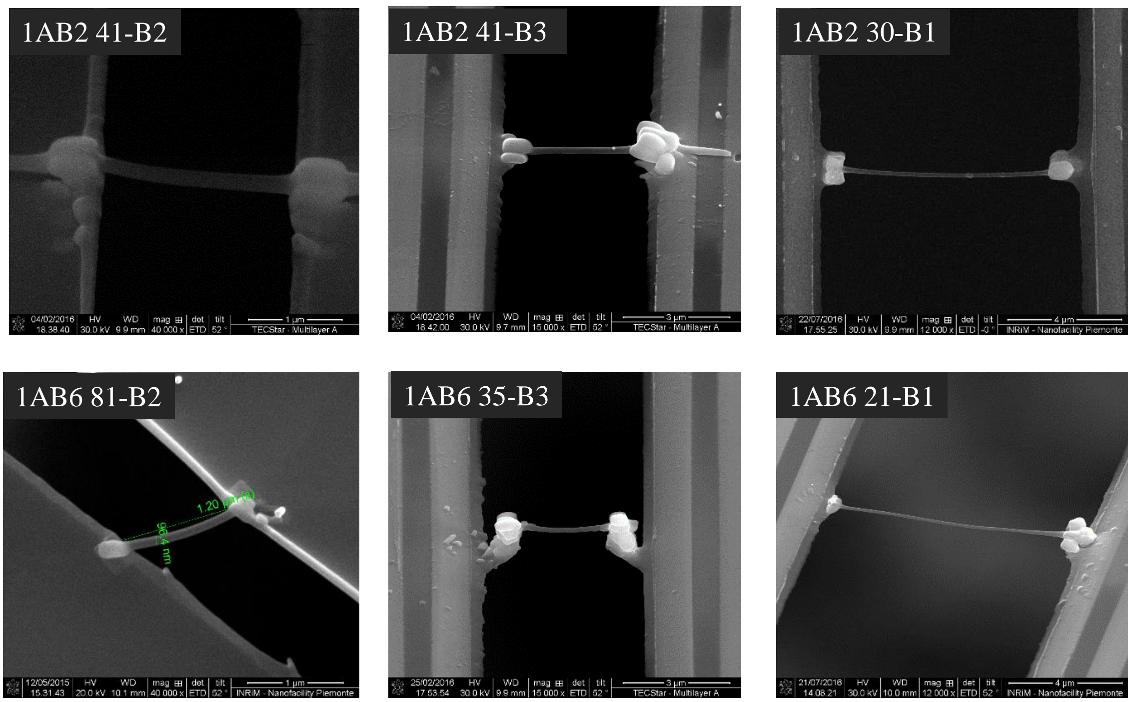

Figure 5.2: SEM images of all the nanowires measured, used for the length and diameter measurements. The wire batch and sensor code are provided. Note that samples 41 and 81 are suspended onto the monocrystalline Si membrane, while the other nanowires are directly attached to the nitride membrane.

Sensor	Recipe ($HF:H_2O_2:H_2O$)	Length (μm)	Diameter (nm)
41-B2	3:1:1 (1AB2)	2.0±0.2	142±5
41-B3	3:1:1 (1AB2)	3.0±0.3	151±5
30-B1	3:1:1 (1AB2)	7.3±0.7	137±5
81-B2	30:1:30 (1AB6)	1.2±0.2	96±5
35-B3	30:1:30 (1AB6)	3.2±0.5	126±5
21-B1	30:1:20 (1AB6)	8.0±0.8	106±5

Table 5.2: Length and diameter of the Si nanowires measured in this work.

TEM images with magnification up to x950000 were taken from nanowires of each batch to measure the pore size and internal structure (Figure 5.3a). They show very small pores, with sizes of about 6-8 nm in the case of the 1AB2 wire and 10-12 nm in the case of the 1AB6 wire. However, it is not possible to estimate the size of the pores from a single transmission image in one direction since the whole thickness of the wire is being observed. Therefore, the previous values have to be taken as rough estimations. The crystalline phase between pores was clearly observed in all the analyzed samples, as shown in Figure 5.3a.

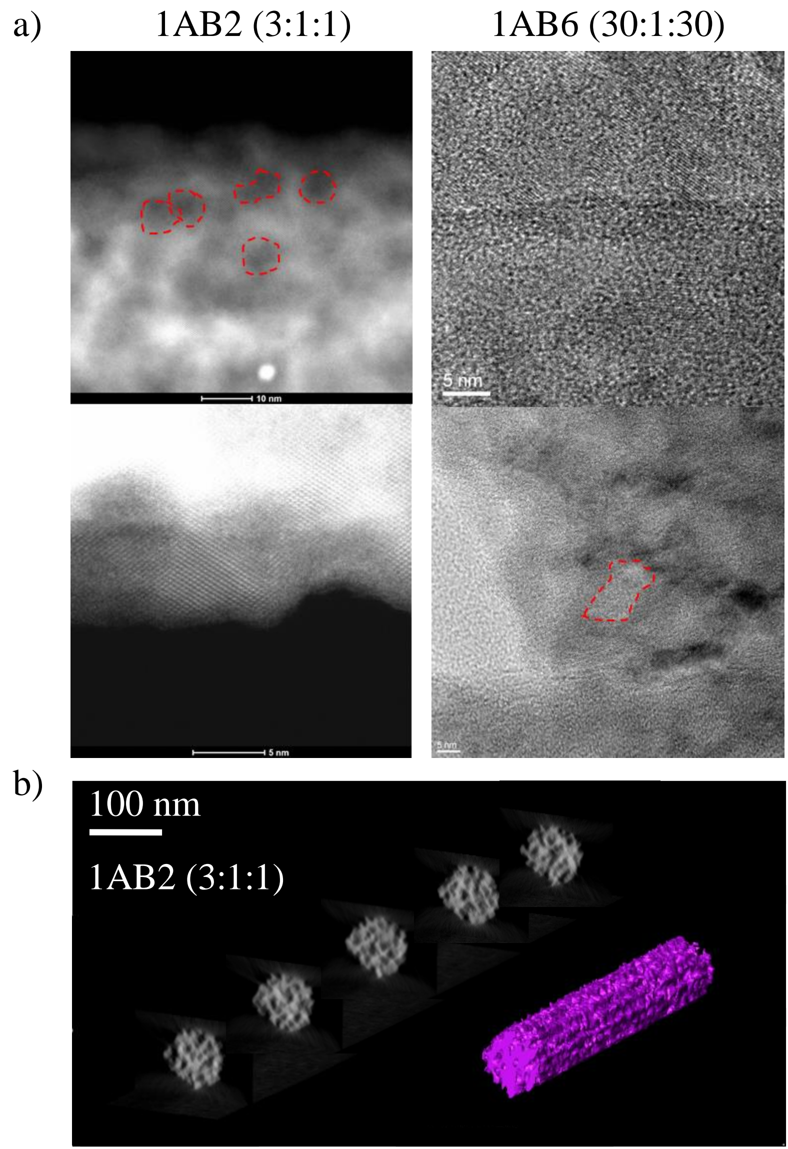

Figure 5.3: a) Representative TEM images of one wire from each batch. Some pores have been marked in red in order to estimate its size. The scale is shown in each image. b) TEM tomography of a wire of the batch 1AB2 with a diameter of around 90 nm. Several sections are shown along with a 3D reconstruction of the wire.

TEM tomography was also performed on the 1AB2 nanowire by taking several TEM images of a portion of the nanowire at different angles (Figure 5.3b). After processing the data, a 3D image was obtained, showing the position of the pores inside the nanowire. From these data the porosity can be calculated by subtracting the volume occupied by the vacuum to the total volume of the nanowire, resulting in 46% of porosity. Nevertheless, this value has a quite high uncertainty due to several factors: First, it depends on how the segmentation is performed, this is, where the limit between material and vacuum is imposed. Second, the differentiation between surface roughness and internal porosity can be ambiguous. Finally, since only a segment of the nanowire was analyzed, any porosity variation through its thickness would be unnoticed.

5.2.4 Thermal measurements

The porous nanowires were measured using the methodology described in Section 3.3. In this case, since the thermal conductance of the wires is low, a correction of the 1D Heat equation using FEM was unnecessary for the 4 wires directly attached to the nitride platform. However, the shortest wires, which have been positioned on a FIB-cut a-Si membrane require a correction to subtract the Si thermal resistance. A sketch of the simulated structure is shown in Figure 5.4. The 67 nm Si membrane is considered amorphous up to 2 µm from the edge, so the thermal conductivity of this region is set to 1.2 $W \cdot m^{-1} \cdot K^{-1}$. The hole produced when cutting the wire after placing it has been also modeled as a rectangular void. The wire has been simulated with 2 different lengths, 1.2 and 2 µm and two different widths, 96 nm and 142 nm and with the hole placed 0.1 µm and 0.5 µm away from the contact, respectively.

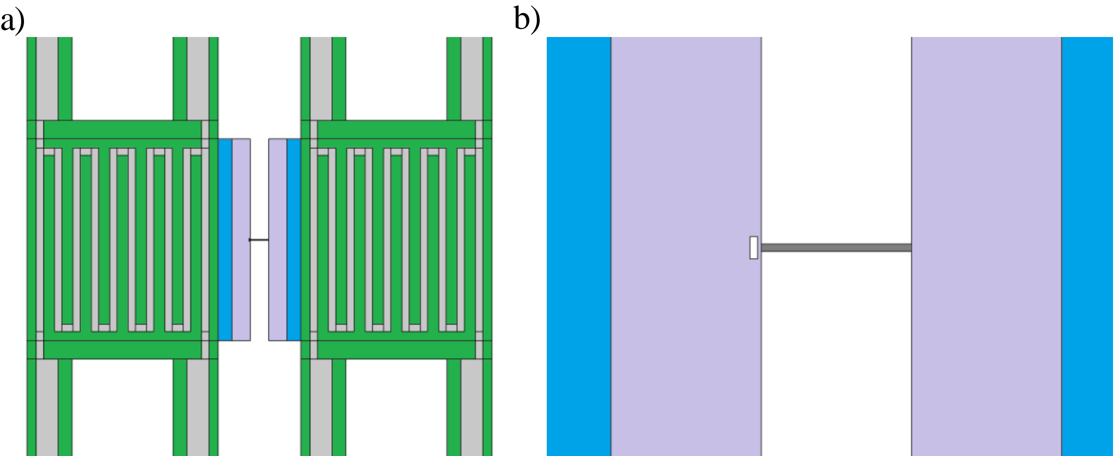

Figure 5.4: FEM used to find the extra resistance produced by the Si amorphous layer. a) sensing platforms with the partially amorphous Si layer, joined by a wire. b) Zoomed image of the wire, where the hole produced when FIB-cutting the wire can be appreciated. In this figure, the materials are SiN_x (green), Pt (light gray), c-Si (blue), a-Si (light purple) and porous Si (dark gray).

Due to the very low thermal conductance of the nanowires, the background thermal conductance plays an important role. This conductance is produced by the heat flowing along the beams of the heating bridge, which slightly heats up the substrate increasing the temperature of the sensing platform (Figure 5.5a). In order to account for this conductance, a structure with no wire bonding the platforms has been measured in the temperature range of 20-320 K (Figure 5.5b). The conductance of this structure is taken as a reference and it is subsequently subtracted at each temperature from the thermal conductances measured with the nanowires bridging the thermal plates. As can be seen, the contribution of the structure to the thermal conductance (background contribution) is

very small, below 1 nW/K, but can have a significant influence on the final value, i.e., up to 30% for the wires of lowest conductance.

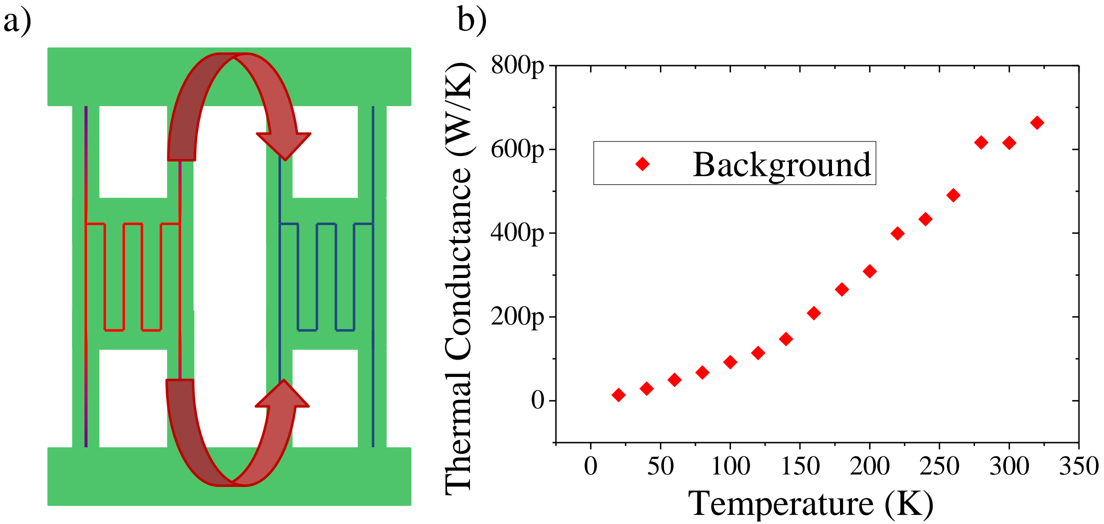

Figure 5.5 a) Scheme of the heat flow in a structure without sample. b) Background thermal conductance of the structure 81-B2.

5.3 Results

All porous nanowires exhibit a drastic reduction of the thermal conductivity with values ranging from 0.8 to 1.5 $W \cdot m^{-1} \cdot K^{-1}$ (Figure 5.6). Although 1AB6 wires are expected to have higher porosity than 1AB2 wires, the former show a higher thermal conductivity. The reason may be related to the higher diameters of 1AB6 wires compared to 1AB2 (see Table 5.2). We suspect that the wires (see below) may show some porosity gradient along the radial direction, with the inner core having a lower porosity than the external region that is more exposed to the etchants. In this case, the larger diameter wires (1AB2) may have a larger porosity variation and therefore a slightly under etched core with higher conductivity.

The thermal conductivity measured in wires with different lengths is similar in both 1AB2 and 1AB6 batches (Figure 5.6a). However, there are some variations. First, the wires with an intermediate length have higher thermal conductivity values than the other wires. In Table 5.2, it can be seen that such wires have the highest diameter values of each batch, which may mean that they have a reduced core porosity, yielding the observed higher thermal conductivity values. Also, the reduced conductivity of wire 41-B2 1AB2, may be due to the enhanced ion-induced damage in the crystalline structure, which reduces the thermal conductivity to that one of amorphous Si. This will be further discussed later.

It can be demonstrated that the amorphization produced by the FIB-induced Pt deposition does not affect significantly the thermal conduction in these long wires. The reduction of the thermal conductivity in a region with the same length in all the nanowires would cause a *de facto* thermal boundary resistance (TBR) with a value of:

$$R_{TBR} = \frac{L_{a-Si}}{k_{a-Si}} \tag{5.1}$$

Where L_{a-Si} is the length of the amorphous part and k_{a-Si} is the thermal conductivity of the amorphous Si. This expression holds in wires with lengths down to $2L_{a-Si}$, since below this length both regions overlap and the R_{TBR} is then reduced.

The R_{TBR} can be experimentally measured by plotting the magnitude A/G, where A is the wire section area, against the wire length. If all the wires have the same R_{TBR}, the linear fit of the data points should have R_{TBR} as the offset. Thus, in the case that R_{TBR} is dominant, the data points should not grow significantly compared with the offset magnitude, while in the opposite case, the linear fit of the data points should tend to 0 at 0 length. Our wires (inset of Figure 5.6a) do not seem to be dominated by the thermal boundary resistance. The linear fit of the data points has a small negative offset, where the minus sign is possibly attributed to the enhanced conductivity of the widest wires of length around 3 μm. However, even if this enhanced conductivity was smaller, the offset would not be as big as the value of A/G in the longest wires. As a rough estimation, if we consider the long and mid-range wires to have the same conductivity, we get a thermal boundary resistance below 10^{-6} m^2KW^{-1}, producing an estimated error below 16% in the longest 1AB2 wire.

Figure 5.6b highlights a clear trend between the thermal conductivity and the wire diameter in all the measured wires but one. Irrespective of the batch, the wires tend to be more conductive if their diameter is higher. In nanowires with homogeneous porosity, this trend would not be expected, since the thermal conductivity would be only limited by the size of the Si bridges between pores. This tendency can be understood invoking the existence of inhomogeneous porosity along the radius of the nanowire, being the core less porous than the shell. In this way, thinner wires are produced with a higher mean porosity than thicker wires. This clear trend also supports the hypothesis that the mid-length wires are not damaged by FIB amorphization and that Pt contamination is not important, since otherwise the data points would have a higher dispersion. Moreover, it

indicates the convenience of producing porous nanowires with small diameters (down to the limit of the technique), where the porosity will be maximum.

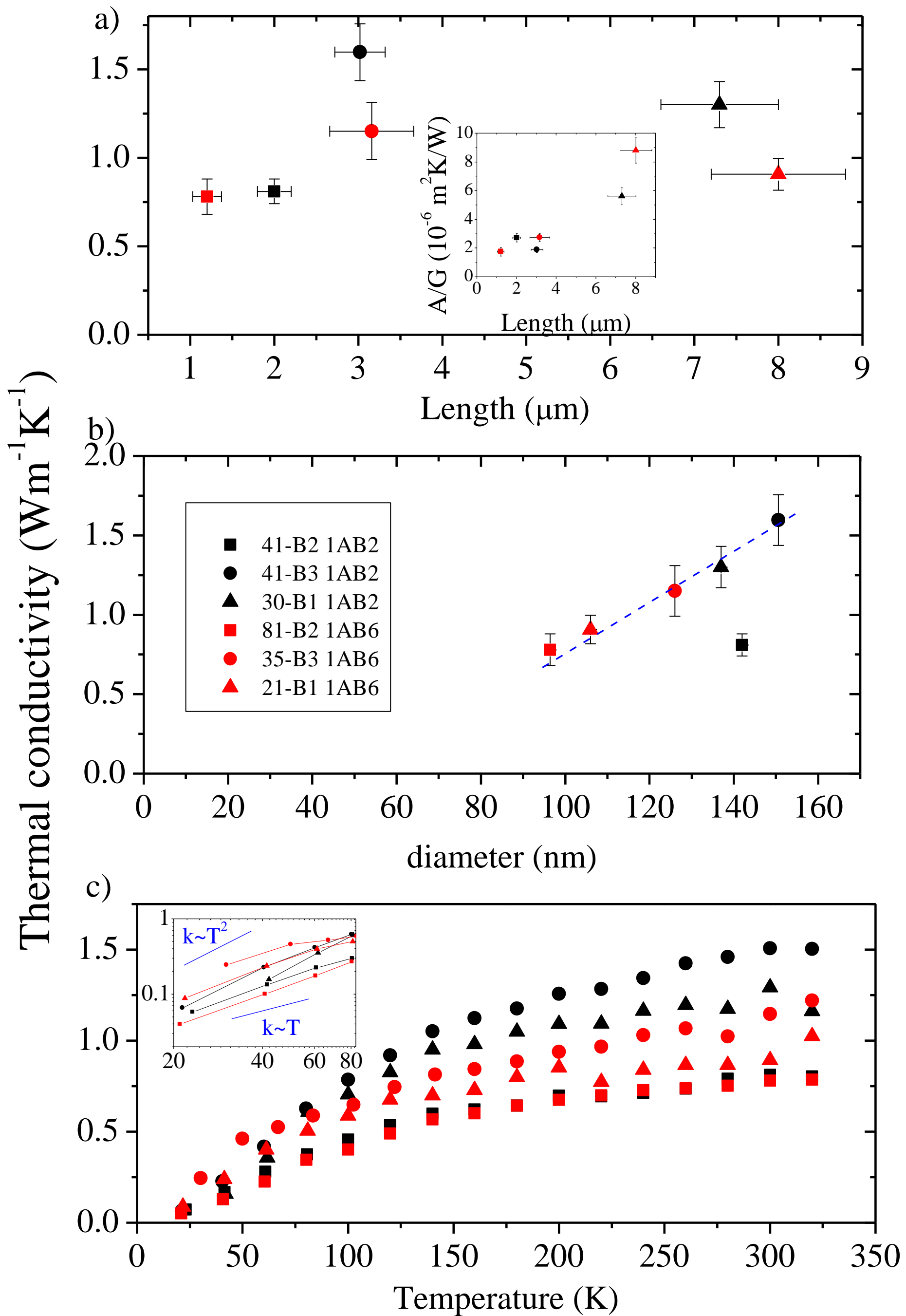

Figure 5.6: Thermal conductivity as a function of the length (a) and temperature (b). Inset of a): thermal resistance multiplied by the area as a function of the length. The legend indicates the reference number of the suspended structure and the batch of the NW positioned.

The question that arises is why the wire 41-B2 1AB2 has such a reduced thermal conductivity value compared to its neighbor wires from the graph in Figure 5.6b, and more importantly, why the shorter wire 81-B2 1AB6 does not show such a reduction. The reason may be FIB damage throughout the wire section, with particular relevance in the core Si. As has been suggested, these wires may have a porosity gradient that would produce dense cores in the widest wires. Such cores would carry the majority of heat through their increased thermal conductivity values. When contacting a short wire to the structure via FIB-induced Pt deposition, some damage may be produced in the crystalline core, especially in the shortest wires. In comparison, the effect of the same ion dose would be unnoticed in thinner wires, since they would be totally porous and the FIB-induced damage would not reduce significantly the already low thermal conductivity.

The thermal conductivity variation with temperature (Figure 5.6c) is dramatically different from bulk Si, showing a modest increase and even a saturation of the conductivity in the mid temperature range (150-300 K). This is very similar to amorphous and nanocrystalline solids[51,144] and has also been previously reported in rough Si nanowires and porous materials[134,138]. The enhanced phonon boundary scattering in these materials and its dominance over the Umklapp scattering explains the difference with crystalline Silicon above 100 K. In the low temperature region ($T < 80$ K) the variation of the thermal conductivity is also very different from crystalline bulk solids. The latter, in agreement with Debye theory, show a T^3 dependence of k, while porous nanowires have lower temperature exponents between 1 and 2 (inset of Figure 5.6b). This is compatible to the findings of Chapter 4 in ultrathin membranes, which once again suggests the frequency dependence of specularity in boundary and pore phonon scattering[54].

In the literature there are few papers with thermal conductivity measurements of porous Si nanowires prepared by MaCE[142,145–148], all of them performed on large arrays of Si NWs. From all of them, only one finds similar thermal conductivity values than our samples[142] (concretely, 1.68 $W \cdot m^{-1} \cdot K^{-1}$). Also, they find that increasing the porosity enhances the Seebeck coefficient and diminishes the thermal conductivity vastly, boosting ZT up to 0.4. In comparison, our thinnest not-damaged wire presents a thermal conductivity of 0.9 $W \cdot m^{-1} \cdot K^{-1}$. For this reason, we expect our wires to have a competitive ZT value.

The thermal conductivity values showed so far are effective values, as we have assumed that the wires are homogeneous. However, since they are porous, the structural silicon actually has a higher thermal conductivity. There are several ways of calculating the structural thermal conductivity in an inhomogeneous medium from the effective value, depending on the internal structure of the material and the relative weight of the inclusions/matrix thermal conductivity. For a medium with spherical inclusions (pores) much less conductive than the matrix (Si), the Maxwell-Eucken relation might be used[139,140]:

$$k_{Si} = \frac{k_{eff}}{F} \tag{5.2}$$

$$F = \frac{1-p}{1+p/2} \tag{5.3}$$

Where p is the porosity of the wire. Applying this factor with the measured porosity of wires 1AB2 (46%) on the longest wire of this kind we get $k_{Si} = 2.96$ W·m^{-1}·K^{-1}, which is around one fiftieth of bulk silicon thermal conductivity. However, the porosity of the thermally characterized wire should be smaller than the one measured with tomography due to the higher diameter of the former wire, so the correction with the Maxwell-Eucken relation should yield a smaller value of k_{Si}. The value found is thus an upper bound of k_{Si}.

Many effects contribute to such reduction in the Si thermal conductivity value: First of all, the doping concentration is very high (from the resistivity values provided in Table 5.1, it can be calculated to be around 10^{19} cm^{-3}), which produces an enhanced impurity scattering in high-frequency phonons in bulk materials. At low temperatures, electron-phonon scattering strongly reduces the thermal conductivity compared to undoped samples[149]. However, boundary scattering is the most important scattering contribution in nanowires, and may hinder the effects of doping in the thermal conductivity. In the case of these nanowires, the external and internal surface area is very high due to a combined effect of roughness and porosity.

It has been shown that roughness alone can efficiently reduce the thermal conductivity down to 5 W·m^{-1}·K^{-1} [53]. In another study, where porous wires were produced by electroless etching, the values measured were as low as 1.6 W·m^{-1}·K^{-1} in a 50 nm wide nanowire. However, as it has already been discussed, this result may be product of unintentional pore formation inside the nanowire since it has not been successfully

reproduced in simulations taking only roughness into account[58,125]. Adding the effect of porosity in the simulations yields lower thermal conductivity, both the effective value and the intrinsic conductivity of Si[150,151].

Our results are compatible with a Monte Carlo simulation of porous Si[150], where they find that the key parameter is the pore MFP, which can be calculated as:

$$l_p = \frac{2d_p}{3p} \tag{5.4}$$

Where d_p is the pore diameter. Wires 1AB2 with a porosity of 46% and a pore size of around 7 nm should have a $l_p = 10$ nm, which is below any value calculated in that paper. However, this MFP together with the effective thermal conductivity value (2.96 $W \cdot m^{-1} \cdot K^{-1}$) are in good agreement with their simulations, although such small pores could produce coherent effects and phonon confinement, which would be responsible of part of the conductivity reduction.

5.4 Conclusions

We have measured the thermal conductivity of several porous Si nanowires that have been top-down fabricated by means of Metal-assisted chemical etching (MaCE), which allows to produce very long nanowires with the desired porosity by tuning the wafer doping and the etchant concentration. TEM images show the pore sizes to be in the order of few nanometers, and the TEM tomography shows a section of a homogeneously porous wire from the batch 1AB2.

The nanowires are grabbed with a nanomanipulator and bonded with FIB Pt on a suspended structure intended for the thermal conductivity measurement. This process may partially amorphize regions of the wire near the bonds, but this effect is estimated to produce an error in the measurement smaller than 16% due to the high nanowire thermal resistance.

The resulting thermal conductivity values are lower than those previously obtained for rough Si nanowires, and smaller than values from previous reports on arrays of porous Si NWs from the literature. Also, the wires measured here show a clear trend between the thermal conductivity and the diameter, suggesting the existence of a radial porosity gradient in wires of larger diameter.

Considering an effective medium, the intrinsic value of the Si material inside the nanowires is 2.96 $W \cdot m^{-1} \cdot K^{-1}$, which is one fiftieth of that of bulk Si. Phonon boundary scattering with the rough surface and the pores can explain such low values; however, phonon confinement and coherent effects could also play a role here. Due to their low thermal conductivity porous wires and porous Si, in general, are promising materials for improved thermoelectric generation and sensing.

6. SiGe graded superlattices

6.1 Introduction

To realize a new generation of devices in thermal-management applications, the manipulation of phonons to control thermal transport across nanostructures is necessary[152]. Tailoring of the heat conductance at the nanoscale can be achieved by means of asymmetries, either geometrical, compositional or structural giving rise to a ‘plethora’ of new physical phenomena[62]. Among them, thermal rectification is the basic ingredient to develop more complex phononic devices. Extensive theoretical efforts have been devoted in recent years to understand the underlying physics of thermal transport to design more efficient rectification devices[128,153–159]. Possible causes of rectification include non-linearity of the structures that produce a strong dependence of the vibrational density of states with temperature, asymmetric electron-phonon interactions occurring at the interface between two dissimilar materials or joining materials with different conductivities. The asymmetry of the network can be achieved, for instance, by varying the mass of the ions in a linear chain. However, experimentally controlling the directionality of heat flow at the nanoscale is still a scientific challenge and very few experiments have demonstrated measurable thermal flow asymmetries. The first experimental realization of a thermal rectifier was based on asymmetrically-loaded nanotubes[129] and heat rectification has also been experimentally achieved in interfaces of dissimilar materials[160]. A step forward in this direction could be the design of graded materials, as recently rationalized[157]. Heat flow asymmetries in superlattices (SLs) have not been reported yet, since SLs are built up by repetition of stacks of two materials which renders the structure symmetric. However, SLs are potential candidates to test the influence of concentration gradients and interfaces on thermal transport while maintaining a low amount of crystalline defects.

From a complementary perspective, SiGe planar superlattices (SLs) have emerged as potential candidates for both thermoelectric cooling of microelectronic devices and medium-temperature TE power generation owing to the poor thermal conductivity of their crystalline lattice[44,161]. Experimental results and theoretical analyses[162–169] indicate

that both the period and total thickness of the SL influence the thermal conductivity as it is governed by the interplay between the scattering dominance of long- and short-wavelength phonons. In that sense, the incorporation of a high interface density in epitaxial heterostructures has been recognized as an efficient approach to enhance boundary phonon scattering at low frequencies with a corresponding decrease in thermal conductivity[45,162–164,170,171]. Recently, Chen et al.[46] showed that Si/Ge SLs with Ge segregation into the Si spacer may be able to scatter phonons at all frequencies. Consequently, their short-period multilayer structures exhibit thermal conductivities below the thin-film alloy limit reported by Cheaito et al.[172] for $Si_{0.80}Ge_{0.20}$ alloy thin films with comparable thickness. However, despite recent progress, a thorough understanding of the effect and interplay of dimensionality and homogeneity on the heat transport in SiGe and other SL structures has not yet emerged.

Compared with most of the previous studies on thermal transport in SLs, we adopt a different approach, engineering $Si/Si_{1-x}Ge_x$ multilayers with well-defined linear compositional gradients in direct (x increasing) and inverse (x decreasing) order to efficiently scatter phonons at all frequencies and to test the existence of heat flow asymmetries. Under a temperature gradient from the top surface, heat travels across $Si/Si_{1-x}Ge_x$ or $Si_{1-x}Ge_x/Si$ interfaces, flowing along or against the Ge compositional gradient in the various grown structures (see the schematics of Figure 6.1). Using this approach, we demonstrate the combined influence of the spatial variation of the Ge concentration and the effect of the thermal boundary resistance on the perpendicular thermal conductivity through the SL. We will also try to unveil the effect of the compositional asymmetry on the thermal conductance. We apply the differential 3ω method to determine the cross-plane thermal conductivity in the temperature range of 100–350 K[76,173]. High-resolution X-ray diffraction is employed to assess the residual strain in the SL and to rule out the possible influence of extended defects on the measured conductivity values, while TEM is used to obtain further information about the crystalline quality of the layers and to measure the space-resolved composition of the SL. We, finally compare our results with preliminary Molecular Dynamics data computed by D. Donadio’s group at University of California, Davis.

6.2 Experimental Section

6.2.1 SL growth

The superlattices have been grown by Molecular Beam Epitaxy (MBE) by M.I. Alonso and M. Garriga from the Materials Science Institute of Barcelona, ICMAB. Before the growth of the SL, the substrates were heated to 850 °C in order to evaporate the native oxide off the wafer. The growth was initiated by depositing a 60-nm-thick Si buffer layer at 750 °C. Then, the substrates were cooled to 400 °C before the rest of the structure was deposited. The Si flux, which was produced by evaporating a Si pellet using an e-beam, was fixed during the entire growth sequence. In contrast, Ge was evaporated from an effusion cell, and its temperature was varied to obtain the desired composition profile in the $Si/Si_{1-x}Ge_x$ layers. The temperature variation of the Ge cell (T_{cell}) was adjusted to yield an approximately linear change in x. Accordingly, the temperature evolution over time was not linear; each graded layer was deposited over 14.5 min while the cell temperature variation changed from 0.75 $°C·s^{-1}$ in the higher-T_{cell} range (where v_{Ge} ~ 0.47 $Å·s^{-1}$) to 1.25 $°C·s^{-1}$ in the lower-T_{cell}range (where v_{Ge} ~ 0.002 $Å·s^{-1}$). The Si deposition rate was fixed at around 0.35 $Å·s^{-1}$ for each deposition run. Ten structures containing four periods with graded compositions were deposited in direct (Ge concentration profile parallel to the growth direction) and inverse growth (Ge concentration profile antiparallel to the growth direction), as well as an extra sample with sixteen periods. An additional 4–5-nm Si layer was grown between the graded layers. The multilayer structures terminated in a 5-nm-thick Si capping layer, except the 16-period that is terminated with a 1 µm thick Si layer. A schematic of the SL is shown in Figure 6.1, and details regarding the various samples are presented in Table 6.1. Reference samples containing only the Si buffer layer were also prepared, for use in the differential 3ω measurements.

The superlattices were grown in direct and inverted concentration profiles in order to measure the thermal conductivity of the graded region in both directions, since thermal rectification is an expected feature in such asymmetric SLs. This would be produced by two different effects that may come in play: First, the thermal boundary resistance (TBR) between the Si/SiGe and the SiGe/Si sharp interfaces is expected to be dissimilar due to the difference in the phonon spectra of both materials[174,175]. A high-frequency phonon going from SiGe to Si should be more likely to cross the interface than a phonon going

from Si to SiGe due to the higher amount of high-frequency states available in Si, as it is a lighter atom. This would create thermal rectification with the high-conductive direction being the one with SiGe/Si interfaces. The second effect is produced by the mass gradient: As has been shown in a theoretical study by Wang et al.[176], an asymmetric 1D chain with gradually increasing particle mass presents thermal rectification, which direction depends on the particle masses.

The samples are fabricated thus by pairs of direct and inverted samples. 5 pairs of samples were fabricated with Ge concentration ranging from 0% to 40-60% and from 20% to 40% and viceversa in order to measure thermal rectification, while another sample with 16 periods was fabricated to test the influence of the thickness and the number of periods in such superlattices.

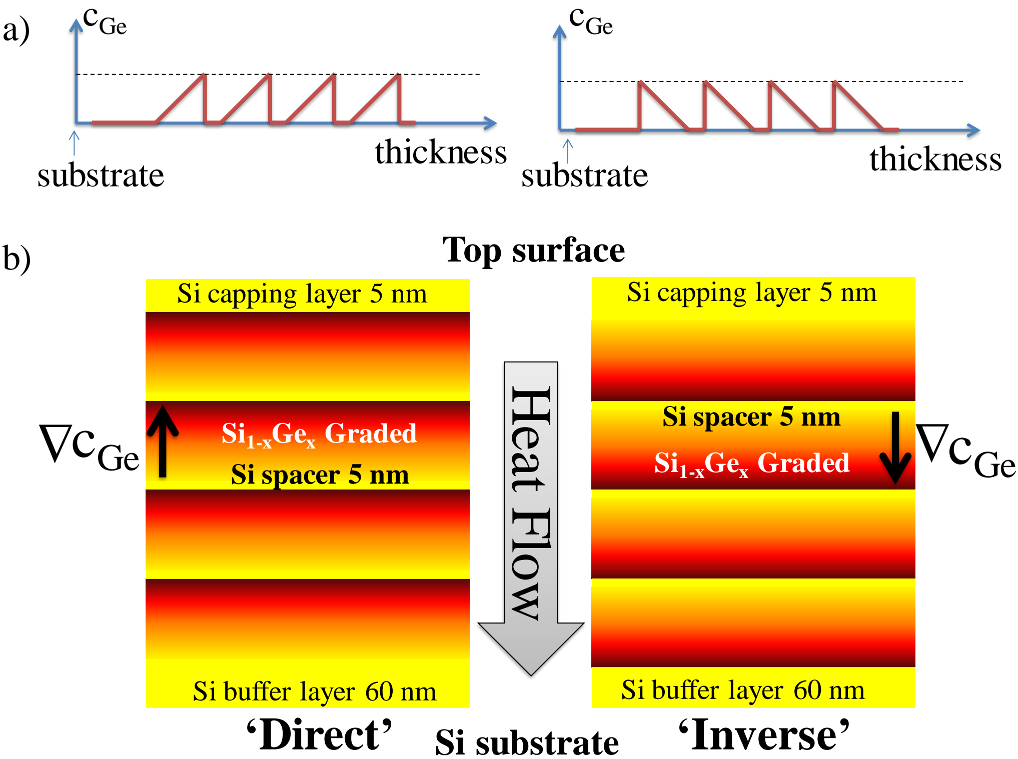

Figure 6.1 a) Compositional profile of Ge (c_{Ge}) along the four periods of the structure. b) Schematic of the graded SiGe SLs and the direction of the heat flow. ∇c_{Ge} stands for the gradient in Ge concentration.

Sample	Ge content (mean)	Total thickness (nm)	Period thickness (nm)
NTH001 (dir)	0%-62% (17%)	143±1	35.75±0.25
NTH002 (inv)	70%-0% (25%)	152±1	38±0.25
NTH010 (inv)	55%-0% (25%)	170±1	42.5±1.00
NTH011 (dir)	0%-58% (14%)	172±1	43±0.25
NTH028 (dir)	0%-41% (17%)	110±1	27.5±0.25
NTH029 (inv)	55%-4% (24%)	110±1	27.5±0.25
NTH030 (dir)	20%-40% (nominal)	120±1 (from XRD)	30±0.25
NTH031 (inv)	40%-20% (nominal)	120±1 (from XRD)	30±0.25
NTH037 (inv)	40%-0% (18%)	167±4	41.75±1.00
NTH038 (dir)	3%-27% (17%)	183±4	45.75±1.00
NTH16P (dir)	0%-52% (33%)	667±1 (16 periods)	41.69±0.06

Table 6.1: Sample characteristics as determined from TEM images and concentration profiles from EDX.

6.2.2 Microstructural characterization

The film crystallinity was assessed by HRXRD using a four-angle goniometer with a 4 × Ge(220) crystal monochromator in the primary optics (MRD X'Pert Pro Panalytical). The monochromator reduces the wavelength and angular spreads to $\Delta\lambda$ = 0.001 Å and $\Delta\theta$ = 0.003°, respectively, for Cu $K_{\alpha 1}$ radiation. The full-width-at-half-maximum of the Si(111) line of a Si single crystal standard is 21", i.e., 0.006°. The X-ray intensity is collected by a position-sensitive detector with a minimum angular resolution of ~0.0001°.

Transmission Electron Microscope (TEM) was also used for characterizing the nanostructures. Prior to that, the samples were prepared in 3 steps: first, the chips were cleaved and glued horizontally to a Cu grid. Then they were polished in order to reduce their thickness down to 50 microns. Finally, using Ar ion bombardment, the final thickness of 100 nm was achieved. The samples were observed with a HRTEM at x71K and x450K magnification to check the superlattice roughness and to find crystalline defects. The local crystallinity was characterized with electron diffraction of selected spots through the superlattice. Finally, the space-resolved composition was measured using Electron Dispersion X-Ray Scattering (EDX) in the Scanning mode of the microscope (STEM). The Si K-line and the Ge L-line were used to quantify the atomic fraction at each position. With the composition profiles, both the period thickness and the Ge density (as atomic percentage) were measured.

6.2.3 Thermal characterization

The thermal conductivity of the SLs was measured using the differential 3ω method, as explained in section 3.4. To enable this measurement, a 100-nm-thick alumina (Al_2O_3) layer was grown by atomic layer deposition (ALD) to electrically isolate the SL from the metallic transducer. Rigorous calibration of the ALD setup guarantees that the thickness from sample to sample in a given run varies less than 2%, i.e., 2 nm. We note that 2 nm of Al_2O_3 corresponds to a temperature difference of 8 mK (given the heating power used in the experiments), which roughly represents 4% of the total thermal gradient across the four-period SL. In addition, a single ALD run with samples spatially close together was performed to minimize the thickness differences and potential shortcomings of the 3ω measurement.

For the 3ω measurements of the 4-period SLs, we used a 1-mm-long, 5-μm-wide, and 100-nm-thick Au sensor with a 3-nm-thick Cr adhesion layer, while for the thicker 16-period sample, a wider and longer sensor was used (33 μm wide and 1.3 mm long). As reported by Tong and Majumdar[83], the temperature change across the film can be considered one dimensional (1D) in the limit of low film thermal conductivity compared to the substrate, large interface thermal conductance, and heater lines wider than the film thickness. In this work, the heater-width-to-film-thickness and the film-to-substrate thermal-conductivity ratios were 50 and ~0.02 at 300 K, respectively. According to these values, the heat spreading in the direction parallel to the film should be small, and the cross-plane thermal conductivity of the film can be calculated using the 1D steady-state heat-conduction model. The suitability of the 3ω technique to measure SL-like structures was confirmed by comparison with time-domain thermoreflectance (TDTR) techniques[171].

6.3 Results and discussion

We first focus on the crystalline quality of the compositionally graded SLs, as extended defects may negatively impact phonon transport across the SL. The left column of Figure 6.2 shows X-ray diffraction $2\theta/\omega$ coupled scans of symmetric 004 reflections for $Si_{1-x}Ge_x$ slabs and the Si substrate of samples NTH028, NTH029, NTH030 and NTH031. The narrow satellites found in the first pair of samples are characteristic of the vertical correlation and sharp definition of the interfaces between repeated slabs in the multilayer structure[177]. The reciprocal space mapping of the -2-24 $Si_{1-x}Ge_x$/Si asymmetric reflection

(right column of Figure 6.2) in the same samples reveals a perfect in-plane lattice matching of the multilayer structure with the Si substrate (same Q_x position for film and substrate peak). However, samples NTH030 and NTH031 show a totally different HRXRD data. In the symmetric 004 reflections no satellites can be found, while the -2-24 asymmetric reflections of the thin film and the Si substrate are completely misaligned. This is characteristic of plastically relaxed superlattices, and suggests that the thermal and electrical conduction in such samples will be reduced. The diffraction profiles of samples NTH028 and NTH029 are representative of all the direct and inverted samples, and therefore the other pairs are not shown here. They exhibit pseudomorphic growth, which is typical of fully strained samples, indicating that the misfit dislocation (MD) density is so low that there is no appreciable relaxation of the lattice parameter. The maximum linear MD density is less than 4×10^4 cm^{-1}. Assuming that these MDs propagate in the form of threading dislocations across the volume of the SiGe multilayer, we estimate a surface dislocation density below 2×10^9 cm^{-2}. This value is lower than the threshold at which dislocations start to impact thermal transport across a Si Ge SL as has been recently shown in detailed simulations of $Si/Si_{0.3}Ge_{0.7}$ SLs[178].

TEM images were taken from the strained superlattices (all but samples NTH030 and NTH031). Representative TEM micrographs are shown in Figure 6.3. They illustrate mostly perfectly crystalline superlattices with low interfacial roughness. The only exception seems to be sample NTH028, which shows both a high interfacial roughness and a higher dislocation density (but below the limit derived from XRD) compared to other samples. Also, sample NTH038 exhibits high roughness but with a low dislocation density. The electron diffraction of all strained samples is similar to that of sample NTH029, showing monocrystalline-like patterns. Interestingly, some of the diffracted peaks are slightly elongated or maybe duplicated due to the effect of the SL periodicity.

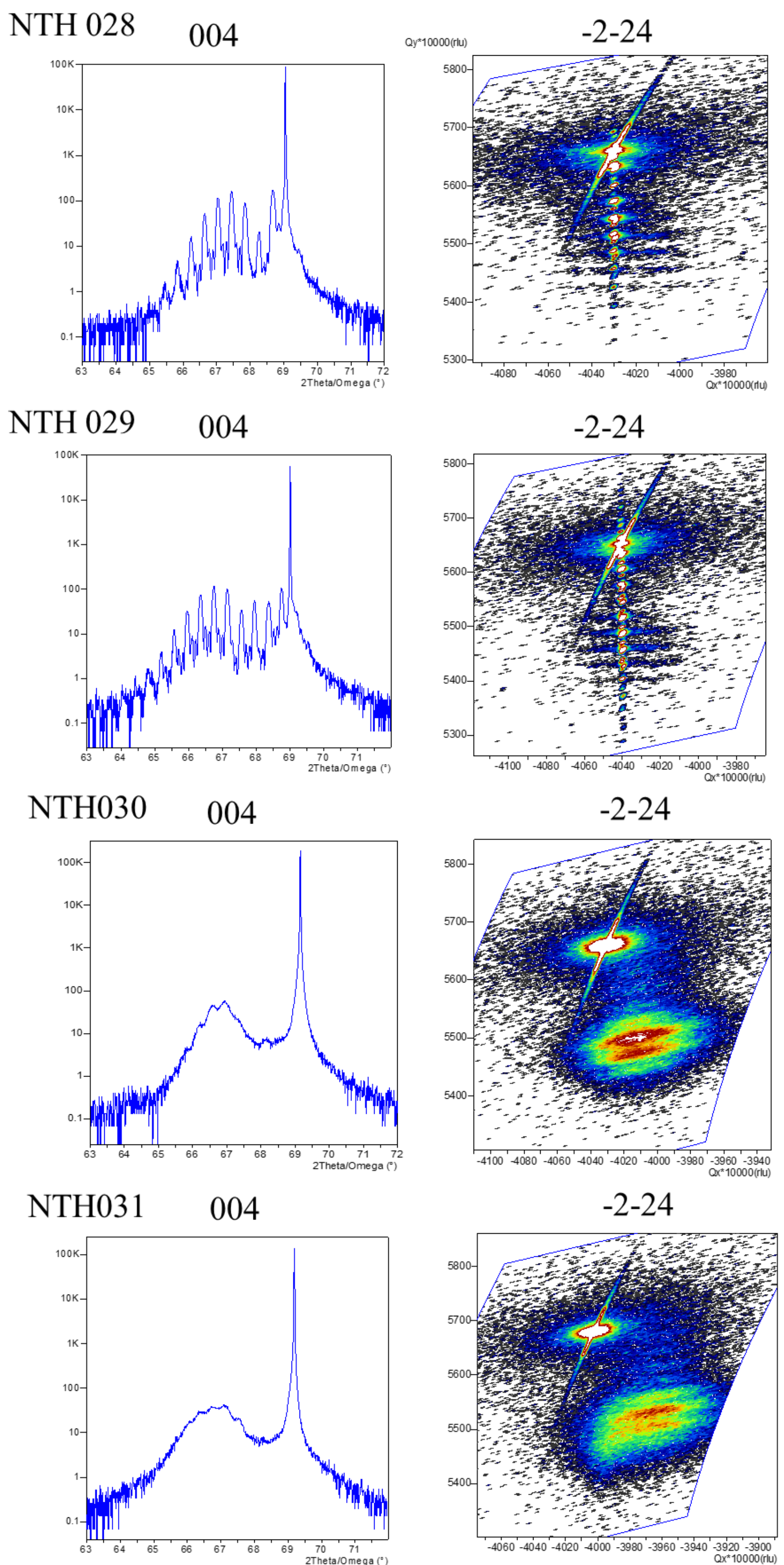

Figure 6.2 High-resolution X-ray 2θ/ω diffraction scans of symmetric 004 reflections for $Si_{1-x}Ge_x$ slabs and Si substrate (left) and reciprocal space mappings of the -2-24 Si/$Si_{1-x}Ge_x$ asymmetric reflection (right). Samples NTH028 and NTH029 are representative of direct and inverted samples, respectively. Only samples NTH030 and NTH031 show plastic deformation.

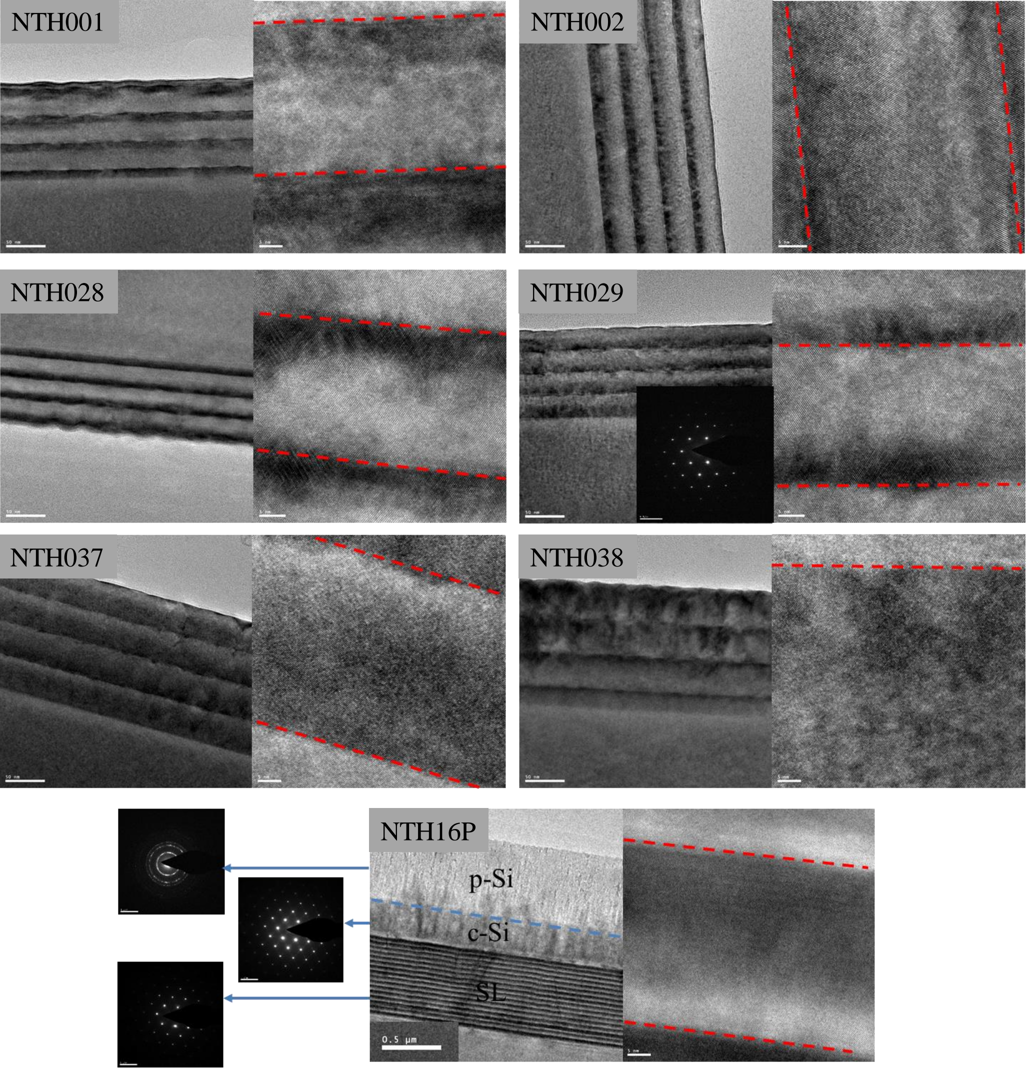

Figure 6.3: TEM image of some of the samples measured. Each sample has a general view of the superlattice (left) and a zoomed image where the one or two interfaces can be observed (right).Sample NTH029 is provided with an electron diffraction pattern.

The 16-period SL requires a special consideration as it has a thick capping layer of 1 µm. The electron diffraction pattern reveals that the heterostructure has a good crystalline quality, but the upper 600 nm of the capping Si layer are unexpectedly polycrystalline, with domain sizes around 20-30 nm, which can affect the thermal conduction. According to Wang et al.[179], poly-Si with such a grain size should have a thermal conductivity of around 10 $Wm^{-1}K^{-1}$, and thus it may add up some thermal resistance to the measurement. For this reason, the contribution of this poly-Si layer will be subtracted from the measured thermal resistance of the SL. Differently to the upper part of the capping layer, the lower Si layer is monocrystalline, but it presents diffraction peaks between the main monocrystalline peaks, suggesting that it has a relatively high dislocation density.

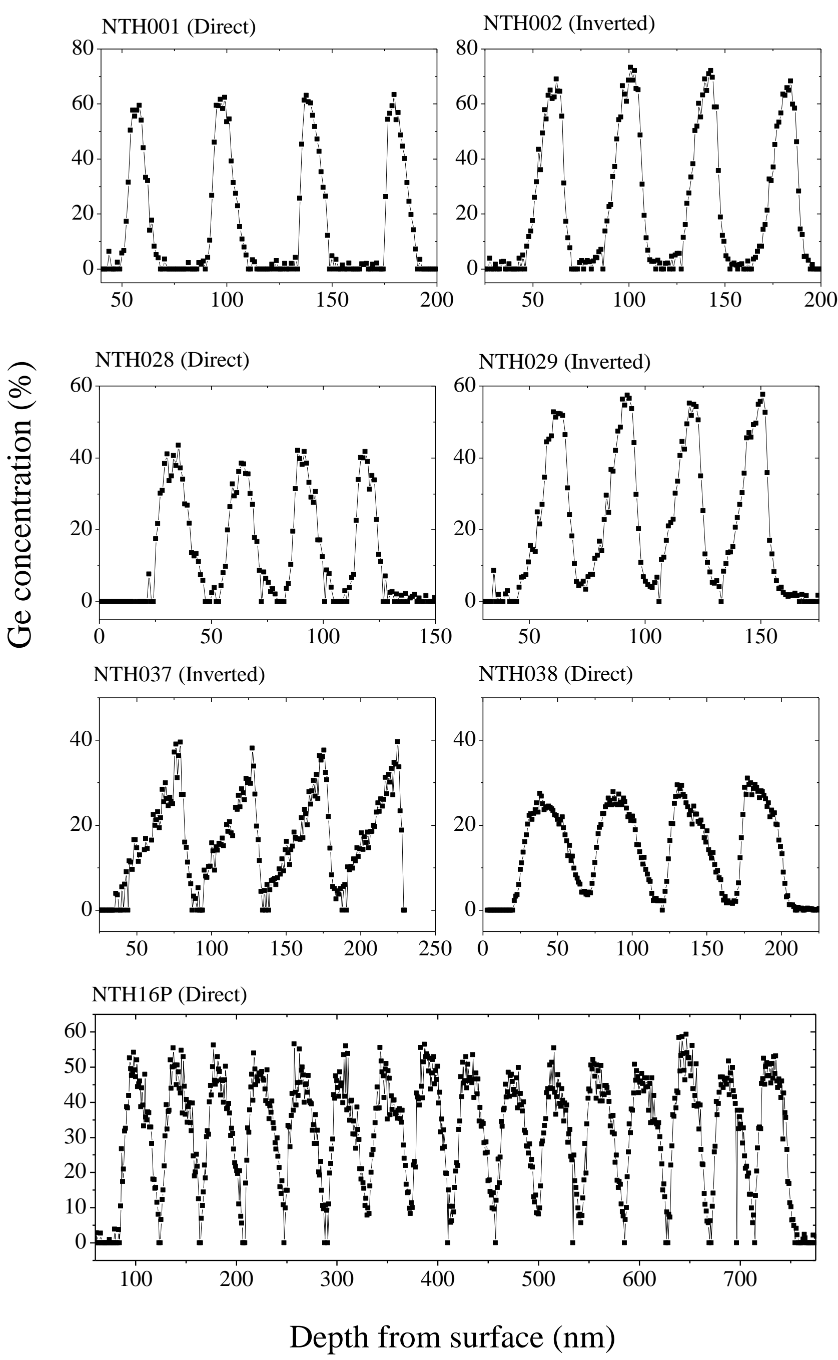

Figure 6.4: Ge concentration profiles measured with EDX (K line of Si, L line of Ge) using TEM. In the case of the 16 period sample, the x-axis does not start at the surface of the sample, but in the Si capping layer.

The compositional profile of the samples shown in Figure 6.3 can be seen in Figure 6.4. In all cases, there are sharp Ge/Si (direct) or Si/Ge (inverted) interfaces in each period, as well as the graded region. The EDX profiles reveal two main features that will have a remarkable impact on the discussion of the thermal conductivity values: i) The compositional profile is not symmetric with respect to direct and inverted samples, i.e.

due to the growth procedure, samples with direct profiles generally present compositional gradients confined in thinner layers than the ones of the inverted samples. The impact of this asymmetry on the thermal conductance is analyzed in the next section. ii) There is a deviation from the intended compositional profile in all samples except NTH037, which presents the clearest graded region with a sharp interface in one side.

The period thickness was calculated from these composition profiles by averaging the thickness of the three upper periods of each SL. The deepest period was not included since it gradually fades into the Si substrate in the direct samples, impeding a proper measurement of its thickness.

6.3.1 Thermal transport across SLs

Figure 6.5 shows the main outcome of the present work: the very low values of the cross-plane thermal conductivity for long-period SLs.

The temperature dependence of the thermal conductivity k displayed in Figure 6.5a is comparable to that observed in other planar SLs and quantum-dot SLs (QDSLs)[180]. The flat profile is compatible with an enhanced phonon scattering produced by both the boundary scattering at low frequencies and impurity scattering at high frequencies, which hinders the temperature dependence of Umklapp scattering, similarly to a nanostructured bulk alloy[181].

The conductivity values measured at 300 K in our samples are shown in Figure 6.5b, accompanied for comparison with other undoped SLs[45,46,163,164,170,171]. Here a direct dependence between thermal conductivity and period thickness can be seen. This suggests that the phonon transport through the superlattice is predominantly ballistic, being the period boundaries the main scattering barriers that these phonons find in their path. This is produced partially because the alloy in the SL scatters efficiently the high-frequency, short-MFP phonons, leaving as the predominant heat carriers phonons with very high MFP: the ratio of heat carried by phonons with MFP larger than 1 μm is higher than 50% in bulk SiGe alloy[172]. This behavior also applies to most of the SLs presented in the literature except at very low period thicknesses, where coherent phonon effects reverse this trend[170*]. These coherent effects are produced when the phonons become actually

[*] In Figure 6.5b, the samples that show the reversed trend may have higher strain for longer periods, which could explain their lower thermal conductivity values.

eigenmodes of the SL vibrations. In this case, a higher boundary density no longer reduces the thermal conductivity values, but the total thickness starts being a significant parameter that controls the thermal conductivity values.

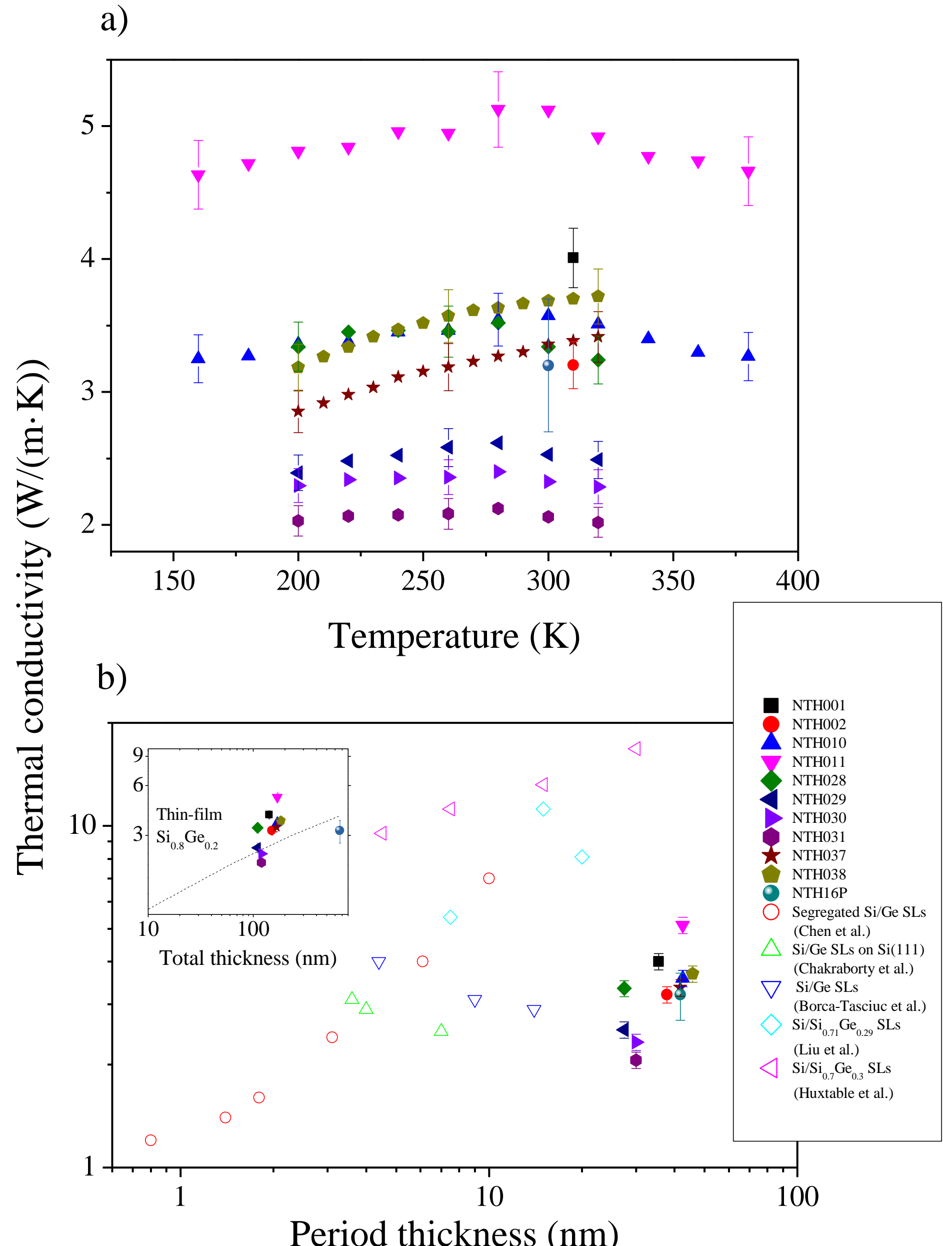

Figure 6.5 a) Thermal conductivity of the graded SLs with respect to the temperature. b) Thermal conductivity with respect to the SL period for our undoped SiGe SLs and others from Chen[46], Chakraborty[170], Borca-Tasciuc[163], Liu[45] and Huxtable[164]. Inset: Thermal conductivity as a function of the total thickness. The thin-film alloy of $Si_{0.8}Ge_{0.2}$ is included for comparison.

Our samples present very low k values, below those found in the literature for the same period thicknesses. This can be attributed to the presence of the concentration gradient in the structures, that generate both an extended alloyed region and sharp $Si/Si_{1-x}Ge_x$

interfaces, with a high value of x. The combination of an extended alloy that scatters high-frequency phonons and the sharp interfaces that scatter efficiently low-frequency phonons is probably the cause for such low thermal conductivity values, as already identified in the work of Chen et al.[46]. In this previous work Ge segregation into the adjacent Si layers occurs due to the diffusion during the high temperature growth and symmetrizes the structure diminishing the influence of the thermal boundary resistance on the thermal transport. In contrast, our multilayers have sharp interfaces and built-in compositional asymmetry. The existence of abrupt interfaces was evidenced through TEM measurements of the multilayers and is due to the low-temperature growth employed during deposition. In this way, as schematically shown in Figure 6.1, the heat-flow propagation encounters additional thermal barriers at the interfaces between $Si_{1-x}Ge_x$ and pure Si, leading to a reduced thermal conductivity.

Comparing our results with the thin-film alloy[172] we find that samples NTH030, NTH031 and NTH16P fall below the thin-film alloy limit, while sample NTH029 has a similar value within the experimental uncertainty (inset of Figure 6.5b). Samples NTH030 and NTH031 show very reduced thermal conductivities due to the plastic deformation of the SL induced by their high Ge concentration. However, samples NTH029 and NTH16P are fully-strained SLs. Looking in detail their compositional profile we find that in those SLs i) the Ge concentration is higher than 20% in a wide region of each period and ii) the interface between periods is very sharp. Statement i) is key to produce high-frequency phonon scattering. As already demonstrated by Cheaito et al.[172], the thermal conductivity of a thin-film alloy presents a minimum plateau between 20% and 60% in Ge concentration. Thus, having Ge concentrations in this range throughout the SL is necessary to reduce the thermal conductivity through high-frequency phonon scattering. However, statement ii) is necessary to produce an efficient low-frequency phonon boundary scattering due to the pronounced mismatch between the $Si/Si_{1-x}Ge_x$ interface. The optimal combination of both effects in these 2 samples seems to be the cause for their very low thermal conductivity values.

In the case of sample NTH16P, we also observe that despite its increased total thickness, the thermal conductivity is very close to that of thinner samples with similar period thickness (NTH037 and NTH002). The similar k values in a much thicker sample is indicative of the lack of coherence effects. In a superlattice, phonons with a wavelength higher than the period length tend not to be scattered by the period boundaries, but only

by the boundary between the SL and the bulk. In our superlattices, these phonons should have wavelengths larger than 40 nm[182]. The low population of such phonons at room temperature in SiGe produces the lack of dependence of k with the total SL thickness.

Having a look into the composition profile of each sample we find that generally direct samples show higher values of the thermal conductivity than inverted ones. Concretely, samples NTH001, NTH011 and NTH028 are more conductive than the inverted samples with similar periods (NTH002, NTH010 and NTH029, respectively). At a first glance, this may induce us to think that there is thermal rectification. However, we notice from the TEM profiles that in these inverted samples the Ge is more spread inside each period than in the direct samples (Figure 6.4). This, as has been discussed, produces a thicker alloyed region that scatters more efficiently high-frequency phonons. In samples NTH037 and NTH038 the Ge is similarly spread through the period producing in both cases very low values. This is under further analysis by the group of D. Donadio (University of California, Davis) that is performing lattice dynamics simulations with the concentration profiles of our structures. We provide below a very brief summary of their main findings since they offer a complementary view to interpret the thermal conductivity values measured during this PhD.

6.3.2 Lattice dynamics

Using the concentration profiles measured with TEM, D. Donadio and coworkers simulated samples NTH001, NTH002, NTH037 and NTH038 using lattice dynamics in order to find theoretical values of k for our SLs. Concretely, Elastic Scattering Kernel Method (ESKM) was used[183]. This method, unlike Molecular Dynamics, takes into account quantum effects, which makes the results more precise. However, all the scattering events are considered elastic, but since anharmonic effects are expected to be unimportant in these samples, it will not affect significantly the results.

The modeled samples consist of a square nanowire with the length of each SL modeled (Figure 6.6a). A periodic boundary is imposed in the in-plane directions of the superlattice (the narrow sides of the nanowire), avoiding any possible confinement effect produced by such a small modeled structure.

The simulated thermal conductivity values at room temperature (Figure 6.6b) are in agreement with experimental results for both the direct and the inverted samples, being only the thermal conductivity of sample NTH037 slightly overestimated. Owing to their

different compositional profiles, the four samples show different thermal conductivity values, as was suspected. Thus, thermal rectification does not have to be invoked to justify the different k values found in the experiment. However, at present we do not rule out yet that second order heat flow asymmetries may exist in our samples. The 16 period sample will be used in the near future to test the influence of the sign of compositional gradient on the heat flow across the superlattice.

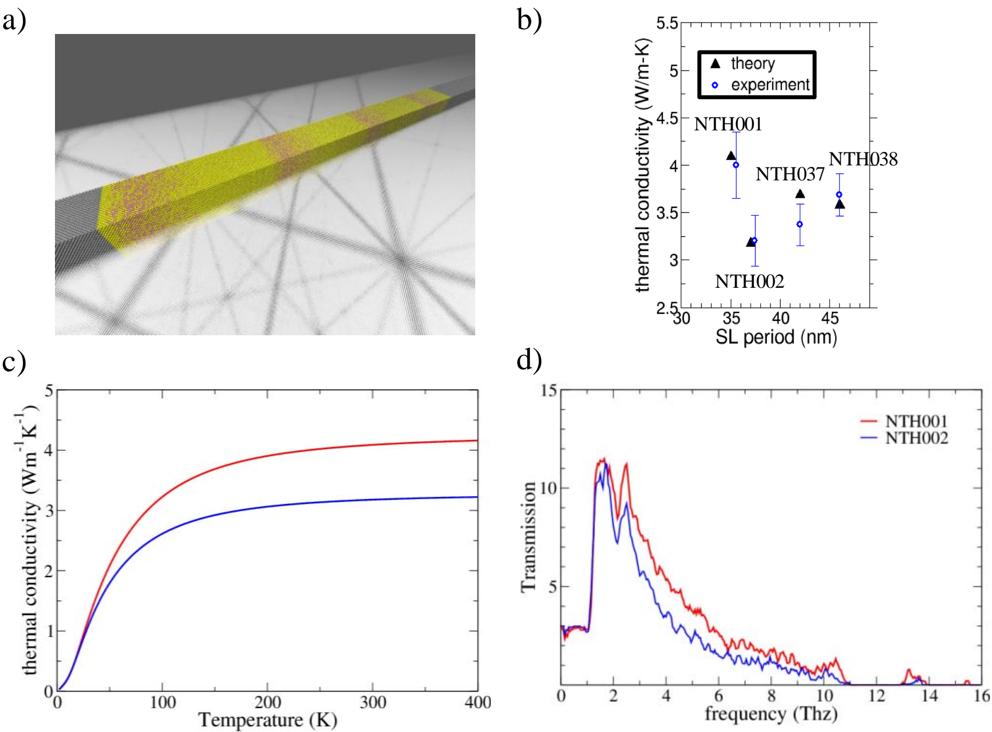

Figure 6.6: a) One of the simulated structures, consisting of a long nanowire with periodic boundaries in the two narrow dimensions. Thermal conductivity of samples NTH001, NTH002, NTH037 and NTH038 compared to the theoretical values. c) and d): Transmission function of phonons as a function of frequency and thermal conductivity vs temperature of samples NTH001 and NTH002.

Figure 6.6c shows a steadily increasing thermal conductivity with the temperature for samples NTH001 and NTH002, very similar to the almost flat profiles measured. The transmission functions shown in Figure 6.6d show a reduced phonon transmission in the whole frequency range for phonons in sample NTH002 compared to NTH001. This is likely produced by the efficient alloy scattering owing to the increased Ge concentration in NTH002. Now the effect of the period boundary is discussed. In sample NTH001, the boundary thickness between periods is only 3 nm thick (meaning that the Ge concentration changes from the minimum value to the maximum one in that region), while the boundary thickness in sample NTH002 is 7 nm thick. We would expect a sample with a more defined boundary to scatter more efficiently low frequency phonons, but the

reverse effect observed in our samples suggest that the increased alloy scattering is more important than this boundary effect.

6.4 Conclusions

By precise control of the growth conditions at a relatively low temperature of 400 °C, we successfully obtained compositionally graded SLs with Ge gradients (x = 0.55, 0.60, or 0.40 to 0) and SLs periods of 45, 35, and 26 nm, respectively. The simultaneous presence of alloy scattering, thermal boundary resistance, and concentration gradients reduced the thermal conductivity to a value of 2.2 $W \cdot m^{-1} \cdot K^{-1}$ for the SL with a period of 26 nm. This value is remarkably low for a long-period SL. Our approach introduces a new perspective for tailoring the thermal properties of artificially grown nanostructured materials and illustrates the effectiveness of the compositional asymmetry for reducing the thermal conductivity. We foresee these artificial nanostructures having a great impact in future applications requiring low-thermal-conductivity materials and significantly influencing the research in that area.

The low thermal conductivity values follow an increasing trend with the period thickness, indicating the important contribution of ballistic phonons to heat conduction. The 16-period sample shows also a reduced value, similar to the 4-period samples, suggesting that coherent phonons are not important for heat conduction in our superlattices.

Thermal rectification was expected in our samples due to the intrinsic asymmetry of the SL and the direction-dependent interface thermal resistance between Si and SiGe. However, the different values of thermal conductivity between direct and inverted samples can be properly accounted for considering their different compositional profiles. This is further studied via molecular dynamics, which reproduces the experimental results in the analyzed samples.

This work puts a spotlight on the importance of the presence of the alloy inside a SL, which combined with the boundary scattering can yield thermal conductivity values below the thin-film alloy limit.

7. Real time thermal conductivity measurement during growth of ultrathin layers

7.1 Introduction

Monitoring the first stages of thin film growth is of key importance to understand and tune the properties for the growing layers. Critical aspects of the microstructure, such as grain size, crystal orientation, grain morphologies, nature of grain boundaries or surface morphology are defined during the early growth process. Real-time measurements have proven useful to understand the growth dynamics during thin film formation and nanoparticle formation on surfaces. In-situ diagnostics during growth, with monolayer sensitivity, have already been achieved by a variety of techniques such as wafer curvature measurements to map the stress evolution[184], ellipsometry[185], X-ray reflectivity[186,187] and resistance-based measurements. Low or medium energy electron diffraction (LEED, MEED) are also very useful tools to monitor 2D ordering during epitaxial growth[188,189]. In particular, electrical measurements are very powerful since the electrical resistance may vary by orders of magnitude above the percolation threshold. The technique has been already used to analyse the percolation threshold and film continuity of metallic thin films[190] or to identify phase transformations during the initial growth stages, such as amorphous-to-crystal transition in Mo films[191]. Unfortunately, although simple and accessible, this approach is limited to metallic or highly conductive layers precluding the analysis of many organic or insulating materials. In spite of the fact that phonons are very sensitive probes to the structure of the films due to their larger mean free path compared to electrons, real-time thermal conductance measurements during film growth are much scarcer, mainly due to technical challenges.

On the other side, in recent years, there has been a growing interest to perform accurate measurements of the thermal conductivity of nanomaterials, thin films and nanostructures because of their potential implementation in heat management or efficient thermoelectric devices. Phonon engineering in low-dimensional materials represents a viable approach to enhance the thermoelectric figure of merit[66,192,193]. The progress in designing novel

nanomaterials has challenged the development of new sensors and methodologies enabling accurate determination of thermal conductivity in such low dimensional architectures. Whether based on optical[194] or electrical[67] signals, the new sensors and methodologies allowed in-plane[69,195] and out-of-plane[82,196] thermal conductivity measurements of nanowires and thin films, even with nanometer spatial resolution[43,130,197]. A remarkable contribution to the field was achieved by Völklein et al. in 1990 who developed a suspended membrane-based sensor using a long and thin Pt electrical transductor operated in DC to measure in-plane thermal conductivity of thin films[195]. More recently, Sikora et al. improved the system by combining the Völklein method with the AC 3ω-method, reaching exceptional thermal conductance sensitivity, $\frac{\Delta G}{G} \cong 10^{-3}$ [84,90].

Here, we use a modification of the 3ω-Volklein technique to analyse two different materials, a metal such as In and an organic conductor, N,N′-Bis(3-methylphenyl)-N,N′-diphenylbenzidine (TPD), often used as hole injector in OLEDs. In both cases, though at different time and length scales, we observe an initial decrease of the thermal conductance that we attribute to enhanced phonon scattering at the nitride/film interface followed by an increase due to the growth of a continuous thin film. We show the very different growth kinetics of both materials. In the case of TPD we investigate the influence of the deposition temperature on the percolation threshold that changes from 2.5 to 6 nm as substrate temperature varies from 267 to 304 K, below the glass transition temperature of TPD, T_g=328 K. We relate this variation to the surface mobility of the molecules.

7.2 Experimental Setup

The sensor presented in Section 3.5.1 is introduced in a high vacuum chamber equipped with an effusion cell enabling low rate evaporation control. A quartz crystal balance is placed at the same level of the sensor for monitoring the layer growth rate with a precision of 0.01 Å/s – that assumes a complete coverage of the surface. In a previous step, the quartz crystal is calibrated using ex-situ film thickness determination with a microprofiler. The temperature of the sample is controlled with a custom-made PID system that reads the temperature of a Pt100 and provides heat through a Kapton heater, yielding a temperature control with fluctuations smaller than 0.003K, from 77 K up to 400 K.

7.3 Results

7.3.1 Organic thin-film layers

We first measure the thermal conductance of the membrane during the growth of TPD at 267±2 K, as shown in Figure 7.1a. The temperature uncertainty comes from the thermal oscillations produced by the current wave of amplitude 300 μA. The evaporation was carried out below 10^{-7} mbar by heating up an effusion cell up to 200ºC, which yielded a deposition rate of 0.29 nm/s. From the slope of the curve $G_{2\omega}(t_{smp})$ and applying equation (3.92) we calculate the thermal conductivity of the TPD layer, resulting in $k_{smp} = (0.153 \pm 0.001)$ W·m^{-1}·K^{-1}. However, if the thermal conductivity is calculated by fitting equation (3.93) we obtain $k_{smp} = (0.145 \pm 0.001)$ W·m^{-1}·K^{-1}. As discussed previously both results are comparable due to the low frequency used in the measurement. The low value of the thermal conductivity is an indication of the glassy character of the TPD layers, as confirmed by previous calorimetric measurements that show a clear signature of the glass transition temperature (Figure 7.2).

At the very beginning of the deposition, as shown in Figure 7.1a, there is a decrease in the thermal conductance of 1-2 % of the initial value. Afterwards, G roughly increases linearly with thickness. In this particular sample, film growth was halted at a film thickness of 340 nm, which is evidenced by the constant value of the thermal conductance after this point.

Figure 7.1b,c show in more detail the initial stages of the evolution of G versus thickness for two TPD films deposited at 267 K and 304 K with a low growth rate of 0.02 nm/s. We identify four different regions in Figure 7.1b,c based on the evolution of the conductance with thickness. In region I the overall conductance decreases exponentially. Region II is characterized by a slowdown of the reduction till a minimum and region III contains the subsequent increase of G up to the linear regime of the conductance with thickness that is labelled as region IV. We identify these regions with growth modes of the TPD layers: region I corresponds to nucleation and island growth, region II to island growth and coalescence, region III starts at the onset of percolation through the whole layer along the substrate (percolation threshold) and finally region IV obeys the dynamics of vertical growth of a continuous film. The extent of each of these regions is represented in the figures through the dashed red lines.

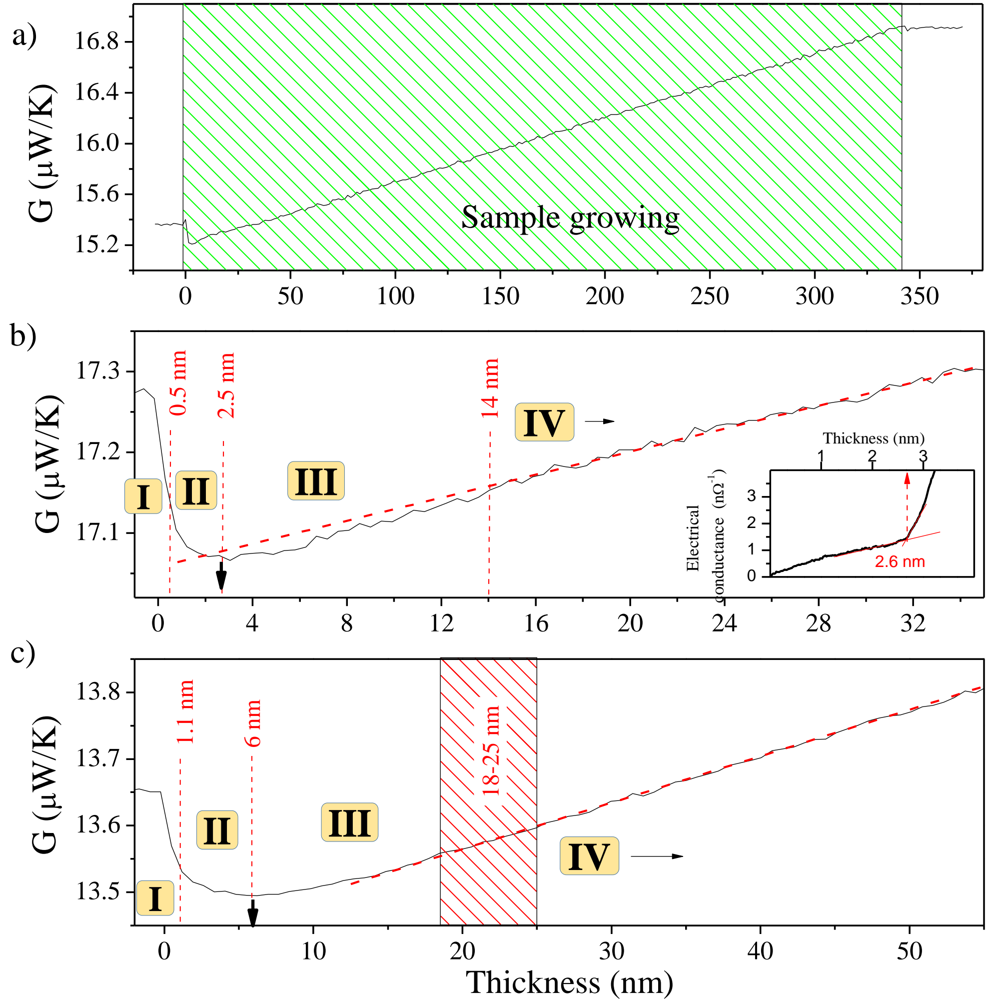

Figure 7.1: Thermal conductance vs thickness during TPD growth: a) T_{dep} = 267±2 K. Growth rate = 0.29 nm/s. b) T_{dep} = 267±2 K. Growth rate = 0.02 nm/s. c) T_{dep} = 304±2 K. Growth rate = 0.02 nm/s. In graphs b) and c) data is box averaged with 10 points/box. The main regions of film growth are separated by dashed red lines. Region I located between 0 nm and the first vertical line correspond to nucleation and isolated island formation; region II to island coalescence; region III to percolation across the layer and region IV to vertical growth of a continuous layer. The slight difference in the initial conductance between all the graphs is mainly due to the use of different sensors/membranes for the experiments. The black downward arrow marks the percolation threshold (separation between regions II and III). The inset of Figure b) shows the abrupt variation of the electrical conductance at the percolation threshold (nominal thickness of 2.5 nm) of the TPD film. This value coincides with the minimum of the thermal conductance (black arrow) in graph b).

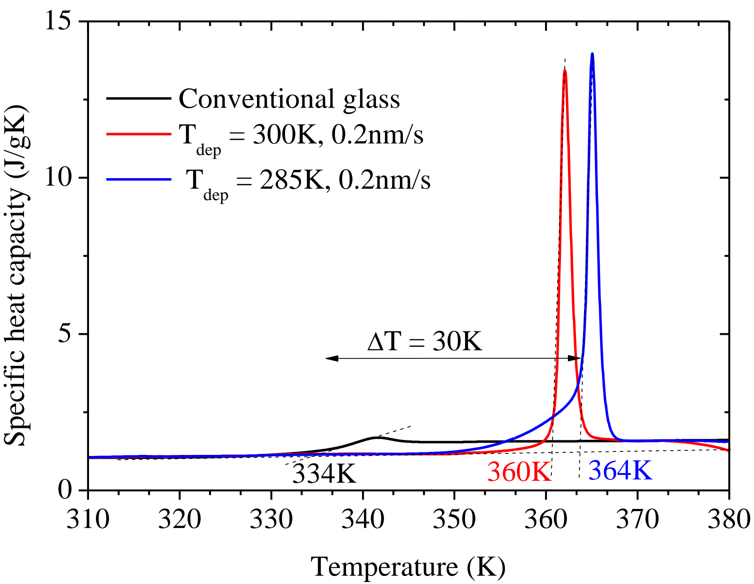

Figure 7.2: Calorimetric curves of TPD samples deposited at different temperatures. They show the peak corresponding to the glass transition, which demonstrates their glassy nature. There is a shift in the onset temperature of the peaks since the sample deposited at a 304 K is less stable and starts the phase change at a lower temperature than the sample deposited at 261 K.

Before examining in detail the conductance vs. thickness curves it is instructive to remark that these glassy organic materials grow following a 3D Volmer-Weber mechanism with isolated islands in the early growth stages. We present evidence of this behavior in Figure 7.3, that shows the presence of isolated islands for a nominal film thickness of 2.6 nm and a continuous layer at 14 nm.

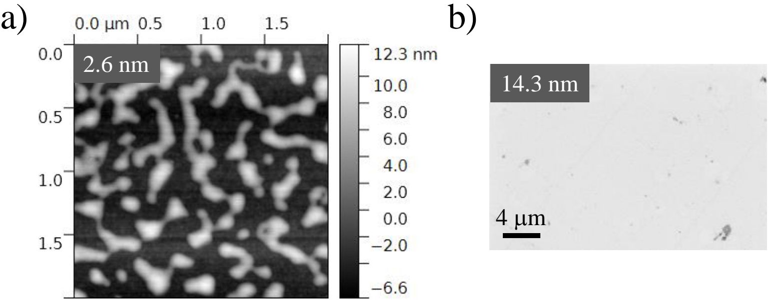

Figure 7.3: a) AFM image of a 2.6 nm thick TPD layer. The use of AFM was necessary to discriminate the material from the background in this discontinuous layer. b) SEM image of a 14.3 nm thick TPD layer showing complete coverage.

However, a thorough analysis of the microstructure evolution using either ex-situ AFM or SEM is precluded by the evidence that dewetting of TPD persists at temperatures well below the glass transition temperature leading to morphological instabilities that evolve over time[198]. This behavior is thought to be related to the enhanced surface mobility of molecular glasses[199]. The fast film dynamics at temperatures in the vicinity of room

temperature below T_g makes in-situ analysis an indispensable tool to gain a better understanding of film formation in molecular glasses.

To analyse the physical origin of the sudden decrease of the thermal conductance in region I, we first rule out any potential artefact that could have led to temperature variations of the sensor: i) it cannot be attributed to a change in the temperature of the sensor during condensation of molecules on the substrate since this extra heat is not modulated at angular frequency ω or any of its harmonics and therefore, does not affect the 3ω component of the voltage; ii) it is neither due to emissivity variations during TPD growth on the membrane, since a measurement at 81 K where radiation effects should be substantially lower shows a similar drop in thermal conductance, as can be seen in Figure 7.4.

At first sight the initial reduction of thermal conductance during the early growth stages of TPD could result surprising since the 180 nm thick SiN_x membrane is already a disordered structure with an average phonon mean free path of the order of the interatomic distance. In this frame, surface modification by an organic molecule should have a minimal impact on the thermal conductance. Previous work by Sultan et al.[88,91] has recently shown that long-phonon modes may still be important in disordered or nanocrystalline SiN_x. These authors measured ex-situ the impact that the growth of metallic layers had on the thermal conductance of a silicon nitride membrane. They observed a decrease of the membrane conductance for small metal thicknesses and a subsequent increase due to the contribution of the growing layer. The behavior was similar for the growth of alumina on top of the membrane.

Our data differs from previous work in several important aspects. First, the magnitude of the conductance drop is much lower and second, our measurements, being carried in-situ with a much higher conductance sensitivity, provide a clear signature of the various growth regimes. The total drop in thermal conductance (although much higher than the uncertainty of the measurement) amounts to only 1.2%, compared to 5-10% in Sultan's work. These authors estimated that 40%-50% of the total G was due to long-wavelength with long mean free path phonons. The estimated average λ-value for these phonons was around 4.5 nm, much higher that thermal phonons at room-temperature that have λ~0.2nm. We believe the main difference with our data arises from the atomic disorder of the silicon nitride membrane.

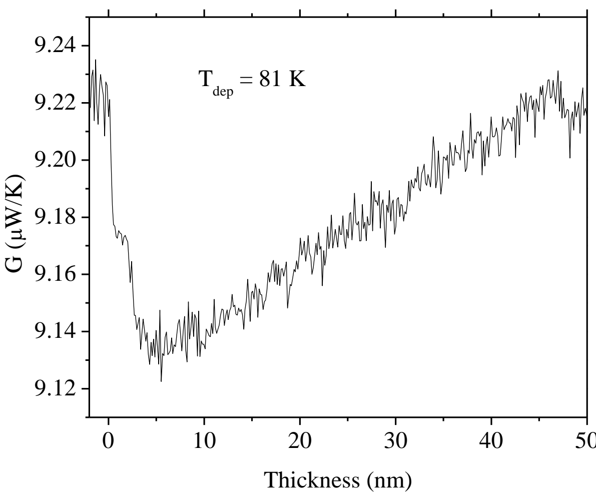

Figure 7.4: Thermal conductance monitored during a TPD deposition at 81 K. The initial reduction discards a change in the thermal emissivity as the cause for it to occur.

The thermal conductivity value of our SiN_x, slightly below the value obtained by Sultan et al.[88,91] and the temperature dependence (Figure 3.27) clearly indicates the nitride grown at IMB-CNM and used in the present work is fully amorphous. Therefore, the lower drop of the thermal conductance of the fully amorphous nitride membrane is consistent with a scenario where the contribution of long-λ phonons is reduced with respect to previous nanocrystalline nitride membranes. Even though, the conductance drop due to enhanced surface scattering requires that phonons slightly larger than the average interatomic distance at room temperature have to be involved in heat transport along the nitride membrane.

We can thus attribute the initial fast decrease of the thermal conductance to the formation of isolated clusters or islands on top of the nitride membrane modifying the interfacial phonon scattering leading to a decrease of the thermal conductance. Although we currently lack a complete understanding of the microscopic processes occurring at the interfaces we believe the growth of new material on top of the membrane changes the specularity of the surface resulting on an effective increase in the phonon scattering rate. We foresee that the future use of crystalline membranes, such a single crystalline Si, will provide a convenient platform to investigate nucleation and island growth dynamics during the early stages of film growth with even higher conductance sensitivity.

Region II starts with a slowdown of the reduction in the thermal conductance. In this thickness range islands start to coalesce providing additional paths for heat transfer through the new material that partially compensate for the interface scattering. Island

coalescence continues and at the conductance minimum percolation builds up new channels across the layer structure (region III) providing additional heat flow paths that start to exceed the contribution of the interface scattering.

The coincidence of the minimum in thermal conductance with the percolation threshold of the TPD layer is demonstrated in the inset of Figure 7.1b. This figure plots the electrical conductance, measured in a separate experiment under identical conditions, as a function of TPD thickness during the growth of a layer on top of the nitride membrane. The sharp variation of the slope at 2.6 nm is due to electrical continuity through the conducting TPD layer and is a clear indication that percolation across the whole structure starts in this thickness range. As percolation persists, the thermal conductance increases reaching a linear regime that we identify with the formation of a continuous layer and marks the onset of region IV. Thus, region IV corresponds to the vertical growth of a continuous film. In this regime the increase in thermal conductance is linear and proportional to the thickness of the growing layer. Compared to the end of region III there is a small reduction in the slope of the conductance vs thickness. The slower increase is produced by the end of percolation since the islands are no longer forming new conductive channels and the conductance changes with a slope imposed by the thermal conductivity of the material.

Figure 7.1b,c highlight the remarkable differences between the growth dynamics at the two temperatures. The TPD sample grown at T_{dep}=267 K shows values of the percolation threshold (black downward arrows) and film continuity at 2.5 nm and 14 nm, respectively. The sample grown at 304 K and therefore embedded with a higher molecular mobility shows a higher value for the percolation threshold, 6 nm. The thickness value for film continuity is located in the region between 18-25 nm but is not clearly resolved from the data. Recent work by Fakhraai and coworkers[198] in TPD films grown at 315K have shown that film continuity was reached for film thickness above 20 nm.

We now focus our attention on the values of the thermal conductivity for the TPD films measured in region IV. At the deposition temperatures employed here both layers are amorphous, as can be seen from the clear glass transition signature shown in the calorimetric traces of Figure 7.2. The in-plane thermal conductivity, k, determined from the slope of the linear region in Figure 7.1a and c by fitting equation (3.93) slightly differs for both samples, k=0.145 $W \cdot m^{-1} \cdot K^{-1}$ (T_{dep}=267K) and 0.132 $W \cdot m^{-1} \cdot K^{-1}$ (T_{dep}=304 K). While the difference only amounts to 10% it is substantially larger than the measurement

uncertainty. We believe the variation is deeply related to the nature of vapor-deposited glasses, in particular to changes of density and molecular orientation at the two deposition temperatures. In the following we provide evidences that support our conclusion.

Vapor-deposited thin-film organic glasses grown at deposition temperatures slightly below their glass transition develop enhanced kinetic and thermodynamic stability with a maximum at T_{dep} in the vicinity of $0.85T_g$[200–203]. Glasses grown in these conditions are coined ultrastable glasses. The glass transition temperature of a conventional glass of TPD (a glass cooled from the liquid at 10 K/min) is 330 K. Glasses grown in the region 0.80-$0.90T_g$ are stable glasses, as evidenced by the higher onset of their glass transition temperature upon heating (Figure 7.2). This figure clearly shows that the glass grown above 300 K is slightly less stable than the ones grown at 0.81-$0.85T_g$. If we translate this behavior to density, it means that the sample grown at 267 K ($0.81T_g$) has a slightly higher density that the one vapor-deposited at 304 K ($0.92T_g$). According to Dalal et al.[204], the difference in density between the 2 samples should be around 0.3%. Another remarkable feature of vapor-deposited stable glasses is that their molecular packing is anisotropic and that molecular orientation depends on the deposition temperature. TPD films grown at $0.82T_g$ have molecules partially aligned parallel to the substrate while those grown at $0.92T_g$ are mostly randomly oriented[204].

Both features, different density and molecular orientation, can be invoked to explain the observed reduction in thermal conductivity of glasses grown at 304 K with respect to those grown at 267 K. The higher density and the in-plane molecular orientation may contribute to a higher thermal conductivity. In the first case it has already been observed that stable glasses embedded with higher density also exhibit higher values of the sound velocity up to 10%[205,206]. It is reasonable to expect that more stable glasses will also exhibit an enhancement of the thermal conductivity. Molecular anisotropy can also play a role since heat transport could be slightly favored in the direction of molecular alignment. More studies of the thermal conductivity variation as a function of deposition temperature are under way to disentangle the effects of density and molecular orientation.

7.3.2 Metallic thin-film layers

We also analyze the thermal conductance variation versus thickness during deposition of an Indium thin film. Figure 7.5a and b show the real-time in-situ measurement of the thermal conductance during growth of this material at two deposition temperatures.

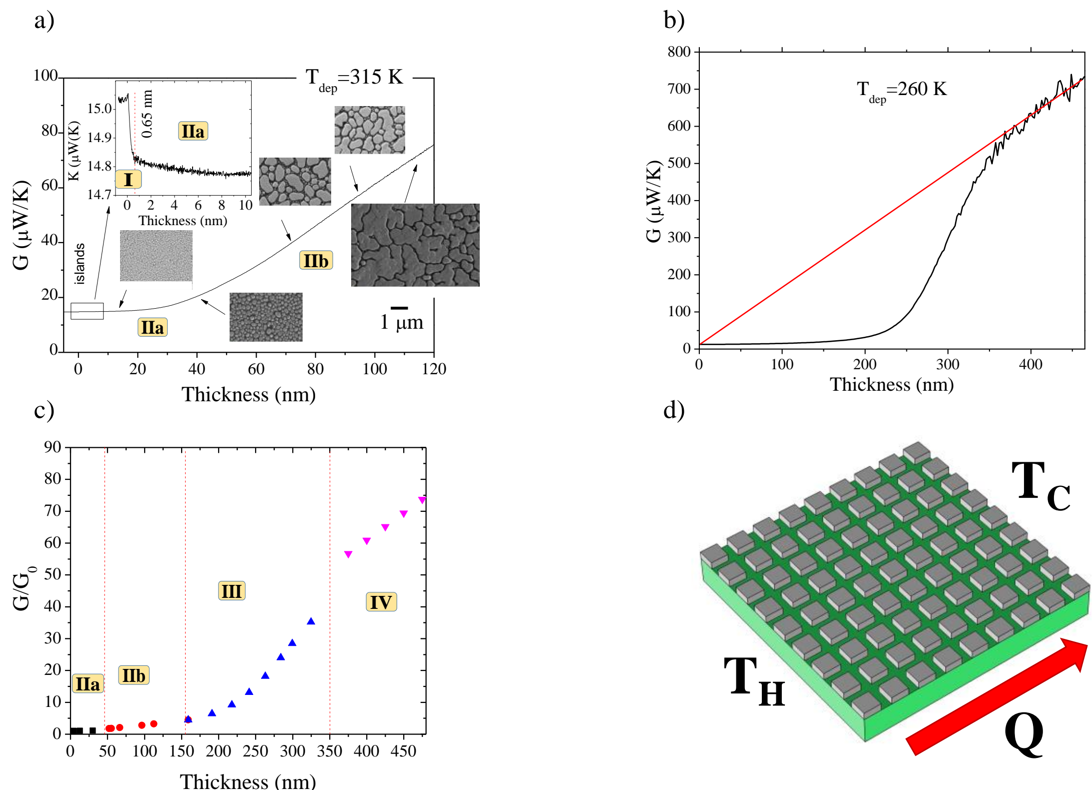

Figure 7.5 Thermal conductance vs thickness during deposition of In films: a) T_{dep}=315 K. The electron microscopy images of films of varying nominal thickness show the microstructural evolution of the In layer. SEM images were measured with a magnification of 100k and an energy of 2 KeV, except the thickest one recorded at 50k. The inset highlights the conductance variation during the early growth stages. b) T_{dep}=260 K. Thickness range is extended to attain complete percolation and coverage (yellow region). c) FEM simulation: normalized conductance vs. In nominal thickness for representative structures with isolated islands and percolated islands as indicated in figure a). The different growth regimes are shown in Roman letters. d) Image of the 3D model, consisting of an array of 9x9 square In islands (grey) on a SiN_x thin film (green).

In both cases, the conductance follows a similar pattern to the one observed in TPD films but with much larger length scales. As shown in Figure 7.5a we identify various regions based on ex-situ microscopy images taken on films of different thickness. As shown in the inset at the very early stages of deposition there is a fast decrease of the conductance as thickness increases. In this thickness range very small isolated islands form on the surface of the SiN_x membrane. The conductance drop amounts to 1.5%, which is again an indication that phonons with mean-free-paths slightly larger than those typically accounted for in disordered solids are being scattered by the In/SiN_x interface. It also suggests, as emphasized before, that the population of these phonons is lower in our

amorphous films compared to the nanocrystalline ones of Sultan et al.[88]. The minimum found here, however, is not correlated with the percolation threshold. In this case, the individual In islands are much more conductive than the TPD ones and although they are still separated at this stage, they contribute significantly to the thermal conduction.

Interestingly, the In grown on the nitride membrane does not reach the percolation threshold through the entire metallic layer even at nominal thickness of 120 nm, as clearly evidenced in the SEM images. This is more clearly shown in Figure 7.5b where growth is prolonged to longer nominal thickness. At thicknesses around 200 nm percolation starts to play a significant role which sharply increases the conductance of the layers due to continuous channels formation. After this, the thermal conductance increase slows down, becoming linear with thickness. The fitting line crosses the origin, meaning that at these thickness values the In layer is already continuous and the thermal conductivity can be evaluated from the slope of the conductance versus thickness, avoiding possible errors that would result from a differential measurement with the empty membrane, as shown in previous studies[88]. The value of k for the continuous In layer is 47 $W \cdot m^{-1} \cdot K^{-1}$, substantially lower than the tabulated value for In, k=83 $W \cdot m^{-1} \cdot K^{-1}$, due to the grain size and boundary effects.

From the images taken by SEM of the In layer at different thicknesses (insets of Figure 7.5a), we extracted the coverage ratio and the mean island area. As indicated in Figure 7.5a,c we can differentiate five growth regimes separated in four stages: I: nucleation and initial small island growth, IIa: growth of small, isolated, islands of almost circular shape, IIb: larger islands with irregular shapes develop leading to a bimodal island distribution, III: island percolation forming continuous channels and IV: vertical growth of a continuous film.

Since the conductance evolution is slightly different than the one previously observed for TPD layers we conduct finite element modelling using the structural information provided by the electron microscopy images. We use a simplified representation of our sample by building an array of 9x9 In square islands on a 180 nm thick SiN_x film (Figure 7.5d). Changing the nominal thickness of the layer implies modulating the size and separation of the islands to match the island size and coverage ratio observed by SEM. Concretely, coverage is calculated as:

$$Coverage = \frac{Covered\ surface}{Total\ surface} \quad (7.1)$$

While the island size is calculated as:

$$size = \sqrt{A_m} \quad (7.2)$$

Where A_m is the island area for which bigger islands cover the same amount of surface than smaller islands. With this data, the nominal thickness of the layer is related to the island size and coverage. In order to tune the coverage from the measured island size, the island separation is varied so that the modeled and observed coverages converge.

The thermal conductance is monitored by imposing a heat flow and measuring the temperature difference arising on the simulated structure. The results of the simulation are shown in Figure 7.5c. The simulation closely predicts the increase of the slope of the curve $G(t_{smp})$ in the thickness range around 30-50 nm. In this thickness range and up to the percolation threshold above 200 nm In islands are still isolated from one another and the increased conductance is due to the formation of larger islands as In evaporation proceeds. At around 200 nm the sudden increase in the slope is related to island percolation. At the end of the percolation regime a continuous film forms and the conductance is heavily dominated by the In film. The conductance increases linearly with a slope given by the thermal conductivity of the film.

7.4 Conclusions

We have presented a versatile and very accurate method to perform real-time in-situ measurements of the thermal conductance of thin layers during film growth. We have shown that phonons are very sensitive to probe the surface state of a SiN_x membrane providing a new tool to monitor the first stages of thin film growth. By analysing the evolution of the thermal conductance versus thickness of two different materials, several different growth stages were identified: First, during the early stages, a fast drop of the thermal conductance is related to nucleation and isolated island formation. This is followed by a regime where island growth through coalescence and absorption of atoms/molecules from the gas phase dominates the variation of the heat conductance with

thickness. At the percolation threshold conductance rises again and once a continuous film is formed the thermal conductance changes linearly with thickness. In this regime the thermal conductivity of the grown layer can be directly derived from the slope of the conductance vs. thickness plot. The methodology presented here, compatible with other substrate materials for epitaxial growth, provides an interesting approach to measure the thermal conductivity of thin films during growth with a high accuracy. Moreover, the use of crystalline membranes will enable even higher sensitivity for real-time monitoring of the early stages of single monolayer growth or nanoparticle formation. Other interesting phenomena such as phase changes during growth, size effects on the thermal conductivity or molecular orientation and density in organic glasses can be analysed from now on.

8. Conclusions

We have developed new approaches to measure the thermal conductance of Si-based nanomaterials with potential interest for heat management and thermoelectric applications.

3 different measurement techniques have been developed along this PhD: i) Suspended structures have been fabricated and deeply analyzed to find the most suitable sample thermal conductance. FEM has been performed to correct errors that appear considering the usual 1D thermal analysis of the structure. ii) The 3ω method has been presented. The generation of the 3ω voltage has been studied in general for any heater and specifically for a metallic strip deposited on a substrate with a thin film, which allows to relate the thermal conductivity of the substrate and the thin film under test with the temperature oscillations of the strip. iii) Finally, the 3ω-Völklein method has been implemented to measure the evolution of the thermal conductance of a growing thin-film. Once again, the sensor has been modeled thermally in order to relate the thermal conductivity of the sample to the measured temperatures. In this case, a novel analysis allows to measure the thermal conductance of the growing sample with a transient measurement by taking into account the evolution of the heat capacity of the system.

The thermal conductivity of ultra-thin Si membranes was measured using suspended structures. The measured thermal conductivity values are vastly reduced compared to the bulk. The temperature dependence in the low-T regime shows a reduced slope due to the relevance of the frequency-dependent boundary scattering term. We have also shown that the suspended membranes can be nanostructured with FIB, producing a generalized amorphization that affects both the Raman spectrum and the membrane thermal conductivity. A systematic study is performed to find the optimal ion dose to nanopattern the membranes by selective doping, finding a spatial resolution of 200 nm when using 50 $\mu C/cm^2$. With this approach, two asymmetric structures are fabricated. None of them show thermal rectification, probably due to their reduced thickness.

Porous Si nanowires have been fabricated and measured using the suspended structures. They show very reduced effective values of the thermal conductivity due to the strong boundary scattering produced by the pores. A clear trend between the conductivity and the diameter is found, which aims to a radius-dependent porosity. The structural Si thermal conductivity is found to be one fiftieth of that of the bulk, promising a good thermoelectric figure of merit.

Novel asymmetric 4-period thick SiGe superlattices have been fabricated and measured. All samples show low values of the thermal conductivity, even below the thin-film alloy limit. This is related to the measured compositional profile, showing that SLs with spread Ge-rich regions and sharp boundaries at the same time effectively scatter phonons of all frequencies. Lattice dynamics simulations predict thermal conductivity values close to the measured ones, confirming the importance of Ge concentration profiles throughout the SL. Finally, the thermal conductivity value of a thicker sample consisting of 16 periods has shown the lack of coherence effects in our samples.

The 3ω-Völklein method is used to measure the thermal conductivity of TPD and In. For the first time, the reduction in the membrane conductance due to enhanced interfacial scattering has been observed in real time. The high sensitivity of the technique enabled to follow the growth dynamics of TPD and In with sub-ML resolution. Different growth modes produce different effects in the conductance values and up to 4 differentiated regimes were identified: nucleation, island growth, percolation and vertical growth. In the case of TPD, the thermal conductivity of the film depends on the deposition temperature. This is related to the different stability and molecular anisotropy of the glassy layers. With respect to In, thanks to ex-situ electron micrographs images, the thermal conductance evolution is compared to a model that takes into account the island size and surface coverage at different growth stages. The good agreement permits to draw solid conclusions on the growth regimes.

9. Bibliography

1. International Energy Agency. Key World Energy Statistics. 1–80 (2014). doi:10.1787/key_energ_stat-2014-en

2. United Nations. Adoption of the Paris Agreement. *Conf. Parties its twenty-first Sess.* **21932,** 32 (2015).

3. Stocker, T. F. *et al. 2013: Technical Summary. In: Climate Change 2013: The Physical Science Basis. Contribution of Working Group I to the Fifth Assessment Report of the Intergovernmental Panel on Climate Change*. *Climate Change 2013: The Physical Science Basis. Contribution of Working Group I to the Fifth Assessment Report of the Intergovernmental Panel on Climate Change* (Cambridge University Press, 2013). doi:10.1017/ CBO9781107415324.005

4. GISTEMP. GISS Surface Temperature Analysis (GISTEMP). (2016). Available at: http://data.giss.nasa.gov/gistemp/. (Accessed: 24th August 2016)

5. Hansen, J., Ruedy, R., Sato, M. & Lo, K. Global surface temperature change. *Rev. Geophys.* **48,** (2010).

6. Keeling, R. CO2 Concentration at Mauna Loa Observatory, Hawaii. Available at: scrippsco2.ucsd.edu/. (Accessed: 24th August 2016)

7. Tans, P. Trends in Atmospheric Carbon Dioxide. *NOAA/ESRL* Available at: www.esrl.noaa.gov/gmd/ccgg/trends/. (Accessed: 24th August 2016)

8. Etheridge, D. M. *et al. Historical CO2 records from the Law Dome DE08, DE08-2, and DSS ice cores. In Trends: A Compendium of Data on Global Change*. (1998).

9. J.H. Laherrère. Learn strengths, weaknesses to understand Hubbert curve. *Oil & Gas Journal* (2000). Available at: http://www.ogj.com/articles/print/volume-98/issue-16/special-report/learn-strengths-weaknesses-to-understand-hubbert-curve.html. (Accessed: 12th April 2016)

10. Sorrell, S. Reducing energy demand: A review of issues, challenges and approaches. *Renew. Sustain. Energy Rev.* **47,** 74–82 (2015).

11. U.S. Energy Information Administration. *Electric Power Annual*. (2016).

12. *Power generation from Coal*. (2010).

13. Fang, X., Misra, S., Xue, G. & Yang, D. Smart Grid — The New and Improved Power Grid: A Survey. *IEEE Commun. Surv. Tutorials* **14,** 944–980 (2012).

14. Davoli, F., Repetto, M., Tornelli, C., Proserpio, G. & Cucchietti, F. Boosting energy efficiency through smart grids. **7,** 80 (2012).

15. United States Environmental Protection Agency. *Light-Duty Automotive*

Technology, Carbon Dioxide Emissions, and Fuel Economy Trends: 1975 Through 2012, EPA-420-R-13-001. (2013).

16. Seebeck, T. J. & Berlin, D. A. der W. zu. *Ueber den Magnetismus der galvanischen Kette*. (1822).

17. Seebeck, T. J. Ueber die magnetische Polarisation der Metalle und Erze durch Temperaturdifferenz. *Ann. Phys.* **82,** 253–286 (1826).

18. Velmre, E. Thomas Johann Seebeck. *Proc. Est. Acad. Sci. Eng.* **13,** 276–282 (2007).

19. Ioffe, A. F. *et al.* Semiconductor Thermoelements and Thermoelectric Cooling. *Phys. Today* **12,** 42 (1959).

20. Hicks, L. & Dresselhaus, M. Effect of quantum-well structures on the thermoelectric figure of merit. *Phys. Rev. B* **47,** 12727–12731 (1993).

21. Biswas, K. *et al.* High-performance bulk thermoelectrics with all-scale hierarchical architectures. *Nature* **489,** 414–418 (2012).

22. Zhao, L. D. *et al.* All-scale hierarchical thermoelectrics: MgTe in PbTe facilitates valence band convergence and suppresses bipolar thermal transport for high performance. *Energy Environ. Sci.* **6,** 3346 (2013).

23. Jou, D., Casas-Vázquez, J. & Lebon, G. *Extended irreversible thermodynamics*. *Extended Irreversible Thermodynamics* (2010). doi:10.1007/978-90-481-3074-0

24. Ziman, J. M. *Electrons and phonons: the theory of transport phenomena in solids*. *Endeavour* **20,** (1960).

25. Chen, G. Nanoscale Energy Transport and Conversion. *Heat Mass Transf.* 531 (2005). doi:10.2221/jcsj.50.53

26. Anderson, C. V. D. R. & Tamma, K. K. An overview of advances in heat conduction models and approaches for prediction of thermal conductivity in thin dielectric films. *Int. J. Numer. Methods Heat Fluid Flow* **14,** 12–65 (2004).

27. Callaway, J. Model for lattice Thermal Conductivity at Low Temperatures. *Phys. Rev.* **113,** 1046–1051 (1959).

28. Guyer, R. A. & Krumhansl, J. A. Thermal Conductivity, Second Sound, and Phonon Hydrodynamic Phenomena in Nonmetallic Crystals. *Phys. Rev.* **148,** 778–788 (1966).

29. de Tomas, C., Cantarero, A., Lopeandia, A. F. & Alvarez, F. X. From kinetic to collective behavior in thermal transport on semiconductors and semiconductor nanostructures. *J. Appl. Phys.* **115,** 164314 (2014).

30. Li, D. *et al.* Thermal conductivity of individual silicon nanowires. *Appl. Phys. Lett.* **83,** 2934–2936 (2003).

31. Snyder, G. J. & Toberer, E. S. Complex thermoelectric materials. *Nat. Mater.* **7,** 105–114 (2008).

32. Christensen, M., Johnsen, S. & Iversen, B. B. Thermoelectric clathrates of type I. *Dalt. Trans.* **39,** 978–992 (2010).

33. Saramat, A. *et al.* Large thermoelectric figure of merit at high temperature in Czochralski-grown clathrate Ba8Ga16Ge30. *J. Appl. Phys.* **99,** 23708 (2006).

34. Nolas, G. S., Cohn, J. L. & Slack, G. A. Effect of partial void filling on the lattice thermal conductivity of skutterudites. *Phys. Rev. B* **58,** 164–170 (1998).

35. Rowe, D. M. Thermoelectrics handbook: macro to nano. *Thermoelectr. Handb. Macro to Nano* **80,** 1014 (2005).

36. Nielsen, M. D., Ozolins, V. & Heremans, J. P. Lone pair electrons minimize lattice thermal conductivity. *Energy Environ. Sci.* **6,** 570–578 (2013).

37. Quintela, C. X., Rodríguez-González, B. & Rivadulla, F. Thermoelectric properties of heavy-element doped CrN. *Appl. Phys. Lett.* **104,** 22103 (2014).

38. Liu, H. *et al.* Ultrahigh Thermoelectric Performance by Electron and Phonon Critical Scattering in Cu2 Se1-x Ix. *Adv. Mater.* **25,** 6607–6612 (2013).

39. Davies, J. *The Physics of Low-Dimensional Semiconductors. Cambridge University Press* **Cambridge,** (1998).

40. Bach, P. L. *et al.* Tuning the thermoelectric properties of SrTiO3 by controlled oxygen doping. (2012).

41. Heremans, J. P. *et al.* Enhancement of thermoelectric efficiency in PbTe by distortion of the electronic density of states. *Science* **321,** 554–7 (2008).

42. Asheghi, M., Leung, Y. K., Wong, S. S. & Goodson, K. E. Phonon-boundary scattering in thin silicon layers. *Appl. Phys. Lett.* **71,** 1798–1800 (1997).

43. Muñoz Rojo, M. *et al.* Fabrication of Bi2Te3 nanowire arrays and thermal conductivity measurement by 3ω-scanning thermal microscopy. *J. Appl. Phys.* **113,** 54308 (2013).

44. Cecchi, S. *et al.* Ge/SiGe superlattices for thermoelectric energy conversion devices. *J. Mater. Sci.* **48,** 2829–2835 (2013).

45. Liu, C. K. *et al.* Thermal conductivity of Si/SiGe superlattice films. *J. Appl. Phys.* **104,** (2008).

46. Chen, P. *et al.* Role of surface-segregation-driven intermixing on the thermal transport through planar Si/Ge superlattices. *Phys. Rev. Lett.* **111,** (2013).

47. Poudel, B. *et al.* High-thermoelectric performance of nanostructured bismuth antimony telluride bulk alloys. *Science* **320,** 634–8 (2008).

48. Zhu, G. H. *et al.* Increased Phonon Scattering by Nanograins and Point Defects in Nanostructured Silicon with a Low Concentration of Germanium. *Phys. Rev. Lett.* **102,** 196803 (2009).

49. Biswas, K. *et al.* Strained endotaxial nanostructures with high thermoelectric figure of merit. *Nat. Chem.* **3,** 160–166 (2011).

50. Kwon, S., Wingert, M. C., Zheng, J., Xiang, J. & Chen, R. Thermal transport in Si and Ge nanostructures in the 'confinement' regime. *Nanoscale* **8,** 13155–13167 (2016).

51. Wingert, M. C. *et al.* Sub-Amorphous Thermal Conductivity in Ultra-Thin

Crystalline Silicon Nanotubes. *Nano Lett.* **15,** 2605–2611 (2015).

52. Hicks, L. D. & Dresselhaus, M. S. Thermoelectric figure of merit of a one-dimensional conductor. *Phys. Rev. B* **47,** 16631–16634 (1993).

53. Lim, J., Hippalgaonkar, K., Andrews, S. C., Majumdar, A. & Yang, P. Quantifying surface roughness effects on phonon transport in silicon nanowires. *Nano Lett.* **12,** 2475–82 (2012).

54. Heron, J. S., Fournier, T., Mingo, N. & Bourgeois, O. Mesoscopic size effects on the thermal conductance of silicon nanowire. *Nano Lett.* **9,** 1861–1865 (2009).

55. Mingo, N. Calculation of Si nanowire thermal conductivity using complete phonon dispersion relations. *Phys. Rev. B* **68,** 113308 (2003).

56. Mingo, N., Yang, L., Li, D. & Majumdar, A. Predicting the Thermal Conductivity of Si and Ge Nanowires. *Nano Lett.* **3,** 1713–1716 (2003).

57. Soffer, S. B. Statistical Model for the Size Effect in Electrical Conduction. *J. Appl. Phys.* **38,** 1710 (1967).

58. Malhotra, A. & Maldovan, M. Impact of Phonon Surface Scattering on Thermal Energy Distribution of Si and SiGe Nanowires. *Sci. Rep.* **6,** 25818 (2016).

59. Pan, Y. *et al.* Significant thermal conductivity reduction of silicon nanowire forests through discrete surface doping of germanium. *Appl. Phys. Lett.* **106,** 93102 (2015).

60. Zhang, X., Hu, M., Giapis, K. P. & Poulikakos, D. Schemes for and Mechanisms of Reduction in Thermal Conductivity in Nanostructured Thermoelectrics. *J. Heat Transfer* **134,** 102402 (2012).

61. Wingert, M. C. *et al.* Thermal Conductivity of Ge and Ge–Si Core–Shell Nanowires in the Phonon Confinement Regime. *Nano Lett.* **11,** 5507–5513 (2011).

62. Maldovan, M. Sound and heat revolutions in phononics. *Nature* **503,** 209–17 (2013).

63. Gorishnyy, T., Ullal, C. K., Maldovan, M., Fytas, G. & Thomas, E. L. Hypersonic Phononic Crystals. *Phys. Rev. Lett.* **94,** 115501 (2005).

64. Yu, J.-K., Mitrovic, S., Tham, D., Varghese, J. & Heath, J. R. Reduction of thermal conductivity in phononic nanomesh structures. *Nat Nano* **5,** 718–721 (2010).

65. Trang Nghiêm, T. T. & Chapuis, P.-O. Phononic thermal resistance due to a finite periodic array of nano-scatterers. *J. Appl. Phys.* **120,** 44305 (2016).

66. Kim, J., Lee, S., Brovman, Y. M., Kim, P. & Lee, W. Diameter-dependent thermoelectric figure of merit in single-crystalline Bi nanowires. *Nanoscale* **7,** 5053–9 (2015).

67. Muñoz-Rojo, M., Caballero-Calero, O., Lopeandia, A. F., Rodriguez-Viejo, J. & Martin-Gonzalez, M. Review on measurement techniques of transport properties of nanowires. *Nanoscale* **5,** 11526–11544 (2013).

68. Li, Z., Bae, M. H. & Pop, E. Substrate-supported thermometry platform for nanomaterials like graphene, nanotubes, and nanowires. *Appl. Phys. Lett.* **105,** 1–

6 (2014).

69. Shi, L. *et al.* Measuring thermal and thermoelectric properties of one-dimensional nanostructures using a microfabricated device. *J. Heat Transfer* **125,** 881–888 (2003).

70. Kim, J., Ou, E., Sellan, D. P. & Shi, L. A four-probe thermal transport measurement method for nanostructures. *Rev. Sci. Instrum.* **86,** 44901 (2015).

71. Moore, A. L. & Shi, L. On errors in thermal conductivity measurements of suspended and supported nanowires using micro-thermometer devices from low to high temperatures. *Meas. Sci. Technol.* **22,** 15103 (2011).

72. Wingert, M. C., Chen, Z. C. Y., Kwon, S., Xiang, J. & Chen, R. Ultra-sensitive thermal conductance measurement of one-dimensional nanostructures enhanced by differential bridge. *Rev. Sci. Instrum.* **83,** 24901–24907 (2012).

73. Zhang, X. *et al.* Thermal and electrical conductivity of a suspended platinum nanofilm. *Appl. Phys. Lett.* **86,** 171912–171913 (2005).

74. Ferrando-Villalba, P. *et al.* In-plane thermal conductivity of sub-20 nm thick suspended mono-crystalline Si layers. *Nanotechnology* **25,** 185402 (2014).

75. Kim, P., Shi, L., Majumdar, A. & McEuen, P. L. Thermal transport measurements of individual multiwalled nanotubes. *Phys. Rev. Lett.* **87,** 215502 (2001).

76. Alvarez-Quintana, J. & Rodriguez-Viejo, J. Extension of the 3ω method to measure the thermal conductivity of thin films without a reference sample. *Sensors Actuators A Phys.* **142,** 232–236 (2008).

77. Ju, Y. S. Phonon heat transport in silicon nanostructures. *Appl. Phys. Lett.* **87,** 153103–153106 (2005).

78. Hao, Z. *et al.* Thermal conductivity measurements of ultra-thin single crystal silicon films using improved structure. in *2006 8th International Conference on Solid-State and Integrated Circuit Technology Proceedings* 2196–2198 (IEEE, 2006). doi:10.1109/ICSICT.2006.306679

79. Ju, Y. S. & Goodson, K. E. Phonon scattering in silicon films with thickness of order 100 nm. *Appl. Phys. Lett.* **74,** 3005–3007 (1999).

80. Liu, W. & Asheghi, M. Thermal conductivity measurements of ultra-thin single crystal silicon layers. *J. Heat Transfer* **128,** 75–83 (2006).

81. Liu, D., Xie, R., Yang, N., Li, B. & Thong, J. T. L. Profiling nanowire thermal resistance with a spatial resolution of nanometers. *Nano Lett.* **14,** 806–12 (2014).

82. Cahill, D. G. Thermal conductivity measurement from 30 to 750 K: the 3ω method. *Rev. Sci. Instrum.* **61,** 802 (1990).

83. Tong, T. & Majumdar, A. Reexamining the 3-omega technique for thin film thermal characterization. *Rev. Sci. Instrum.* **77,** 104902 (2006).

84. Sikora, A. *et al.* Highly sensitive thermal conductivity measurements of suspended membranes (SiN and diamond) using a 3ω-Völklein method. *Rev. Sci. Instrum.* **83,** 54902 (2012).

85. Spiegel, Murray R.; Liu, John; Abellanas, L. *Fórmulas y tablas de Matemática aplicada*. (McGraw-Hill, 2005).

86. Lee, S. M. & Kwun, S. L. Heat capacity measurement of dielectric solids using a linear surface heater: Application to ferroelectrics. *Rev. Sci. Instrum.* **65,** 966–970 (1994).

87. Lee, S.-M. & Cahill, D. G. Heat transport in thin dielectric films. *J. Appl. Phys.* **81,** 2590 (1997).

88. Sultan, R. *et al.* Heat transport by long mean free path vibrations in amorphous silicon nitride near room temperature. *Phys. Rev. B* **87,** 214305 (2013).

89. Völklein, F. & Starz, T. Thermal conductivity of thin films-experimental methods and theoretical interpretation. *XVI ICT '97. Proc. ICT'97. 16th Int. Conf. Thermoelectr. (Cat. No.97TH8291)* (1997). doi:10.1109/ICT.1997.667630

90. Sikora, A. *et al.* Erratum: 'Highly sensitive thermal conductivity measurements of suspended membranes (SiN and diamond) using a 3ω-Völklein method' [Rev. Sci. Instrum. 83, 054902 (2012)]. *Rev. Sci. Instrum.* **84,** 29901 (2013).

91. Sultan, R., Avery, A. D., Stiehl, G. & Zink, B. L. Thermal conductivity of micromachined low-stress silicon-nitride beams from 77 to 325 K. *J. Appl. Phys.* **105,** 43501 (2009).

92. Pop, E. Energy dissipation and transport in nanoscale devices. *Nano Res.* **3,** 147–169 (2010).

93. Peng, K. Q. *et al.* Aligned single-crystalline Si nanowire arrays for photovoltaic applications. *Small* **1,** 1062–1067 (2005).

94. Kelzenberg, M. D. *et al.* Photovoltaic measurements in single-nanowire silicon solar cells. *Nano Lett.* **8,** 710–714 (2008).

95. Garnett, E. C. & Yang, P. Silicon nanowire radial p-n junction solar cells. *J. Am. Chem. Soc.* **130,** 9224–9225 (2008).

96. Lee, K.-N. *et al.* Fabrication of suspended silicon nanowire arrays. *Small* **4,** 642–648 (2008).

97. Martinez, J., Martinez, R. V & Garcia, R. Silicon Nanowire Transistors with a Channel Width of 4 nm Fabricated by Atomic Force Microscope Nanolithography. *Nano Lett.* **8,** 3636–3639 (2008).

98. Jin, S. *et al.* Scalable interconnection and integration of nanowire devices without registration. *Nano Lett.* **4,** 915–919 (2004).

99. Cui, Y., Zhong, Z. H., Wang, D. L., Wang, W. U. & Lieber, C. M. High performance silicon nanowire field effect transistors. *Nano Lett.* **3,** 149–152 (2003).

100. Melosh, N. A. *et al.* Ultrahigh-density nanowire lattices and circuits. *Science (80-.).* **300,** 112–115 (2003).

101. Liu, W. & Asheghi, M. Phonon–boundary scattering in ultrathin single-crystal silicon layers. *Appl. Phys. Lett.* **84,** 3819–3821 (2004).

102. Zhang, H. *et al.* Measurement of thermal conductivity of ultra-thin single crystal silicon film using symmetric structure. *Bandaoti Xuebao(Chinese J. Semicond.* **27,** 1961–1965 (2006).

103. Chávez-Ángel, E. *et al.* Reduction of the thermal conductivity in free-standing silicon nano-membranes investigated by non-invasive Raman thermometry. *APL Mater.* **2,** 12113 (2014).

104. Neogi, S. *et al.* Tuning Thermal Transport in Ultrathin Silicon Membranes by Surface Nanoscale Engineering. *ACS Nano* **9,** 3820–3828 (2015).

105. Li, D., Wu, Y., Fan, R., Yang, P. & Majumdar, A. Thermal conductivity of Si/SiGe superlattice nanowires. *Appl. Phys. Lett.* **83,** 3186–3188 (2003).

106. Chen, R. *et al.* Thermal conductance of thin silicon nanowires. *Phys. Rev. Lett.* **101,** 105501 (2008).

107. Zink, B. L., Pietri, R. & Hellman, F. Thermal conductivity and specific heat of thin-film amorphous silicon. *Phys. Rev. Lett.* **96,** 55902 (2006).

108. Uma, S., McConnell, A. D., Asheghi, M., Kurabayashi, K. & Goodson, K. E. Temperature-dependent thermal conductivity of undoped polycrystalline silicon layers. *Int. J. Thermophys.* **22,** 605–616 (2001).

109. Mavrokefalos, A., Pettes, M. T., Zhou, F. & Shi, L. Four-probe measurements of the in-plane thermoelectric properties of nanofilms. *Rev. Sci. Instrum.* **78,** 34901–34906 (2007).

110. Liang, L. & Li, B. Size-dependent thermal conductivity of nanoscale semiconducting systems. *Phys. Rev. B* **73,** 153303 (2006).

111. Asheghi, M., Touzelbaev, M. N., Goodson, K. E., Leung, Y. K. & Wong, S. S. Temperature-Dependent Thermal Conductivity of Single-Crystal Silicon Layers in SOI Substrates. *J. Heat Transfer* **120,** 30 (1998).

112. Lee, J., Lim, J. & Yang, P. Ballistic Phonon Transport in Holey Silicon. *Nano Lett.* (2015). doi:10.1021/acs.nanolett.5b00495

113. Hippalgaonkar, K. *et al.* Fabrication of microdevices with integrated nanowires for investigating low-dimensional phonon transport. *Nano Lett.* **10,** 4341–8 (2010).

114. Hone, J. *et al.* Quantized phonon spectrum of single-wall carbon nanotubes. *Science* **289,** 1730–3 (2000).

115. Murphy, P. G. & Moore, J. E. Coherent phonon scattering effects on thermal transport in thin semiconductor nanowires. *Phys. Rev. B* **76,** 155313 (2007).

116. Lee, J. *et al.* Thermal Transport in Silicon Nanowires at High Temperature up to 700 K. *Nano Lett.* (2016). doi:10.1021/acs.nanolett.6b00956

117. Tritt, T. M. *Thermal Conductivity: Theory, Properties, and Applications*. *Journal of Chemical Information and Modeling* **53,** (2004).

118. Kim, Y. K., Danner, A. J., Raftery, J. J. & Choquette, K. D. Focused ion beam nanopatterning for optoelectronic device fabrication. *Sel. Top. Quantum Electron. IEEE J.* **11,** 1292–1298 (2005).

119. Lehrer, C. *et al.* Defects and gallium-contamination during focused ion beam micro machining. in *2000 International Conference on Ion Implantation Technology Proceedings. Ion Implantation Technology - 2000 (Cat. No.00EX432)* 695–698 (IEEE, 2000). doi:10.1109/.2000.924248

120. Gamo, K. Recent advances of focused ion beam technology. *Nucl. Instruments Methods Phys. Res. Sect. B Beam Interact. with Mater. Atoms* **121,** 464–469 (1997).

121. Gamo, K. Nanofabrication by FIB. *Microelectron. Eng.* **32,** 159–171 (1996).

122. Goettler, D. F. *et al.* Realization of a 33 GHz phononic crystal fabricated in a freestanding membrane. *AIP Adv.* **1,** (2011).

123. Cahill, D. G., Watson, S. K. & Pohl, R. O. Lower limit to the thermal conductivity of disordered crystals. *Phys. Rev. B* **46,** 6131 (1992).

124. Okada T. Iwaki, and H. Kasahara, T. Probing the Crystallinity of Evaporated Silicon Films by Raman Scattering. *Jpn. J. Appl. Phys.* **24,** 161–165 (1985).

125. Murphy, K. F., Piccione, B., Zanjani, M. B., Lukes, J. R. & Gianola, D. S. Strain- and defect-mediated thermal conductivity in silicon nanowires. *Nano Lett.* **14,** 3785–92 (2014).

126. B.A. Boxall. A change of etch rate associated with the amorphous to crystalline transition in CVD layers of silicon. *Solid. State. Electron.* **20,** 873–874 (1977).

127. Dong, Y. Thermal rectification based on phonon hydrodynamics and thermomass theory. *Commun. Appl. Ind. Math.* **7,** 26–38 (2016).

128. Dames, C. Solid-State Thermal Rectification With Existing Bulk Materials. *J. Heat Transfer* **131,** 61301 (2009).

129. C. W. Chang, D. Okawa, A. Majumdar, A. Z. Solid-State thermal rectifier. *Science (80-.).* **314,** 1121–1124 (2006).

130. Grauby, S., Puyoo, E., Rampnoux, J.-M., Rouvière, E. & Dilhaire, S. Si and SiGe Nanowires: Fabrication Process and Thermal Conductivity Measurement by 3ω-Scanning Thermal Microscopy. *J. Phys. Chem. C* **117,** 9025–9034 (2013).

131. Hsiao, T.-K. *et al.* Observation of room-temperature ballistic thermal conduction persisting over 8.3 µm in SiGe nanowires. *Nat. Nanotechnol.* **8,** 534–8 (2013).

132. Ma, J. *et al.* Coherent phonon-grain boundary scattering in silicon inverse opals. *Nano Lett.* **13,** 618–24 (2013).

133. Boukai, A. I. *et al.* Silicon nanowires as efficient thermoelectric materials. *Nature* **451,** 168–171 (2008).

134. Hochbaum, A. I. *et al.* Enhanced thermoelectric performance of rough silicon nanowires. *Nature* **451,** 163–167 (2008).

135. Moore, A. L., Saha, S. K., Prasher, R. S., Shi, L. & Prasher. Phonon backscattering and thermal conductivity suppression in sawtooth nanowires. *Appl. Phys. Lett.* **93,** 83112 (2008).

136. Alvarez, F. X., Jou, D. & Sellitto, A. Pore-size dependence of the thermal

conductivity of porous silicon: A phonon hydrodynamic approach. *Appl. Phys. Lett.* **97,** 33103 (2010).

137. Sellitto, A., Cimmelli, V. A. & Jou, D. in 91–108 (Springer International Publishing, 2016). doi:10.1007/978-3-319-27206-1_4

138. Gesele, G., Linsmeier, J., Drach, V., Fricke, J. & Arens-Fischer, R. Temperature-dependent thermal conductivity of porous silicon. *J. Phys. D. Appl. Phys.* **30,** 2911–2916 (1997).

139. Hashin, Z. & Shtrikman, S. A Variational approach to the theory of the effective magnetic permeability of multiphase materials. *J. Appl. Phys.* **33,** 3125–3131 (1962).

140. Smith, D. S. *et al.* Thermal conductivity of porous materials. *J. Mater. Res.* **28,** 2260–2272 (2013).

141. Huang, Z., Geyer, N., Werner, P., De Boor, J. & Gösele, U. Metal-assisted chemical etching of silicon: A review. *Adv. Mater.* **23,** 285–308 (2011).

142. Zhang, T., Wu, S., Xu, J., Zheng, R. & Cheng, G. High thermoelectric figure-of-merits from large-area porous silicon nanowire arrays. *Nano Energy* **13,** 433–441 (2015).

143. Wolkin, M. V., Jorne, J., Fauchet, P. M., Allan, G. & Delerue, C. Electronic States and Luminescence in Porous Silicon Quantum Dots: The Role of Oxygen. *Phys. Rev. Lett.* **82,** 197–200 (1999).

144. Lee, S. M. & Cahill, D. G. Heat transport in thin dielectric films. *J. Appl. Phys.* **81,** 2590 (1997).

145. Weisse, J. M. *et al.* Thermal conductivity in porous silicon nanowire arrays. *Nanoscale Res. Lett.* **7,** 554 (2012).

146. Curtin, B. M., Fang, E. W. & Bowers, J. E. Highly Ordered Vertical Silicon Nanowire Array Composite Thin Films for Thermoelectric Devices. *J. Electron. Mater.* **41,** 887–894 (2012).

147. Bin Xu, Khouri, W. & Fobelets, K. Two-Sided Silicon Nanowire Array/Bulk Thermoelectric Power Generator. *IEEE Electron Device Lett.* **35,** 596–598 (2014).

148. Abramson, A. R. *et al.* Fabrication and Characterization of a Nanowire/Polymer-Based Nanocomposite for a Prototype Thermoelectric Device. *J. Microelectromechanical Syst.* **13,** 505–513 (2004).

149. Asheghi, M., Kurabayashi, K., Kasnavi, R. & Goodson, K. E. Thermal conduction in doped single-crystal silicon films. *J. Appl. Phys.* **91,** 5079 (2002).

150. Jean, V., Fumeron, S., Termentzidis, K., Tutashkonko, S. & Lacroix, D. Monte Carlo simulations of phonon transport in nanoporous silicon and germanium. *J. Appl. Phys.* **115,** 24304 (2014).

151. Tarkhanyan, R. H. & Niarchos, D. G. Reduction in lattice thermal conductivity of porous materials due to inhomogeneous porosity. *Int. J. Therm. Sci.* **67,** 107–112 (2013).

152. Wang, Z. L. Energy harvesting for self-powered nanosystems. *Nano Res.* **1,** 1–8

(2008).

153. Terraneo, M., Peyrard, M. & Casati, G. Controlling the energy flow in nonlinear lattices: a model for a thermal rectifier. *Phys. Rev. Lett.* **88,** 94302 (2002).

154. Li, B., Wang, L. & Casati, G. Thermal Diode: Rectification of Heat Flux. *Phys. Rev. Lett.* **93,** 184301 (2004).

155. Zeng, N. & Wang, J.-S. Mechanisms causing thermal rectification: The influence of phonon frequency, asymmetry, and nonlinear interactions. *Phys. Rev. B* **78,** 24305 (2008).

156. Tamura, S. & Ogawa, K. Thermal rectification in nonmetallic solid junctions: Effect of Kapitza resistance. *Solid State Commun.* **152,** 1906–1911 (2012).

157. Pereira, E. & Ávila, R. R. Increasing thermal rectification: Effects of long-range interactions. *Phys. Rev. E* **88,** 32139 (2013).

158. Jou, D., Carlomagno, I. & Cimmelli, V. A. *Rectification of low-frequency thermal waves in graded SicGe1−c. Physics Letters A* **380,** (2016).

159. Machrafi, H., Lebon, G. & Jou, D. Thermal rectifier efficiency of various bulk–nanoporous silicon devices. *Int. J. Heat Mass Transf.* **97,** 603–610 (2016).

160. Hu, M., Keblinski, P. & Li, B. Thermal rectification at silicon-amorphous polyethylene interface. *Appl. Phys. Lett.* **92,** 211908 (2008).

161. Samarelli, A. *et al.* The thermoelectric properties of Ge/SiGe based superlattices: From materials to Energy Harvesting Modules. in *ECS Transactions* **64,** 929–937 (2014).

162. Lee, S.-M., Cahill, D. G. & Venkatasubramanian, R. Thermal conductivity of Si–Ge superlattices. *Appl. Phys. Lett.* **70,** 2957 (1997).

163. Borca-Tasciuc, T. *et al.* Thermal conductivity of symmetrically strained Si/Ge superlattices. *Superlattices Microstruct.* **28,** 199–206 (2000).

164. Huxtable, S. T. *et al.* Thermal conductivity of Si/SiGe and SiGe/SiGe superlattices. *Appl. Phys. Lett.* **80,** 1737–1739 (2002).

165. Kiselev, A. A., Kim, K. W. & Stroscio, M. A. Thermal conductivity of Si/Ge superlattices: A realistic model with a diatomic unit cell. *Phys. Rev. B* **62,** 6896–6899 (2000).

166. Broido, D. A. & Reinecke, T. L. Lattice thermal conductivity of superlattice structures. *Phys. Rev. B - Condens. Matter Mater. Phys.* **70,** (2004).

167. Garg, J., Bonini, N. & Marzari, N. High thermal conductivity in short-period superlattices. *Nano Lett.* **11,** 5135–5141 (2011).

168. Savic, I., Donadio, D., Gygi, F. & Galli, G. Dimensionality and heat transport in Si-Ge superlattices. *Appl. Phys. Lett.* **102,** (2013).

169. Alvarez, F. X., Alvarez-Quintana, J., Jou, D. & Viejo, J. R. Analytical expression for thermal conductivity of superlattices. *J. Appl. Phys.* **107,** (2010).

170. Chakraborty, S. *et al.* Thermal conductivity in strain symmetrized Si/Ge superlattices on Si(111). *Appl. Phys. Lett.* **83,** 4184 (2003).

171. Pernot, G. *et al.* Precise control of thermal conductivity at the nanoscale through individual phonon-scattering barriers. *Nat. Mater.* **9,** 491–495 (2010).

172. Cheaito, R. *et al.* Experimental investigation of size effects on the thermal conductivity of silicon-germanium alloy thin films. *Phys. Rev. Lett.* **109,** (2012).

173. Cahill, D. G., Katiyar, M. & Abelson, J. R. Thermal Conductivity of a-Si:H Thin Films. *Physical Review B* **50,** 6077–6081 (1994).

174. Roberts, N. A. & Walker, D. G. A review of thermal rectification observations and models in solid materials. *Int. J. Therm. Sci.* **50,** 648–662 (2011).

175. Li, B., Lan, J. & Wang, L. Interface Thermal Resistance between Dissimilar Anharmonic Lattices. *Phys. Rev. Lett.* **95,** 104302 (2005).

176. Wang, J., Pereira, E. & Casati, G. Thermal rectification in graded materials. *Phys. Rev. E* **86,** 10101 (2012).

177. Zhylik, A. *et al.* High-resolution x-ray diffraction investigation of relaxation and dislocations in SiGe layers grown on (001), (011), and (111) Si substrates. *J. Appl. Phys.* **109,** (2011).

178. Watling, J. R. & Paul, D. J. A study of the impact of dislocations on the thermoelectric properties of quantum wells in the Si/SiGe materials system. *J. Appl. Phys.* **110,** 114508 (2011).

179. Wang, Z., Alaniz, J. E., Jang, W., Garay, J. E. & Dames, C. Thermal Conductivity of Nanocrystalline Silicon: Importance of Grain Size and Frequency-Dependent Mean Free Paths. *Nano Lett.* **11,** 2206–2213 (2011).

180. Alvarez-Quintana, J. *et al.* Cross-plane thermal conductivity reduction of vertically uncorrelated Ge/Si quantum dot superlattices. *Appl. Phys. Lett.* **93,** 13112 (2008).

181. Joshi, G. *et al.* Enhanced thermoelectric figure-of-merit in nanostructured p-type silicon germanium bulk alloys. *Nano Lett.* **8,** 4670–4674 (2008).

182. Lin, K.-H. & Strachan, A. Thermal transport in SiGe superlattice thin films and nanowires: Effects of specimen and periodic lengths. *Phys. Rev. B* **87,** 115302 (2013).

183. Duchemin, I. & Donadio, D. Atomistic calculation of the thermal conductance of large scale bulk-nanowire junctions. *Phys. Rev. B* **84,** 115423 (2011).

184. Floro, J. A., Chason, E. & Lee, S. R. Real Time Measurement of Epilayer Strain Using a Simplified Wafer Curvature Technique. *MRS Proc.* **406,** 491 (1995).

185. An, I., Nguyen, H. V., Nguyen, N. V. & Collins, R. W. Microstructural evolution of ultrathin amorphous silicon films by real-time spectroscopic ellipsometry. *Phys. Rev. Lett.* **65,** 2274–2277 (1990).

186. You, H., Chiarello, R. P., Kim, H. K. & Vandervoort, K. G. X-ray reflectivity and scanning-tunneling-microscope study of kinetic roughening of sputter-deposited gold films during growth. *Phys. Rev. Lett.* **70,** 2900–2903 (1993).

187. Dendooven, J. *et al.* Atomic layer deposition-based tuning of the pore size in mesoporous thin films studied by in situ grazing incidence small angle X-ray scattering. *Nanoscale* **6,** 14991–14998 (2014).

188. Yeom, H. W. *et al.* Initial stage growth of In and A1 on a single-domain Si(001)2 × 1 surface. *Surf. Sci.* **341,** 328–334 (1995).

189. Schwartzkopf, M. *et al.* From atoms to layers: in situ gold cluster growth kinetics during sputter deposition. *Nanoscale* **5,** 5053 (2013).

190. Schuisky, M., Elam, J. W. & George, S. M. In situ resistivity measurements during the atomic layer deposition of ZnO and W thin films. *Appl. Phys. Lett.* **81,** 180 (2002).

191. Colin, J. J. *et al.* A load-lock compatible system for in situ electrical resistivity measurements during thin film growth. *Rev. Sci. Instrum.* **87,** 23902 (2016).

192. Pei, Y., Wang, H. & Snyder, G. J. Band engineering of thermoelectric materials. *Adv. Mater.* **24,** 6125–35 (2012).

193. Hong, M. *et al.* Enhancing thermoelectric performance of Bi2Te3-based nanostructures through rational structure design. *Nanoscale* **8,** 8681–8686 (2016).

194. Cahill, D. G. Analysis of heat flow in layered structures for time-domain thermoreflectance. *Rev. Sci. Instrum.* **75,** 5119–5122 (2004).

195. Völklein, F. Thermal conductivity and diffusivity of a thin film SiO2/Si3N4 sandwich system. *Thin Solid Films* **188,** 27–33 (1990).

196. Koh, Y. K. *et al.* Comparison of the 3ω method and time-domain thermoreflectance for measurements of the cross-plane thermal conductivity of epitaxial semiconductors. *J. Appl. Phys.* **105,** 54303 (2009).

197. Lefèvre, S., Volz, S. & Chapuis, P.-O. Nanoscale heat transfer at contact between a hot tip and a substrate. *Int. J. Heat Mass Transf.* **49,** 251–258 (2006).

198. Zhang, Y. *et al.* Length Scale of Correlated Dynamics in Ultra-thin Molecular Glasses. (2016).

199. Zhu, L. *et al.* Surface Self-Diffusion of an Organic Glass. *Phys. Rev. Lett.* **106,** 256103 (2011).

200. Swallen, S. F. *et al.* Organic glasses with exceptional thermodynamic and kinetic stability. *Science* **315,** 353–6 (2007).

201. León-Gutierrez, E. *et al.* In situ nanocalorimetry of thin glassy organic films. *J. Chem. Phys.* **129,** 181101 (2008).

202. Leon-Gutierrez, E., Sepúlveda, A., Garcia, G., Clavaguera-Mora, M. T. & Rodríguez-Viejo, J. Stability of thin film glasses of toluene and ethylbenzene formed by vapor deposition: an in situ nanocalorimetric study. *Phys. Chem. Chem. Phys.* **12,** 14693–14698 (2010).

203. Rodríguez-Tinoco, C., Gonzalez-Silveira, M., Ràfols-Ribé, J., Lopeandía, A. F. & Rodríguez-Viejo, J. Transformation kinetics of vapor-deposited thin film organic glasses: the role of stability and molecular packing anisotropy. *Phys. Chem. Chem. Phys.* **17,** 31195–31201 (2015).

204. Dalal, S. S., Walters, D. M., Lyubimov, I., de Pablo, J. J. & Ediger, M. D. Tunable molecular orientation and elevated thermal stability of vapor-deposited organic semiconductors. *Proc. Natl. Acad. Sci.* **112,** 4227–4232 (2015).

205. Pogna, E. A. A. *et al.* Probing equilibrium glass flow up to exapoise viscosities. *Proc. Natl. Acad. Sci.* **112,** 2331–2336 (2015).

206. Kearns, K. L., Still, T., Fytas, G. & Ediger, M. D. High-Modulus Organic Glasses Prepared by Physical Vapor Deposition. *Adv. Mater.* **22,** 39–42 (2010).

207. Tian, Z., Esfarjani, K., Shiomi, J., Henry, A. S. & Chen, G. On the importance of optical phonons to thermal conductivity in nanostructures. *Appl. Phys. Lett.* **99,** 53122 (2011).

10.Glossary

Greek symbol

δ	Uncertainty / $\omega(\boldsymbol{k})$ exponent
Δ	Error / Increment
ε	Energy from the conduction band level
η	Efficiency
μ	Chemical potential
ζ	Chemical potential from the conduction band level
Π	Peltier coefficient
ρ	Density
σ	Electrical conductivity
τ	Relaxation time
ω	Angular frequency

Latin symbols

c	Specific heat
C	Heat capacity
d	Penetration depth / diameter
D	Thermal diffusivity / Density of states
$\boldsymbol{E} = (E_x, E_y, E_z)$	Electric field
E_c	Conduction band energy
G	Thermal conductance
I	Electrical current
k	Thermal conductivity
k_e	Electronic thermal conductivity
k_l	Lattice thermal conductivity
$\boldsymbol{k} = (k_x, k_y, k_z)$	Wave vector
k_B	Boltzmann constant

l	Mean free path
L	Length
m	Mass
N	Number of particles
p	Porosity
$\boldsymbol{p}$	Momentum
q	Heat generated per unit volume per unit time
$\boldsymbol{q} = (q_x, q_y, q_z)$	Directional heat flow per unit area
Q	Heat flow or heat generated per unit time
$\boldsymbol{r}$	Position
R	Absolute resistance
ΔR	Resistance increase
R_{Th}	Absolute thermal resistance
S	Seebeck coefficient (Thermopower)/Section
t	Time
t_{film}	thickness film
T	Absolute temperature
ΔT	Temperature increase
TCR	Temperature coefficient of resistance
U	Internal energy
V	Voltage
$\boldsymbol{v}_g = (v_{g,x}, v_{g,y}, v_{g,z})$	Group velocity
w	Width

Subindex

0	Initial value
b	Beams
B	Boundary
SMP	Sample
S	Sensor
H	Heater

HL	Heating line
HT	Total heater (including the beamlines)

Acronyms

ALD	Atomic Layer Deposition
BOX	Buried Oxide
BTE	Boltzmann Transport Equation
DoS	Density of States
EDX	Electron Dispersion X-Ray Scattering
FFT	Fast Fourier Transform
HRXRD	High-resolution X-Ray Diffraction
LPCVD	Low Pressure Chemical Vapor Deposition
MaCE	Metal-assisted Chemical Etching
MFP	Mean free path
ML	Monolayer
PECVD	Plasma-Enhanced Chemical Vapor Deposition
QDSL	Quantum Dot Superlattice
RIE	Reactive Ion Etching
SEM	Scanning Electron Microscope
SL	Superlattice
STEM	Scanning Transmission Electron Microscope
TEM	Transmission Electron Microscope
TMAH	TetraMethylAmmonium Hydroxide
TPD	N,N′-Bis(3-methylphenyl)-N,N′-diphenylbenzidine
VLS	Vapor Liquid Solid

11. Publications

1. **Ferrando-Villalba P**, Lopeandia A F, Abad L, Llobet J, Molina-Ruiz M, Garcia G, Gerbolès M, Alvarez F X, Goñi A R, Muñoz-Pascual F J and Rodríguez-Viejo J (2014) In-plane thermal conductivity of sub-20 nm thick suspended mono-crystalline Si layers, *Nanotechnology* **25** 185402.

2. Perez-Marín A P, Lopeandía A F, Abad L, **Ferrando-Villaba P**, Garcia G, Lopez A M, Muñoz-Pascual F X and Rodríguez-Viejo J (2014) Micropower thermoelectric generator from thin Si membranes, *Nano Energy* **4** 73–80

3. Molina-Ruiz M, **Ferrando-Villalba P**, Rodríguez-Tinoco C, Garcia G, Rodríguez-Viejo J, Peral I and Lopeandía A F (2015) Simultaneous nanocalorimetry and fast XRD measurements to study the silicide formation in Pd/a-Si bilayers, *J. Synchrotron Radiat.* **22** 717–22

4. **Ferrando-Villalba P**, Lopeandía A F, Alvarez F X, Paul B, de Tomás C, Alonso M I, Garriga M, Goñi A R, Santiso J, Garcia G and Rodriguez-Viejo J (2015) Tailoring thermal conductivity by engineering compositional gradients in $Si_{1-x}Ge_x$ superlattices, *Nano Research* **8** 2833–41

5. **Ferrando-Villalba P**, Takegami D, Ràfols J, Lopeandía A F, Abad L, Garcia G, Rodríguez-Viejo J, Real time thermal conductivity measurement during growth of ultrathin layers. **(Submitted to Nanoscale)**